VISCOUS RESPONSE IN SHEAR OF CLAYEY GEOMATERIAL

Nor Shahidah Binti Mohd Nazer

Thesis submitted to the Department of Civil and Environmental Engineering, University of Strathclyde, Glasgow, in fulfillment of the requirements for the degree of

Doctor of Philosophy

in

Civil and Environmental Engineering

August 2016,

Glasgow, UK

Declaration of authenticity and author's right

This thesis is the result of the author's original research. It has been composed by the author and has not been previously submitted for examination which has led to the award of a degree.

Signed:

Date: 30 August 2016

ACKNOWLEDGEMENT

To my supervisor, Professor Alessandro Tarantino, you are the greatest teacher I've ever met. Thank you, Prof.

To my beloved husband, Abdullah Khanif, my beloved kids, Awra Awliya and Nuh Afnan, my beloved Mother, Sabariah, my beloved father, Mohd Nazer and to all my beloved siblings, this thesis is for you guys.

To the examiners, Dr Roberto Vassallo and Dr Stella Pytharouli, thank you for the great feedbacks and recommendations.

To everyone in the Civil and Environmental Engineering Department, University of Strathclyde, thank you for everything.

Nor Shahidah,

Glasgow (2013-2016)

Abstract

Translational slides in clays are often characterized by long-lasting intermittent movements associated with the fluctuations of pore-water pressures. These are in turn associated with either the rise or fall of the groundwater table for the case where the failure surface develops in the saturated zone below the phreatic surface or the infiltration of rainwater for the case where the failure surface is located above the phreatic surface in the unsaturated zone.

Physically-based models designed to support hazard analysis of landslide movements and early warning systems require the integration of time-dependent (viscous) constitutive models for the shear displacements because landslide movements are typically controlled by the viscous behaviour of the clay geo-material. However, little information is available on the creep response of clay geo-materials under unsaturated conditions concerning different water content and matric suction values.

This thesis presents an investigation of the viscous response of a clay geo-material under saturated and unsaturated conditions. Creep and relaxation tests have been first carried out on saturated clay samples by means of direct shear box. For the creep tests, the shear force was increased to a target value and maintained constant while monitoring the shear displacements. For the relaxation tests, shear displacement was applied to a target value and maintained constant while monitoring the shear stress decay. To gain a conceptual understanding of the viscous response of the clay in shear, analogue models were developed based on combinations of springs and dashpots. The aim of this modelling simulation was to identify a single mechanical model to simulate both creep and relaxation response using single set of parameters. Tests on unsaturated samples at different water content were finally carried out to gain insight into viscous response of the clay under unsaturated conditions.

Table of Contents

Table of Figures

List of Tables

CHAPTER 1
INTRODUCTION

When evaluating the kinematics of rainfall-triggered landslides, be it a natural or a man-made slope, engineers and researchers tend to look at the empirical correlations between the displacement and rainfall distributions and these are extrapolated to simulate slope displacement associated with future rainfall events. However, a sound Early Warning System (EWS) should be based on a model of the slope kinematics and historical data should be used to calibrate the model rather than developing an empirical correlation.

Since slope movements associated with rainfall cause potential damage to houses, buildings, roads, and other man-made structures, as well as the risk of fatality, proper land planning should be implemented in landslide prone area so as to avoid such incidence from happening. Although it may sound impossible to stop a landslide from occurring, choosing the right and adequate risk mitigation may help to at least minimise, the risk of fatality. This mitigation programs basically act as a temporary-solution and its performance depends on many factors, amongst all are the type of landslides, scale of slope, location of slope (if in remote area, less or no mitigation is needed), the suitability of proposed mitigation work and of course, the budget to run the program. Government from all over the world have been spending huge amount of money to overcome this issue and despite many researchers have been working extensively on this problem, yet there are still gaps to be addressed.

The main interest in this dissertation is to focus on landslide risk from the geotechnical point of view. We will focus on fundamental aspects controlling the kinematics (movement) of landslide body. Viscous behaviour of clay geo-materials is a critical point to look at, especially for those translational slides with existing slip failures. The time-dependent (viscous) behaviour of clay is controlling ‘creep’ shear displacement of landslide. Creeping landslide incidence has been reported over few decades back but only recently it became national concern due to the rapid modernization which requires steep and hilly areas to be fully explored and commercialized.

Some studies have shown that creeping slope may moves at imperceptible rate (several mm per year) and the movements may continue for long periods without reaching failure (Picarelli et al., 2004b). However, this kind of slopes even though impersonate stable condition, may endangers anything above it especially to man-made buildings or someone living on it, since the slow slope movements can accelerate into a destructive landslide when subjected to heavy rainfall due to the pore pressure build-up within the slope body that cause decrease in soil shear strength.

When considering landslide’s failure mechanism, relationships between pore-water pressure and rainfall become the subject of interest due to their inevitable contribution to landslide movements (Picarelli et al., 2000; Schulz et al., 2009; Bernardie et al., 2014). When rain water infiltrates into the ground, it causes fluctuations of pore water pressure in the upper portion of the soil profile (unsaturated zone). Seasonal fluctuations in pore water pressure cause significant decrease in soil shear strength as a result of pore pressure build

up and may trigger slope movements. The Sarno landslide in town Campania, Italy is one example of landslides which cyclically mobilized by pore-water pressure fluctuations (Capparelli & Versace, 2014).

Early warning systems (EWS) are generally designed to forecast landslide hazard by detecting hazards and risk zones. Designing simple EWS is important so as to avoid confusion and loss of time during emergencies (Intrieri et al., 2013). Sound EWSs must be underpinned by properly designed mechanical models, in turn calibrated against field monitoring data, to allow for accurate projection of future movements. A large number of creep models in the literature, associated with early warning system for rainfall-induced landslides, are based on empirical models rather than physically-based models (Furuya et al., 1999). Empirical models are known to be limited to a specific boundary condition and did not provide clear conceptual understanding of landslide kinematics. Empirical models therefore offer limited application and also lack in theoretical basis (Huang et al., 2014).

In this research, we aim to simulate viscous response in shear of clayey geo-material using a mechanical analogue model built upon the combinations of spring and dashpots. In this way, creep and relaxation can be simulated using a single model, i.e. using a single set of parameters, and not treated separately as often happens when empirical models are used. Using a single model to capture both creep and relaxation is important in modelling the kinematics of a landslide since viscous response of clay geo-materials that controls landslide movements is never purely 'creep' mode because effective stress varies due to rainwater infiltration and/or groundwater fluctuation (Lai et al., 2014). Experimental tests in this thesis were therefore carried out under both saturated and unsaturated conditions to gain insight into viscous responses in shear.

1.1 AIM

The aim of this Doctorate's thesis is to study the viscous effect of creep in shear of clayey geo-materials by looking at its impact on mechanics of rainfall-induced landslides. We are looking at creep and relaxation responses in saturated and unsaturated condition to understand the role of time-dependent behaviour (viscous) of clay into the slope movements when subjected to rain water infiltration. The long-term objective of this work (outside the scope of this thesis) is to develop an Early Warning System tool that uses physical based model by taking into account kinematics of the slope, in particular creep, for the projection of future landslide movement.

Two sets of experimental test will be carried out using a direct shear box apparatus, one is a displacement-controlled test for stress relaxation and the other one is a force-controlled test for creep deformation. Since the conventional shear box is only suitable for a displacement-controlled test, modification to carry out creep tests will be implemented to the shear box by adding a pulley system. By doing this, applied horizontal force can be converted into tangential stress and maintained constant during shear to allow the soil to creep. Results obtained from the experimental datasets are capable of capturing the primary creep and secondary creep (tests at 90% of peak shear strength) and this can be useful in analysing the kinematics of a landslide body.

Then, we aim to develop a physically-based model to simulate creep and relaxation response from experimental data so as to gain a conceptual understanding on creep behaviour in shear of clayey geo-materials. The models (generalized Kelvin model) were constructed from a unique combination of spring and dashpots and each parameter are controlled by the spring elasticity and dashpot-viscous elements. Here, we are keen to construct a model that can be used to simulate both creep and relaxation response by a single set of viscous model parameters. A single model to capture different aspect of viscous behavior of clays is very important as clays in real conditions are rarely subjected to pure creep or relaxation.

Ideally, a single model should be used to model both saturated and unsaturated response and this route will be pursued in this thesis.

1.2 SCOPE OF WORK

The work in this thesis is carried out in stages as follows so as to achieve the following objectives:

1. Literature review of creep effects in shear response of clayey geo-materials in relation with rainfall-induced landslides and experimental-related and physical-based models for clay viscous response in shear
2. Experimental investigation – creep and stress relaxation tests under saturated and unsaturated conditions
3. Modelling – simulation of experimental data using mechanical models (generalized Kelvin models)
4. Interpretation and discussion
5. Recommendations for future work

1.3 LIMITATIONS

Time is the real issue in this research due to the time-dependent behaviour of clay that requires longer duration of experimental activities. The initial plan was to measure matric suction on each unsaturated specimens for every cycle of viscous tests using high-capacity tensiometer. Since the value of matric suction of the unsaturated specimens were found to be very high (more than 1200kPa), beyond the capability of the tensiometer to measure in long-duration tests, we have given up the measurement of matric suction during the shearing process. Measurements of matric suction and degree of saturation of the specimens were then acquired before and after each test only, so as to estimate matric suction and degree of saturation upon shearing.

1.4 ORGANISATION OF THE THESIS

1. Chapter 1 is the Introduction. It has discussed the overall aim and the specific objective of the research.

2. Chapter 2 is the Literature Review. All relevant work related to this research will be discussed in this chapter. The purpose behind the literature review is to identify what is the gap in the literature that we are trying to address in this research.
3. Chapter 3 presents the material tested and the equipment used. This includes the sample specimen preparation (from the ingredient mixing to the ready-to-shear specimens) and the calibration and validation of the equipment. Basically, there are three types of specimens prepared; saturated specimens at pre-peak condition, saturated specimens at post peak (residual) condition, and specimens under unsaturated conditions.
4. Chapter 4 discusses the Experimental Procedures. All experimental procedures involving saturated and unsaturated condition will be illustrated in detail in this chapter including their validation.
5. Chapter 5 presents the experimental results and the models developed to simulate the experimental data Simulation. Viscous response from each viscous test performed and modelling simulation using analogue viscoelastic models of combinations of spring and dashpots (3=element model, (3+1)-element model, and (5+1)-element model) will be presented in this chapter.
6. Chapter 6 focuses on the data interpretation and discussion. Both qualitative and quantitative interpretation is addressed in this chapter.
7. Chapter 7 addresses the conclusions of the research along with the recommendation for future work.

CHAPTER 2
LITERATURE REVIEW

2.1 INTRODUCTION

This chapter presents an overview of the main topics covered in this research. The literature discussion is sub-divided into three categories, starting with the creep theories, followed by Early Warning System for rainfall-induced landslides and, lastly, the role of viscosity in rainfall-induced landslides.

2.2 CREEP THEORIES

The theories behind creep in soil will be touched briefly. Creep is a viscous phenomenon that is relevant in clays and is of major concern to the engineers after series of prolonged deformation takes place in the building activities, causing significant financial losses. Creep behaviour can be divided into two types; volumetric creep and deviatoric creep. Volumetric creep can be regarded as a one-dimensional secondary effect if the deviatoric stress present in the K_o state induces no creep. In a two-dimensional situation under constant effective stress, apart from the volumetric creep, deviatoric creep also occurs. Volumetric creep or so-called secondary compression, is a deformation under constant effective stress, and is not to be confused with the primary consolidation. Primary consolidation involves volume change due to expulsion of water from voids and transferring load from the pore water pressure to the soil (Bjerrum, 1967).

In 1975, Ter-Stepanian from his long duration experiment concludes that deviatoric creep process consists of two phases, the mobilization phase and the rupture phase. The mobilization phase marked by logarithmic creep curves showing a decreasing strain rate with time, whereas the rupture phase is denoted by the parabolic curves, showing a jump-like changes in the strain rate with time (Figure 2.1).

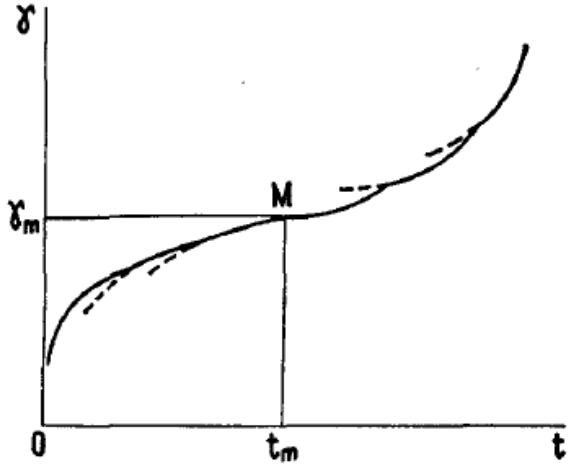

Figure 2.1 Creep curve during shear; M is the mobilization unit (source: Ter Stepanian, 1975)

The most widely acknowledged concept of creep distinguishes between the phases of creep movement (Okamoto et al., 2004; Petley et al., 2005a, 2005b, 2008) and it consists of three distinct stages, namely the primary, secondary and tertiary creep. In the primary creep stage, strains are initially high but decrease with time. During the secondary creep phase the material suffers diffuse damage but strains generally occur slowly with time at almost steady state rate (Okamoto et al., 2004), or may even stop altogether (Petley et al., 2008). When diffuse micro-cracks start to interact to form a shear surface, the critical point into the tertiary phase is reached (Reches and Lockner 1994; Main 2000). This phase is characterized by a rapid acceleration of displacement until final failure.

Based on triaxial apparatus for creep test under constant effective stress, similarly, the three stages of creep (Figure 2.2) according to Augustesen et al (2004) was established, 1) Primary creep (damping, unsteady), 2) secondary creep (steady, constant rate) and 3) tertiary creep (undamped or progressive flow). Di Maio et al (2013) obtained similar creep stages from shear creep tests conducted by means of modified Casagrande shear apparatus (Figure 2.3).

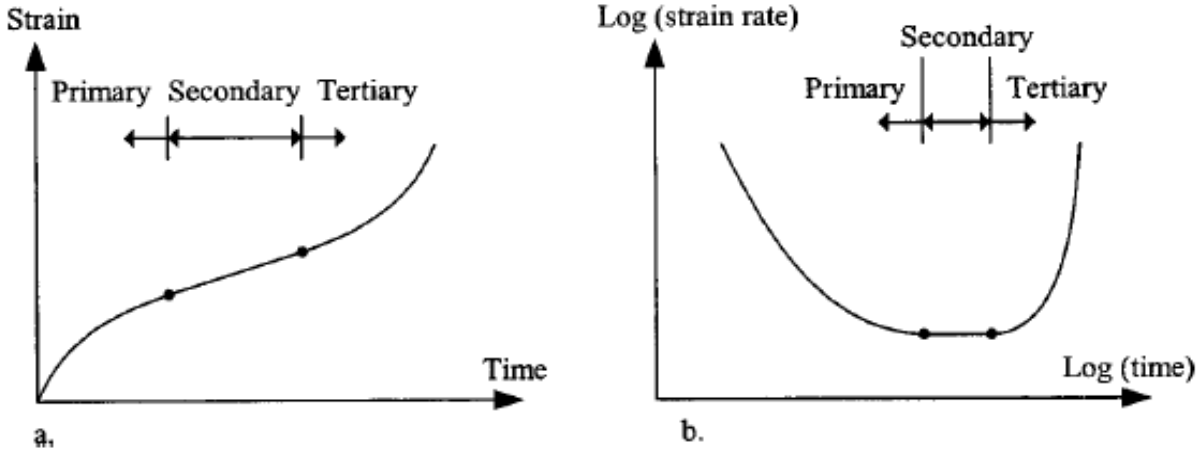

Figure 2.2 (a) Creep stages and (b) strain rates in creep test by triaxial apparatus (source: Augustesen et al., 2004)

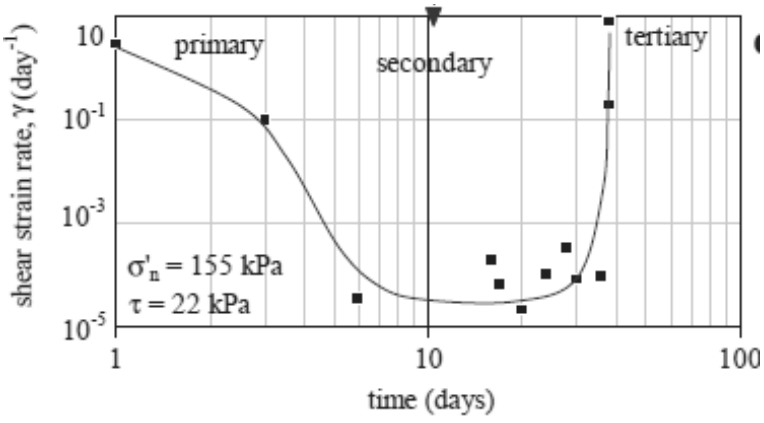

Figure 2.3 Log strain rate against time (source: Di Maio et al., 2013)

There are basically two approaches when dealing with soil creep prediction, Hypothesis A and Hypothesis B. These two hypotheses differ from each other through the origin of time defining the exact moment the creep process actually starts. Hypothesis A suggests that creep deformation will start only after the primary consolidation finishes or after the dissipation of excess pore water pressures completes. It is assumed that creep has no contribution to primary consolidation and should be treated separately. Hypothesis B, on the other hand, assumes that creep deformation starts simultaneously with primary consolidation, which means that it takes place throughout the whole compression process. Hypothesis B has been widely accepted by other researchers even if its prediction method is quite complex (Fatahi et al., 2012).

Many theories explaining the mechanism of creep deformation in solid materials and one that is widely accepted is the theory of rate process proposed by Muruyama and Shibata (1961). The creep deformation is generated by the movements of the atoms and molecules under the effect of constant stress to a new equilibrium position. Sufficient activated energy is required to conquer the virtual energy barriers which resist the movements between atoms and molecules. Similarly, the creep deformation of soils is evaluated based on the activation energy and the number of inter-particle bond per unit area (Fatahi et al., 2012).

Veveakis et al. (2007) proposed that shear heating as the primary mechanism for the long-term phase of accelerating creep due to the temperature rise within the location where creep localized, a clay-rich water saturated layer. He used rigid block modelling and calibrated it using real velocity measurements from Vaiont landslide. He concluded that the total loss of the strength in the slipping zone during the last minutes prior to the slide can be explained by the onset of thermal pressurization, triggered by the temperature rise within the clay-rich layer.

Further information of creep theories can be found in details by Le (2015). Summary of creep mechanism occurring in soft soils of fine grained materials are shown in Table 2.1. There appear to be a great number of constitutive models proposed in the literature to account for the time-dependent behaviour of soils. In general, three categories of constitutive models exist in the literature (Liingaard et al., 2004):

- Empirical models: mainly acquired by fitting experimental results from creep, stress relaxation and constant rate strain tests, and its constitutive relations are given by closed-form solutions or differential equations. They are known to be limited to specific boundary and loading conditions, so the relations are not general. The models may be used as a base to develop 3-D constitutive relations.
- Rheological models: describe uniaxial conditions and they are given as closed-form solution or in a differential form. Often used to obtain a conceptual understanding of time effects in soil.
- General stress-strain-time models: a 3-D model. Often given in incremental form so they are readily adaptable to numerical implementation and suitable for a finite element procedure. The models are not limited to specific boundary from which they are calibrated i.e. all possible stress paths can be simulated

At present, there are numbers of creep models proposed, each with different variables approach. Water is seen as main dominant factor to creep (Young, 1972), but there are many other variables seems to relevantly contribute to soil creep such as vegetation effect (Van Asch et al., 1989; Lebouteiller, 2008), soil plasticity (Desai et al., 1995), soil density, slope angle (Komamura and Huang, 1974) and swelling effect (Yin and Tong, 2011). Amongst all, three-dimensional (3D) models based on the viscoplasticity framework of Perzyna (1963, 1966) are broadly produced by researchers (Zienkiewicz and Cormeau, 1974; Adachi and Oka, 1982; Borja and Kavazanjian, 1985; Desai and Zhang, 1987; Kaliakin and Dafalias, 1990; Kutter and Sathialingam, 1992; Vermeer and Neher, 1999). Apart from 3D modelling, there is also 1D modelling which based on elasto-visco plastic modelling (EVP) (Yin and Graham, 1989, 1994). The extended model of 1D EVP is later produced to account with swelling effect in soil creep and known as 1D EVPS model (Yin and Tong, 2011). It is of no intention to go into detail all the constitutive models existed in the literature. Further details can be found in the review paper written by Liingaard et al (2004) – for saturated soils or Sheng (2011) – for unsaturated soils.

Table 2.1 Main creep mechanisms in soft soils (source: Le 2015)

Mechanism	Main factors/Focus	Introduced or supported by
Breakdown of interparticle-bonds	Relative movement of particles, soil structure rearrangement	Taylor & Merchant (1940), Terzaghi (1941), and accepted by Gibson & Lo (1961), Mesri (1973, 2003), Mesri & Godlewski (1977), and Crooks et al. (1984).
Jumping of molecule bonds	Active energy, temperature and deviatoric stress	Muruyama & Shibata (1961), Christensen & Wu (1964), Mitchell (1964), Kwok & Bolton (2010)
Sliding particles	Activate energy, contact forces	Grim (1962), Gupta (1964), Kuhn & Mitchell (1993)
Water flows between two drainage structures (Macro-micro structures)	Two levels of soil structures, water flows in two pore structures and deformations in pores	De Jong & Verruijit (1965), Berry & Poskitt (1972), Zeevaart (1986), Navarro & Alonso (2001), Mitchell & Soga (2005) and Wang & Xu (2007)
Structural viscosity	Different viscosity of absorbed water system, clay mineral-water interaction	Terzaghi (1941), Barden (1969), Bjerrum (1967), Garlanger (1972), Christie & tonks (1985), Graham & Yin (2001)

.

2.3 EARLY WARNING SYSTEM OF RAINFALL-INDUCED LANDSLIDES

Slow moving landslides impose many problems to the modern world. Impact from rapid development especially in hilly areas causes excessive burden on slopes. As a consequence, the slopes become unstable inducing the risk of mass movements. Areas with landslide incidence, will give impacts not only to the infrastructures and communities living nearby, but also to the socio-economic growth. In any regional-scale town planning, avoiding/minimising the landslide risk is a crucial aspect to be addressed.

Landslide remedial measures program require huge amount of money to be spent. In addition, landslides cannot be completely stopped from deforming due to the morphological factors (mountainous terrain, hilly), materials characteristics (internal strain) and hydrological effects (ground water, rain water, surface runoff) of the slopes. However, we can at least minimise the risk of fatality by adopting appropriate and proper Early Warning System to area prone to landslides so as to alarm people from any possible danger (Corominas et al., 2005). This can be extended to those who live in the vicinity of slow moving landslide where prediction of long time effects is necessary to avoid such incidence.

Prediction of future movements based on the actual slope displacements (landslide indicator) and rainfall thresholds (landslide precursor) known to be the most adopted approach in risk management planning for landslides. When developing a risk mitigation strategy for landslides prone areas, especially for the case of creeping landslides where the behaviour is controlled by the time-dependent behaviour of clay materials, a reliable mechanical model through deep understanding of the mechanism of slope behaviour should be incorporated (Picarreli et al., 2004a & Corominas et al., 2005). Quantitative risk assessment approach formed as a basis towards assessing the state of risk at present time and for forecasting sustainability of landslide-prone communities (Ranalli et al., 2013). According to Intrieri et al (2012), the implementation of Early Warning System requires different components combination to form a reliable mitigation measures. These chain-like components, including the identification of the risk scenarios, emergency plans, societal considerations and public awareness, act together in such a way that if any of the element fails, would collapsed the whole operational system. Landslide EWS can therefore be described as a balance combination of four main activities as proposed by Dibiagio and Kjekstad (2007). The four activities comprises of:

- Monitoring, including data acquisition, transmission and maintenance of the instruments;
- Analysis and forecasting, which were done by using thresholds, expert judgement forecasting methods and so on;
- Warning, i.e. the dissemination of understandable messages alerting for the impending threat;
- Response, concerning if people are able to understand and how they react to the warning

It is also well understood that designing EWS of rainfall-induced landslides is a complex task and usually site-specific due to the large variability of parameters controlling the

mechanism of landslides (Intrieri et al., 2013). However, it is not impossible to produce EWS that works perfectly as long as sound knowledge of the behaviour of landslides is properly captured. These include the mechanism, the potential triggers aspects and their respective thresholds (i.e. rainfall intensity and duration), the expected time to failure or reactivation, the expected velocity, and the areal of extent including the runout distance, where appropriate (Corominas et al., 2005).

2.4 EFFECT OF VISCOSITY ON KINEMATICS OF LANDSLIDES TRIGGERED BY RAINFALL OR GROUNDWATER FLUCTUATION

Long term monitoring of landslide displacements is crucial in understanding the changes that may trigger to massive landslide movement. Among the well documented case with long monitoring of landslide displacements is the Vallcebre landslide in the Eastern Pyrenees, Italy. The Vallcebre landslide was considered as an active landslide as the movement never completely stopped moving since the beginning of continuous monitoring in 1996 although noticeable dropped in velocities (Figure 2.4) were observed during dry periods (Corominas et al., 2005). Figure 2.5 shows the typical vertical profile of landslide displacement taken from a landslide of complex clayey formation of the Italian Southern Apeninnes acquired from fixed-in-place inclinometer probes. The displacement on the slip surface (between point A and B) can be considered representative of the displacement along the whole height of the landslide with uniform displacements observed in the verticals I8 and I10 (Di Maio et al., 2010). Figure 2.6a and b shows the inclinometer profile for Costa della Gaveta landslide, with and without slip surface. Three components of displacement can be clearly distinguished and analysed: sliding AB along the slip surface and the resultants of internal deformations (creep) BC and CD. The AB component of which occurs in a very narrow layer largely prevails and gives the character of substantial uniformity to the profiles (Di Maio et al., 2013).

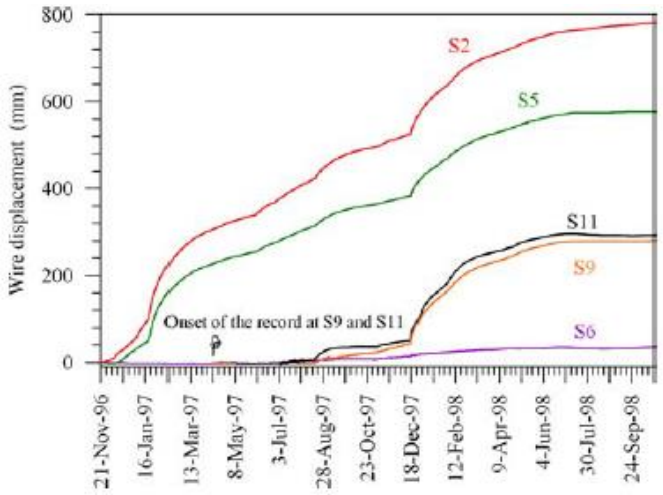

Figure 2.4 Wire displacements at boreholes S2, S5, S6, S9 and S11 (source: Corominas et al., 2005)

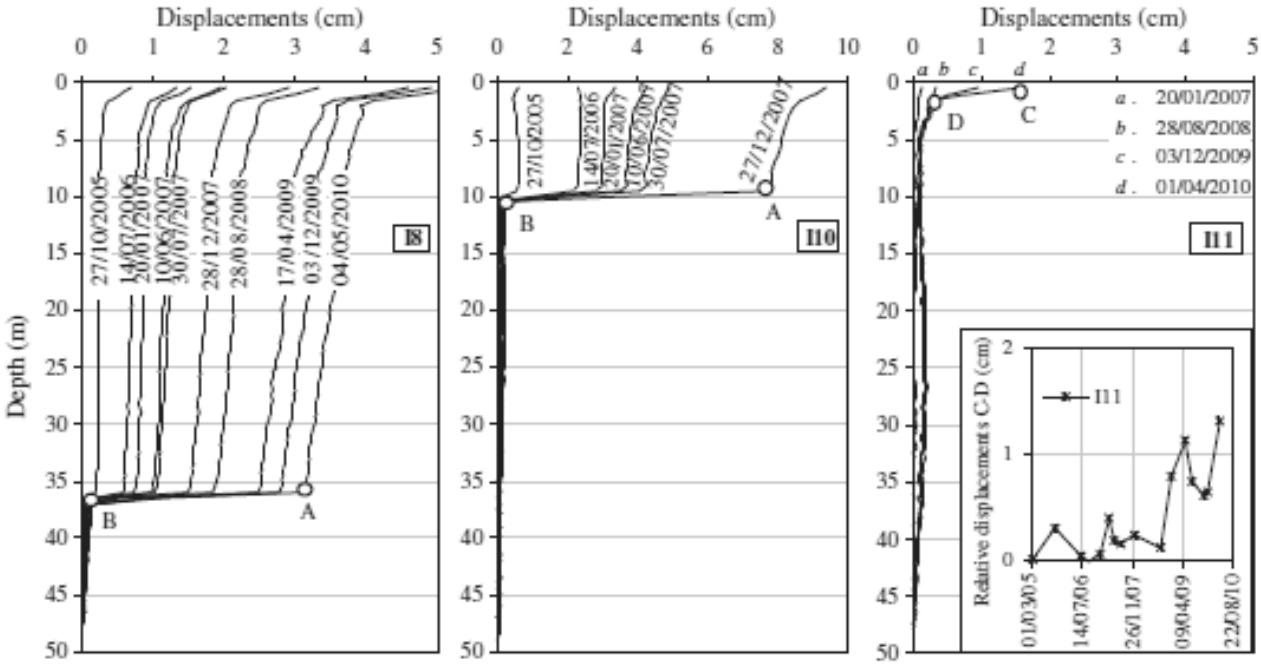

Figure 2.5 Inclinometer displacement profiles (zero measurements: March 2005) (source: Di Maio et al., 2010)

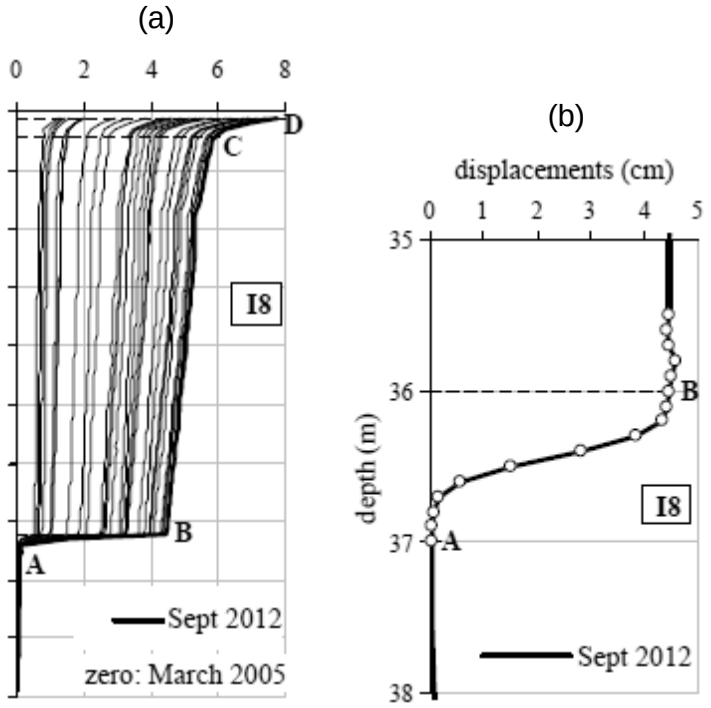

Figure 2.6 Longitudinal median section of the landslide with inclinometer profiles a) Inclinometer profile of the boreholes b) Inclinometer profile in correspondence with slip surface (source: Di Maio et al., 2013)

Landslides induced by rainfall are an important class of landslides. Different approaches were used by researchers to predict landslide movements when subjected to rainfall infiltration. These include Vassallo et al (2015) who developed a physically based approach by means of 3-D finite difference code (MODFLOW) to understand the process relating rainfall regime to pore water pressure distributions and displacements, Bernardie et al. (2015) who combined statistical with mechanical approach into 1-D viscoplastic model to predict the changes in landslide displacement rate with the amount of rainfall as a result of pore water pressure change, and Ranalli et al. (2013) who adopted probabilistic approach based on Bayesian theorem into its viscoplastic-dynamic model. Some consider the use of rainfall thresholds to analyse the relationship between the triggering precipitation and the movement, for example Intensity-duration (I-D) threshold (Larsen and Simon, 1993 & Guzzetti et al., 2007) and intensity-antecedent rain-duration (I-A-D) model based on power law function (Guzzetti et al., 2008).

Behaviour of slopes subject to failure can be subdivided into four different stages; the pre-failure, failure, post-failure and reactivation (Leroueil et al., 1996). Slope experiences small strains due to progressive change in the stress field or soil properties at the beginning of the pre-failure stage. Slip surface formed by the occurrence of local failure within the zones of stress concentrations characterized by shear strain localization and formation of a shear surface. The onset of general failure (first-time failure) starts when the failure zone spread up to the ground surface. In the post-failure stage, the landslide body moves along the slip surface. Landslide body will then reaches an equilibrium condition in the long term and finally the reactivation of landslides will slide along the existing slip surface once the induced shear stress exceeds the residual value (Picarelli et al., 2004).

Figure 2.7 shows a possible evolution of horizontal slope displacement in the pre-failure stage. The rate of movement increases, as a result of a reduction of soil stiffness and increasing creep. When at some points in the subsoils the stress path reaches failure envelope, local failure occurs at point A. Figure 2.8 shows the aspect of slope behaviour in the post-failure stage. In brittle soils, due to shear strength reduction, acceleration is expected after the onset of failure. In contractive soils, if deformations develop quickly enough, movements may further accelerated by induced pore pressure increases. Dissipation of excess pore pressure contributes to landslide deceleration (Picarelli et al., 2004).

Figure 2.9 shows the typical stress-strain curves for commonly accepted concepts of peak and residual shear strength (after Skempton, 1964). Peak shear strength is the maximum value of shear stress a soil can sustain and usually obtained at relatively small displacement. To achieve residual shear strength, larger displacement is somehow needed in which the soil particles have become aligned in the directions parallel with the direction of sliding. Ring shear apparatus is commonly used for this purposed, however one can used direct shear box (multiple reversal shearing) or cut plane triaxial testing for similar.

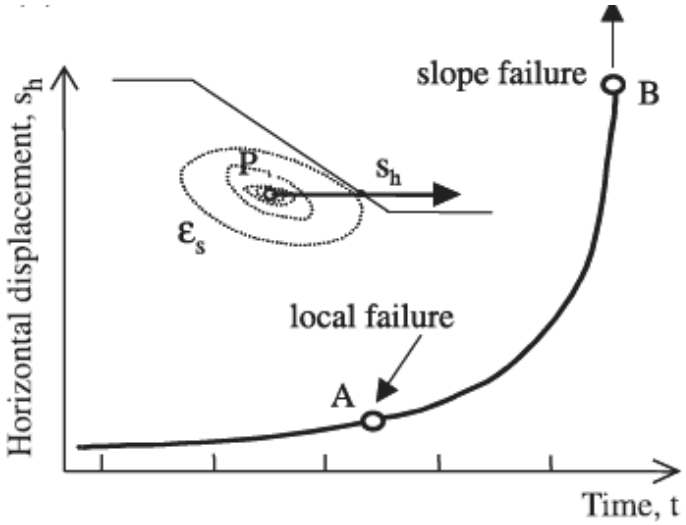

Figure 2.7. Schematic slope behaviour in the pre-failure stage as a function of pore pressure fluctuations (source: Picarelli et al., 2004)

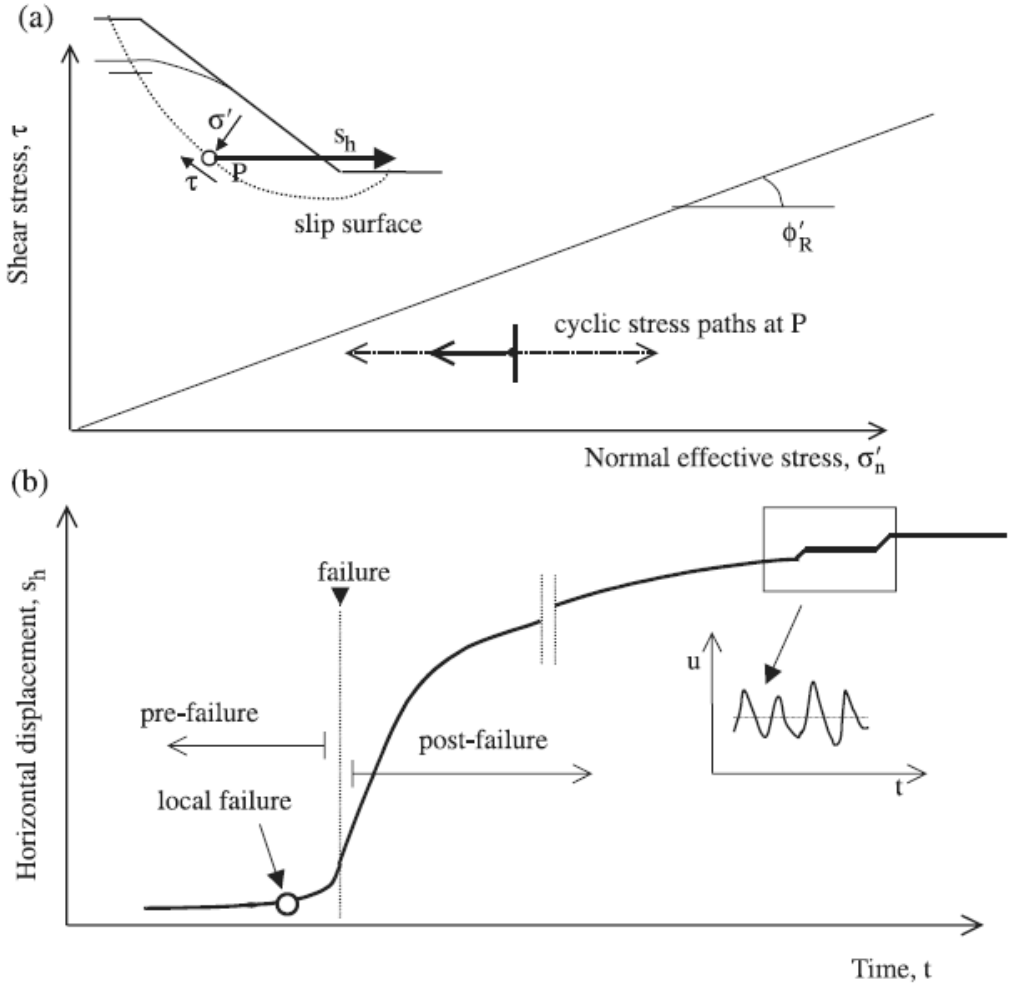

Figure 2.8. Schematic slope behaviour in the post-failure stage as a function of pore pressure fluctuations a) cyclic stress path b) horizontal displacement (source: Picarelli et al., 2004)

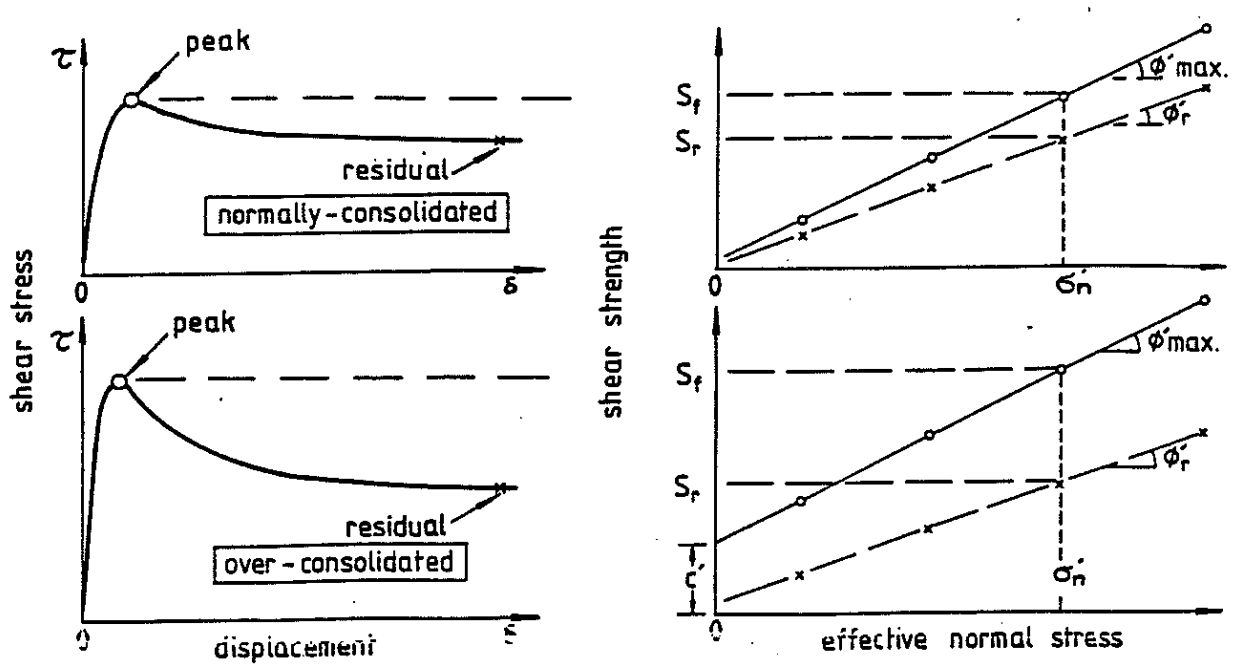

Figure 2.9 Simplified shear strength properties (source: Skempton, 1964)

Some soils exhibit a time dependent behaviour that can be described using a typical fluid property as viscosity. Slow slope movements are usually associated with creep, a time-dependent deformation imposed by the viscous behaviour in clayey geomaterials (Ranalli et al., 2010 & Bhat et al., 2011). Creep can appear over the whole thickness of the mass in movement or only in one localised band zone, the shearing zone. This shearing zone varies in thickness, typically several millimetres. Movements along pre-sheared slip surfaces are strongly affected by ground water table fluctuations, where they are showing periodic events at rest and activation with the rainfall infiltration (Ranalli et al., 2013). Changes in pore water pressure due to ground water fluctuations and/or rainfall infiltration cause changes in effective stress in the shearing zone often resulting in significant changes to the landslide displacement rate (Conte et al., 2013). Creep can be maintained for long periods, however, creep gradually decreases shear strength and eventually the slope may fail.

2.4.1 Field investigation

Vassallo et al. (2015), based on the field investigation at the Costa Della Gaveta landslide, showed that the variations of pore pressure caused by rain water infiltration are only significant at depths lower than about 10m. Because the depth of slip surface varies, all parts along the slip surface are subjected to different pore pressure perturbation, hence different shear strengths which in turn, result in different overall landslide deformations. The landslide is characterised by a maximum depth of about 40 m with hydraulic conductivity $k = 10^{-9}$ m/s in the stable Varicoloured Clays and 10^{-8} m/s in the earth slide body. The earth slide body is mainly constituted by destructured clays with abundant rock fragments

with clay fraction c.f. up to 50%. Liquid limit w_L was found to be between 40% and 80% and below the first 2 m, the degree of saturation *Sr* ranges between 95% and 100%.

Conte et al. (2013) used a finite element approach into elasto-viscoplastic constitutive model in conjunction with a Mohr-Coulomb yield function to analyse the mobility of an active slow-moving landslide. Their work focused on describing the behaviour of soil in a shear zone, a narrow part of the landslide body where deformations were concentrated and directly influenced by the fluctuations of ground water table. This is similar to what have been done by previous researchers, Corominas et al. (2005) who focused on the influence of viscous behaviour on Vallcebre landslide displacement and velocity in relation to groundwater fluctuations. They proposed a dynamic-physical model that uses momentum equation with addition of a viscous term (Bingham and power law) to account for viscous force effects during movement.

A classical static analysis was found to be more suitable for stability analysis, usually for the determination of slope factor of safety (FS), rather than modelling the actual kinematics of soil mass behaviour. For the case of continuously moving landslides, some researchers adopted dynamic analysis (Corominas et al., 2005, Ranalli et al., 2010 & 2013, Bernardie et al., 2015) by introducing the viscous force into the equation of motion and predicting landslide movements under the influence of viscous behaviour. Corominas et al. (2005) highlighted the importance of viscous behaviour based on two evidences from the studies of Vallcebre landslide in the Eastern Pyrenees, Spain, first by looking at the one to one relationship between acceleration and position of the groundwater level and second by comparing the groundwater level changes with wire displacements from borehole. Measurements of pore pressure related to the fluctuations of the water table governed by rainfall were given by Peizometric readings along with extensometer for landslide displacement (Figure 2.10).

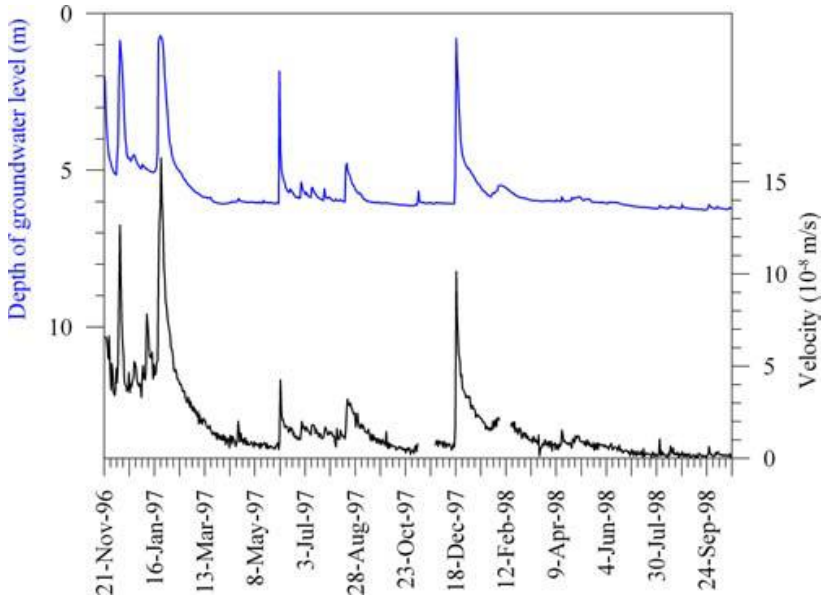

Figure 2.10 Piezometric record (blue line) and landslide velocity (black line) (source: Corominas et al., 2005)

The dynamics of landslide can be explained with momentum equation written as:

$$F - F_r = ma \quad [1]$$

where *m* is the mass of a portion of an infinite slope and *a* is its acceleration. By adopting the Mohr-Coulomb criterion, resisting forces acting at the base of the slope can be estimated depending on the cohesion and friction angle. By computing forces over a unit surface, shear stress of the slip surface can be considered by:

$$\tau - [c' + (\sigma - p_w)tan\emptyset'] = ma \quad [2]$$

where τ is the applied (destabilising) shear stress, c' is the cohesion, σ is the normal stress, p_w is the ground water pressure and $\emptyset'$ is the friction angle. Field record during dry period is showing constant velocity though acceleration would be expected if the system is having such an unbalanced force. The scientific community once debates about if the shear strength of clays really depends on velocity, even at the low displacement rates that frequently "creeping" landslide have. However, it appears that without a viscous force the equation, after integration, would give a very high displacements, like a ball on an inclined plane, in a very short time. Therefore, a viscous component should be considered in Eq. (2) apart from the inertial terms (Corominas et al., 2005, Ranalli et al., 2010). This corroborates the importance of viscous force as important components in the momentum equations and not just some sort of numerical expedient to simulate something.

If the viscous behaviour is modelled as via the Bingham law for the sake of simplicity, the equation representing the infinite slope kinematic can be written as follows:

$$\gamma\, l \sin a \cos a - [c' + (cos^2\alpha - p_w)tan\emptyset'] = ma + \eta\frac{v}{z} = m\frac{dv}{dt} + \eta\frac{v}{z} \quad [3]$$

where γ is the specific weight of the sliding mass, η is the viscosity, v is the velocity and z is the thickness of the shear zone. The viscosity, η was obtained by nonlinear regression to minimize differences between the measured and the computed displacements. The displacements were obtained from displacements measured in wire extensometers. Figure 2.11 shows the infinite slope model used in this approach along with its variables.

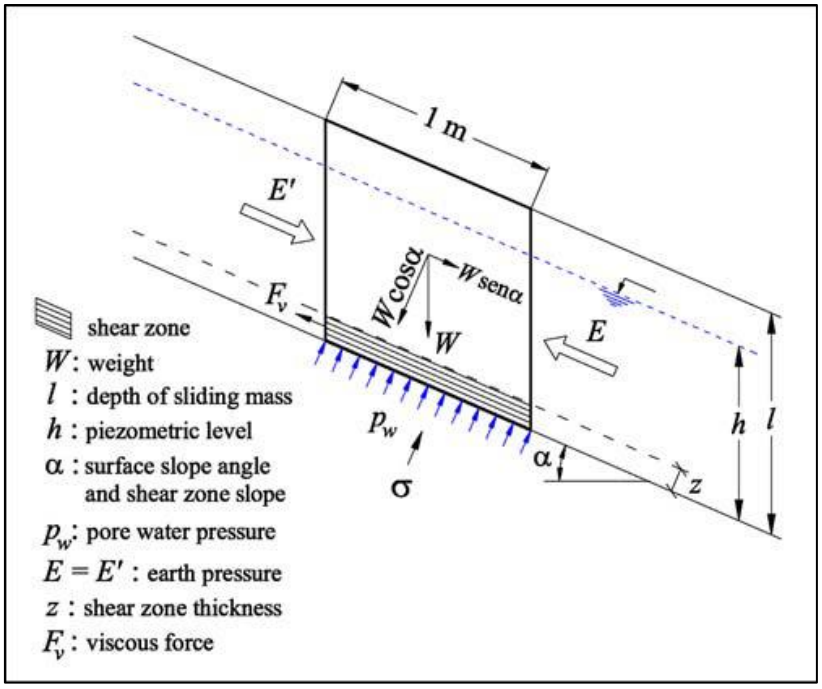

Figure 2.11 Geometry and variables used in the local analyses (source: Corominas et al., 2005)

Some researchers used mathematical approaches when dealing with creeping slopes deformation. Maugeri at al. (2006) proposed mathematical model for creeping slopes at Gagliano Castelferrato, Italy by introducing single-layer scheme and multi-layer scheme to predict the deformation evolution of a hypothetical vertical line inside a slope due to pore pressure rising. Different viscosity parameters, η_i were adopted to different depth layers by taking into account the boundary velocity values, v_i and v_{i-1}, for each layer (Figure 2.12).

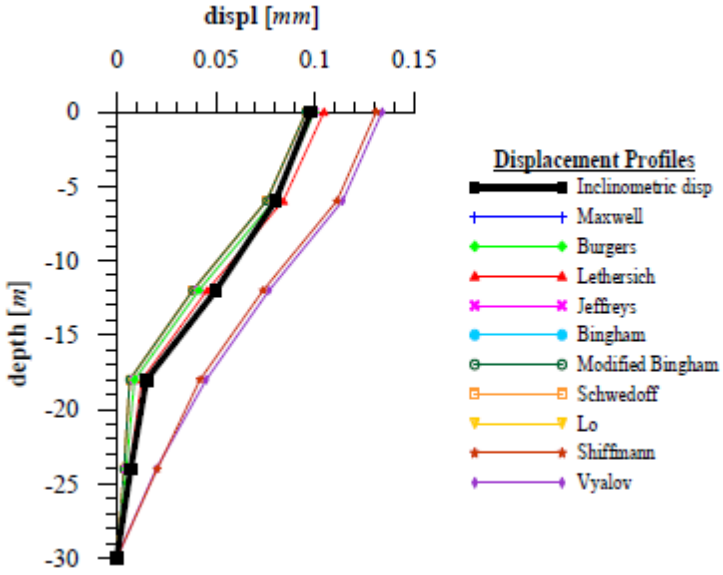

Figure 2.12 Gagliano Castelferrato landslide: displacement profiles (source: Maugeri et al., 2006)

Puzrin & Schmid (2011, 2012) adopted a simple analytical model based on visco-elastic-plasticity to quantify the evolution of a constrained creeping landslide when stabilised at the bottom of the sliding mass (either by retaining wall or natural barrier). They discovered that for first-time failure, zone of intense shearing is likely to involve the whole clay layer, either being smeared or localized in a number of parallel discontinuous thin shear bands where the shear strength on slip surface τ^* reduces to residual value τ_r when the shear strain reaches the critical value γ_r (Figure 2.13).

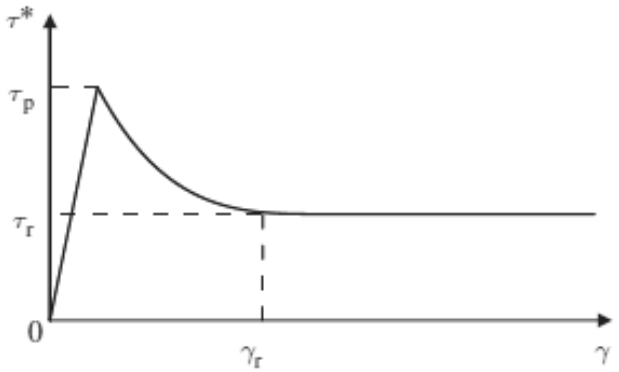

Figure 2.13 Shear behaviour of strain softening-material (source: Puzrin & Schmid, 2011)

Previous studies on creep investigation are mainly focusing on saturated (below ground water table) pre-peak conditions. Relatively few studies are indeed focusing on residual (post-peak) conditions and unsaturated states. Infiltration in unsaturated materials is a complex process and strongly dependent on initial conditions such as antecedent soil water conditions, degree of saturation, pore pressure field, hydraulic conductivity and amount of water required for saturation. As a result, it is difficult to relate rainfall conditions to pore water pressures and to the occurrence of landslides. Seasonal variations of pore pressures close to surface are not necessarily reflected by deeper layers if materials are rich in clay and thus have low permeability (Leroueil, 2004).

2.4.2 Laboratory creep test

Triaxial apparatus is widely used by researchers to conduct creep tests (Augustesen et al., 2004, Lai et al., 2015). Bhat et al. (2013) carried out residual-state shear creep tests using an apparatus modified from existing torsional ring shear apparatus (Figure 2.14).

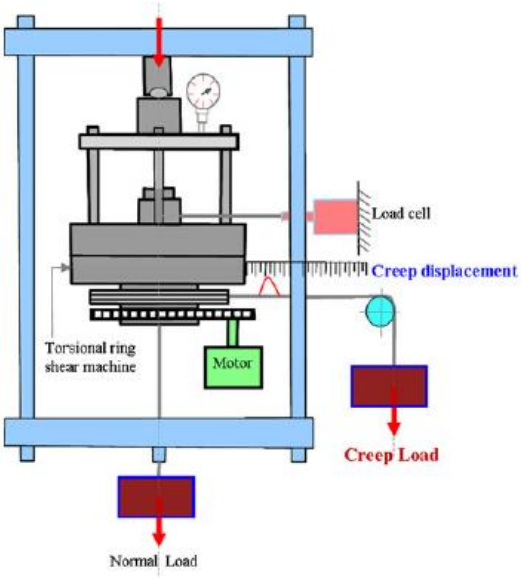

Figure 2.14 Modified torsional ring shear apparatus for residual-state creep test (source: Bhat et al., 2013)

Di Maio et al. (2013) used Casagrande direct shear apparatuses that have been modified for shear creep tests to investigate the attitude of a clayey material to undergo shear creep and to evaluate the creep threshold values and the flow parameters (Figure 2.15). They conducted creep tests on the specimen pre-sheared to the residual condition and on an "intact" specimen. Figures 2.16a, b, c and d show the result of creep tests for both specimens. For creep tests on pre-sheared specimen, only primary creep was observed at shear stress $\tau \leq \tau_r$. At $\tau > \tau_r$, short primary creep was observed followed by secondary creep with an average rate of 0.1mm/day for 34 days. It later achieved fast tertiary creep and failed. For creep tests on an "intact" specimen, only primary and secondary creep is observed.

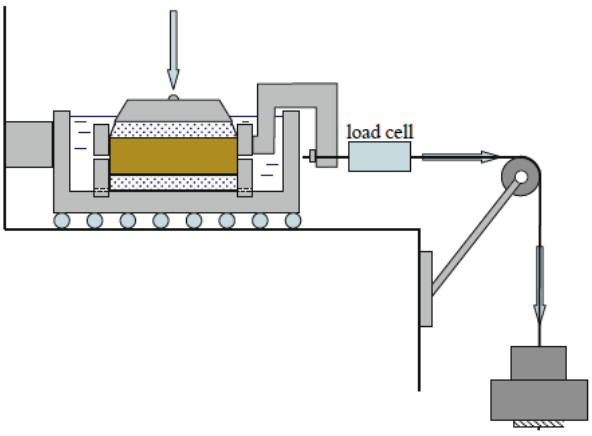

Figure 2.15. Casagrande direct shear apparatus modified for shear creep tests (source: Di Maio et al., 2013)

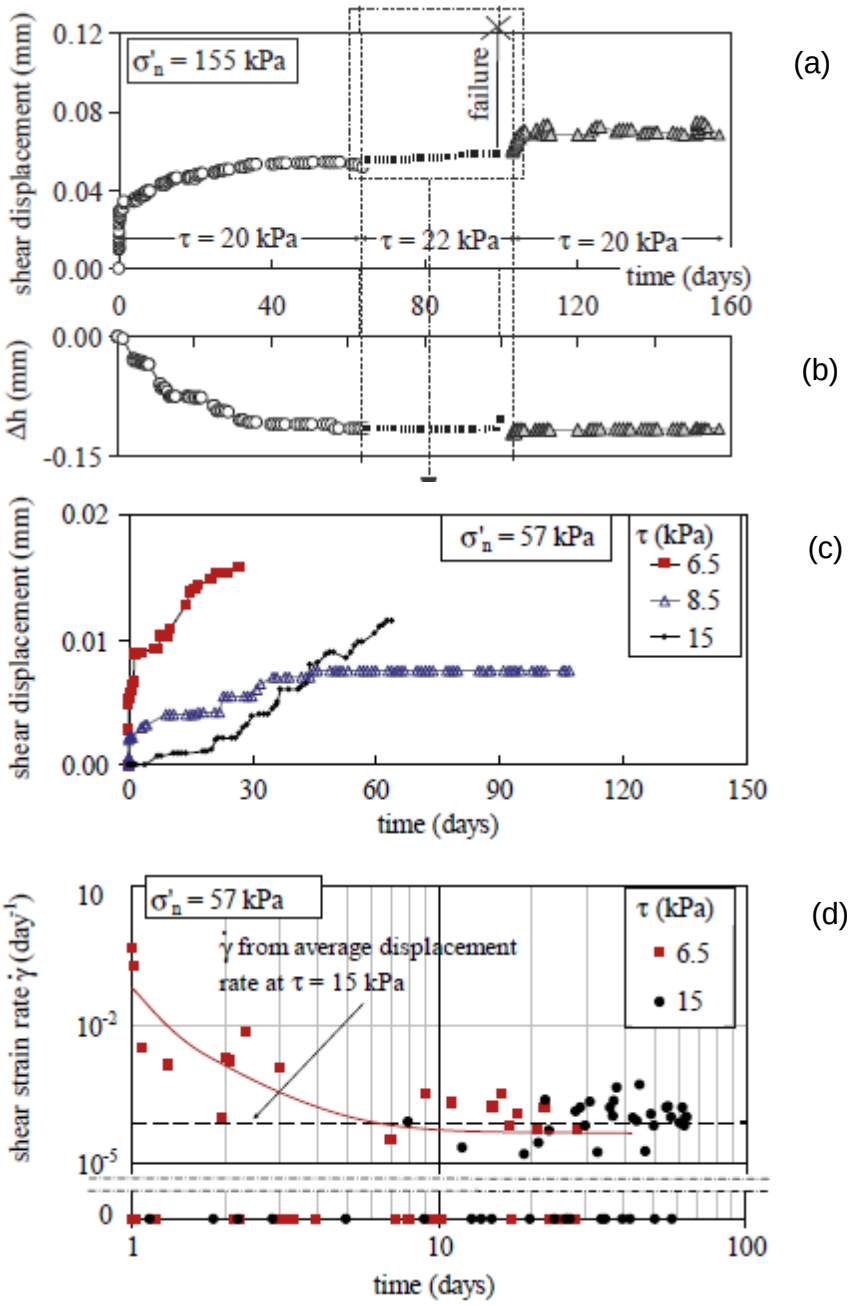

Figure 2.16. Creep tests a) shear creep displacement against time for pre-sheared specimens b) vertical displacement against time for pre-sheared specimens c) shear creep displacement against time for "intact" specimens d) shear strain rate against time for "intact" specimens (source: Di Maio et al., 2013)

Lai et al. (2014) investigated the creep behaviour in the laboratory of unsaturated clay via suction-controlled creep tests using a triaxial apparatus to analyse the long-term deformations of landslide when subjected to water content variations. A series of tests were conducted under drained conditions ranging from $\sigma_3 - \sigma_a$ = 100, 200 and 300 kPa, and

suction *s* = 100, 200 and 300 kPa. They concluded that the axial strain increased linearly with time while axial strain rate decreased linearly with time in a double-logarithmic space and the straight lines at different deviator stress levels were almost parallel for a wide range of time (Figure 2.17). Both strain and strain rate were stress and suction dependent where the axial strain and strain rate increased with increasing deviator stress level and decreasing matric suction (Figure 2.18).

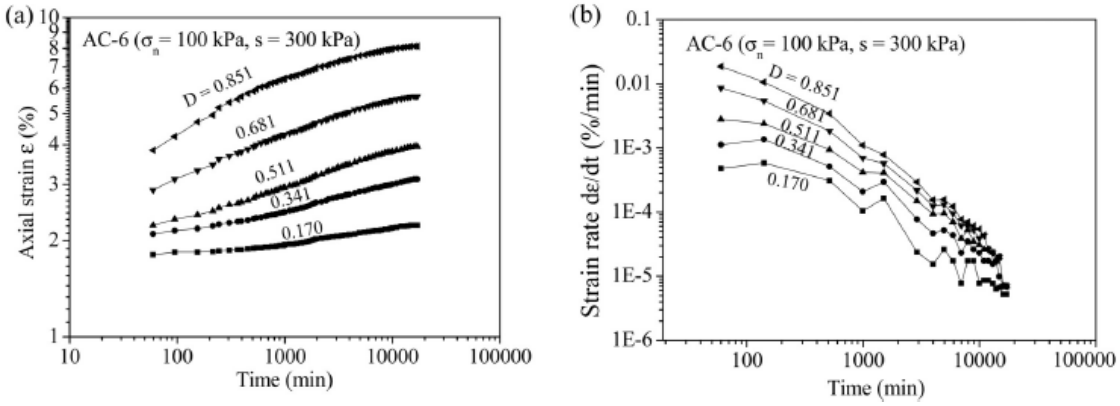

Figure 2.17. Creep test results: a) strain-time curves b) strain rate-time curves (source: Lai et al., 2014)

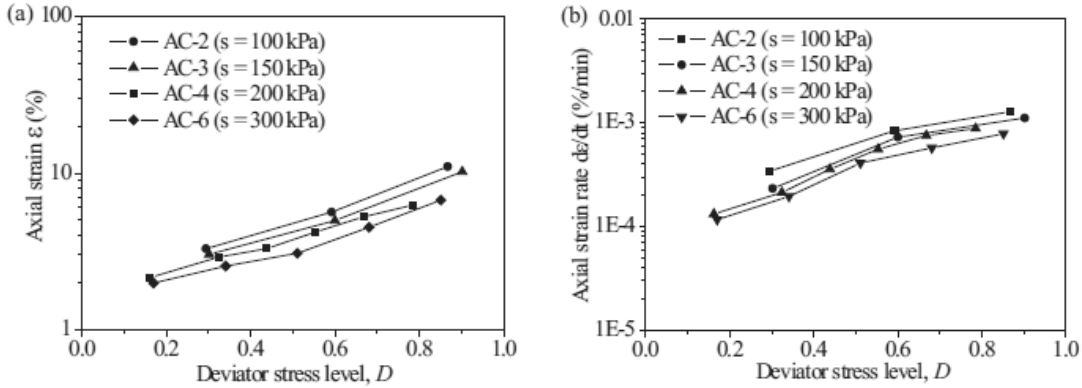

Figure 2.18. Creep test results at σ_n=100kPa t=24h: a) strain-stress level relationship and b) strain rate-stress level relationship (source: Lai et al., 2014)

Melinda et al. (2004) measured the shear strength of unsaturated soil by means of modified direct shear test and investigated the role of matric suction during infiltration. Based on their observation from the shearing-infiltration tests conducted, a significant magnitude of matric suction still existed in the specimen at failure hence suggesting that a slope may fail during rainfall under unsaturated conditions.

Residual soil slopes are commonly related to negative pore water pressure, u_w during dry periods. According to Lim et al. (1996), matric suction was found to be depth-dependent and played a significant role on the stability of soil slopes. When subjected to rain water infiltration, matric suction may reduce rapidly at shallow depths. Bhat et al. (2014) proposed a regression model based laboratory data on the critical displacement and residual friction

angle relationship. They suggested that the clayey soil will exhibit creep behaviour only when the R_{RCS} >1 and no significant creep effect on and below the residual-state of shear. R_{RCS} is the ratio of the applied constant creep stress to the residual strength. Their tests show that specimens can resist the applied constant creep load upon the R_{RCS} value of 1.025. Once reached to 1.03, the specimens failed immediately. Therefore, a conclusion was made that the creep behaviour of the clayey soils exhibit up to the applied creep stress equivalent to the 1.03 times of its residual strength.

Lacerda and Houston (1973) based on stress relaxation tests with triaxial apparatus observed that the normalised deviator stress (q/q_0) in which q and q_0 are the deviator stresses at time t and at the beginning of the test, respectively, decreased linearly with the increase of the logarithm of time. The strain rate at the beginning of the test influenced the time at which the relaxation begins, hence, the slower the initial strain rate, the longer the delayed time to start the relaxation process. Similarly, Yin and Cheng (2006) observed the similar pattern of initial strain-rate dependency where higher initial strain rate at the beginning of stress relaxation results in a significant decrease of the effective stress. The use of conventional direct shear box for stress relaxation test has never been adopted by any researcher before and it is of great interest to explore due to the simplicity it offers.

Existing viscous models typically address either strain/displacement creep or stress relaxation which is not ideal when dealing with landslide case study where in reality the landslide is never subjected to ‘pure’ creep because effective stress changes as a result of rainwater infiltration and/or groundwater pressure fluctuation. Although the idea of modelling time-dependent (viscous) behaviour of landslides is not new, adopting a single model that works simultaneously for creep and stress relaxation appears to be original and significant for the implementation in an Early Warning System for rainfall-induced landslides. The direct shear box is a commercially available apparatus that can be conveniently used to investigate creep response. However, conventional direct shear box operate in displacement-control and can be used only to conduct stress relaxation tests. If a unified creep/relaxation model is used to interpret the relaxation tests, relaxation data can be then used to simulate creep response.

CHAPTER 3
MATERIALS AND TESTING EQUIPMENT

3.1 INTRODUCTION

This chapter will illustrate the materials and equipment used in this research. Material properties of Ball clay such as mineralogical properties, grain size distribution, Liquid Limit (LL) and Plastic Limit (PL) and all testing equipment including Conventional Direct Shear Box, Modified Direct Shear box, Water Potentiometer (WP4), Odeometer, and High-Capacity Tensiometer will be presented herein. Since this is a laboratory-based research aimed at addressing fundamental aspects of viscous behavior of clays, a commercially available material were selected, the Ball Clay, to ensure homogeneity and reproducibility of the specimens.

3.2 MATERIAL PROPERTIES

The material used in this research is Ball clay that was mined from Cornwall, England and supplied by Imerys Mineral (Lopes, 2016). Table 3.1 shows the soil properties of Ball Clay. Index properties were determined by Lopes (2016) following the BS1377-2 (1990) standard. Liquid limit test were performed by the Casagrande apparatus method, the plastic limit test was performed by the rolling thread method, and the particle size distribution test was performed using sieves and hydrometer method.

Table 3.1 Ball Clay properties (modified after Lopes, 2016)

Properties	Ball Clay
Specific gravity, G_s [-]	2.6
Liquid Limit, w_L [%]	63
Plastic Limit, w_p [%]	24
Plasticity Index, Ip [%]	39

Table 3.2 shows the mineralogy of the Ball clay. From the mineralogical content, we can see that Ball clay, although being dominated by Kaolin minerals, is not as pure as Kaolin clay due to the existence of other minerals such as feldspar and quartz, as well as the presence of organic matter.

Table 3.2 Mineralogy of the Ball Clay (modified after Lopes, 2016)

Soil	Mineralogy
Ball Clay	Kaolin with varying amounts of mica, feldspar, quartz and organic matter (Imerys Minerals, 2015)

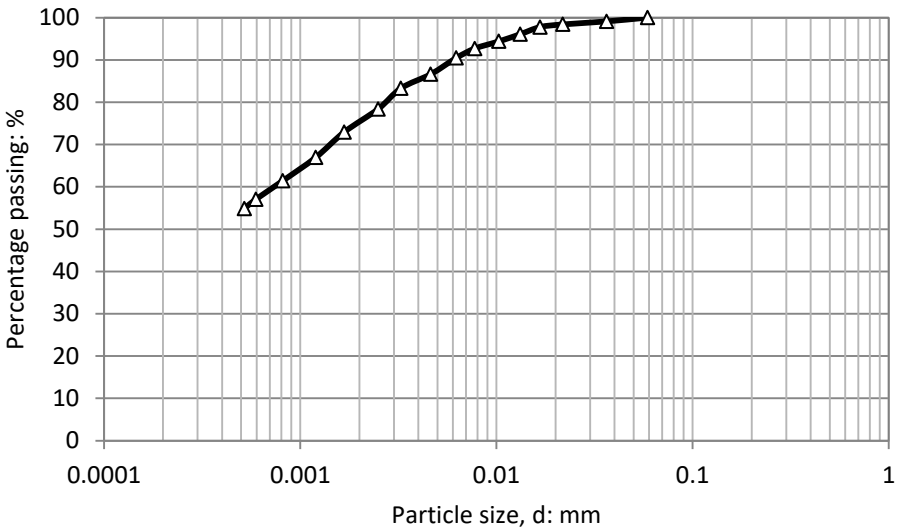

Figure 3.1. Particle size distribution curves according to BS1377-2 (1990) (after Lopes, 2016)

Figure 3.1 shows the particle size distribution of Ball clay, which is characterised by 74% clay and 26% silt. The curve suggests that Ball Clay could be described as Silty Clay soil and according to the Unified Soil Classification System (USCS), it can be classified as clay of high plasticity whereas according to the AASHTO Soil Classification System, it is classified as A-7 Clayey-soils (Lopes, 2016).

3.3 SPECIMEN PREPARATION

Specimens can be divided into 4 categories, depending on the kind of test to be carried out: 1) specimens prepared for testing viscous response in the pre-peak range (saturated pre-peak specimens), 2) specimens prepared for testing viscous response in the residual state (saturated post-peak specimens), 3) specimens prepared for testing viscous response in the pre-peak range in unsaturated state (unsaturated pre-peak specimens), and 4) specimens prepared for determining the Water Retention Curve (WRC).

3.3.1 Saturated pre-peak

To prepare specimens at saturated pre-peak condition, slurry was formed by mixing 70 g of clay powder with 70 g of demineralised water to achieve 100% water content, almost twice the liquid limit. The slurry was then placed in the 60 mm side shear box and initially let to consolidate under the weight of the loading cap ($\sigma_{loading\ cap}$ ~2.5 kPa) for 1 day. To ensure that the sample remains saturated, the shear box container was completely filled with water. Then, samples were consolidated in steps to the target normal stress. All tests were performed in a temperature-controlled room (Figure 3.2).

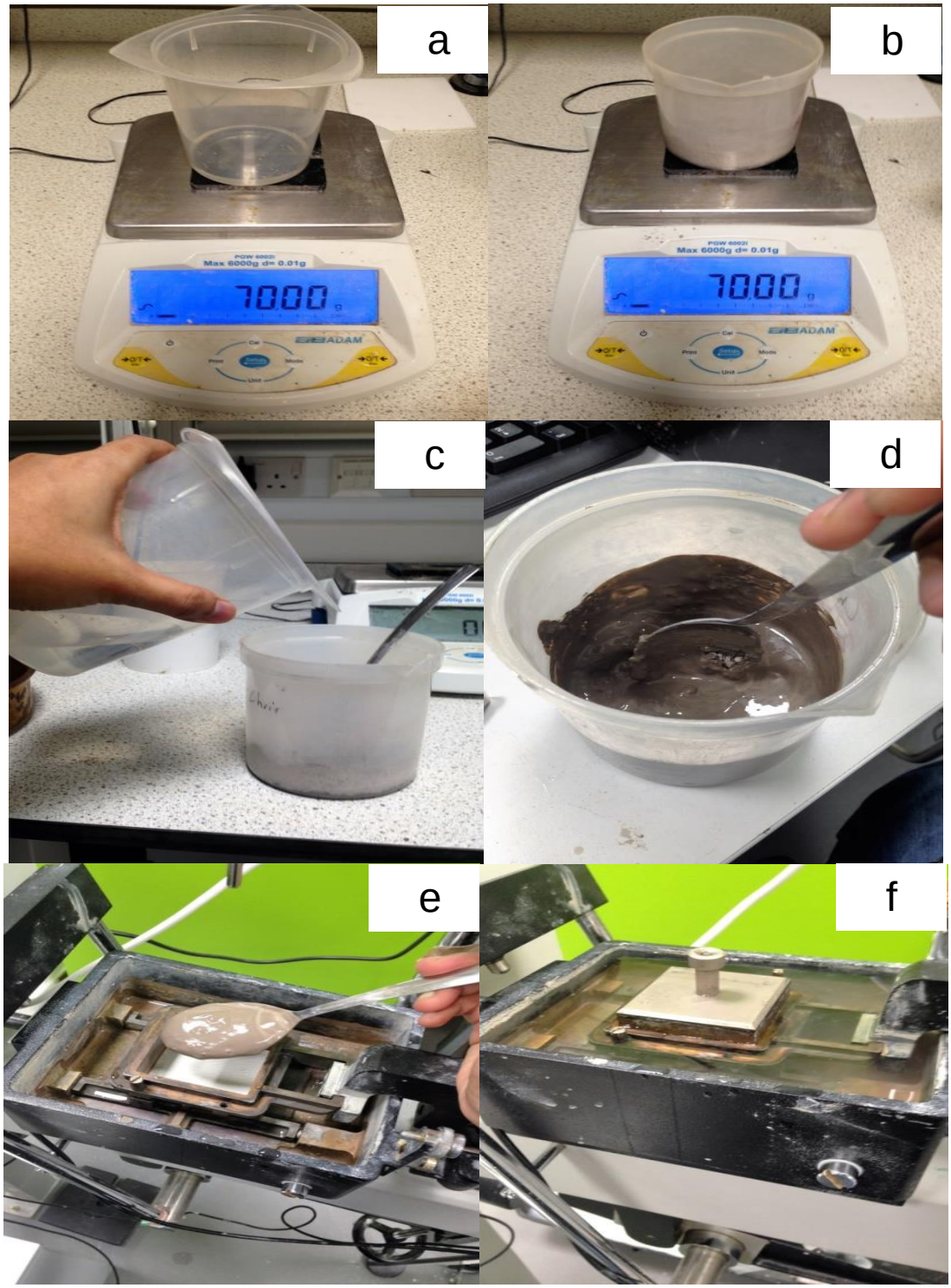

Figure 3.2. Sample preparation. a) prepare 70g of demineralised water b) prepare 70g of clay powder c) Mix water with clay powder d) Stir well to get a slurry e) Pour the slurry inside the shear box container e) Fill the box with water to ensure drained conditions

3.3.2 Saturated post-peak

Preparation of saturated post-peak specimens was similar to the preparation of saturated pre-peak specimens except that they were subjected to multiple shearing reversals to achieve residual conditions. For each shearing, the specimen was set to shear until approximately 8mm displacement. Figure 3.3 shows the multiple reversals shearing for the preparation of saturated specimens at 200kPa vertical stress. The peak in first forward shearing (FS-1) represents the maximum shear strength of specimens and it was found to be around 90kPa. 5 more cycles of backward (BS) and forward shearing (FS) were found to be sufficient to ensure the attainment of the residual state.

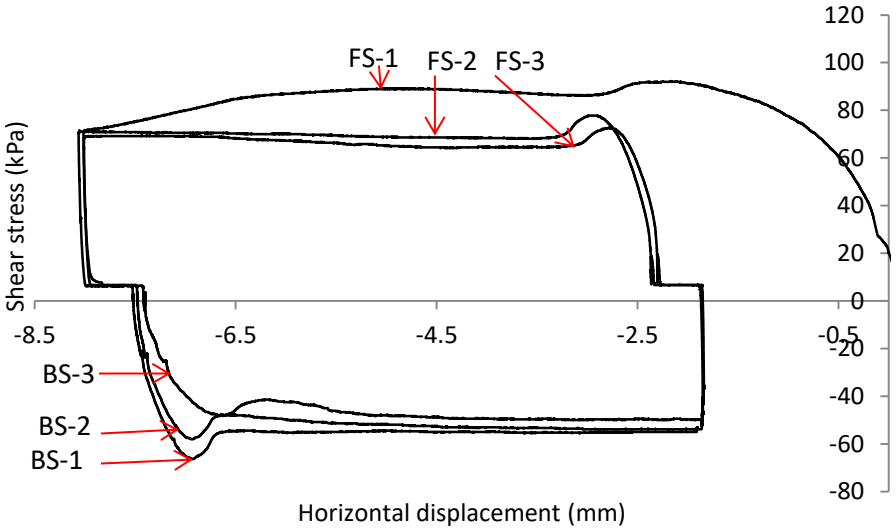

Figure 3.3. Multiple reversal shearing for saturated-post peak specimen

3.3.3 Unsaturated pre-peak

To prepare specimens at unsaturated pre-peak condition, slurry was formed by mixing 200g of clay powder with 200g of demineralised water to achieve 100% water content, almost twice the liquid limit.The slurry was then consolidated in steps to 100kPa normal stress. Once consolidation was achieved, the sample was removed from the 100 mm side shear box frame and its weight was determined. To get information about the initial water content of the sample, small part of the sample was taken out for oven-drying process. At least 6 hours were needed to dry the small piece of soil sample.

The sample was then subjected to air-drying until target water content was attained (calculated based on the initial water content and the amount of water loss). The sample was wrapped with parafilm and sealed in polythene bag preceding cutting and trimming to allow moisture equalization. The sample was then cut and trimmed using a 60 mm x 60 mm square cutter. The specimen was advanced slowly from the cutter into the sample using a clamp. Prior to moving the specimen into the shear box, silicon grease was placed between the bottom plate and the lower frame and between the lower and upper frames. This is to

ensure an air-tight condition in the shear box container and also act as anti-evaporation system during the whole process of viscous test (Figure 3.4).

Figure 3.4. Unsaturated specimen. a) trimmed and cut specimen b) specimen placed in the shear box frame c) parafilm and silicon grease (Vaseline) applied to the frames for anti-evaporation system d) specimen ready for viscous test

3.3.4 Water Retention Curve (WRC)

Nine specimens air-dried to different water contents (55%, 50%, 45%, 40%, 34%, 32%, 29%, 26%, and 23%) were prepared for the determination of the WRC. Initially, samples were prepared by mixing 200g of Ball Clay powder with 200g of demineralised water in the 100mm side shear box and let to consolidate with the weight of loading cap (~2.7kPa) overnight. The sample was consolidated in steps, starting from the lower stress (10kPa) and doubling up until 100kPa normal stress. Samples were then removed from the shear box frame and cut into 4 square-shaped parts, each with the size of approximately 50mm x 50mm. All 4 sub-samples were put on balance to measure their weight. Then, one of the sub-samples was put into the oven for 6 hours or more to measure the sample initial water content. The remaining 3 sub-samples were then wrapped with parafilm and sealed in polythene bag to allow moisture equalization. Later, they were air-dried to different target water contents estimated by weighing the samples. Once the target water content was reached, the sub-samples were once again wrapped and sealed in polythene bag for one day to allow moisture equalization.

A portion of the sub-sample was used for total suction measurement using the chilled-mirror psychrometer WP4C machine while the rest was used for volume and water content measurements. To get a specimen for volume calculation, a cylinder-shape cutter was used having a diameter of 16 mm. The cutter was advanced slowly into the sample using a clamp. Since the samples were stiff, cutting could be achieved with ease using this method. Once done, the sample height, diameter and weight was recorded. The sample was put into the oven for 6 hours or more. The oven-dried samples were then weighted again to record the loss of water. Void ratio and degree of saturation could then be calculated.

From the WRC curve (Figure 3.5a), the air entry value was found to be around 1000kPa. Figure 3.5b shows the relation between suction and gravimetric water content. This relation can be used to infer suction based on the gravimetric water content based on the equation given in the graph. Figure 3.5c shows the relation between degree of saturation and suction. The degree of saturation was calculated by assuming a rigid soil.

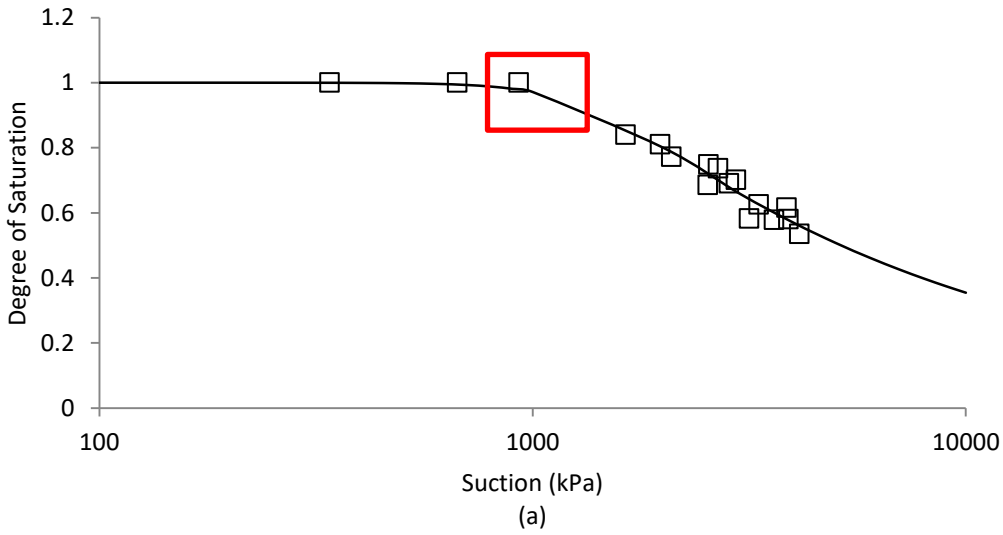

(a)

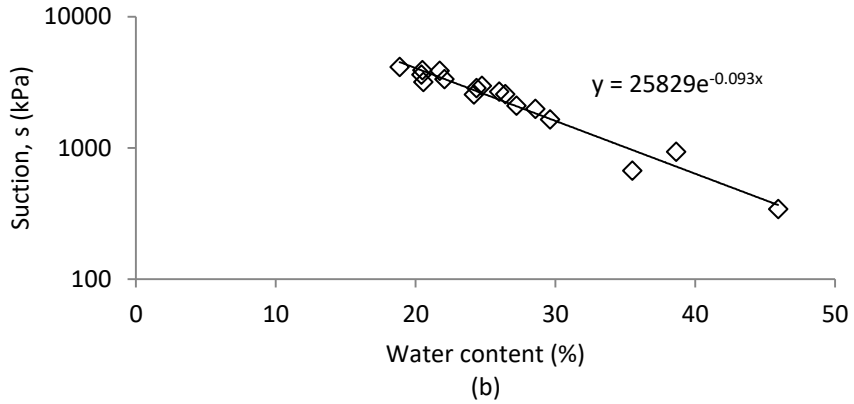

(b)

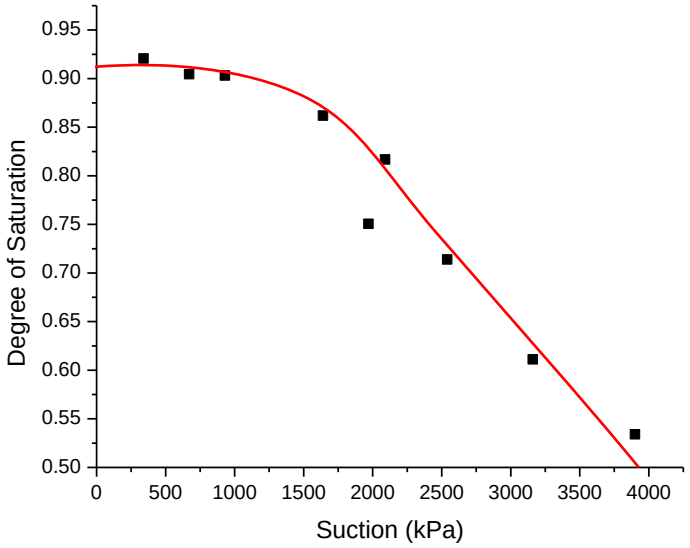

Figure 3.5. a) SWCC curve for Ball Clay b) Suction determination for any given water content c) Degree of saturation corresponding to suction

3.4 TESTING EQUIPMENT

All testing equipment belongs to the Geotechnics Laboratory, University of Strathclyde. Direct shear box (conventional and modified) was used for viscous testing, high-capacity tensiometer and WP4 were used for matric and total suction measurement respectively. Direct shear box was also used to consolidate samples for unsaturated specimen preparation.

3.4.1 Conventional direct shear box (displacement-controlled)

Figure 3.6 shows the conventional direct shear box used in this research. A conventional direct shear box measures shear strength of soils. Even though the stress pattern is complex where the stress conditions in the specimen during the test are not known and the directions of the planes of principal stress rotate as the test proceeds and the distribution of stresses along the plane of shear is non-uniform, however, test duration is relatively short, making it very suitable for practical applications (Caruso & Tarantino, 2004).

This direct shear box consists of a shear box body for testing specimens 60 mm square or 100 mm square section, a shear box carriage running on roller bearings, and a step motor drive unit to apply horizontal displacements at constant rate. The apparatus was equipped with a S-load cell for measuring the horizontal shear force (5000 N capacity with a measured standard deviation of accuracy of ± 3 N) and two potentiometer displacement transducers for measuring the horizontal and vertical displacements (15 mm travel with measured standard deviation of accuracy of ±3 μm). Vertical load was applied with a lever-arm loading system with 10: 1 beam ratio.

Figure 3.6. Conventional direct shear box

3.4.2 Modified direct shear box (force-controlled)

The conventional direct shear box was modified to study creep behaviour (Figure 3.6). The modification involves an additional pulley system, which was connected to the external container and, hence, to the lower frame. The pulley was a non-friction pulley with string made of steel. During loading, tension force was applied by the pulley system to the lower frame and converted into shear force applied to the specimen by load cell, causing this latter to be sheared at constant shear force (Figure 3.7).

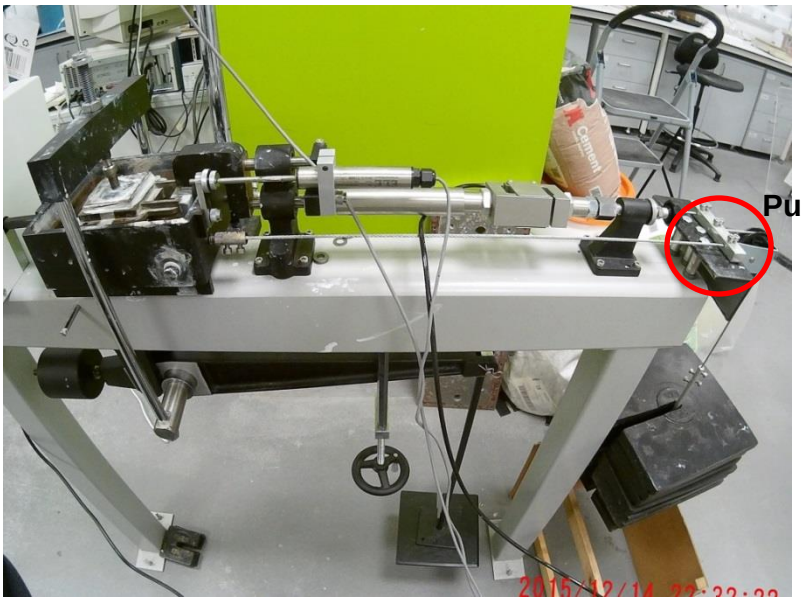

Figure 3.7. Modified direct shear box

3.4.3 Suction measurement device

We intended to measure matric suction of soils in the unsaturated range using a tensiometer. However, due to some specimens having high matric suction that are beyond the tensiometer measurement range, determination of suction for specimens with high matric suctions were conducted using the WP4 device which measures the total suction of soils.

Total suction equals to the sum of matric or soil water suction and osmotic suction. The definitions of total suction, matric suction and osmotic suction as given by Krahn and Fredlund (1972) are as follow:

- Total suction is the negative gauge pressure relative to the external gas pressure on the soil water to which a pool of pore water must be subjected in order to be in equilibrium through a semi-permeable membrane with the soil water.
- Matric suction is the negative gauge pressure relative to the external gas pressure on the soil water, to which a solution identical in composition with the soil water must be subjected in order to be in equilibrium through a porous permeable wall with the soil water.
- Osmotic suction is the negative gauge pressure to which a pool of pure water must be subjected in order to be in equilibrium through a semipermeable (i.e., permeable to water molecules only) membrane with a pool containing a solution identical in composition with the soil water.

Potentiometer (WP4)

Figure 3.8 shows a WP4 device that has been used in this research for the development of Water Retention Curve (WRC). This device is another alternative besides tensiometer that can provide quick measurement for specimen's suction. However, the equipment measures total suction rather than matric suction.

In principal, the WP4 device measures water potential by determining the relative humidity of the air above a sample in a closed chamber using the chilled mirror method. This method entails chilling a tiny mirror in the chamber until dew just starts to form on it. At the dew point, the WP4C measures both mirror and sample temperature with 0.001°C accuracy. This allows the WP4C to deliver water potential readings with unparalleled accuracy in the -0.1 MPa to -300 MPa range. It was also capable of measuring suction below 3MPa (Decagon Devices, 2015).

To perform the measurement, a small chunk of specimens was put inside a container, sealed it into the measurement chamber, and left for about 10-15 minutes (depending on water content of the specimen) until the light flashes. Reading shown on the display represents the total suction of the tested specimen.

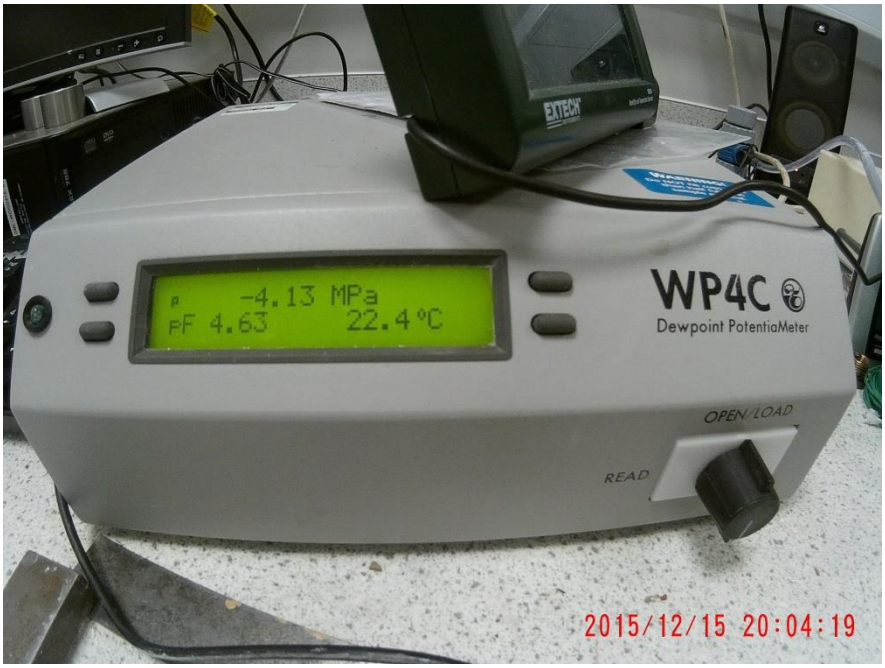

Figure 3.8. Potentiometer (WP4)

High-capacity tensiometer

Figure 3.9 shows the schematic layout of tensiometer. The tensiometer used in this research was designed and constructed by Professor Alessandro Tarantino at the University of Strathclyde. It is similar to the one that has been developed at the University of Trento. The concept of the tensiometer was similar to the one that has been developed at Imperial College except that this tensiometer has been modified in such a way that it allows direct calibration in the negative range of pore water pressure (Tarantino & Mongiovi, 2003).

Tensiometer allows direct measurement of matric suction as ambient air pressure remains atmospheric. The measurement diaphragm and the porous ceramic interface are the two key elements that control the performance of the tensiometer. The major drawbacks of these instruments are the water cavitation, the high air-water interface and the saturation of the porous ceramic, since if the porous ceramic is not adequately saturated it may lead to inaccurate results that might be difficult to detect (Bruna, 2016).

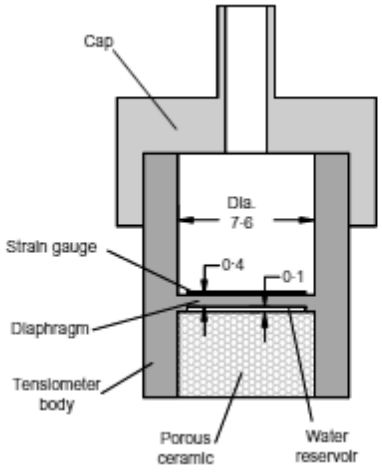

Figure 3.9. Schematic layout of Trento tensiometer (after Tarantino & Mongiovi, 2003)

3.5 CALIBRATION

Calibration of the shear box was first carried out before performing any viscous tests to assess the accuracy of measuring transducer. The calibration involved the vertical displacement transducer, the horizontal displacement transducer, and the horizontal force transducer (load cell).

3.5.1 Displacement transducers (vertical and horizontal) and load cell

The displacement transducers have a full-scale range of 15mm whereas the load cell of S-type has a full-scale range of 5kN. Calibration for displacement transducer was done by using a micrometric screw and the measurement was taken by reading the voltage signal at every 1mm displacement. Readings were taken by performing a full compression-decompression cycle from 0 mm up to 15 mm and from 15 mm back to 0 mm, and these were repeated twice. For the S-type load cell, the calibration was performed using a dead-weight calibration device performing a loading and unloading stage, and signal reading was taken at every 1kN, starting from 1kN to 4.5kN. 4.5kN was the maximum force applied to avoid overloading the cell resulting in a cell malfunctioning.

Figure 3.10 shows the calibration curves of the three transducers associated with the conventional shearbox (displacement-controlled). The standard deviation of the error associated with the calibration curves shown in the figure where found to be ±13μm for the vertical displacement transducer (0.09% full scale range), ±9μm for the horizontal displacement transducer (0.06% full scale range), and ±17N for the load cell (0.3% full scale range).

For the case of the force-controlled shearbox, the standard deviation of the error associated with the calibration curves (not shown in the figure) where found to be ±3μm for the vertical displacement transducer (0.02% full scale range), ±7μm for the horizontal displacement transducer (0.05% full scale range), and ±2N for the load cell (0.04% full scale range).

Overall, the accuracy of all transducers can be considered satisfactory as it shows to be lower than the accuracy stated in the data specification sheet by the manufacturer.

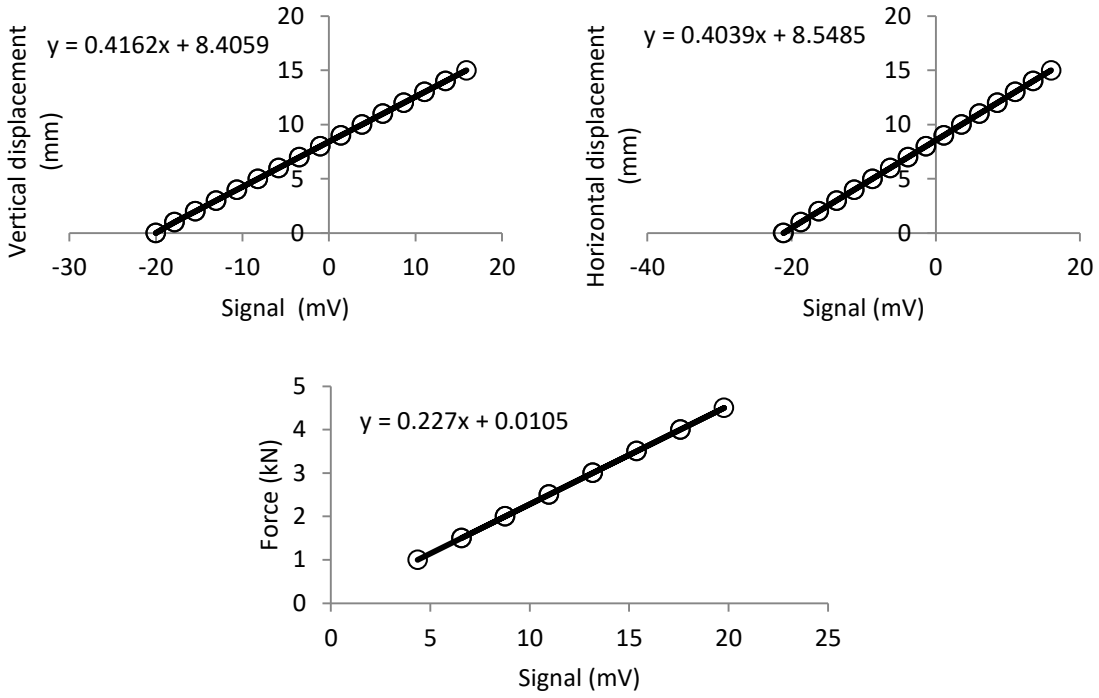

Figure 3.10. Calibration of displacement and force transducers for the shearbox in displacement-controlled mode

3.5.2 Loading system compliance

The loading system was calibrated by assessing its elastic and/or viscous response, which should be discounted in the creep and relaxation tests carried out on the soil specimens. A rigid dummy sample made of steel was used to ensure that any displacement recorded during the calibration tests was generated by the elastic and/or viscous response of the loading system only. Assumption was made that the steel dummy sample did not exhibit any creep.

It was desirable that the loading system exhibited negligible viscous response to minimise errors in the measurement of the viscous response of the clay. On the other hand, it was expected that the loading system exhibited some deformability, which needed to be assessed due to its effects on the measured stress decay in relaxation tests. During the calibration tests, the displacements undergone by the upper and lower frames were recorded with displacement transducers (Figure 3.11).

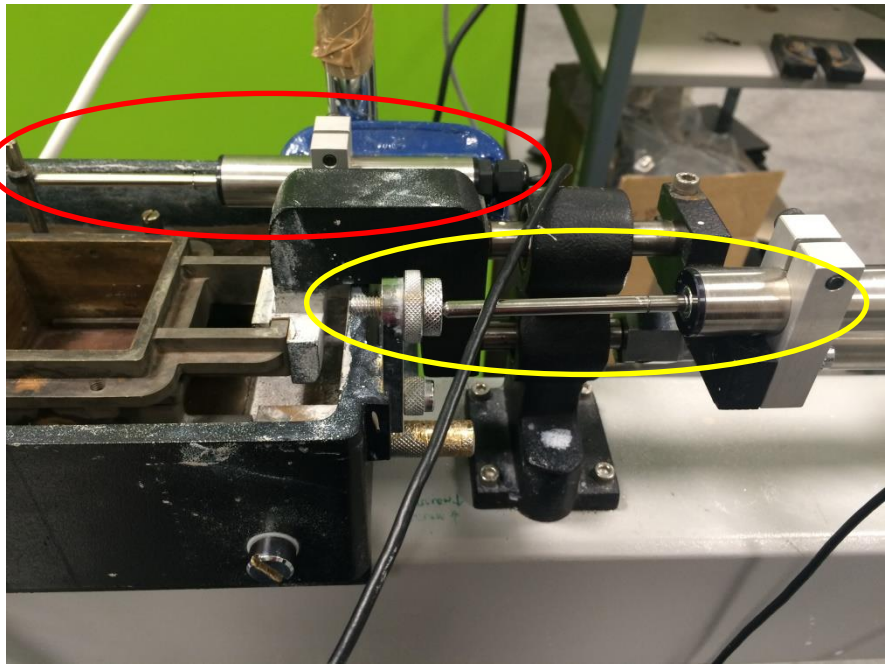

Figure 3.11. Calibration of the loading system; two horizontal transducers to measure relative displacements of bottom half (yellow) and top half (red).

Calibration in 'creep' mode: stiffness of the holding arm

Figure 3.12 shows the schematic layout of the calibration test in 'creep' mode. The horizontal load was applied to the bottom frame via the external container while the upper frame was maintained in place by the horizontal holding arm connected in series with the load cell. In principle, when the specimen is tested in creep mode, the bottom frame is the one moving in the direction of shear whereas the upper frame should remain locked in place by the horizontal holding arm. However, calibration test using dummy sample has revealed that the horizontal holding arm deforms when compressed axially as a consequence of the shear force applied to the bottom frame via the external container.

Figure 3.13 shows the relationship between the deformation of the horizontal holding arm (measured by the displacement transducer circled in red in Figure 3.11) and the horizontal arm axial force expressed in equivalent shear stress for a 60 mm side specimen. The slope of the shear stress versus the upper-frame displacement plot represents the stiffness of the horizontal holding arm.

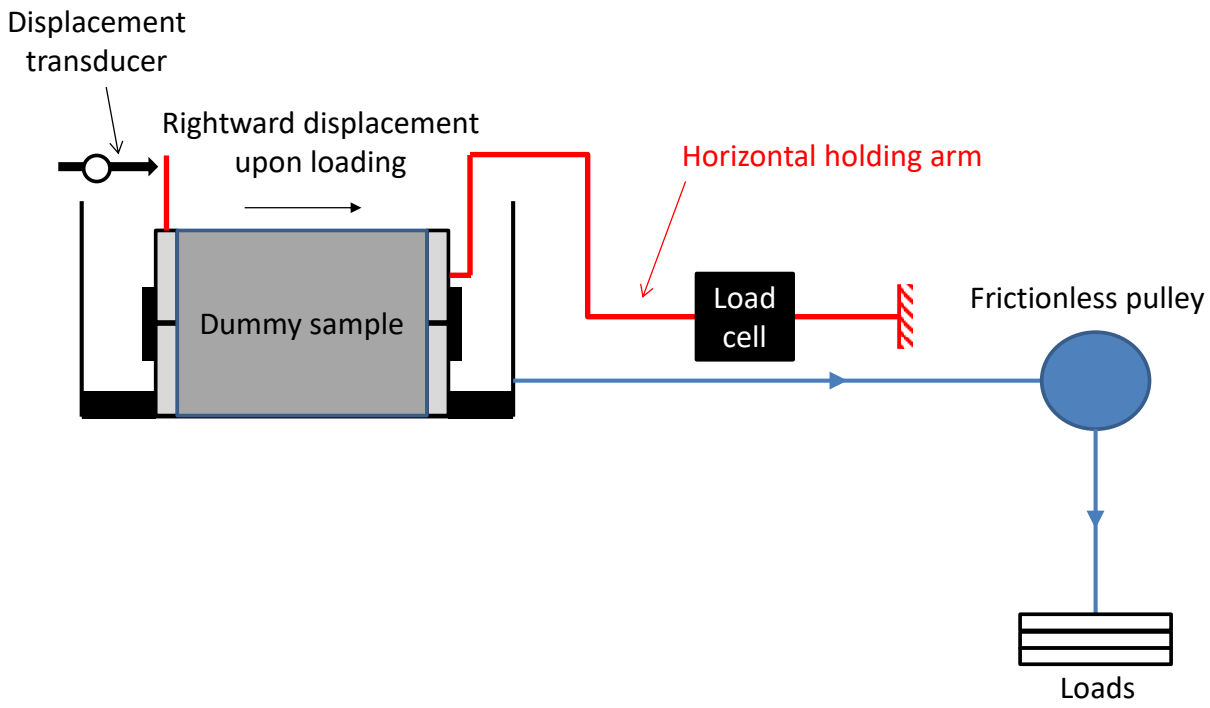

Figure 3.12. Schematic layout of calibration test in 'creep' mode

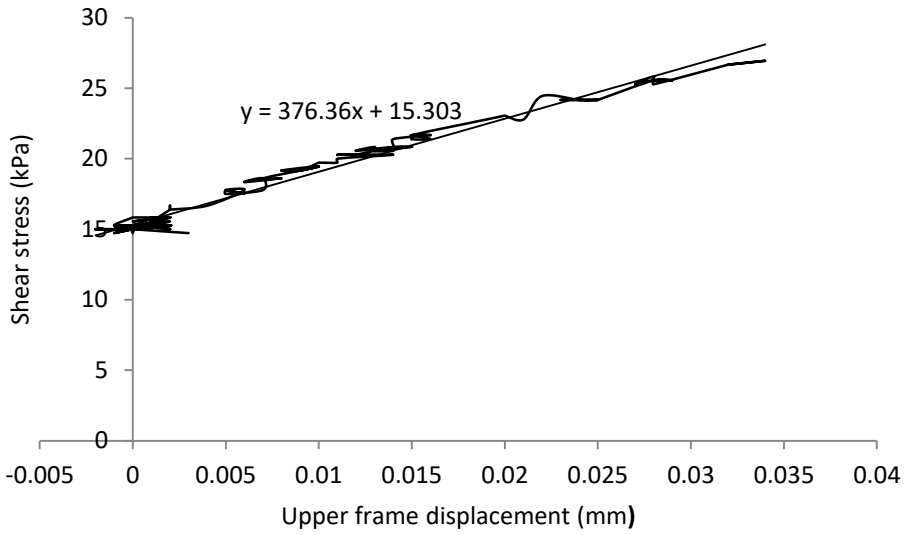

Figure 3.13. Stiffness of horizontal holding arm

Calibration in 'relaxation' mode: stiffness of the loading arm

Figure 3.14 shows the schematic layout of the calibration test in 'relaxation' mode. In the stress relaxation test, the shear stress 'relaxes' at constant horizontal displacement. Therefore, a condition where no displacement is generated to allow for pure stress relaxation will only be achieved if the lower frame remains locked in place, i.e. the horizontal

loading arm connected to the external container does not deform, and also the upper frame remains locked in place, i.e. the horizontal holding arm does not deform.

Initially, the calibration of the system was performed using a dummy sample made of steel. However, the deformations of the horizontal loading arm and the horizontal holding arm recorded once the step motor was stopped were very small (same order of magnitude as the accuracy of the displacement transducer). As a result, the stiffness of the loading system could not be calculated and another approach had to be pursued.

It was then noted that, during the relaxation test performed on the soil specimen, the displacement of the external container and, hence, of the lower frame was not constant once the step motor was stopped. The decay in shear stress caused the horizontal loading arm to decompress generating a further right-ward movement of the external container.

This is clearly illustrated in Figure 3.15a. When the horizontal displacement was imposed at constant rate, the shear stress increased as expected. At the horizontal displacement of around 0.20 mm, the step-motor was stopped to virtually impose a no further displacements between the two shear box frames. However, it can be seen that the lower frame keeps moving forward due to the decompression of the horizontal loading arm as the shear stress decays.

The slope of the shear stress versus the lower-frame displacement in the ‘relaxation stage’ as shown in Figure 3.15b could therefore be taken as the stiffness of the horizontal loading arm.

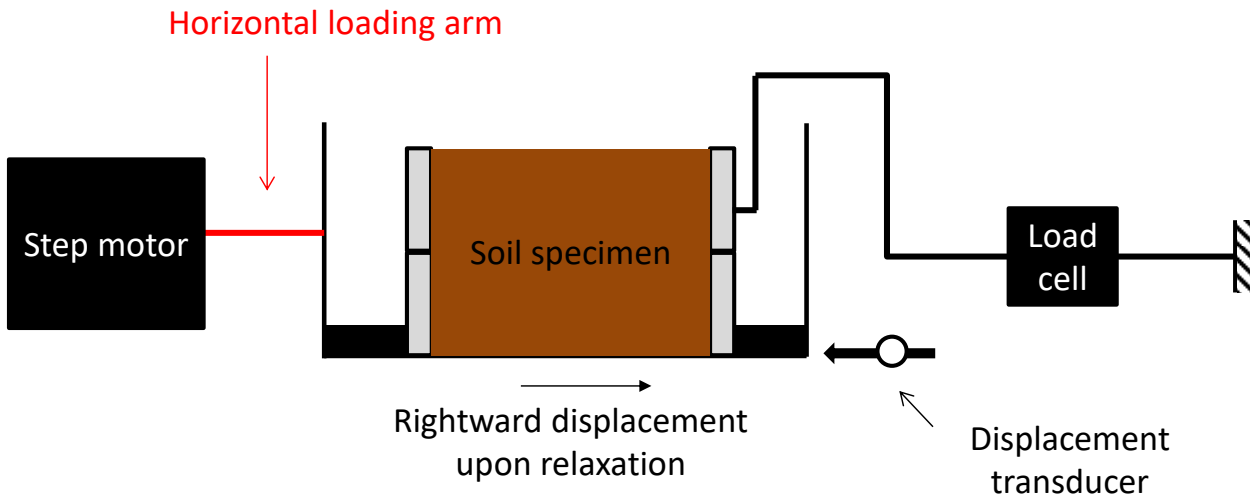

Figure 3.14. Schematic layout of calibration test in ‘relaxation’ mode

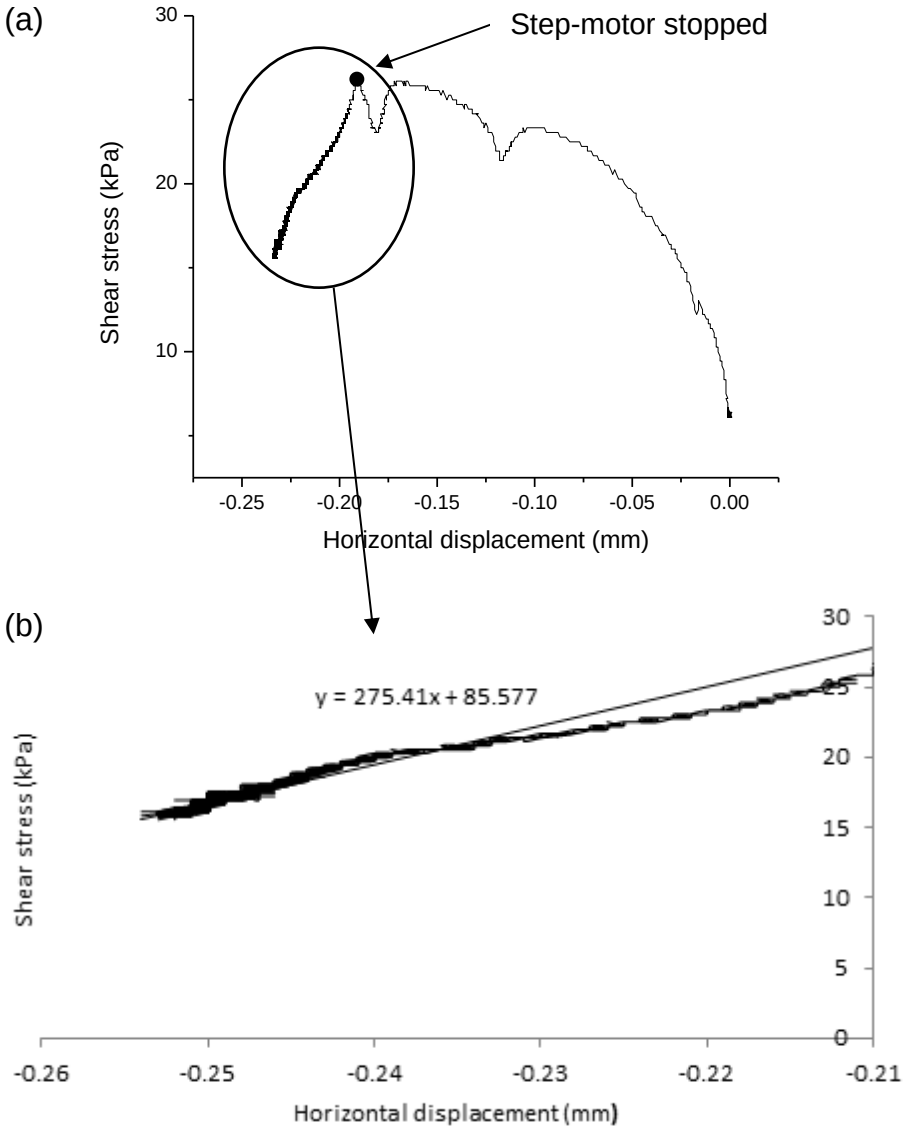

Figure 3.15. Stiffness of horizontal loading arm. (a) Shear stress versus horizontal displacement in a displacement-controlled direct shear test. (b) Horizontal displacement accumulated once the step-motor was stopped

Viscous response of the loading system

In the calibration tests in 'creep' mode, the displacement was recorded versus time to detect possible viscous behaviour of the loading system. No displacements were recorded versus time 1) once the load was applied in creep mode as shown in Figure 3.16 and 2) once the step-motor was stopped in relaxation mode using the dummy sample as shown in Figure 3.17.

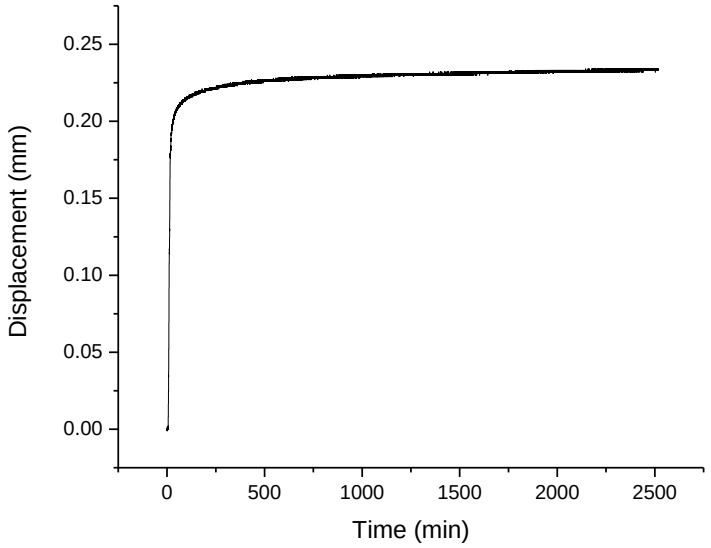

Figure 3.16. Time response in creep mode once the load was applied to the system

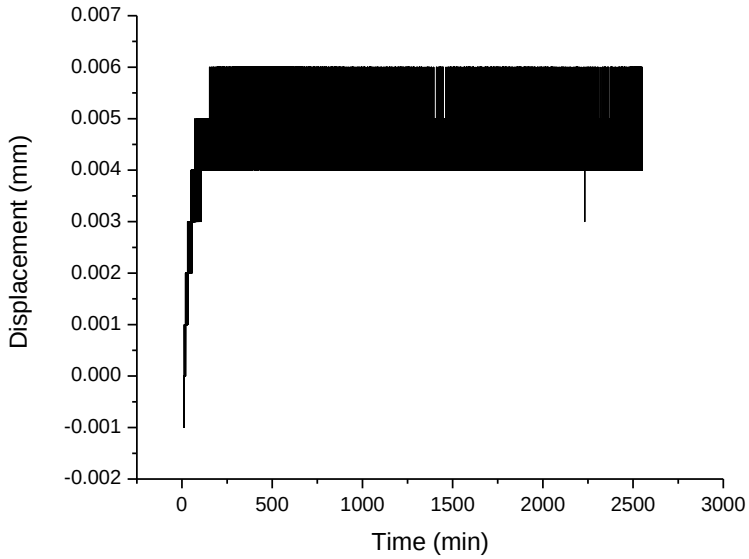

Figure 3.17. Time response in relaxation mode using a dummy sample once the step-motor was stopped

CHAPTER 4
EXPERIMENTAL PROCEDURES

4.1 INTRODUCTION

This chapter will discuss the experimental procedures involved in this research. All experimental programmes were carried out at the Geotechnics Laboratory, University of Strathclyde, Glasgow.

4.2 SHEARING RATE

Preliminary direct shear tests in displacement-controlled mode were carried out to determine a suitable shearing rate for our clay specimens. Since Ball Clay is a fine-grained material, excess-pore-water pressure may build up during shearing. The shearing rate should therefore be kept as low as possible to prevent pore-water pressure build-up and maintained drained conditions. At the same time, the shearing rate cannot be selected excessively low otherwise viscous effects can become significant during the loading stage preceding the stage where viscous behaviour is investigated either in relaxation or creep mode.

4.2.1 Displacement-controlled tests

Figure 4.1 shows 3 direct shear tests at different horizontal displacement rates, 0.05mm/min, 0.025mm/min and 0.0125mm/min.

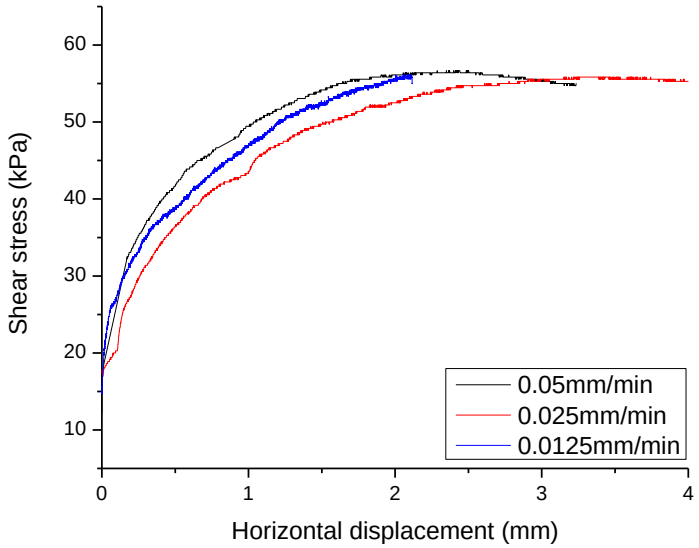

Figure 4.1. Direct shear tests at different shearing rates in displacement-controlled tests

As shown from consolidation curve in Figure 4.2, the rates were selected based on the time to failure, t_f when normal stress was imposed on the specimens under 1-D conditions, based on 100% consolidation (t_{100}) using the relationship:

$$t_f \cong 10.\, t_{100} \quad [1]$$

By estimating the strain (displacement) at failure, s_f to be around 2-3 mm, the velocity of the shear to achieve that deformation in the allotted time was calculated following the equation below:

$$V = \frac{s_f}{t_f} \quad [2]$$

It appears that the shear response among these three shearing rates is pretty similar and consistent even though they were sheared at different horizontal displacement rates. It is worth noticing that even though there seems to be slight differences for shear stress at similar horizontal displacements, the variance was considered small and insignificant. Based on similar peak shear strength obtained between tests at 0.05 mm (the fastest rate) and 0.0125 mm (the slowest rate), the shearing rates therefore appear to be sufficiently low to allow excess pore-water pressure to dissipate. As a result, the fastest shearing rate of 0.05mm/min was selected. With this shearing rate, 2 mm horizontal displacement for example are achieved in 40 min, which is a time sufficiently smaller than the duration of the viscous stage of the test (typically 24h).

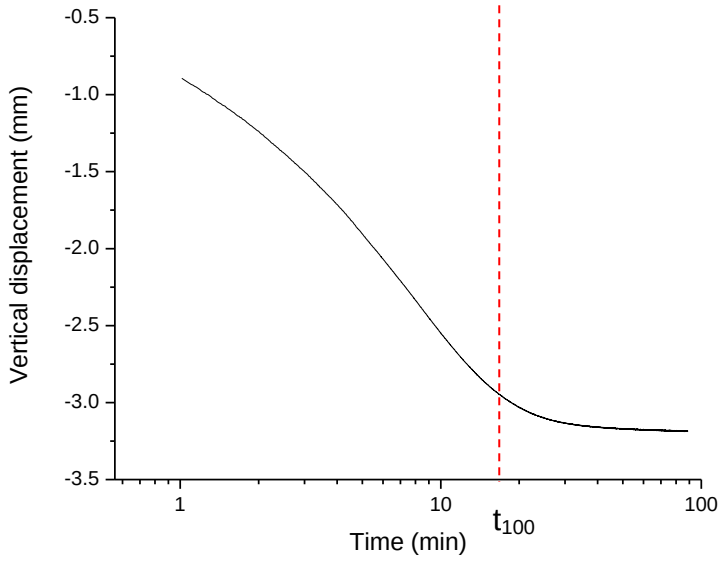

Figure 4.2. Consolidation curve

4.2.2 Stress-controlled tests

The loading rate in stress-controlled tests was selected to reproduce similar loading response as the displacement-controlled tests. In particular, the time taken to achieve target shear stress was taken from its corresponding displacement-controlled tests. This time was divided in ten time intervals and the shear stress imposed in ten steps. For the case shown in Figure 4.3, the resulting loading rate was 2.5kPa per 1.2 min. Figure 4.3a compares the loading stage for the displacement-controlled and stress–controlled tests and these are reasonably similar. Figure 4.3b compares the axial strain between the two tests and more strains were accumulated in the displacement-controlled test. At the end of the loading stage, the shear stress remains constant in the stress-controlled test (creep mode) whereas it decays in the displacement-controlled test as a result of the constant displacement imposed (relaxation mode).

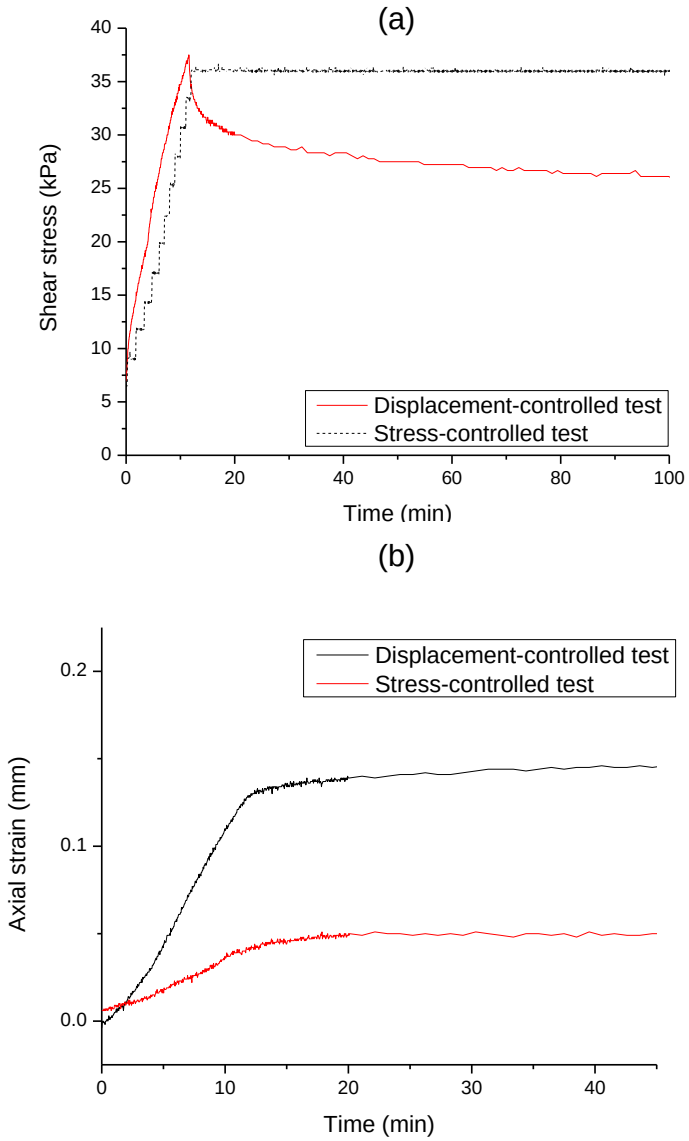

Figure 4.3. Viscous tests a) shear stress vs time b) axial strain vs time

4.3 PRELIMINARY VISCOUS TESTS

We performed, initially, single stage viscous tests on saturated clay specimens using both the conventional displacement-controlled shear box and the modified stress-controlled shear box. Single stage means that the shear stress corresponding to the initial condition of the viscous stage of the test is reached by a monotonic loading path.

4.3.1 Displacement-controlled test with single-stage loading

A relaxation test was performed using the conventional displacement-controlled direct shear box. The test was conducted on a specimen that was initially consolidated to a vertical stress of 100kPa. Then, a horizontal displacement was applied to the specimen with the shearing rate of 0.05mm/min until a target shear stress was reached. Target shear stress was determined based on a prescribed ratio with the maximum shear stress (shear strength) for the Ball Clay, i.e. Figure 4.4 was selected at 67%. The horizontal displacement was then maintained constant (by stopping the step-motor) for approximately one day to allow for the shear stress to 'relax'.

Figure 4.4 shows the stress relaxation over the time in single stage loading. One can observe that, when the displacement is set to constant, the stress decays over the time and reaches an asymptotic value (further in Chapter 5).

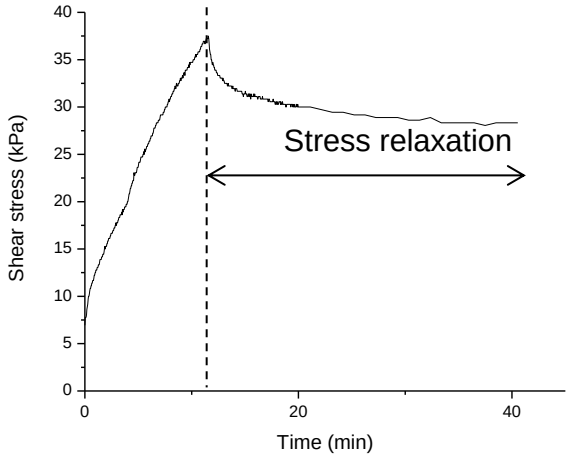

Figure 4.41. Stress relaxation for single stage loading

4.3.2 Stress-controlled test in single stage loading

Creep test was performed using a modified stress-controlled direct shear box, as mentioned in the previous chapter. The test was performed by applying shear force in steps to reach a target shear stress. This was then maintained constant for approximately one day to allow for the horizontal displacement to 'creep'. During creep phase, evolution of displacement is the one to be measured. By referring to Figure 4.5, we can see the increase in horizontal displacement when subjected to constant shear stress.

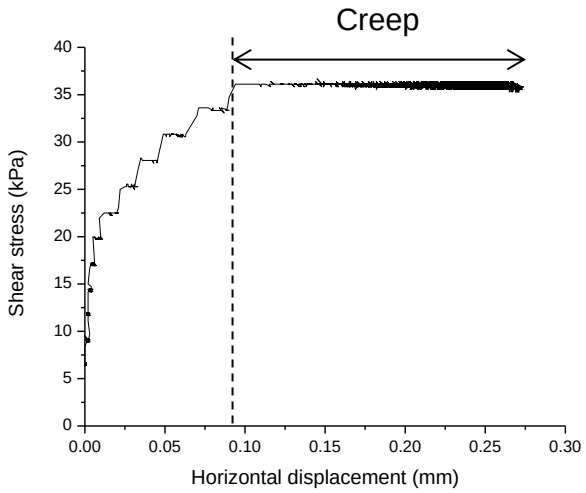

Figure 4.52. Creep at single stage

4.3.3 Test validation: similar loading path between displacement and stress-controlled test

Creep and stress relaxation test are two different tests that are closely related to one another. Creep test is a test where the stress is kept constant to allow the displacement to creep. Stress relaxation, on the other hand, is a test where the horizontal displacement is kept constant to allow the stress to relax or decay. In principle, the loading path between these two tests in a single stage loading should be the same to enable creep and relaxation to be compared.

Figure 4.6 shows the loading stage of these two tests until a target shear stress is reached. It can be observed that those two curves with respect to the horizontal displacement tend to overlap with each other, suggesting similar loading path even under different modes of loading.

It should be noted that stress relaxation should be ideally characterised by a vertical path if the horizontal displacement could be effectively maintained constant during relaxation. However, as shown in Chapter 3, the loading arm and the holding arm are not infinitely stiff and their deformation when the stress decays is responsible for the non-vertical stress relaxation path.

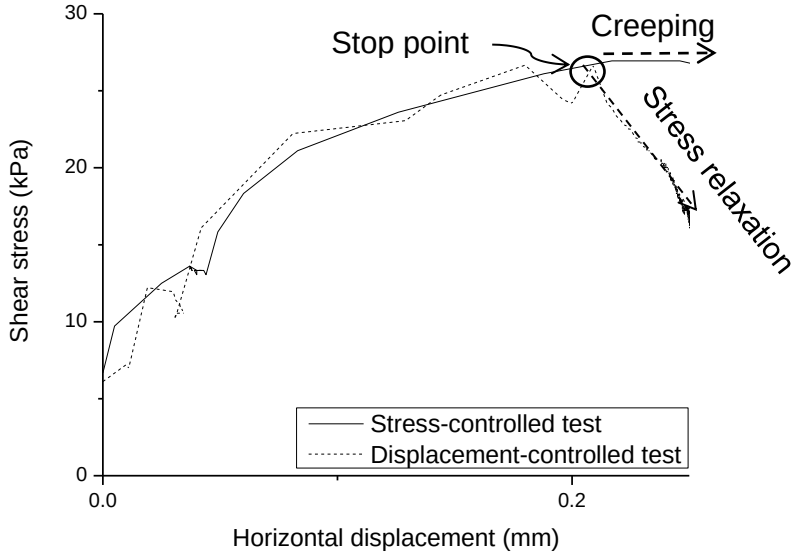

Figure 4.63. Displacement controlled test and stress-controlled test

4.4 VISCOUS-MULTISTAGE TEST

Creep and relaxation tests were conducted in multistage by stopping the test at several levels of target shear stress. On normal occasion, each single stage-test is taking merely 5 days to complete, and these include specimen preparation, consolidation, shearing and finally the viscous tests (either creep or relaxation). By running multistage tests where more than one target shear stress can be applied to one single specimen, the experimental time can be saved up to 50%.

4.4.1 Displacement-controlled test in multistage loading

Figure 4.7 shows 2 different stress levels which were stopped to relax during multistage relaxation test. The test was conducted by shearing the specimen until it reached the 1st target shear stress. Similar to single stage test, the displacement was kept constant (i.e. the step motor was stopped), allowing the shear stress to relax. The second stage of shearing continues by letting the specimen to shear again until it reached the 2nd target shear stress. From the graph, it can be seen that shear stress after decaying at the end of the 1st stage started to increase in the 2nd stage until it reached the 2nd target shear stress. Then, the procedure continued by stopping the step-motor and allowing the shear stress to relax again.

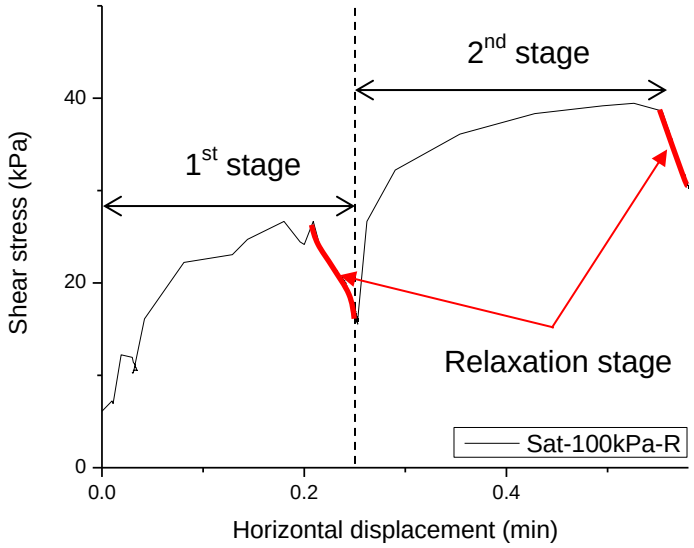

Figure 4.7. Multistage tests for stress relaxation

4.4.2 Stress-controlled test in multistage loading

Figure 4.8 shows 2 different stress levels, which were maintained constant to allow the displacement to creep during multistage creep test. The test was conducted by shearing the specimen in steps to reach the 1st target shear stress. The stress was kept constant, allowing the displacement to creep for one day. The test was then continued to the 2nd target shear stress where the shear force was again applied in steps to reach the next target shear stress. At this point, the shear stress was kept constant to allow the displacement to creep again.

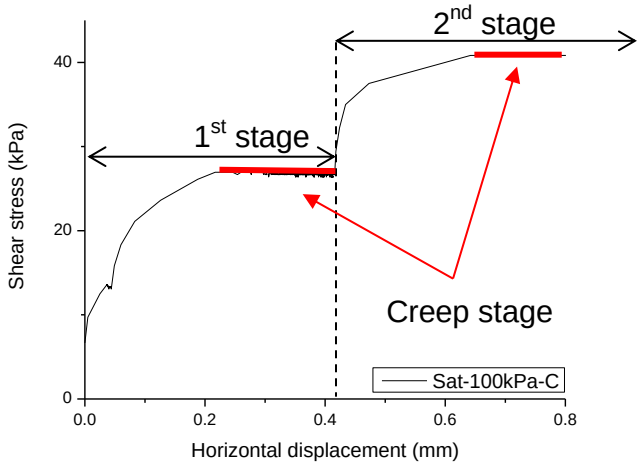

Figure 4.8. Multistage tests for creep

4.4.3 Comparison: multistage test vs single-stage test

The multistage tests were compared with the single-stage tests to identify whether these two tests produce identical viscous response. The loading and relaxation stage for the multistage and single-stage test are compared in Figure 4.9. Once a shear stress of about 40.5 kPa was reached, the shear stress was allowed to relax. From observations, these two tests are able to stop at similar target shear stress even though both were subjected under different loading stage, with accumulation of shear displacement in multistage test.

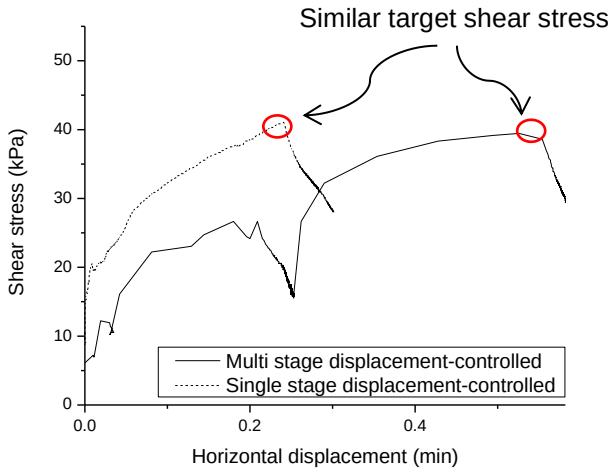

Figure 4.94. Multistage and single stage test for relaxation

Figure 4.10 shows the comparison between the stress relaxation for the single stage and the multistage test. It can be observed that the relaxation response is pretty similar regardless of the mode the initial target stress was reached (single stage or multistage). The stress was observed to decay from 40.5kPa to 27.5kPa in both test modes. It therefore appears that initial stress controls the relaxation response regardless of the previous stress history.

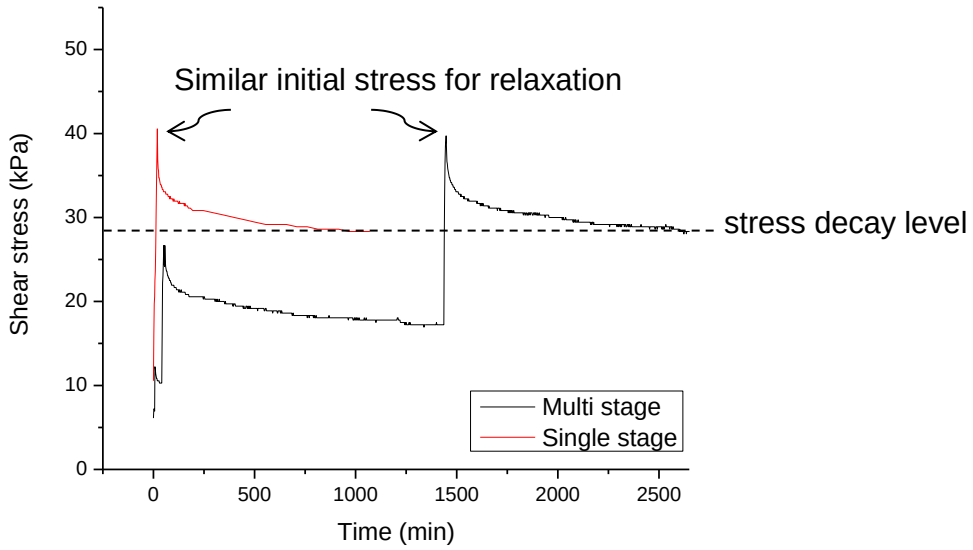

Figure 4.105. Relaxation stage for multistage and single stage test

The loading and creep stage for the multistage and single stage test are compared in Figure 4.11. Once a shear stress of about 40.5 kPa was reached, the displacement was allowed to creep. **Error! Reference source not found.**Figure 4.12 shows the comparison between the displacement creep for the single stage and the multistage test. It can be observed that the creep response is different and this can be attributed to the different displacement accumulated at the onset of the creep test.

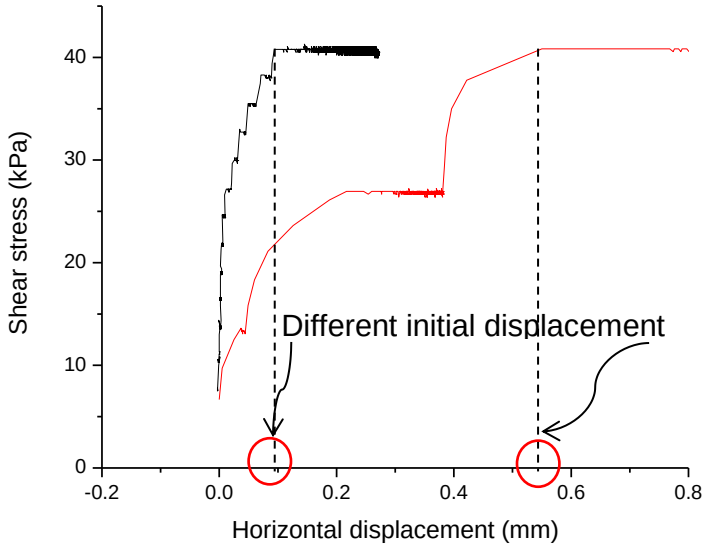

Figure 4.11. Multistage and single stage test for creep

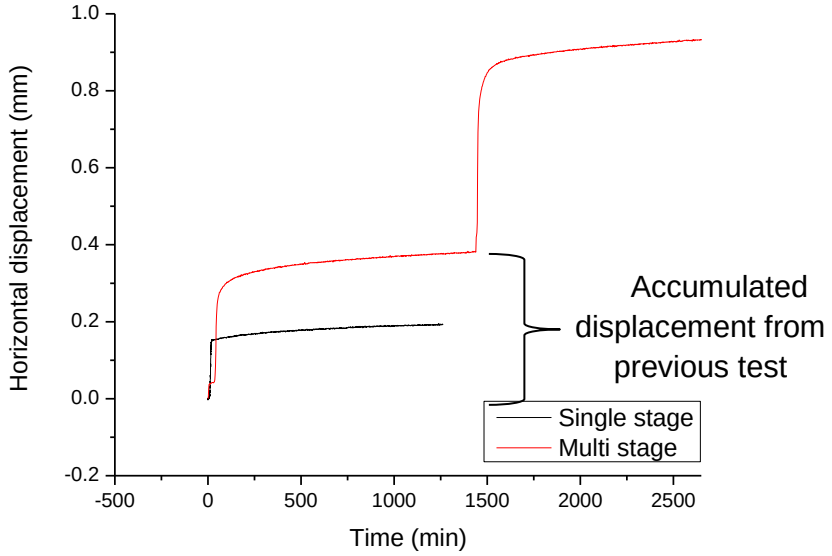

Figure 4.12. Creep stage for multistage and single stage test

4.5 FINAL VISCOUS TESTS

Viscous test on saturated specimens provides a key guideline for viscous test on unsaturated specimens. The idea of multistage viscous test has been utilised in the unsaturated testing with additional aspects of matric suction and degree of saturation to consider. Following the designated experimental procedures, investigations of the viscous behaviour in shear of Ball Clay were then conducted at different level of vertical stress and tangential stress and stress history (pre-peak and post-peak). For the case of unsaturated specimens, viscous behaviour at different water content and, hence, suction, and degree of saturation was considered. Tables 4.1 and 4.2 show the summary of all tests conducted at saturated and unsaturated conditions, respectively.

Table 4.1 List of all specimens at saturated conditions and details of each the tests carried out

Soil condition	Soil history	Mode of testing	Normal stress, σ (kPa)	Target shear stress for viscous tests, τ (%)	Code
Saturated (Sat)	Pre-peak (PRP)	Multi stage (MS)	100	50	Sat-PRP-MS-100-50
				75	Sat-PRP-MS-100-75
				90	Sat-PRP-MS-100-90
	Pre-peak (PRP)	Single stage (S)	100	75	Sat-PRP-S-100-75
				90	Sat-PRP-S-100-90
	Pre-peak (PRP)	Multi stage (MS)	200	25	Sat-PRP-MS-200-25
				50	Sat-PRP-MS-200-50
				75	Sat-PRP-MS-200-75
				90	Sat-PRP-MS-200-90
	Post-peak (POP)	Single stage (S)	100	68	Sat-POP-S-100-68
			200	98	Sat-POP-S-200-98

Table 4.2 List of all specimens at unsaturated conditions and details of each the tests carried out

Soil condition	Soil history	Water content (%)	Mode of testing	Normal stress, σ (kPa)	Target shear stress for viscous tests, τ (%)	Code
Unsaturated (Unsat)	Pre-peak (PRP)	23	Multi stage (MS)	100	30	Unsat23-PRP-MS-100-30
					60	Unsat23-PRP-MS-100-60
					90	Unsat23-PRP-MS-100-90
	Pre-peak (PRP)	29	Multi stage (MS)	100	30	Unsat29-PRP-MS-100-30
					60	Unsat29-PRP-MS-100-60
					90	Unsat29-PRP-MS-100-90

4.5.1 Viscous tests on saturated specimens in the pre-peak range

Figure 4.13 and Figure 4.14 show the stress/displacement paths for the viscous tests (creep and relaxation respectively) for the saturated specimens tested in the pre-peak (PRP) range. Tests were carried out at normal stresses of 100kPa and 200kPa. Peak shear strength was found to be 54kPa at 100kPa vertical stress and 85kPa at 200kPa vertical stress. The multistage relaxation and creep tests were carried out from target shear stresses equal to 50%, 75% and 90% of the peak shear strength.

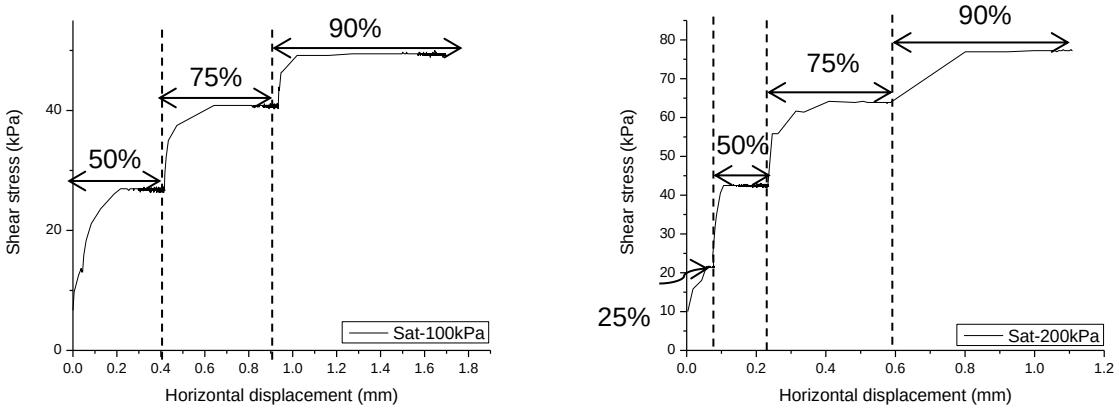

Figure 4.136. Saturated pre-peak creep tests

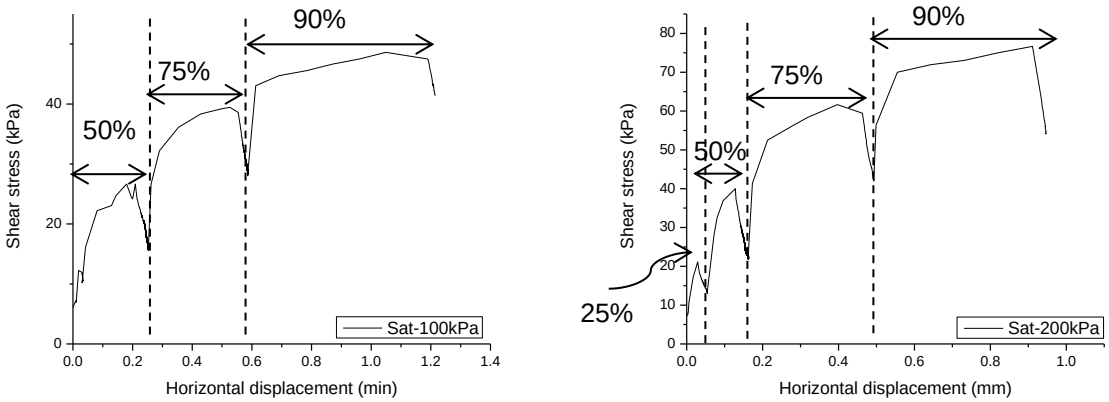

Figure 4.14. Saturated pre-peak relaxation tests

4.5.2 Viscous tests on saturated specimens pre-sheared to residual conditions

Viscous tests in the post-peak range were conducted on a pre-sheared specimen so as to have the first insight into creep and relaxation behaviour in shear at the residual state (Figure 4.15 & Figure 4.16). Since post-peak (residual) state is closely related to reactivated landslides, we were keen to explore more on how the clay responds to creep when it is far from failure (far from residual shear strength) or when it is near to failure (closer to residual shear strength). Thus, we conducted two different tests at two different conditions where the target shear stress was far from failure, Sat-POP-S-100-68 and near to failure Sat-POP-S-200-98.

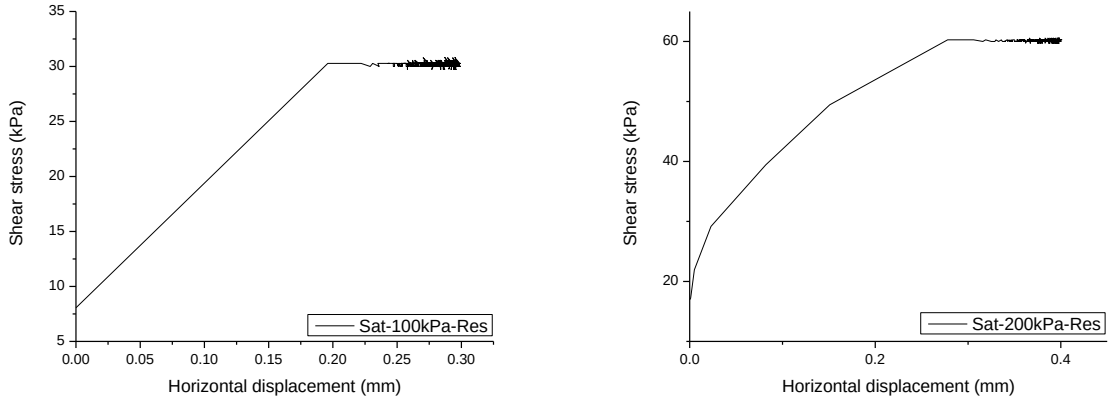

Figure 4.15. Creep tests on saturated specimens at the residual state at two different stress levels

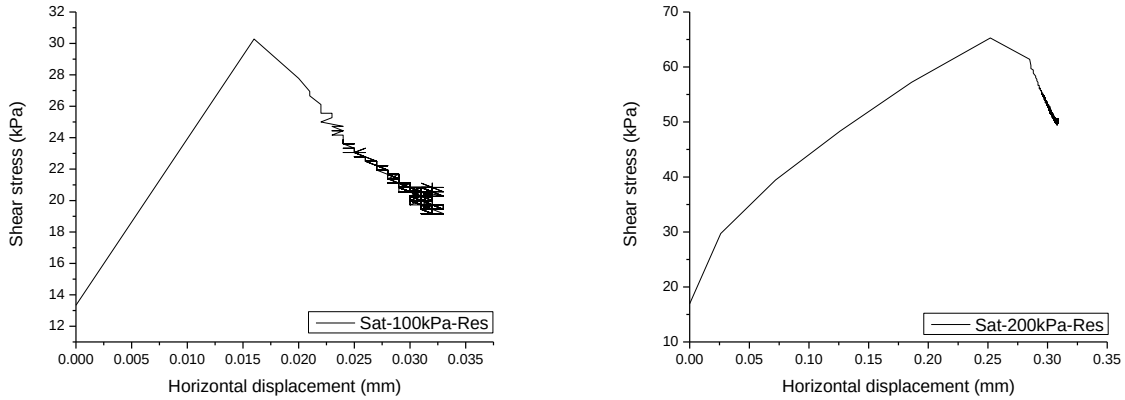

Figure 4.16. Relaxation tests on saturated specimens at the residual state at two different stress levels

4.5.3 Creep test at unsaturated pre-peak

Viscous tests on unsaturated clay were carried out only in the pre-peak range. The tests were conducted at water contents of 23% and 29%, below plastic limit of Ball Clay. Three levels of shear stresses were chosen for the multistage tests (30%, 60% and 90% of peak shear strength) . Figure 4.17 shows the multistage creep tests on unsaturated specimens in the pre-peak range at 100kPa vertical stress for the water contents of 23% and 29%, whereas Figure 4.18 shows the multistage relaxation tests of unsaturated pre-peak at 100kPa vertical stress for the water content of 23% and 29%.

Viscous tests in unsaturated conditions required the determination of specimen water content and matric suction before and after the test. Anti-evaporation systems were implemented during the tests so as ensure water-tight condition in the shear box carriage as well as to minimize evaporation from the specimens (see chapter 3). At the end of viscous tests, the value of suction and water content recorded were used to identify the effects of shearing on suction and also to see if the system was water-tight enough to avoid any moisture loss into the atmosphere.

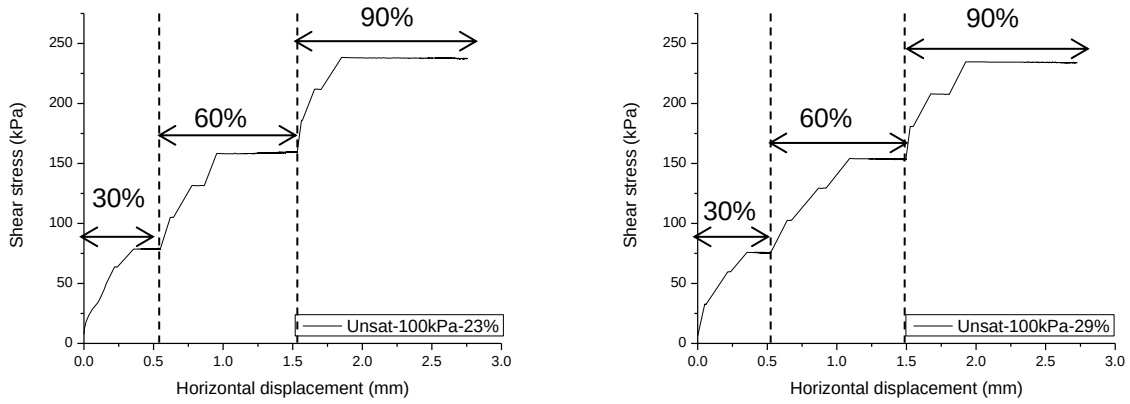

Figure 4.17. Unsaturated pre-peak creep tests at 100kPa vertical stress

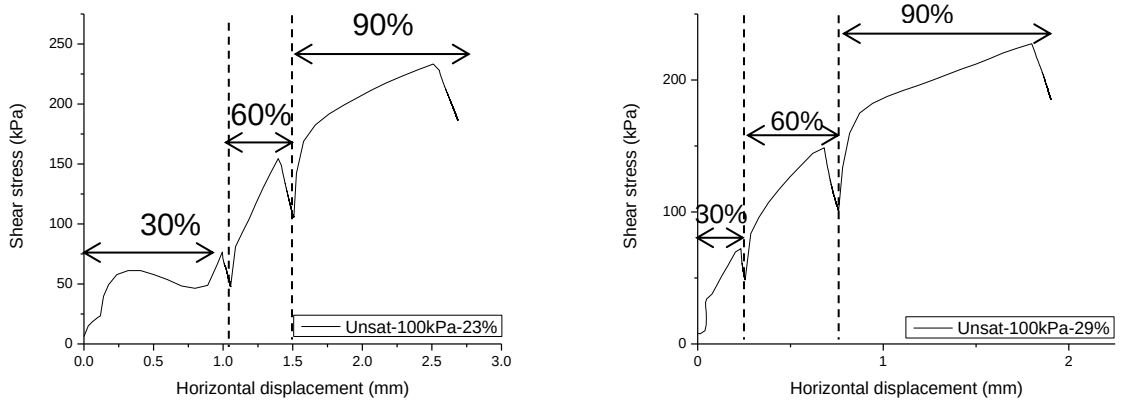

Figure 4.187. Unsaturated pre-peak relaxation tests at 100kPa vertical stress

CHAPTER 5
EXPERIMENTAL RESULTS AND MODELLING

5.1 INTRODUCTION

In this chapter, experimental results for all viscous tests will be presented and discussed. The viscous test results are divided into 3 sub-categories, saturated pre-peak (specimens tested under saturated conditions at the pre-peak range), saturated post-peak (specimens tested under saturated conditions after the attainment of the residual state), and unsaturated pre-peak (specimens tested under unsaturated conditions at the pre-peak range). Pre-peak refers to a condition before soil reaches the maximum shear strength it can sustain. The maximum shear strength is also known as peak shear strength. On the other hand, post-peak is a condition where the soil reaches a residual condition, usually attained when sheared at higher displacement. All test programs were multi stage based, except saturated pre-peak at 100kPa vertical stress and saturated post-peak at 100kPa and 200kPa vertical stresses where the tests were done in single stage. In unsaturated test, the soils were tested at different water content in the partially saturated range, w=23% and w=29% and both were below Ball clay's plastic limit.

5.1.1 Pre-peak determination for all specimens

Figures 5.1, 5.2, and 5.3 show the shear tests conducted to determine the peak shear strength of specimens at saturated pre-peak, saturated post-peak (residual) and unsaturated pre-peak, respectively. Table 5.1 shows the values of peak shear strength for all specimens under various conditions.

Table 5.1 Peak shear strength

Specimens	Peak shear strength (kPa)
Sat-PRP-100	54
Sat-PRP-200	86
Sat-POP-100	43
Sat-POP-200	68
Unsat23-100	268
Unsat29-200	253

Figure 5.4 shows the shear strength lines for specimens at saturated with all target shear stress in the same plane. It can be seen that the target shear stress at 90% of peak shear strength from both 100kPa and 200kPa normal stress lies within shear strength line at residual, suggesting a secondary/tertiary viscous response. The rest of the target shear stresses fall below the shear strength line for residual, indicating a primary viscous response.

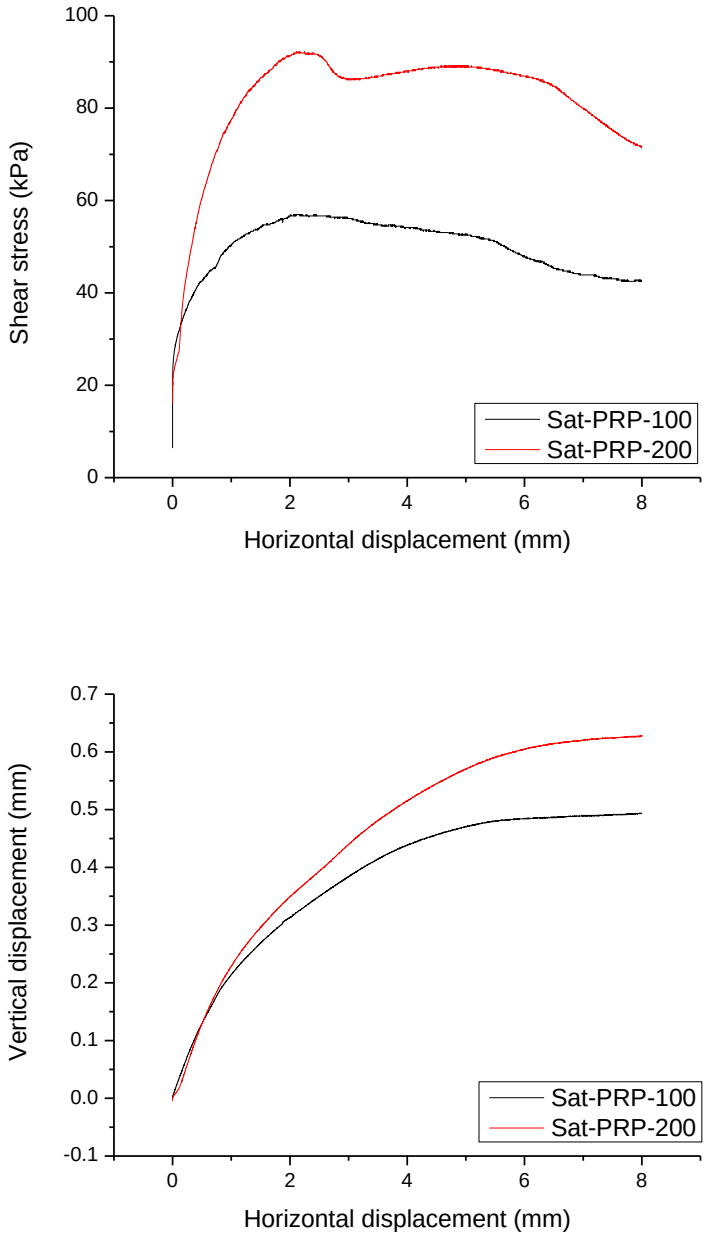

Figure 5.1. a) Peak shear strength of saturated pre-peak at 100kPa and 200kPa normal stress b) vertical displacement vs horizontal displacement plot

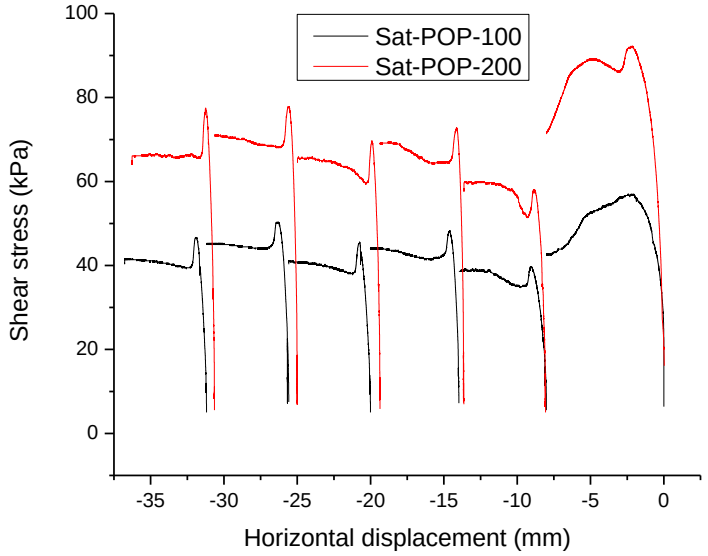

Figure 5.2. Residual shear strength at 100kPa and 200kPa normal stress

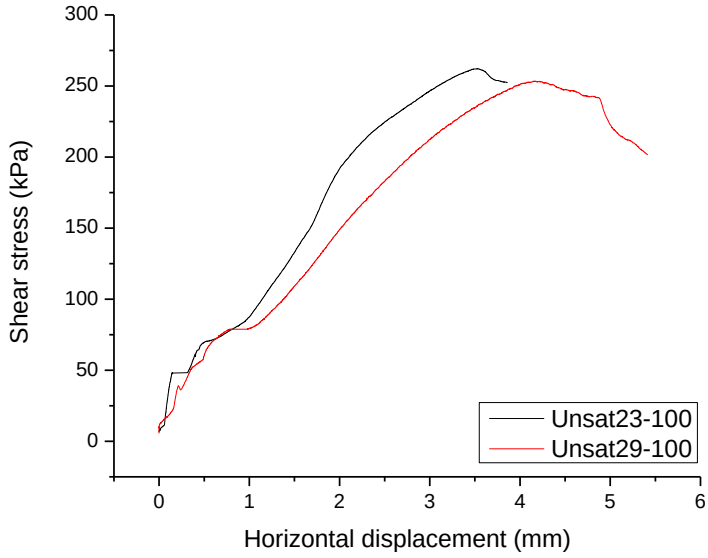

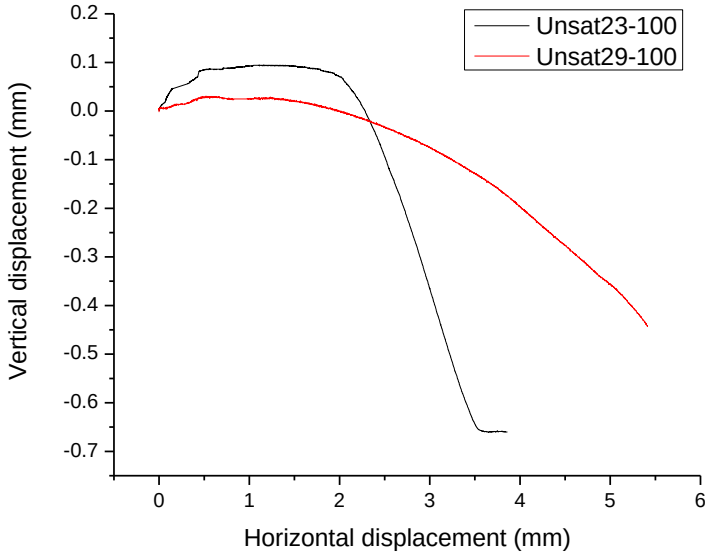

Figure 5.3. a) Peak shear strength of unsaturated pre-peak at 100kPa and 200kPa normal stress b) vertical displacement vs horizontal displacement plot

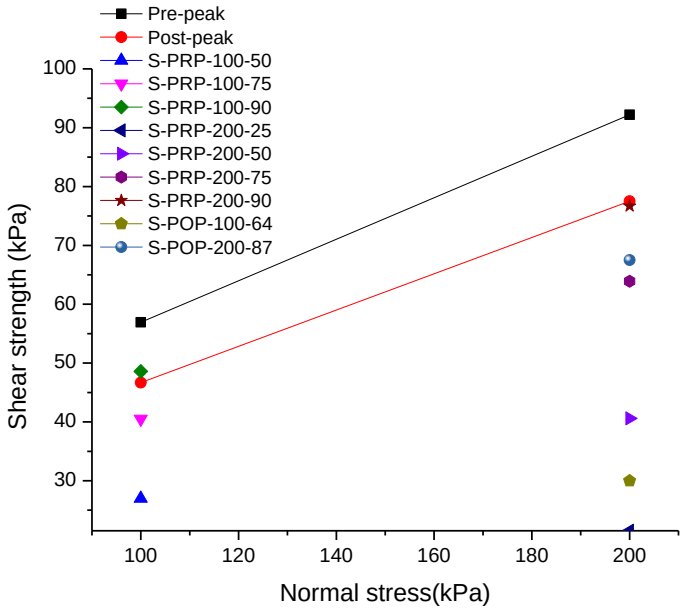

Figure 5.4. Shear strength lines for saturated specimens at pre-peak and post-peak (residual) conditions

5.2 VISCOUS RESPONSE IN SATURATED PRE-PEAK

Viscous response in saturated pre-peak Ball Clay were acquired under 2 different conditions, first considering two different test modes (single stage and multistage) and second by subjecting the specimens to two different vertical stresses (100kPa and 200kPa respectively). For each tests, target shear stress were selected at 50%, 75% and 90% of peak shear strength. For test at 200kPa vertical stress, additional target shear stress of 25% of peak shear strength was added into the test programme.

5.2.1 Single-stage pre-peak at 100 kPa vertical stress

Figure 5.5 shows the creep and stress relaxation response in saturated Ball Clay, at pre-peak condition with applied vertical stress of 100kPa for a single stage test. Two tests were performed, Sat-PRP-S-100-75 and Sat-PRP-S-100-90. These tests were conducted as a 'benchmark' for the tests carried out under multi-stage loading.

Creep displacement and relaxation stress evolve towards an asymptotic value. The ratio between the final displacement (after one day creep) and the initial displacement tends to reduce with increasing initial shear stress (0.27mm/0.09mm=3.0 at Sat-PRP-S-100-75-C and 0.64mm/0.36mm=1.7 at Sat-PRP-S-100-90-C). Same applies to the stress relaxation if one considers the ratio between the initial and final shear stress after one day relaxation (40.5kPa/28.0kPa=1.45 at Sat-PRP-S-100-75-R and 48.6kPa/33.6kPa=1.45 at Sat-PRP-S-100-90-R).

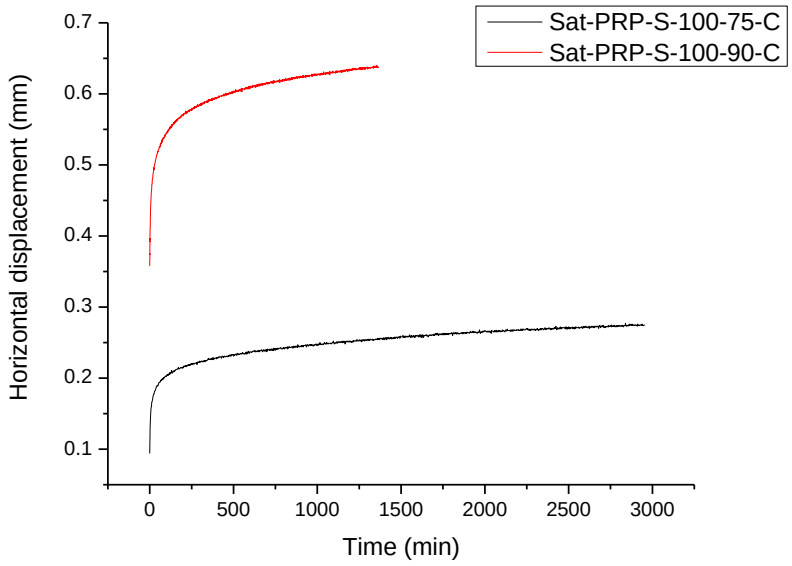

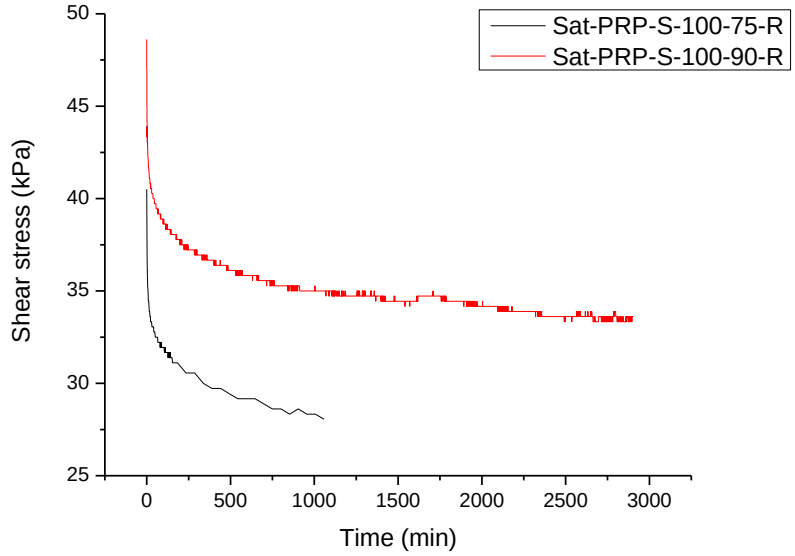

Figure 5.5. Creep and stress relaxation response at single stage pre-peak, 100kPa vertical stress

5.2.2 Multi stage pre-peak at 100 kPa vertical stress

Figure 5.6 shows the creep and stress relaxation response in saturated Ball Clay, at pre-peak condition with applied vertical stress of 100kPa. Three target shear stresses equal to 50%, 75% and 90% of the peak shear stress respectively were attained and then either the displacement was allowed to creep or the stress was allowed to decay.

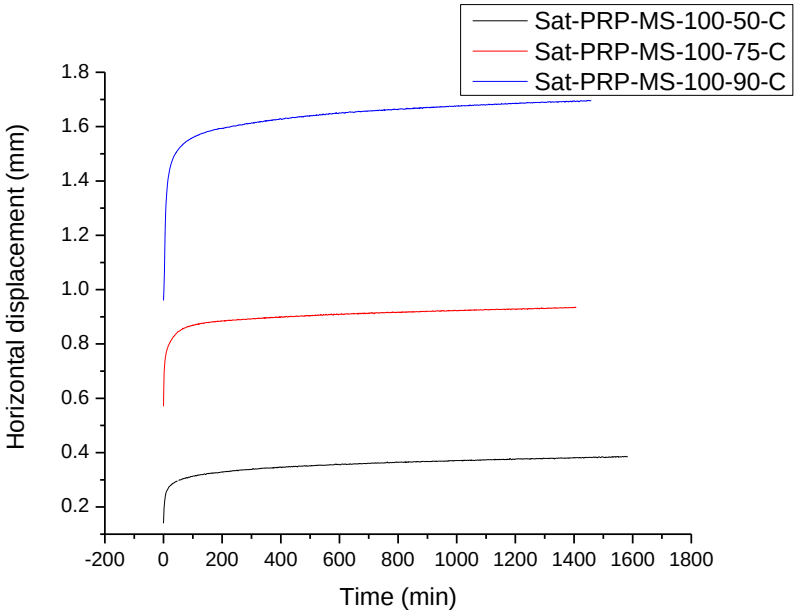

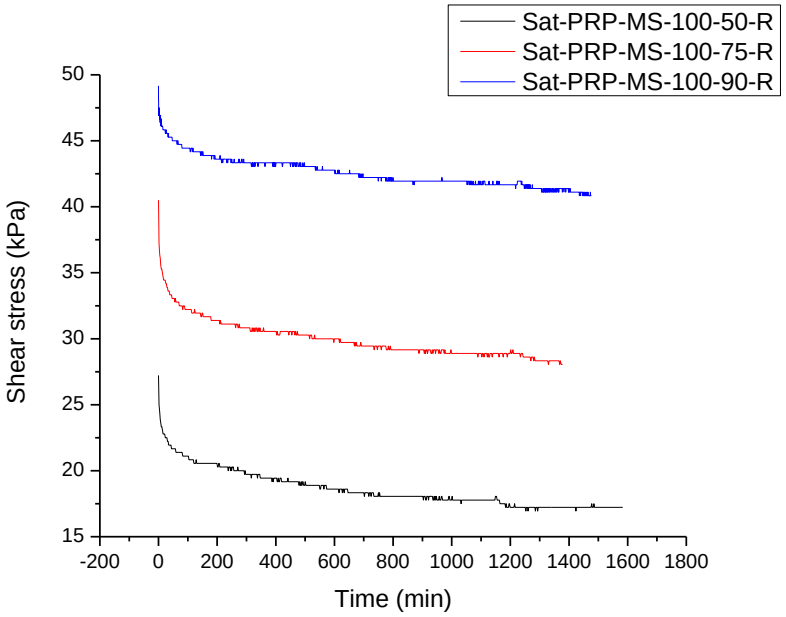

Figure 5.6. Creep and stress relaxation response at multi stage pre-peak, 100kPa vertical stress

Creep displacement and relaxation stress evolves towards an asymptotic value. The ratio between the final displacement (after one day creep) and the initial displacement tends to reduce with increasing initial shear stress (0.43mm/0.14mm=3.1 at Sat-PRP-MS-100-50-C, 0.93mm/0.57mm=1.63 at Sat-PRP-MS-100-75-C and 1.71mm/0.93=1.84 at Sat-PRP-MS-100-90-C). These values are in line with those recorded in the single-stage tests thus corroborating the use of the multi-stage procedure.

Same applies to the stress relaxation if one considers the ratio between the initial and final shear stress after one day relaxation (27.2kPa/15.8kPa=1.7 at Sat-PRP-MS-100-50-R, 40.5kPa/28.1kPa=1.44 at Sat-PRP-MS-100-50-R, and 49.2kPa/40.8kPa=1.2 at Sat-PRP-MS-100-50-R). Again, these values are in line with those recorded in the single-stage tests thus corroborating the use of the multi-stage procedure.

5.2.3 Multi stage pre-peak at 200 kPa vertical stress

Figure 5.7 shows the creep and stress relaxation response in saturated Ball Clay, at pre-peak condition with applied vertical stress of 200kPa. Four target shear stresses equal to 25%, 50%, 75%, and 90% of the peak shear stress respectively were attained and then either the displacement was allowed to creep or the stress was allowed to decay.

Creep displacement and relaxation stress evolve towards an asymptotic value. The ratio between the final displacement (after one day creep) and the initial displacement tends to reduce with increasing initial shear stress with the exception of the 25% (0.08mm/0.05mm=1.6 at Sat-PRP-MS-200-25-C, 0.23mm/0.10mm=2.30 at Sat-PRP-MS-200-50-C, 0.59mm/0.34=1.73 at Sat-PRP-MS-200-75-C, and 1.1mm/0.73mm=1.50 at Sat-PRP-MS-200-90-C). These values are in line with those recorded for the multistage test at 100 kPa.

As for stress relaxation, the ratio between the initial and final shear stress after one day relaxation also appears again to decrease with increasing initial shear stress with the exception of the 25% (21.4kPa/13.3kPa=1.6 at Sat-PRP-MS-200-25-R, 40.6kPa to 22.5kPa=1.80 at 50% Sat-PRP-MS-200-50-R, 63.9kPa/41.9kPa=1.52 at Sat-PRP-MS-200-75-R, and 76.7kPa/54.2kPa=1.41 at Sat-PRP-MS-200-90-R). Again, these values are in line with those recorded for the multistage test at 100 kPa.

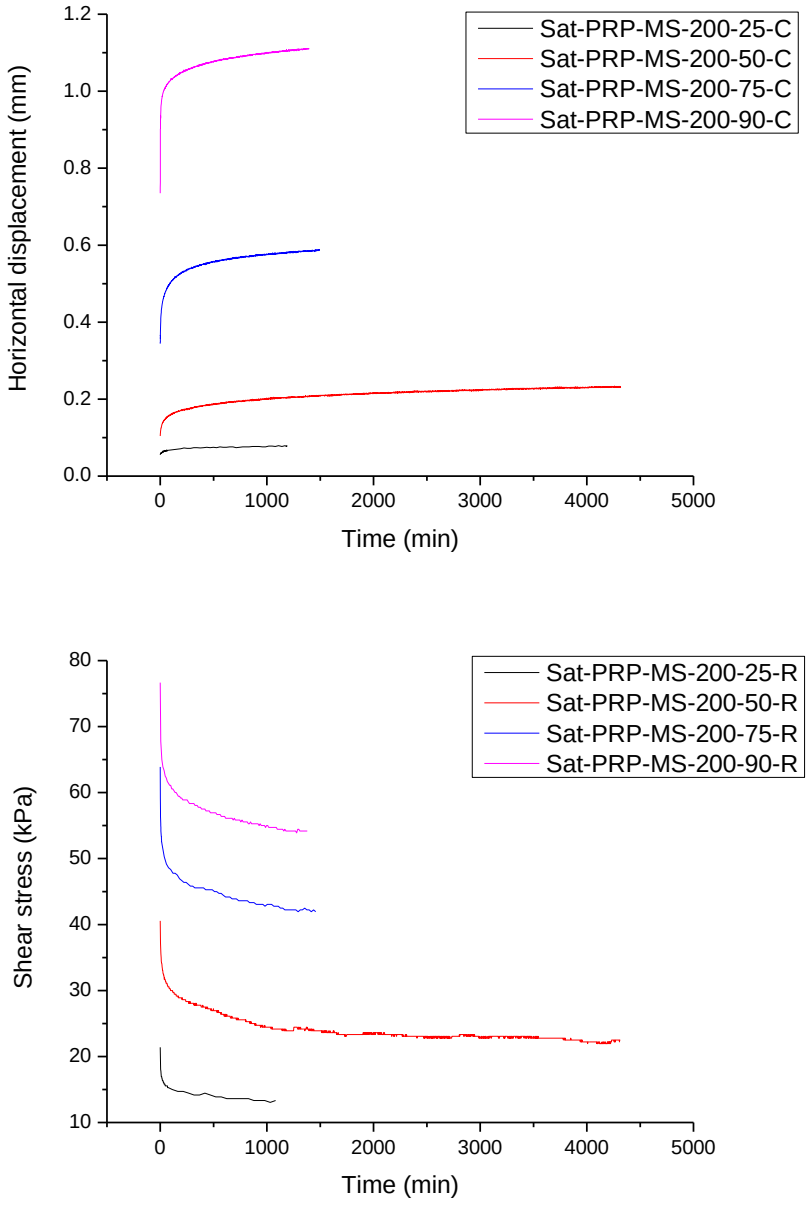

Figure 5.7. Creep and stress relaxation response at multi stage pre-peak, 200kPa vertical stress

5.3 VISCOUS RESPONSE FOR SATURATED POST-PEAK

Viscous response for saturated post-peak were acquired from 2 different vertical stresses levels, 100kPa and 200kPa and both were conducted by single stage test. The target shear stress for 100kPa vertical stress was 68% of residual shear strength (and similar to 50% peak shear stress at 100kPa stress) and corresponds to a condition far from failure. The target shear stress for 200kPa vertical stress was 98% of residual shear strength (and similar to 75% peak shear stress at 200kPa stress), a condition close to failure.

5.3.1 Single stage post-peak

Figure 5.8 shows the creep and stress relaxation response in saturated Ball Clay, at post-peak condition with applied vertical stress of 100kPa and 200kPa, conducted under single stage test.

The creep displacement in post-peak single stage always increased towards an asymptotic value. At Sat-POP-S-100-68-C, the ratio between the final displacement (after one day creep) and the initial displacement is 0.47mm/0.356mm=1.3, lower than the value observed for the Sat-PRP-MS-100-50-C. At Sat-POP-S-200-98-C, the ratio between the final displacement (after one day creep) and the initial displacement is 0.40mm/0.25mm=1.6, not very different from the value observed for the Sat-PRP-MS-200-75-C.

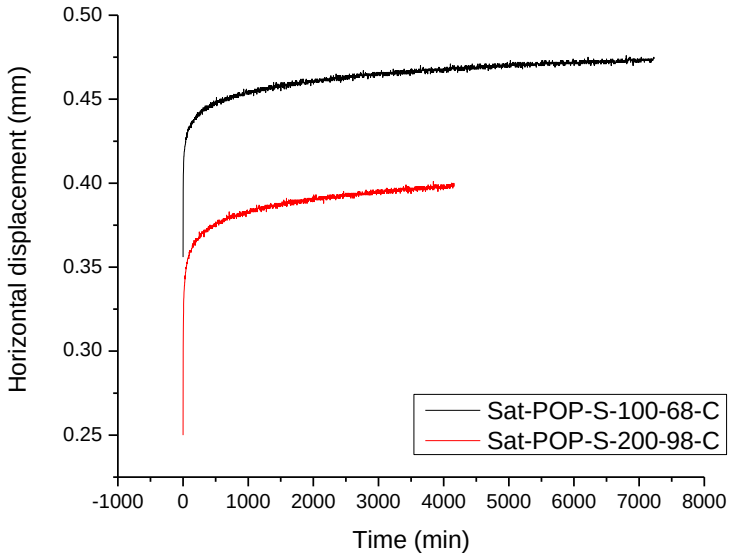

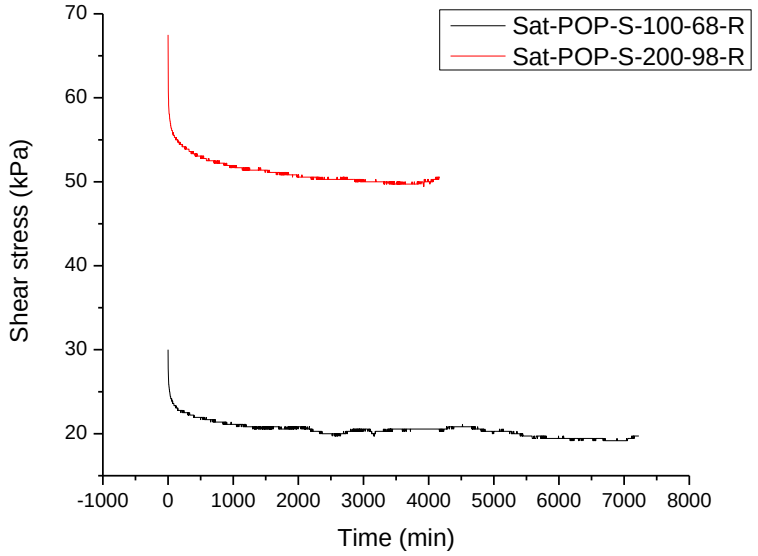

Figure 5.8. Creep and stress relaxation response at single stage post-peak of 100kPa and 200kPa vertical stresses

The shear stress in post-peak single stage always decreased towards an asymptotic value. At Sat-POP-S-100-68-R, the ratio between the initial and final shear stress after one day relaxation is equal to 30.0kPa/19.7kPa=1.52, slightly lower than the value observed for the Sat-PRP-MS-100-R. At Sat-POP-S-200-98-R, the ratio between the initial and final shear stress after one day relaxation is equal to 67.5kPa/50.6kPa =1.33, slightly lower than the value observed for the Sat-PRP-MS-200-75-R.

5.4 VISCOUS RESPONSE FOR UNSATURATED PRE-PEAK

Viscous response in unsaturated pre-peak Ball Clay was acquired from viscous tests at water content of 23% and 29%, respectively. Both tests were conducted under similar applied vertical stress of 100kPa, in a multi stage test. Target shear stresses were 30%, 60% and 90% of peak shear strength. Due to the existence of matric suction and effects of degree of saturation in unsaturated soils, the peak shear strength of the specimens are very high as compared to the saturated specimens. The creep and stress relaxation responses for unsaturated pre-peak condition with the effect of matric suction are presented herein.

5.4.1 23% water content at 100 kPa vertical stress

Figure 5.9 shows the creep and stress relaxation response in pre-peak saturated Ball Clay, at w=23% with applied vertical stress of 100kPa. Three target shear stresses of 30%, 60% and 90% were considered and either the displacement was allowed to creep or the stress to relax in viscous multi stage test.

Creep increases to an asymptotic value. The initial displacement of 0.34mm creeps to 0.55mm at Unsat23-PRP-MS-100-30-C, the initial displacement of 0.93mm creeps to

1.53mm at Unsat23-PRP-MS-100-60-C, and the initial displacement of 1.74mm creeps to 2.75mm at Unsat23-PRP-MS-100-90-C.

On the other hand, stress relaxation decays exponentially over the time. The shear stress decays from 78.1kPa to 47.5kPa at Unsat23-PRP-MS-100-30-R, from 156.1kPa to 105.8kPa at Unsat23-PRP-MS-100-60-R, and from 234.2kPa to 186.7kPa at Unsat23-PRP-MS-100-90-R.

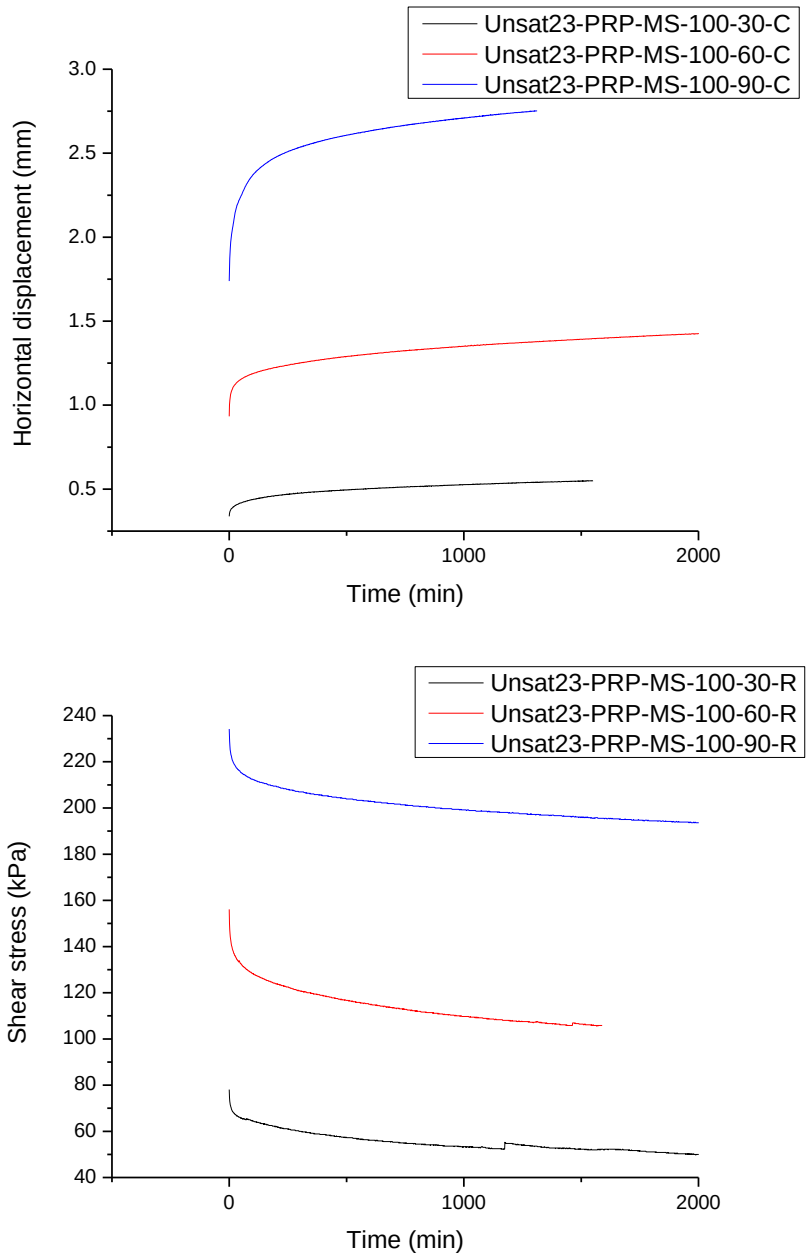

Figure 5.9. Creep and stress relaxation response at unsaturated multi stage pre-peak, of 23% water content and 100kPa vertical stress

5.4.2 29% water content at 100 kPa vertical stress

Figure 5.10 shows the creep and stress relaxation response in pre-peak saturated Ball Clay, at w=29% with applied vertical stress of 100kPa. 3 target shear stresses of 30%, 60% and 90% of peak strength were considered and either the displacement was allowed to creep or the stress to relax in viscous multi stage test.

Creep increases to an asymptotic value. The initial displacement of 0.32mm creeps to 0.52mm at Unsat29-PRP-MS-100-30-C, the initial displacement of 0.99 creeps to 1.5mm at Unsat29-PRP-MS-100-60-C, and the initial displacement of 1.84m creeps to 2.73mm at Unsat29-PRP-MS-100-90-C.

On the other hand, stress relaxation decays exponentially over the time. The shear stress decays from 75.8kPa to 48.6kPa at Unsat29-PRP-MS-100-30-R, from 151.9kpa to 100.8kPa at Unsat29-PRP-MS-100-60-R, and from 227.8kPa to 185kPa at Unsat29-PRP-MS-100-90-R.

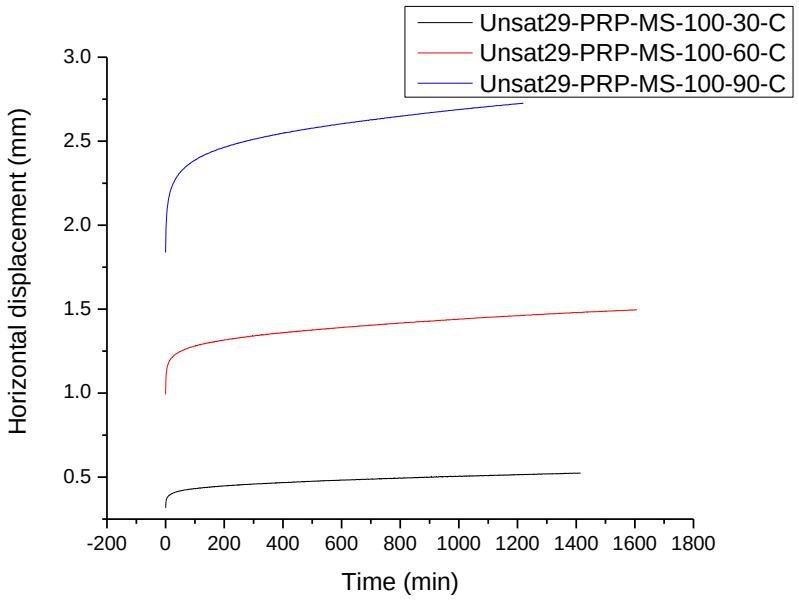

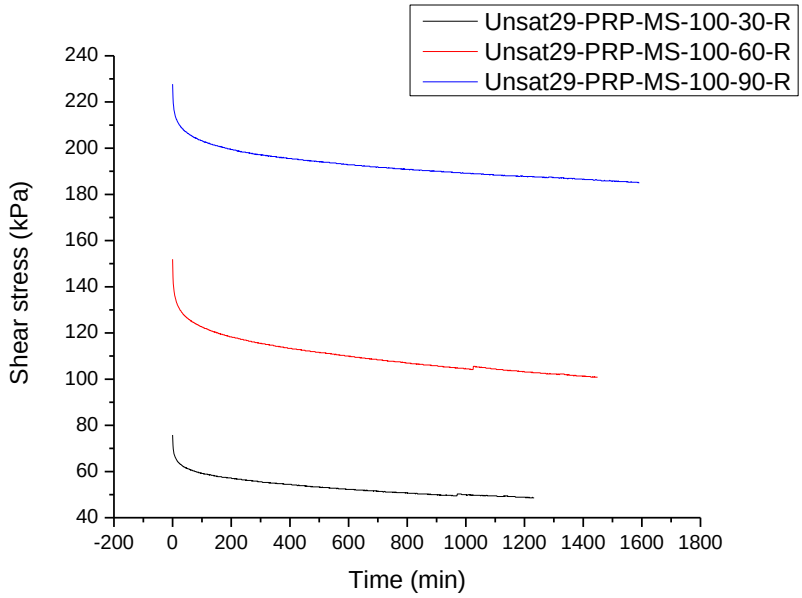

Figure 5.10. Creep and stress relaxation response at unsaturated multi stage pre-peak, of 29% water content and 100kPa vertical stress

5.4.3 Matric suction and water content measurements of unsaturated specimens, before and after shearing

Table 5.2 shows the matric suction and water content for unsaturated soil tested in the lab. Differences in water content values before and after shearing were observed suggesting that evaporation did take place throughout the shearing and viscous stages. Although the corresponding change in suction was not very significant, it clearly appeared that the anti-evaporation system should be improved. Presence of matric suction as a whole seems to give less significant impact to the viscous behaviour in unsaturated state. Based on modelling simulation at w=23% and 29%, both were showing viscous curves response that looks pretty identical to one another under two different water content, given at two different suction value.

Table 5.2. Matric suction and water content for unsaturated soil

	Relaxation				Creep			
	Before		After		Before		After	
Initial Water content, w_i	Water content	suction (MPa)	Water content	suction (MPa)	Water content	suction (MPa)	Water content	suction (MPa)
29%	25.98	2.68	24.75	2.95	26.41	2.55	24.37	2.84
23%	22.07	3.33	20.42	3.61	21.72	3.86	18.86	4.13

5.4.4 Comparison of all datasets at various conditions

This section summarizes viscous response under various conditions, such as repeatability, effect of normal stress increase, effect of increase in the ratio between applied shear stress and peak shear strength and effect of suction increase.

Repeatability viscous response under different test mode

Figure 5.11 shows the repeated viscous response by taking an example from Sat-PRP-100-75 at multistage and single-stage test. At similar target shear stress, repeated creep test under different mode of loading is not identical having different initial displacement (creep), whereas the repeated relaxation test is showing pretty much identical stress relaxation response with similar initial stress.

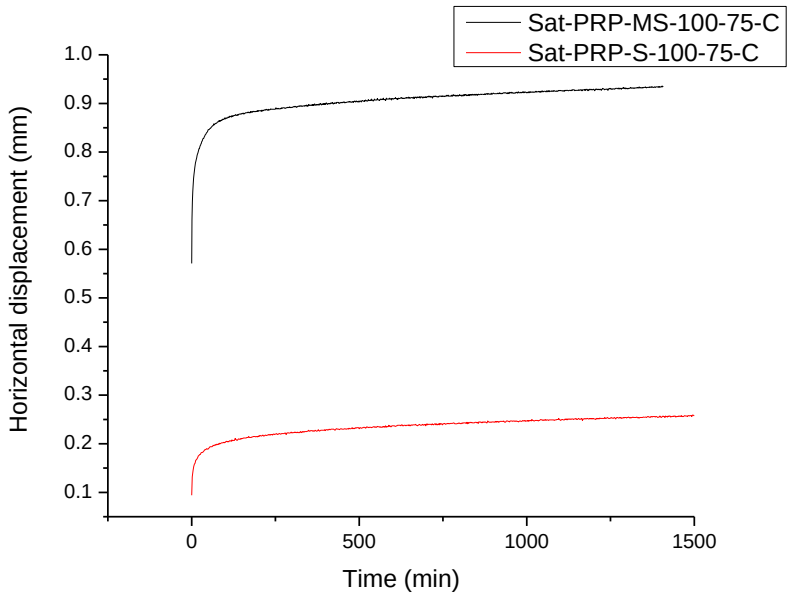

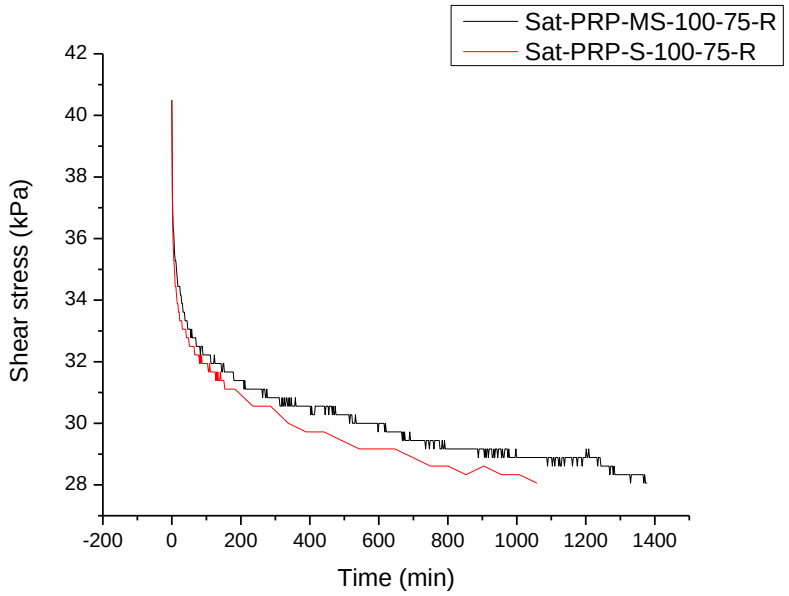

Figure 5.11. Repeatability viscous response

Effect of normal stress increase

Figure 5.12 shows effect of normal stress increase by taking an example from Sat-PRP-MS-90 at 100kPa and 200kPa normal stress. From observation, soil stiffness is showing direct relationship with stress relaxation where increase in normal stress corresponds to higher stress decays. On the other hand, creep response is inversely proportional to the stiffness of soils where less creeping was observed at 100kPa normal stress as compared to 200kPa normal stress. .

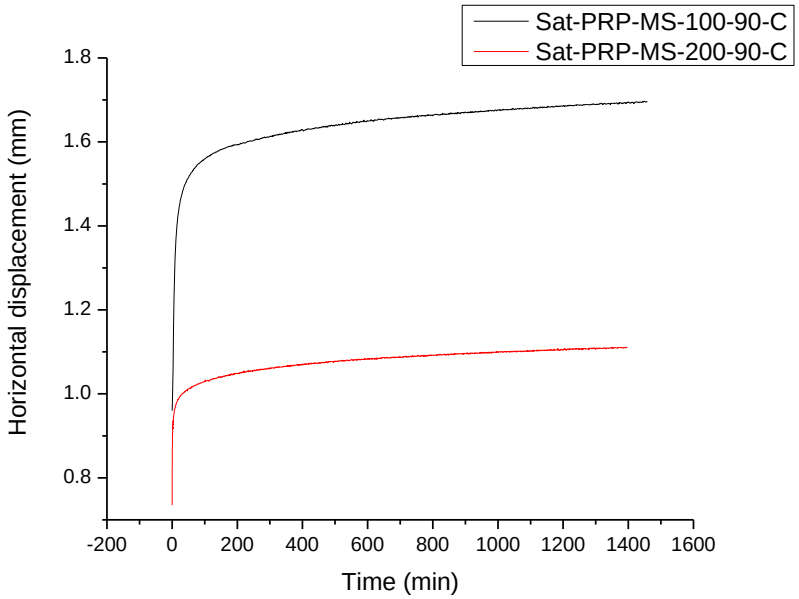

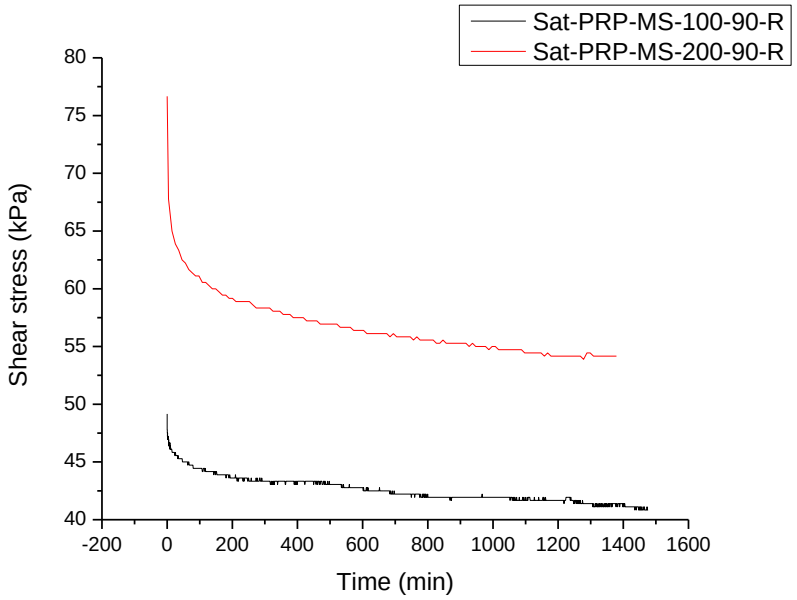

Figure 5.12. Effect of normal stress increase

Effect of an increase in the ratio between applied shear stress and peak shear strength

Figure 5.13 shows effect of an increase in the ratio between applied shear stress and peak shear strength at Sat-PRP-MS-100. From observation, creep response increased with increasing of stress ratio. Stress relaxation response is showing similar trend except that it became non-monotonic at 90% of peak shear strength.

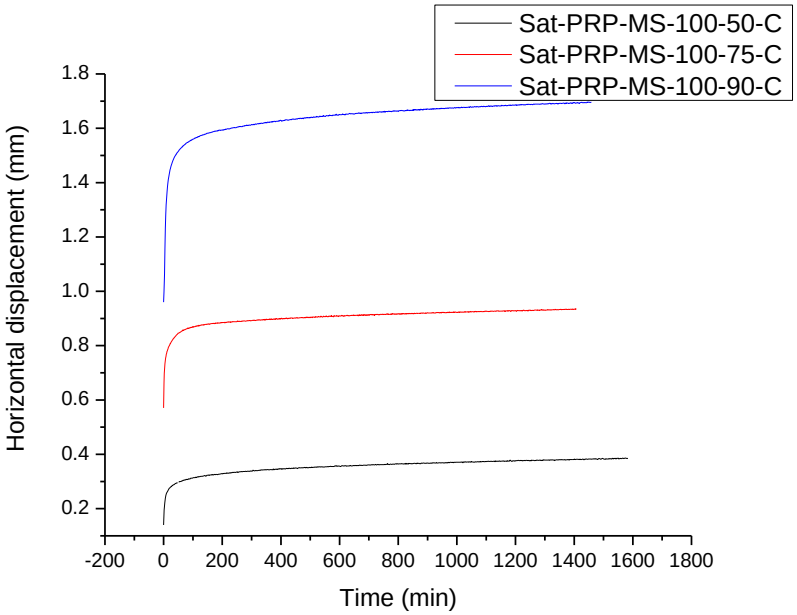

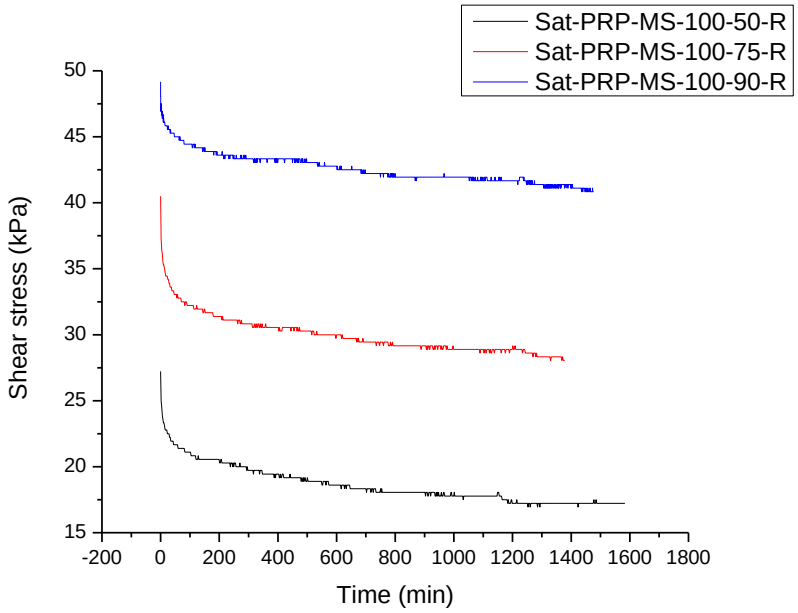

Figure 5.13. Effect of an increase in the ratio between applied shear stress and peak shear strength

Effect of suction increase

Figure 5.14 shows effect of suction increase by taking the example from saturated dataset, Sat-PRP-MS-100-90, to represent a condition of low (zero) suction, and unsaturated datasets, Unsat-PRP-MS-100-90 at w=23% and w=29%, to represent conditions of high suction. From observations, creep response in unsaturated as suction increases are showing curves trend that is yet to reached plateau as compared to the one in saturated. The same trend applies in the stress relaxation response. Unsaturated viscous response seemed to be pretty identical to one another with little variations observed between them.

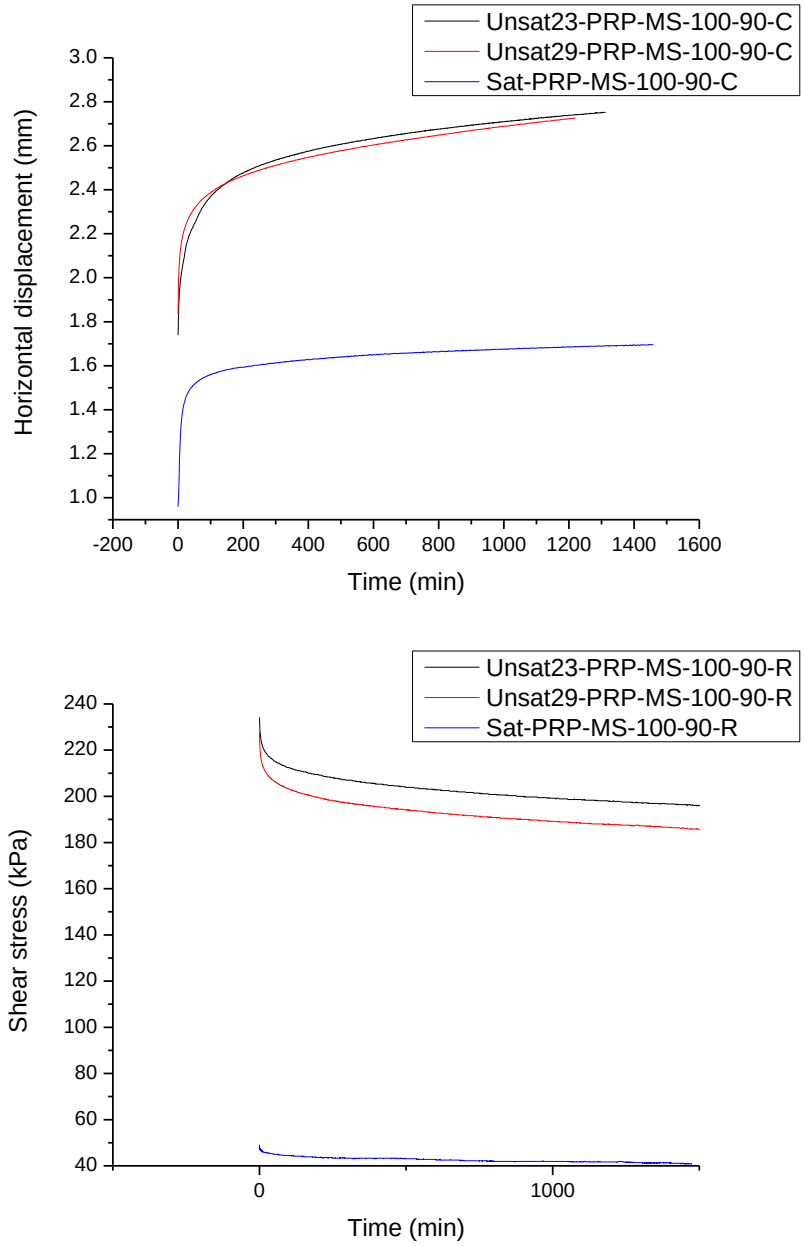

Figure 5.14. Effect of suction increase

5.5 MODELLING

To understand viscous response of the Ball Clay, analogue mechanical models built upon combinations of springs and dashpot, i.e. generalized kelvin and Maxwell models, were considered. These models allow capturing creep and relaxation response using a single set of parameters. The models were developed analytically and constitutive equations derived from the models were used to simulate experimental results. At first, we decided to quantify viscous response in Ball Clay with simple models that require a few parameters. Three

element models were initially selected. However, because the loading system of direct shear box is not stiff and is showing some creep/relaxation interplay during viscous test, another elastic element was added to the model to address the issue of deforming loading system. The 3-element model works well in capturing the final value of creep displacement and relaxation stress (end here refers to end of viscous test, not the viscous process as a whole) using a single set of parameters. The only downside of the 3-element model is that viscous part is poorly captured. Therefore, to get a better curve simulation especially in the viscous part, we add another viscous element to the existing model for an overall 5-element viscous model. The generalized Kelvin model with additional springs connected in series was considered for a better fitting of the viscous behaviour. Due to the complexity in solving the constitutive equation for stress relaxation, only creep response was considered for the 5-element viscous model.

5.5.1 3 elements visco-elastic models

Figure 5.15 shows the 3 elements mechanical models based on the analogues of spring and dashpots. Model in Figure 5.15a is a Kelvin model connected in series with a spring element.

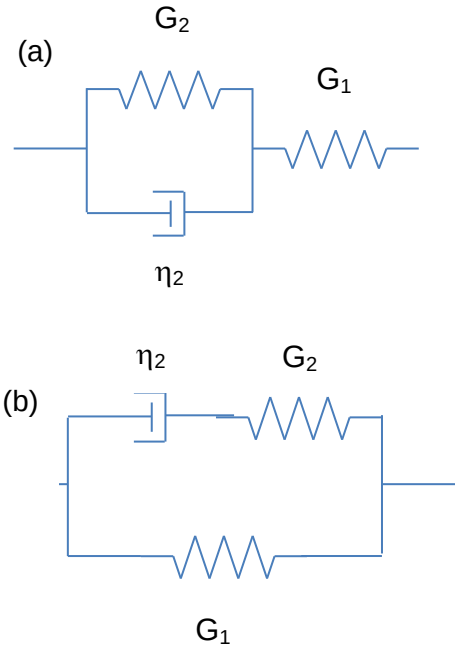

Figure 5.15. 3-element mechanical models

The creep and relaxation constitutive equations for this model (M3a) are given by:

$$Creep \qquad \gamma = \underbrace{\left\{\left[1 - exp\left(-\frac{t}{\tau_2}\right)\right]\frac{G_1}{G_2} + 1\right\}}_{J(t)}\gamma(0) \qquad \tau_2 = \frac{\eta_2}{G_2} \qquad [1]$$

$$Relaxation \qquad \sigma = \underbrace{\frac{1}{G_1 + G_2}\left\{G_2 + G_1 \cdot exp\left(-\frac{t}{\tau'}\right)\right\}}_{\boldsymbol{G(t)}}\sigma(0) \qquad \tau' = \frac{\eta_2}{G_1 + G_2} \qquad [2]$$

where J(t) is the creep compliance, G(t) is the relaxation modulus, t is the time, G_1 and G_2 are the elastic elements from spring, η_2 is the viscous element of dashpot, σ is the shear stress, γ is the horizontal displacement, $\sigma(0)$ is the initial shear stress, and $\gamma(0)$ is the initial horizontal displacement.

Figure 5.15b shows a Maxwell model connected in parallel with a spring. The creep and relaxation constitutive equations for this model (M3b) are given by:

$$Creep \qquad \gamma = \underbrace{\left\{1 + \frac{G_2}{G_1} - \frac{G_2}{G_1} exp\left(-\frac{t}{\tau'}\right)\right\}}_{\boldsymbol{J(t)}}\gamma(0) \qquad \tau' = \frac{G_1 + G_2}{G_1}\frac{\eta_2}{G_2} \qquad [3]$$

$$Relaxation \qquad \sigma = \underbrace{\frac{1}{G_1 + G_2}\left\{G_2 + G_1 \cdot exp\left(-\frac{t}{\tau'}\right)\right\}}_{\boldsymbol{G(t)}}\sigma(0) \qquad \tau_2 = \frac{\eta_2}{G_2} \qquad [4]$$

where J(t) is the creep compliance, G(t) is the relaxation modulus, t is the time, G_1 and G_2 are the elastic elements from spring, η_2 is the viscous element of dashpot, σ is the shear stress, γ is the horizontal displacement, $\sigma(0)$ is the initial shear stress, and $\gamma(0)$ is the initial horizontal displacement (refer Annex D for more details).

Figure 5.16 shows the performance of the 3-element models M3a and M3b for Sat-PRP-MS-100-50. These models strictly predict an asymptotic behaviour that is stabilization of displacement in creep mode and of stress in relaxation mode.

It can be seen that the same model based on a single set of parameters fails to capture both creep and relaxation response. The model parameters were fitted onto the creep response. However, it appears that the same set of parameters is not capable of capturing the relaxation response. If the parameters were adjusted to fit the stress relaxation response, the creep on the other hand would have been poorly captured.

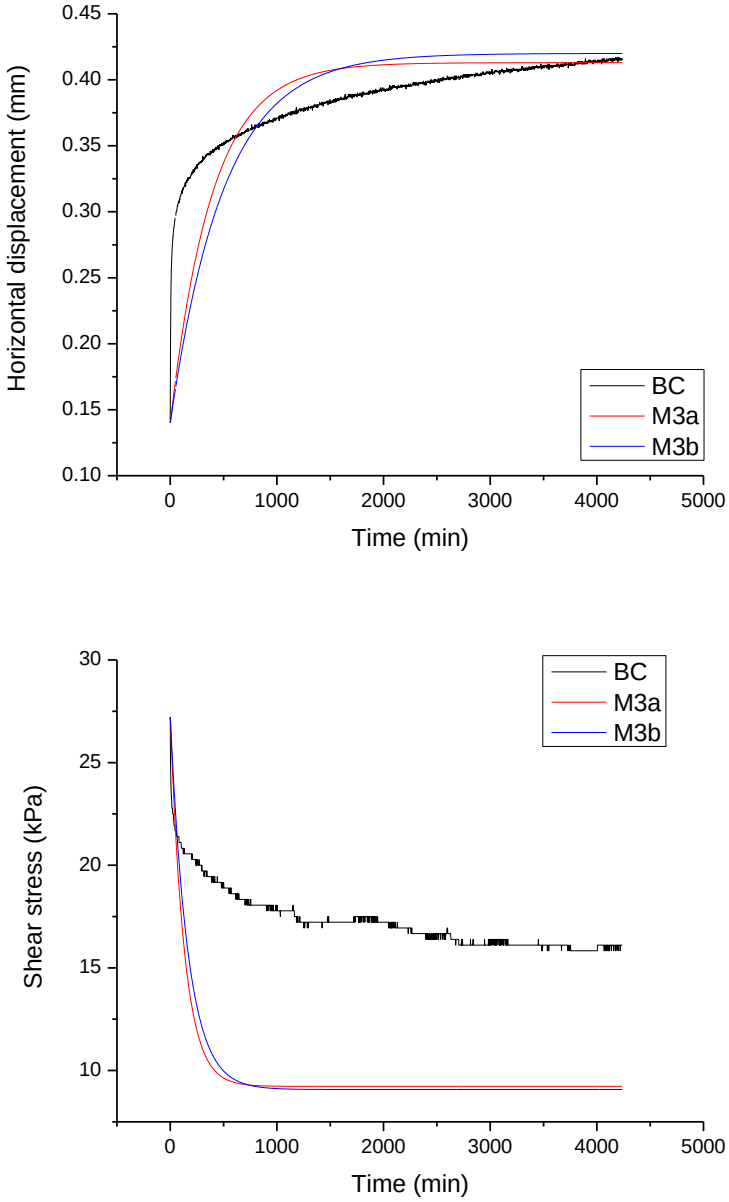

Figure 5.16 Simulation of creep and relaxation response with 3-elements models, M3a and M3b

The reason why a single set of parameters fails in capturing simultaneously creep and relaxation response is not surprising if the relaxation and creep equations are inspected in model detail. If γ_0 and γ_∞ are the initial and final (creep) displacement and σ_0 and σ_∞ are the initial and final (relaxation) stress respectively, it can be easily shown that the models return the same ratios for γ_∞/γ_0 and σ_0/σ_∞

$$\frac{\gamma_\infty}{\gamma_0} = \frac{\sigma_0}{\sigma_\infty} = \frac{G_1}{G_2} + 1 \qquad [5]$$

$$\frac{\gamma_\infty}{\gamma_0} = \frac{\sigma_0}{\sigma_\infty} = 1 + \frac{G_2}{G_1} \qquad [6]$$

Data clearly shows that the ratios γ_∞/γ_0 and σ_0/σ_∞ are not equal experimentally. This is the case shown in Figure 5.16 and similar observation could be made for tests carried out at other stress levels in terms of normal stress and target shear stress. As a result, the same model cannot simulate creep and relaxation with a single set of parameters.

It was therefore suspected that this inconsistency was associated with the compliance of the system, i.e. the initial displacement γ_0 is affected by the deformation of the loading system and the relaxation stress σ_∞ is also controlled by the stiffness of the loading system. If this was true, creep and relaxation should be captured by a single set of parameters if the compliance of the system is properly accounted for.

5.5.2 (3+1)-element visco-elastic models (additional spring to account for loading system compliance)

Figure 5.17 shows the 3 elements mechanical models with additional spring to account for loading system deformation (G_3). Figure 5.17.a shows a Kelvin model connected in series with 2 spring elements. The creep and stress relaxation constitutive equations for this model are given by:

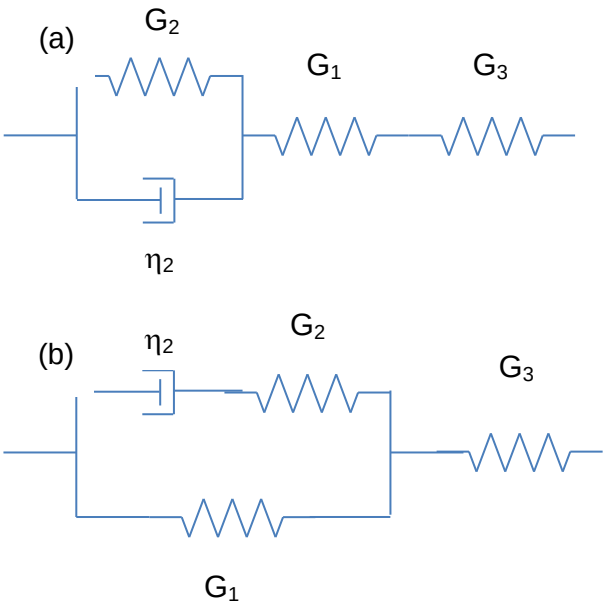

Figure 5.17. (3+1)-element mechanical model with additional spring to account for compliance of the loading system

$$Creep \qquad \gamma = \underbrace{\left\{\left[1 - exp\left(-\frac{t}{\tau_2}\right)\right]\frac{G_1 + G_3}{G_2} + 1\right\}}_{J(t)}\gamma(0) \qquad \tau_2 = \frac{\eta_2}{G_2} \qquad [7]$$

$$Relaxation \qquad \sigma = \underbrace{\frac{1}{G_1 + G_3 + G_2}\left\{G_2 + (G_1 + G_3)\cdot exp\left(-\frac{t}{\tau'}\right)\right\}}_{G(t)}\sigma(0) \quad \tau' = \frac{\eta_2}{G_1 + G_3 + G_2} \qquad [8]$$

where $J(t)$ is the creep compliance, $G(t)$ is the relaxation modulus, t is the time, G_1, G_2, and G_3 are the stiffness of the springs, η_2 is the viscosity of the dashpot, σ is the shear stress, γ is the horizontal displacement, $\sigma(0)$ is the initial shear stress, and $\gamma(0)$ is the initial horizontal displacement (refer Annex E for more details).

Figure 5.17.b shows a Maxwell model connected with 2 springs, one of which represents the compliance of the system. The creep and relaxation constitutive equations for the model M(3+1)b are given by:

$$Creep \qquad \gamma = \left[\frac{\left(1 + \frac{G_2}{G_1}\right)}{1 + \frac{G_2}{G_1 + G_3}} - \frac{G_2}{G_1}\frac{1}{1 + \frac{G_1}{G_3} + \frac{G_2}{G_3}}exp\left(-\frac{t}{\tau'}\right)\right]\gamma(0) \qquad \tau' = \frac{G_1 + G_2}{G_1}\frac{\eta_2}{G_2} \qquad [9]$$

$$Relaxation \quad \sigma = \frac{1}{1 + \frac{G_1}{G_3}}\left[G_1\left(\frac{G_1}{G_3} + \frac{G_2}{G_3} + 1\right) + G_2 exp\left(-\frac{\frac{G_1}{G_3} + 1}{\frac{G_1}{G_3} + \frac{G_2}{G_3} + 1}\frac{t}{\tau_2}\right)\right]\frac{1}{(G_1 + G_2)}\sigma(0); \qquad \tau_2 = \frac{\eta_2}{G_2} \qquad [10]$$

where $J(t)$ is the creep compliance, $G(t)$ is the relaxation modulus, t is the time, G_1, G_2, and G_3 are the stiffness of the springs, η_2 is the viscosity of the dashpot, σ is the shear stress, γ is the horizontal displacement, $\sigma(0)$ is the initial shear stress, and $\gamma(0)$ is the initial horizontal displacement.

Figure 5.18 shows a modelling simulation example with (3+1)-element model, M(3+1)a and M(3+1)b, for the case of saturated pre-peak at 100kPa vertical stress, with shear stress level of 50% of peak shear strength (taken from multistage test). These 2 models were originated from the 3-element models mentioned above but with additional elastic element to account for the compliance of the loading system.

The stiffness of the additional spring G_3 was derived from the calibration illustrated in Chapter 3. For the simulation of creep, only the stiffness of the holding arm was considered and derived from the calibration shown in Figure 3.12. For the simulation of relaxation, both the loading arm and the holding arm were considered. The stiffness of the holding arm was again derived from the calibration shown in Figure 3.12. The stiffness of the loading arm was derived by test according to the procedure illustrated in Figure 3.14.

For a given test in terms of initial shear stress, normal stress, state of saturation, and stress history, a single set of parameters were used to model both creep and relaxation of Ball clay. A single set of parameters seems to capture fairly well the final creep displacement and relaxation stress, especially by the Model 3+1a as shown in Figure 5.18. Model 3+1a well captured the response in creep but underestimate the stress relaxation response. By comparison with the Model M3a performances, the simulations by the Model 3+1a were considered satisfactory. Model 3+1b, despite well captured the response in creep, is less satisfactory in simulating the stress relaxation response.

This shows that relaxation and creep responses are associated with the same viscous response. This conclusion is less trivial than it seems at first glance. In the literature, creep and relaxation are very often treated separately and empirical models are generally used to fit experimental data. The simulation below shows that viscous behaviour can be tested and calibrated in ‘relaxation’ mode and then extrapolated to the creep mode.

The importance of including the compliance of the system in the modelling of the viscous response is shown in Figure 5.19 where the performance of the models M3a and M(3+1), without and with the additional spring to account for the system compliance respectively, are compared. In both cases, model parameters were derived to match the creep simulation. It can be observed that the additional spring to account for the system compliance significantly improves the simulation.

Overall, the (3+1) element model, although capable of simulating the final creep displacement and relaxation stress, was not capable of capturing well the transient viscous response of the clay. To improve the simulation especially of the viscous part, we can add one more viscous element to the model.

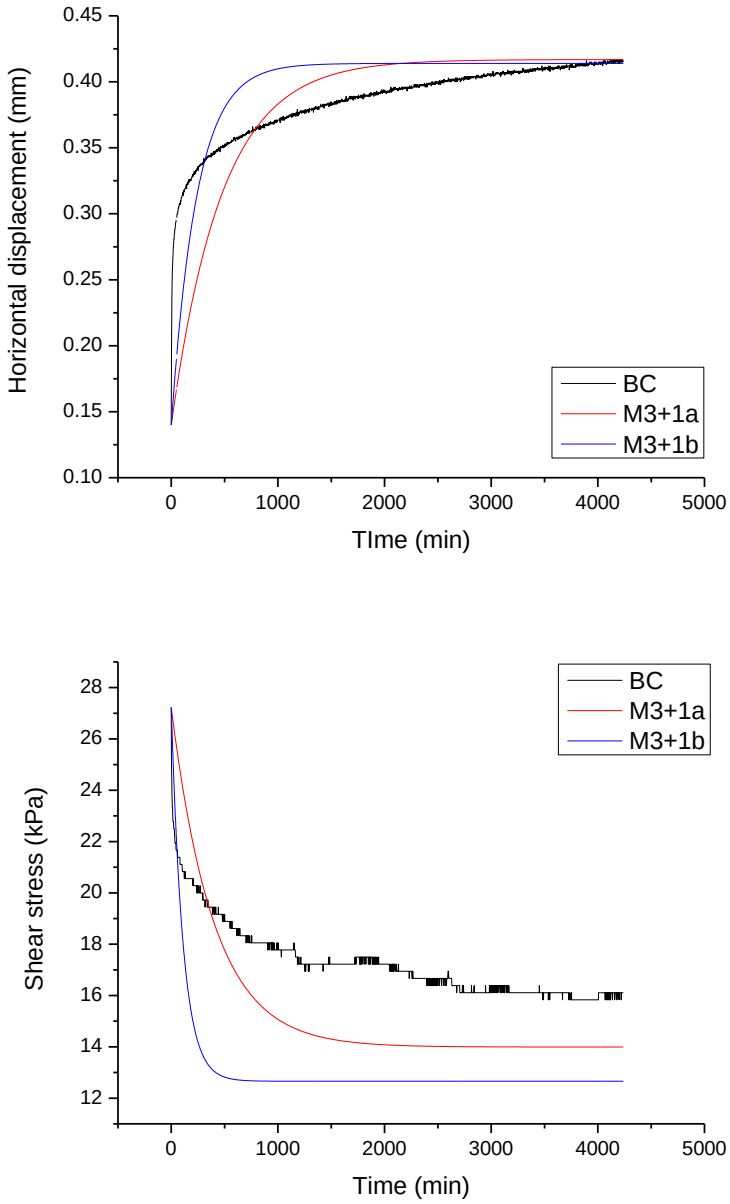

Figure 5.18 Simulations of creep and relaxation with (3+1)-element models, M(3+1)a and M(3+1)b.

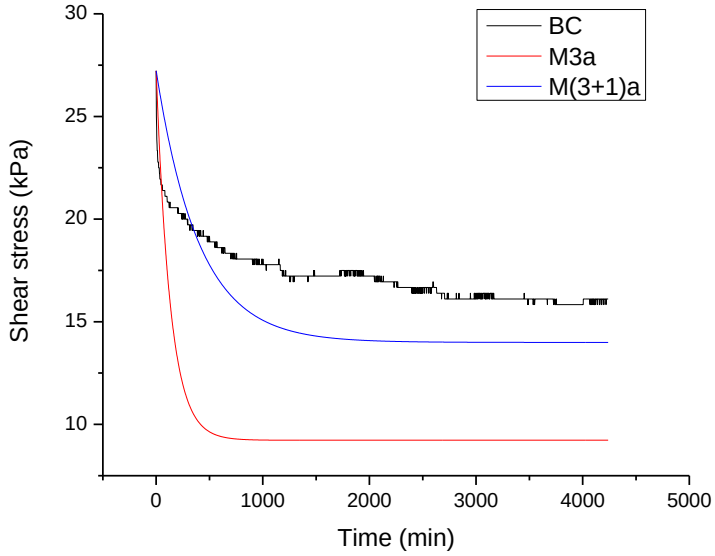

Figure 5.19 Comparison between simulation in stress relaxation for 3-elements model, with and without additional spring to account for loading system compliance

5.5.3 (5+1)-element visco-elastic models (additional spring to account for loading system compliance)

Figure 5.20 shows the 5 elements mechanical model with additional spring to account for loading system deformation (G_4). This generalized Kelvin model is similar to the one with 3+1 elements model shown above, except that this time round, another set of Kelvin model was added in series to better capture the viscous response of clay. Since this model requires complex analytical solution for stress relaxation constitutive model, we proposed herein only the constitutive equation for creep. The creep constitutive equation for this model is given by:

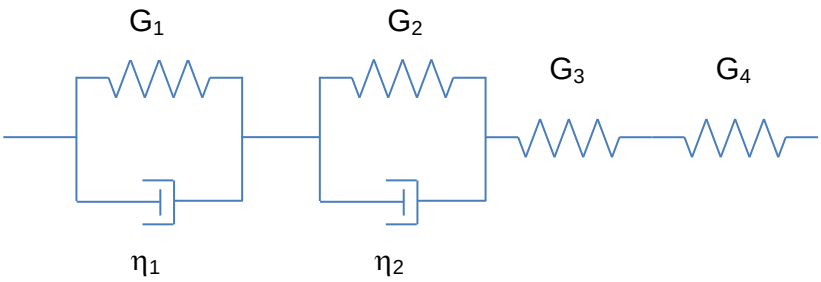

Figure 5.20 (5+1)-element mechanical model with additional spring to account for loading system

$$Creep \quad \gamma = \left\{\frac{1}{G_1}\left[1 - exp\left(-\frac{t}{\tau_1}\right)\right] + \frac{1}{G_2}\left[1 - exp\left(-\frac{t}{\tau_2}\right)\right] + \frac{1}{G_3} + \frac{1}{G_4}\right\}\frac{G_3 G_4}{G_3 + G_4}\gamma(0) \qquad [11]$$

$$with \quad \tau_1 = \frac{\eta_1}{G_1}, \tau_2 = \frac{\eta_2}{G_2}$$

where t is the time, G_1, G_2, G_3, and G_4 are the stiffness of the springs, η_1 and η_2 are the viscosity of the dashpots, γ is the horizontal displacement and $\gamma(0)$ is the initial horizontal displacement (refer Annex F for more details)

The need for two Kelvin models in series to simulate the viscous response is shown in Figure 5.21a, which shows the creep response in a log-scale. Two different creep modes can be distinguished, which justifies the adoption of the two Kelvin models in series. The 1st and the 2nd branch are clearly identified in log-scale plot. The 1st branch is the shortest, covers from the onset of displacement (creep) up to a point where an inflection is observed. The 2nd branch is usually the longest, covering from the inflection point until the end of displacement.

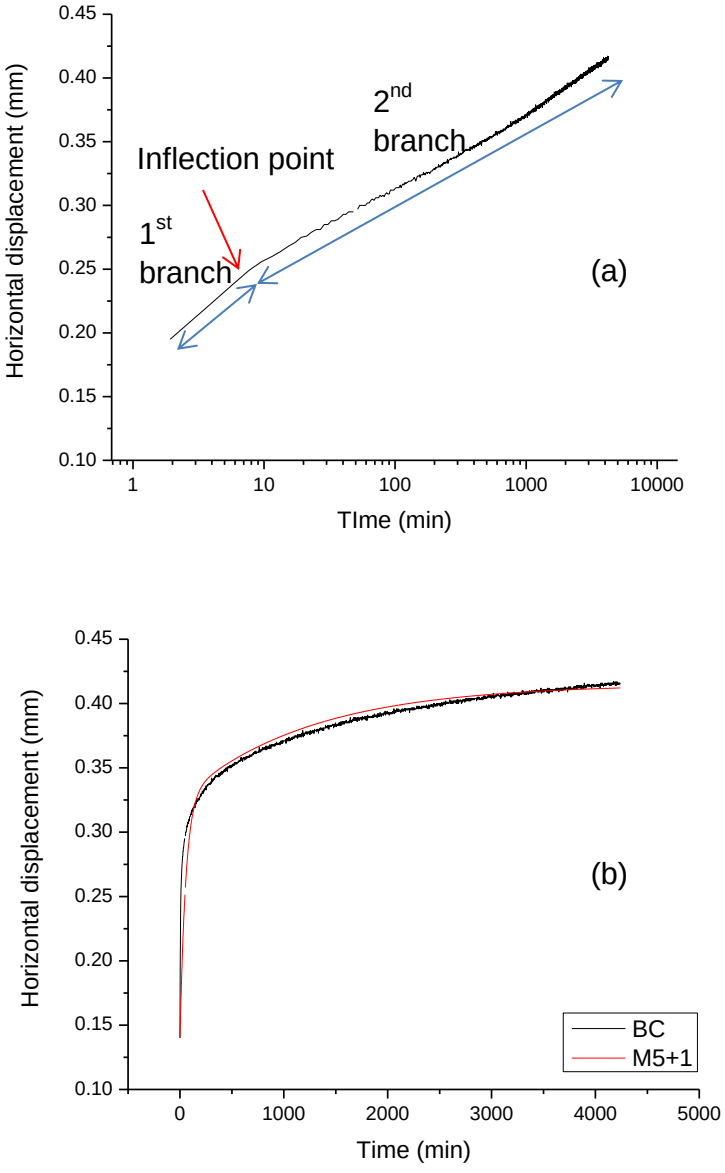

Figure 5.21. Simulation of creep with 5+1 elements model. (a) log-scale; (b) natural scale

Figure 5.21b shows the simulation for creep with 5+1 elements model. The creep response is well captured and viscous issue was successfully addressed. The model provides higher simulation accuracy as compared to the 3+1 models, but is more complicated and require more parameters to consider.

The (5+1)-parameter model requires a large number of parameters to be determined; these cannot be derived using best-fitting procedure as there are likely a large number of combinations of 5 parameters that are returning a good simulation. An attempt was therefore made to determine some of the parameters directly from the experimental data with procedures that are illustrated below. Tables reporting all parameters will be presented in the Chapter 6 along with an analysis of the parameter values.

5.6 DETERMINATION OF THE PARAMETERS FOR THE M(5+1)a MODEL

The parameters for the Model 5+1 comprises of 3 elastic elements associated with the soil, G1, G2, and G3, one elastic parameter associated with the loading system G4, and 2 viscous elements, η_1 and η_2 respectively, also associated with the soil. Each parameter is associated with different parts of the response curve as shown in Figure 5.22. We found that different parameters combinations may produce the same viscous response. To have a full control on the modelling, parameters were determined both by experimentally and by using the equations derived from the model constitutive equations.

As far as the parameter G4 is concerned, procedures to estimate it have been discussed and explained in Chapter 3. Such parameter is the additional elastic element added to the model to represent the compliance system of the direct shear box. Parameter G4 was estimated differently for creep and relaxation. For creep, only the stiffness of the holding arm was considered. For relaxation, the stiffness of both the holding and loading arm were considered.

Parameter G3 represents the 'instantaneous' short-term elastic response of the soil. When loaded, the soil showed a short-term increase in horizontal displacement. Because of the effect of the system compliance, the initial short-term displacement observed experimentally, is actually controlled by the springs G3 and G4.

Transient viscous response was controlled by viscous elements characterized by the viscosity parameters η_1 and η_2. Their corresponding elastic elements were characterized by the parameters G1 and G2. Parameter G1 and η_1 were controlling the response associated with the first branch of creep. On the other hand, the parameters G2 and η_2 were assumed to control the second branch of creep response.

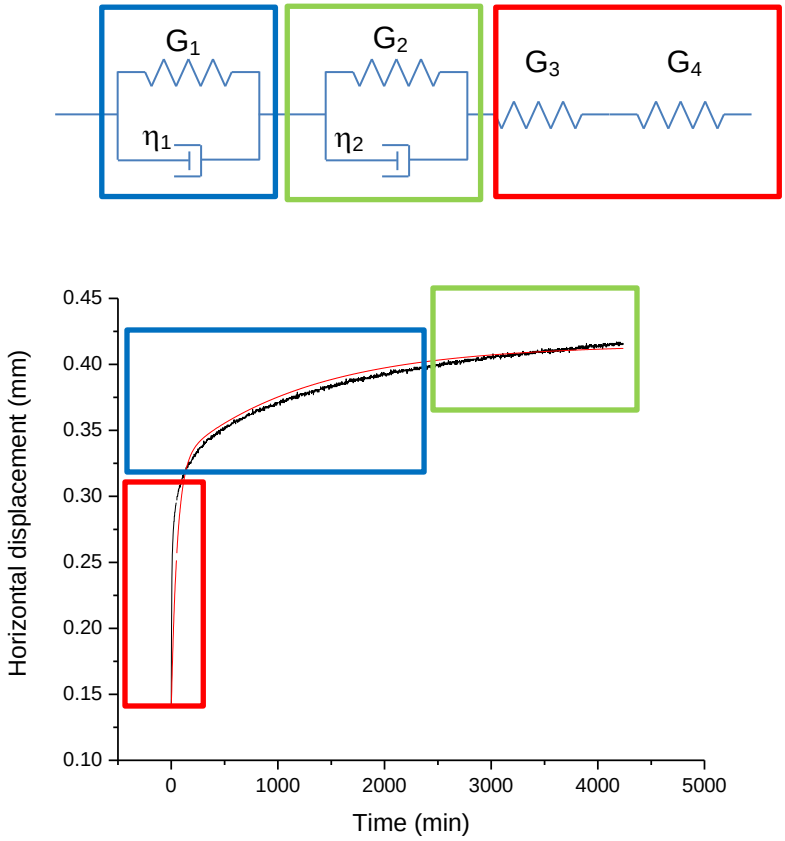

Figure 5.22. Parameters and curve's simulation relationship

5.6.1 G3

Parameter G3 was obtained from the tangent to the shear stress versus horizontal displacement curve at the point where the target stress was reached and creep initiated by maintaining the shear stress constant over time. In other words, G3 was taken as tangent modulus.

This modulus was actually read from the shear stress versus horizontal displacement curve obtained in the displacement-controlled test as the tangent could be determined more clearly. Figure 5.23 shows the example of tangent taken from the curve of saturated pre-peak at 200kPa vertical stress, at 90% of peak shear strength. The calculated slope from the respective tangent represents the parameter G3 for the respective soil conditions (refer Annex B for further details).

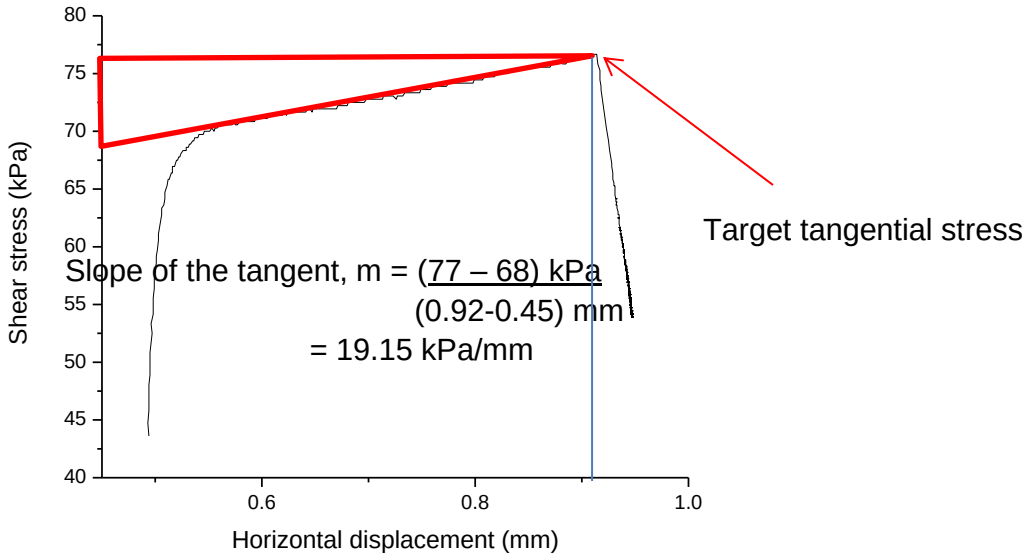

Figure 5.23. Tangent at the target tangential stress for parameter G3 determination

5.6.2 G2

As shown in Figure 5.21.a, the creep curve of Ball Clay was showing a bilinear response when plotted in semi-logarithmic scale. The 2nd branch was more prominent and easier to distinguish than the 1st branch. Parameter G2 was obtained by taking the tangent to the inflection point of the second branch as shown in Figure 5.24 below. The calculated slope from the respective tangent, $\left[\frac{d\gamma}{dln(t)}\right]_{IP2}$ was then used to compute the value of parameter G2 by considering that:

$$G2 \qquad G_2 = \frac{G_3 G_4}{G_3 + G_4} \frac{1}{\left[\frac{d\gamma}{dln(t)}\right]_{IP2}} \gamma_0 \cdot exp(-1) \qquad \text{For t} >> \tau_1 \qquad [12]$$

where t is the time, τ_1 is the reference time, G_3 is the parameter associated with initial creep response, G_4 is the parameter associated with the compliance of the system, $\left[\frac{d\gamma}{dln(t)}\right]_{IP2}$ is the slope of the tangent from 2nd branch and $\gamma(0)$ is the initial horizontal displacement. Eq. 12 was derived from Eq. 11 (Refer Annex C for further details).

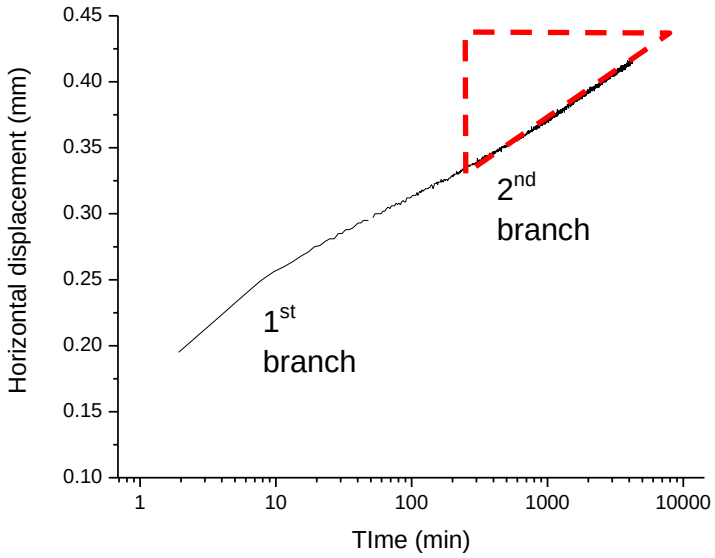

Figure 5.24 Tangent of the 2nd branch

5.6.3 G1

Parameter G1 corresponds to the first branch of the creep curve as shown in Figure 5.21. In principle, the parameter G1 could have been assessed similarly to the procedure adopted for parameter G2, i.e. by considering the tangent at the inflection point of the first branch. However, this tangent was not always clearly distinguishable. The parameter G1 was therefore selected by matching the experimental ratio between the final (creep) displacement γ_∞ and the initial displacement γ_0. This ratio can be derived from Eq. 11 as follows:

$$\frac{\gamma_\infty}{\gamma_0} = \frac{\frac{1}{G_1} + \frac{1}{G_2}}{\frac{1}{G_3} + \frac{1}{G_4}} + 1 \qquad [13]$$

The parameter G1 was therefore derived as:

$$G_1 = \frac{1}{\left[\left(\frac{\gamma_\infty}{\gamma_0} - 1\right)\left(\frac{1}{G_3} + \frac{1}{G_4}\right)\right] - \frac{1}{G_2}} \qquad [14]$$

where G_2 is the parameter calculated from the second branch, G_3 is the parameter associated with the initial 'elastic' response, and G_4 is the parameter associated with compliance of the system.

5.6.4 η_1 and η_2

Parameters η_1 and η_2 were obtained as best-fit parameters using the least squares method, i.e. by minimizing the square of the errors between experimental creep displacements and simulated creep displacements.

$$E^2 = (Experimental\ creep\ displacements - simulated\ creep\ displacements)^2 \quad [15]$$

where E^2 is the square differences between experimental and simulated creep displacements or the error.

For the optimization, we used a program in Excel called, Solver to find an optimal value for the sum of errors, E^2. Solver works by adjusting the values in the decision variable cell to satisfy the limits on constraint cells and produce the result we want for the objective cell. In our case, the sum of errors, E^2 was set as an objective cell to be minimized, and the parameters η_1 and η_2 were put in the decision variable cells that were later, determined by trials and errors (Refer Annex A for the sensitivity tests). Other parameters (G1, G2, G3, G4) were set as constraint cells that will be kept constant during optimization.

CHAPTER 6
MODELLING SIMULATION AND DISCUSSION

6.1 INTRODUCTION

This chapter presents the simulation of the creep and relaxation response and discusses the effects of normal stress, initial shear stress, initial horizontal displacement stress, state of saturation, and stress history on the viscous parameters. Simulation of the viscous behaviour of the Ball Clay was conducted using 3-element and 5-element models with the additional spring to account for the compliance of the loading system.

6.2 SIMULATION USING MECHANICAL VISCOUS MODELS

Simulations for all dataset were performed using 3-element and 5-element models (with additional spring to account for the loading system compliance). These models were aimed to gain conceptual understanding into the viscous behaviour in shear of Ball Clay.

One first research question explored in this dissertation was whether a single set of parameters are capable of simulating creep and relaxation response (initiated from the same target shear stress). It is worth noticing that these two responses are conjugate. The shear stress is kept constant in creep test to allow the shear displacement to 'creep' whereas the shear displacement is kept constant in stress relaxation test to allow the shear stress to 'relax'. This aspect was addressed using the M(3+1)-element model

6.2.1 Simulation using M(3+1)-element model

Figures 6.1, 6.2, 6.3, 6.4, 6.5, and 6.6 show the simulation for all datasets using the M(3+1)a model. The simulations were set to fit the creep response by capturing the initial (elastic) and final (creep) displacement (by setting the elastic constants G_1 and G_2 according to Figure 5.6a). The same single set of parameters was then used to simulate the stress relaxation response. The model returns the same ratios between final (creep) displacement γ_∞ and initial (creep) displacement γ_0, and between the initial shear stress σ_0 and final shear stress σ_∞ under single set of parameters given by the following equations:

Creep

$$\frac{\gamma_\infty}{\gamma_0} = \frac{G_1 + G_2 + G_3}{G_2} \quad [5]$$

Relaxation

$$\frac{\sigma_0}{\sigma_\infty} = \frac{G_1 + G_3 + G_2}{G_2} \quad [6]$$

Table 6.1 shows the ratios of γ_∞/γ_0 and σ_0/σ_∞ between the model and experimental datasets. The model parameters were fitted against the creep response and this is the

reason why the error between the simulated and the experimental ratio γ_∞/γ_0 is equal to zero. For the relaxation, there is a difference between the experimental ratio σ_0/σ_∞ and the one simulated using the same elastic parameters fitted against the creep data, which quantifies the error associated with the simulation of final relaxation shear stress.

The average error between experimental and simulated ratios, γ_∞/γ_0 and σ_0/σ_∞ respectively, represents overall the capability of a single set of parameters the model to simulate relaxation and creep simultaneously. The standard deviation of the average error is equal to 6.2%, which demonstrates that a single set of parameters can effectively model both relaxation and creep if the compliance of the system is properly accounted for.

Table 6.1 Ratios of γ_∞/γ_0 and σ_0/σ_∞ for model and experimental dataset

	Creep (γ_∞/γ_0)			Relaxation (σ_0/σ_∞)			Average error
	Model	Experiment.	Error	Model	Experiment	Error	
Sat-PRP-MS-100-50	2.98	2.96	0.00	1.95	1.69	15.1%	7.6%
Sat-PRP-MS-100-75	1.63	1.64	0.00	1.29	1.44	-10.9%	-5.4%
Sat-PRP-MS-100-90	1.77	1.77	0.00	1.34	1.03	29.9%	14.9%
Sat-PRP-S-100-75	2.95	2.93	0.00	1.70	1.44	17.7%	8.8%
Sat-PRP-S-100-90	1.79	1.78	0.00	1.29	1.45	-10.7%	-5.3%
Sat-PRP-MS-200-25	1.42	1.40	0.00	1.28	1.60	-20.0%	-10.0%
Sat-PRP-MS-200-50	2.24	2.23	0.00	1.79	1.80	-0.5%	-0.2%
Sat-PRP-MS-200-75	1.71	1.71	0.00	1.45	1.52	-5.1%	-2.5%
Sat-PRP-MS-200-90	1.51	1.51	0.00	1.34	1.42	-5.7%	-2.8%
Sat-POP-S-100-68	1.41	1.33	0.01	1.34	1.52	-12.1%	-6.1%
Sat-POP-S-200-98	1.59	1.59	0.00	1.34	1.34	0.1%	0.0%
Unsat23-PRP-MS-100-30	1.64	1.63	0.00	1.41	1.64	-14.0%	-7.0%
Unsat23-PRP-MS-100-60	1.64	1.64	0.00	1.39	1.48	-5.8%	-2.9%
Unsat23-PRP-MS-100-90	1.58	1.58	0.00	1.29	1.25	2.9%	1.5%
Unsat29-PRP-MS-100-30	1.66	1.65	0.00	1.50	1.56	-3.8%	-1.9%
Unsat29-PRP-MS-100-60	1.51	1.51	0.00	1.33	1.51	-11.9%	-5.9%
Unsat29-PRP-MS-100-90	1.48	1.48	0.00	1.27	1.23	3.1%	1.5%

This result appears trivial at first glance. As creep and relaxation are in principle conjugate responses of the same viscous behaviour, it should not be surprising that a single set of parameters can capture stress and relaxation simultaneously. Nonetheless, there appear to be very few studies showing that relaxation and creep in clays are actually conjugate responses of the same viscous behaviour. This outcome has two practical implications. Firstly, viscous response of clays in practical applications (e.g. creeping landslides) is rarely associated with pure creep or pure relaxation. In this case, full viscous models need to be implemented to simulate the landslide kinematics. However, most of the models presented in the literature are empirical in nature and only address the creep response. The approach put forward in this work presents an approach theoretically sound, though relatively simple.

Secondly, the characterisation of creep response requires the development of a load-controlled system whereas the traditional shear box operates in displacement-control mode. The results presented in Table 6.1 shows that model parameters can be derived from relaxation tests using the displacement-controlled shear box to predict creep response. In other words, the conventional displacement-controlled shear box, which is available in the majority of research and commercial laboratories, can be successfully employed to characterise response in creep (in particular, the primary) and there is no need to modify the shear box to operate in the stress-controlled mode.

Figures 6.1 to 6.6 show that the transient viscous response is not captured very well by a single dashpot. This is the reason why the modelling was refined by adding another Kelvin model in series with the first one. Results from this modelling exercise are discussed in the next section.

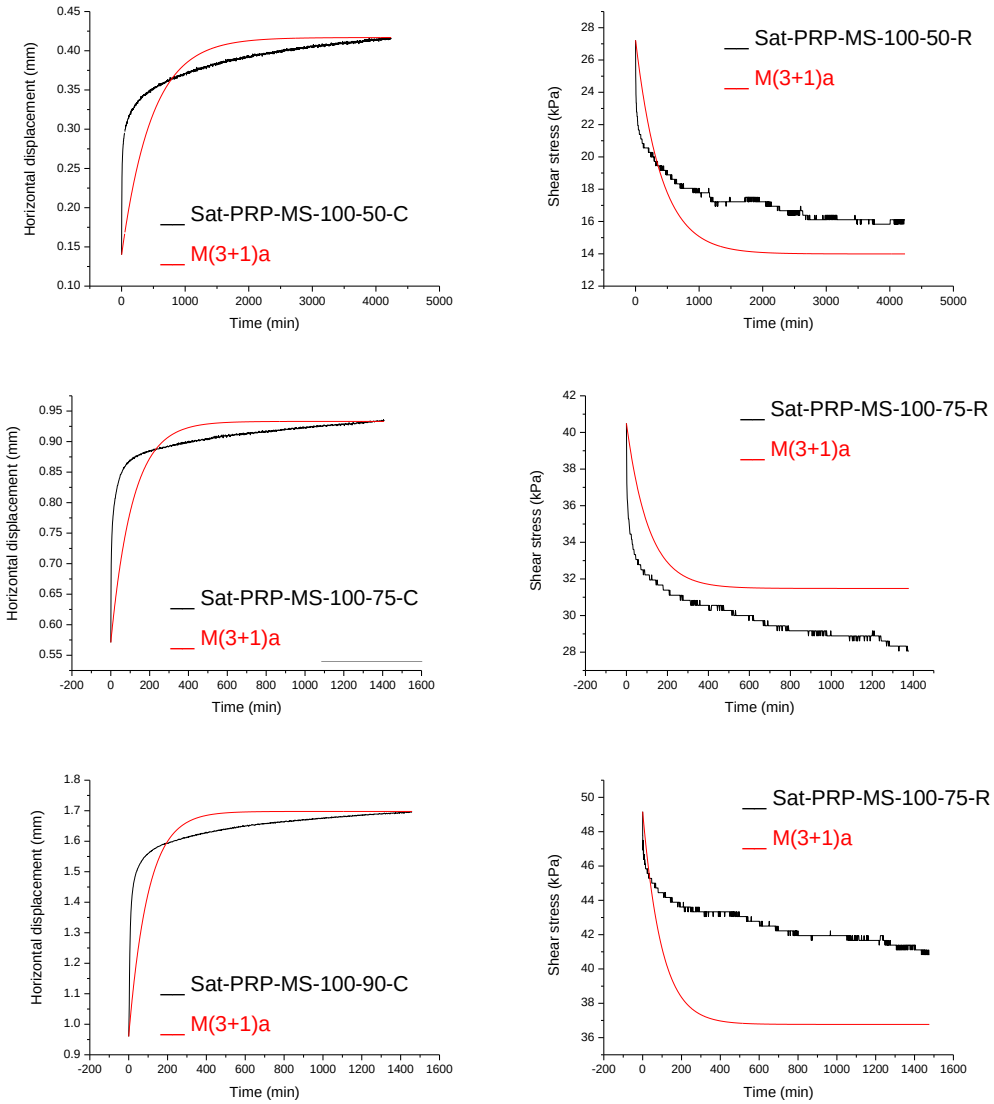

Figure 6.1 Simulation of saturated pre-peak at 100kPa vertical stress (multistage)

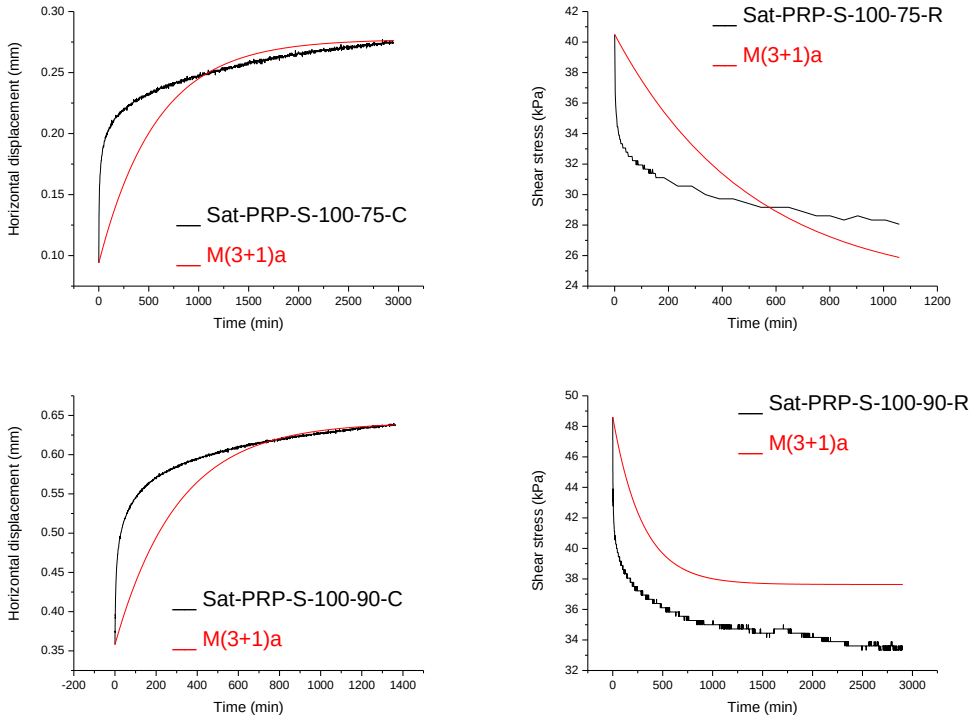

Figure 6.2 Simulation of saturated pre-peak at 100kPa vertical stress (single stage)

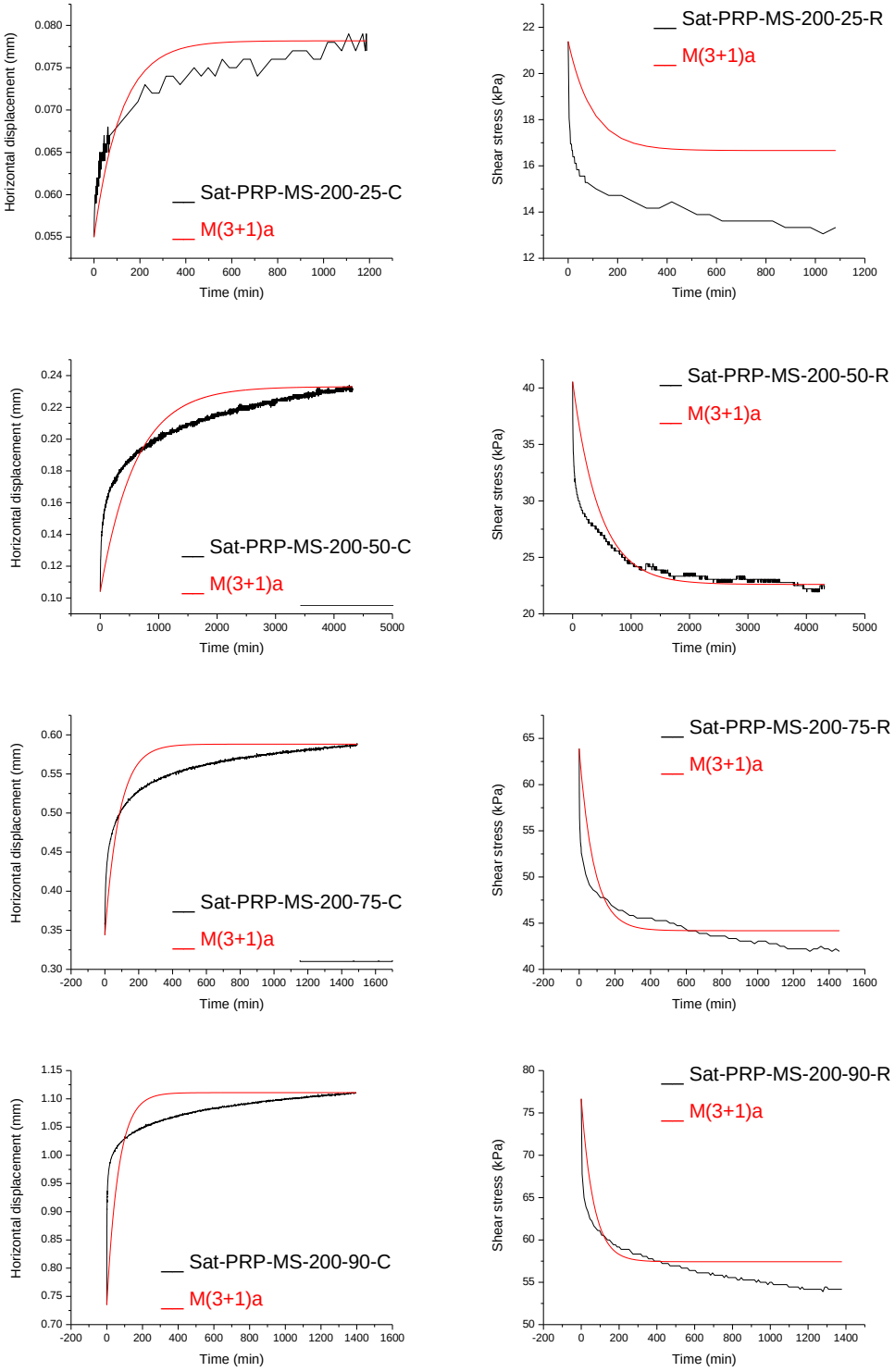

Figure 6.3 Simulation of saturated pre-peak at 200kPa vertical stress

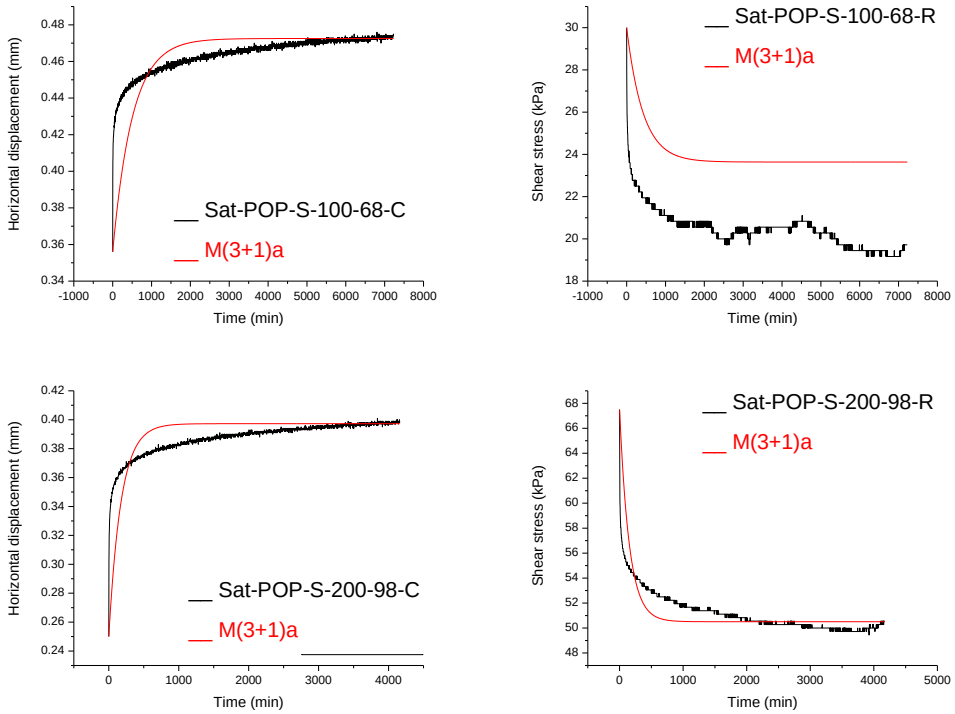

Figure 6.4 Simulation of saturated post-peak at 100kPa and 200kPa vertical stresses

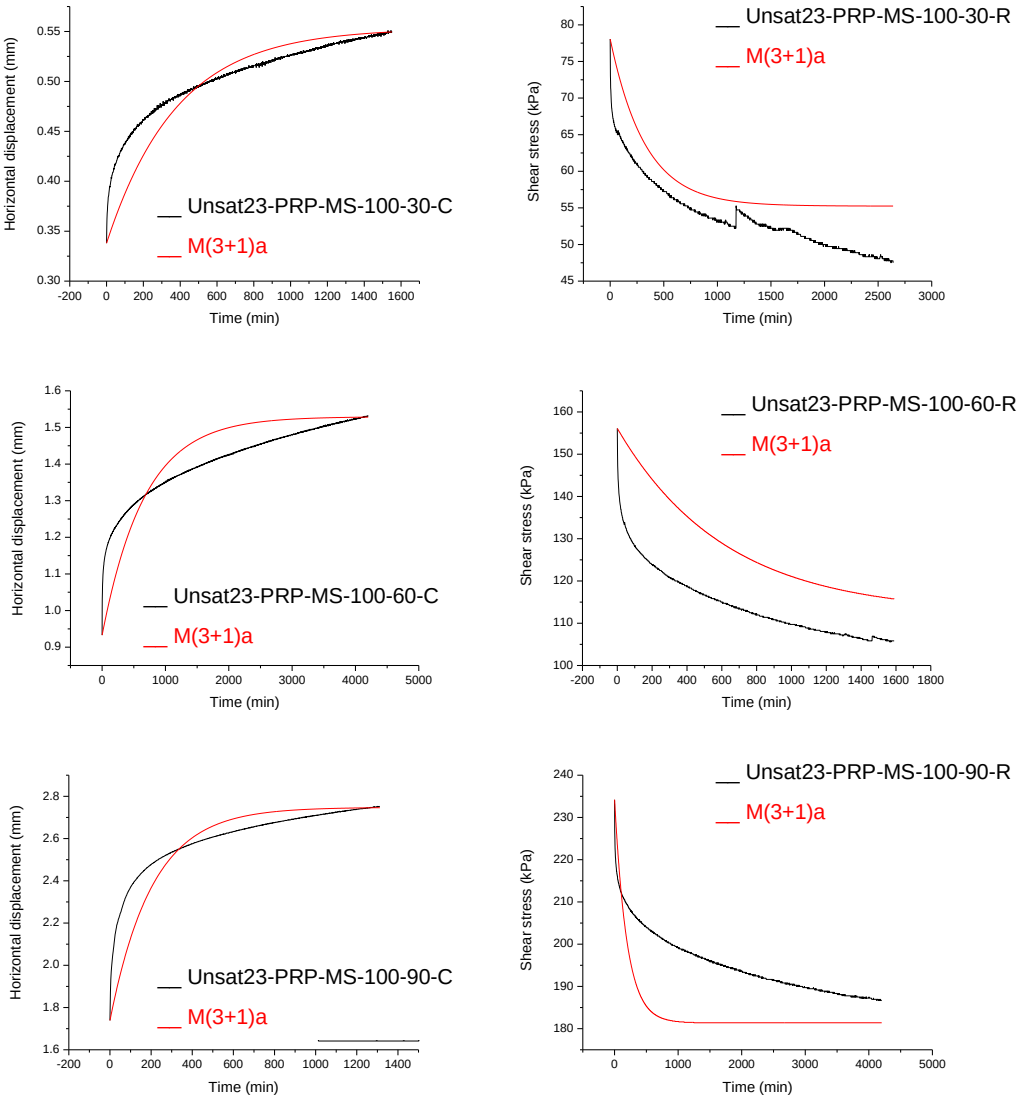

Figure 6.5 Simulation of unsaturated pre-peak at 100kPa vertical stress and w=23%

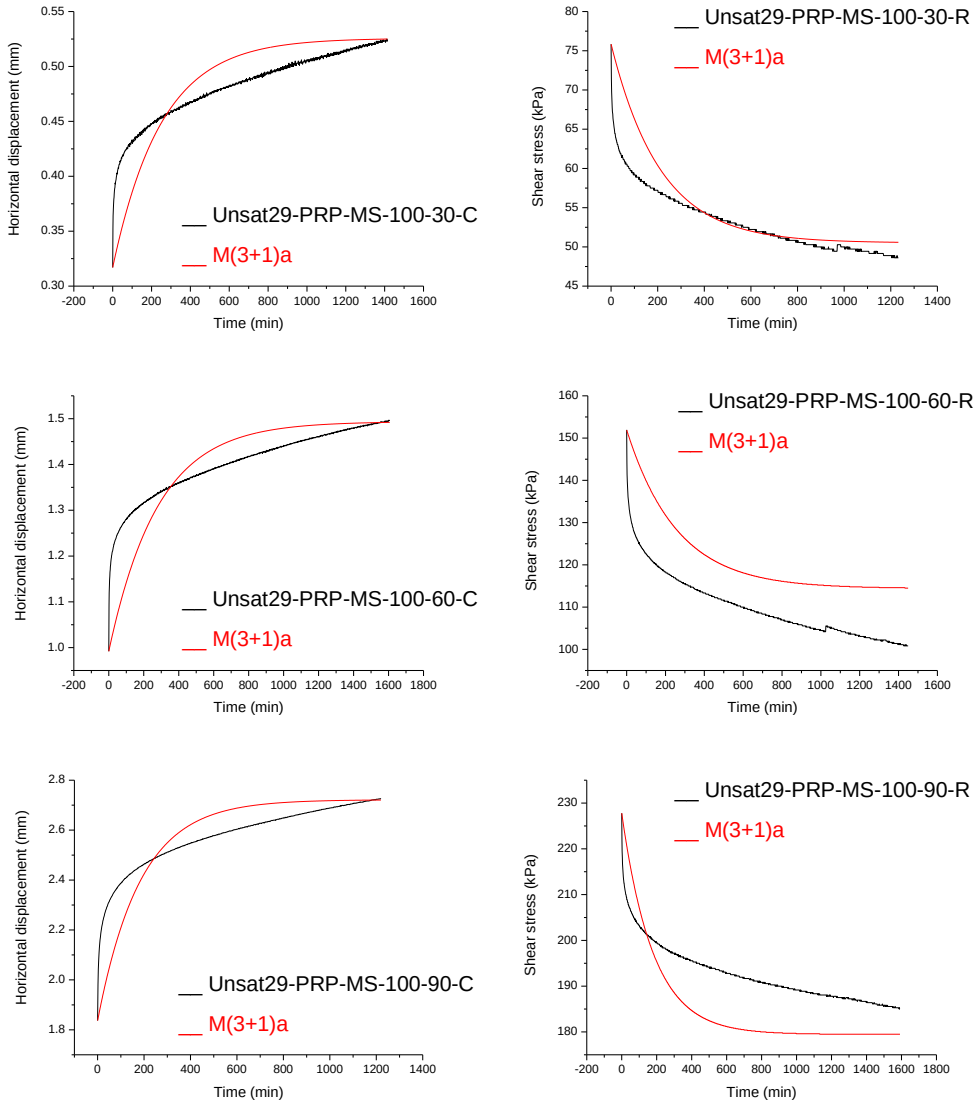

Figure 6.6 Simulation of unsaturated pre-peak at 100kPa vertical stress and w=29%

6.2.2 5-elements model

Figures 6.7, 6.8, 6.9, 6.10, 6.11 and 6.12 show the simulation of all datasets using the visco-elastic model with 5+1 elements. Simulations were carried out for the creep response only due to the difficulty of deriving a closed-form solution of the relaxation ordinary differential equation.

The performance of the M(5+1)-parameter model appears to be satisfactory, regardless of the test mode (single stage or multi-stage), normal stress applied (100kPa and 200kPa), and stress history (pre-peak or residual condition).

In the unsaturated state, the quality of the simulation is not of the same standard. This may not be surprising since the model was essentially developed based for the saturated soil specimens where the viscous response appears to be more pronounced than the

unsaturated soil state. Matric suction and degree of saturation therefore seems to change the viscous response to some extent. However, overall performance was considered satisfactory and the evolutions of parameters from this model were then used to assess the response of viscous behaviour in the unsaturated state.

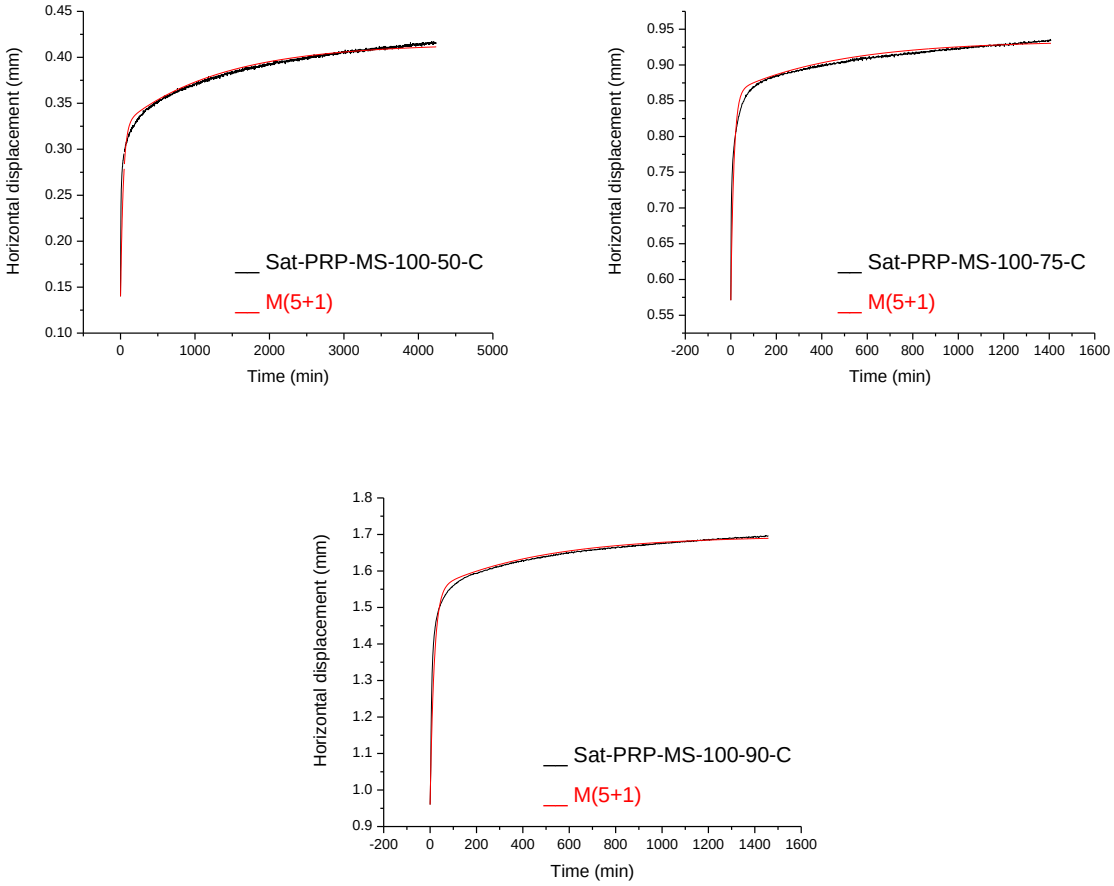

Figure 6.7 Simulation of creep for saturated pre-peak at 100kPa vertical stress (multistage)

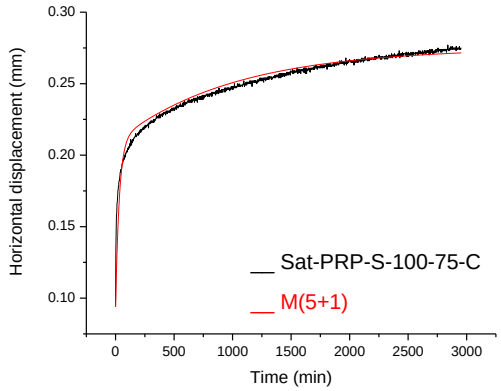

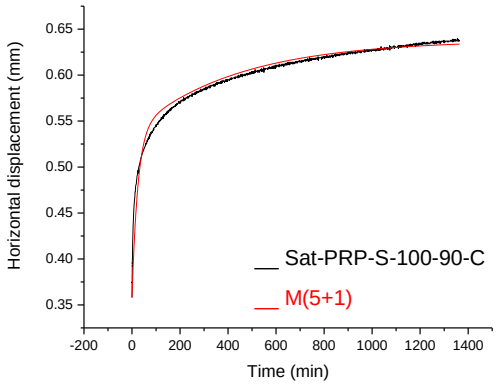

Figure 6.8 Simulation of creep for saturated pre-peak at 100kPa vertical stress (single stage)

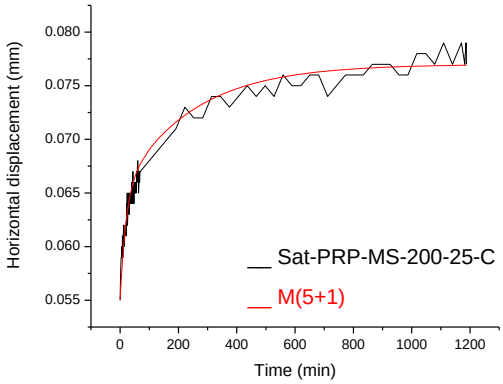

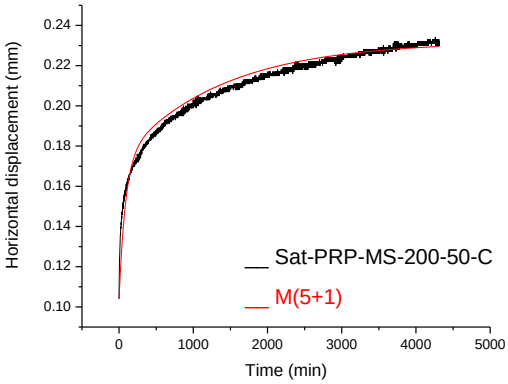

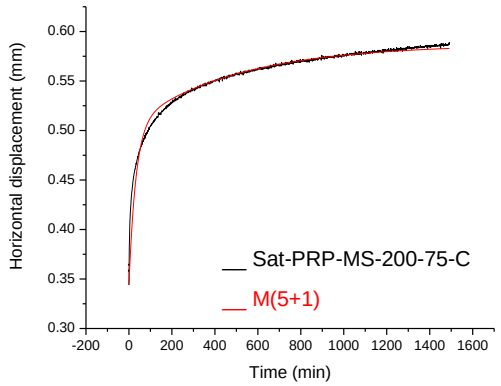

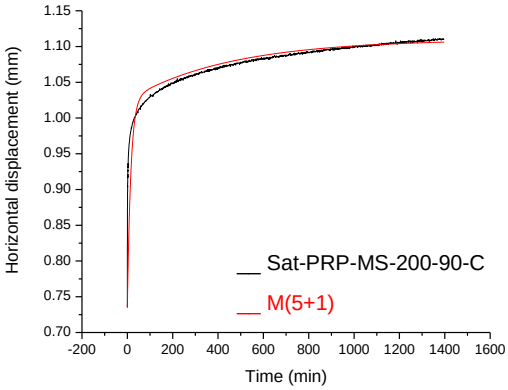

Figure 6.9 Simulation of creep for saturated pre-peak at 200kPa vertical stress

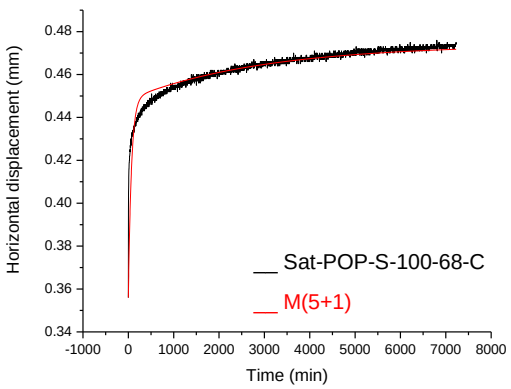

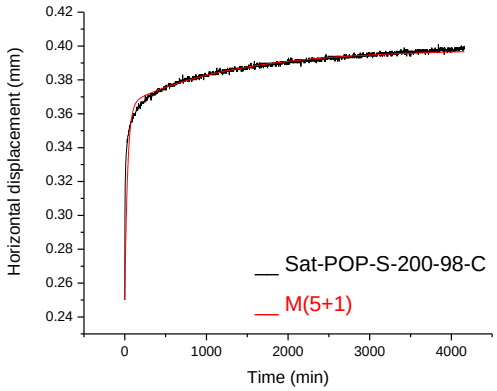

Figure 6.10 Simulation of creep for saturated post-peak at 100kPa and 200kPa vertical stresses

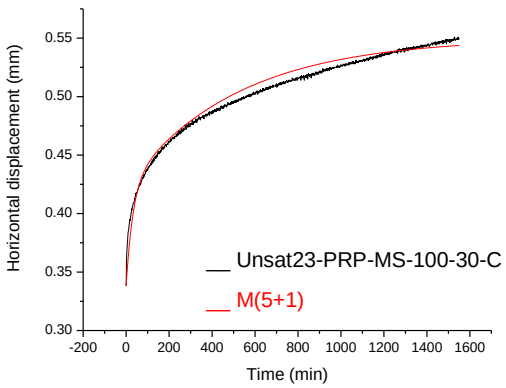

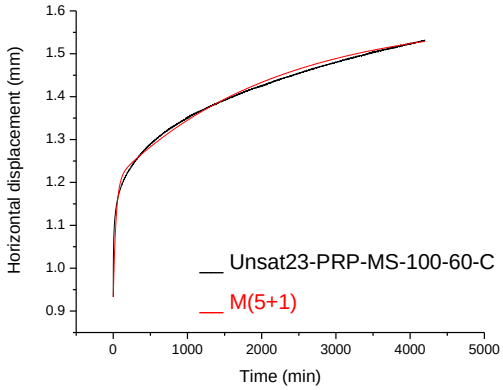

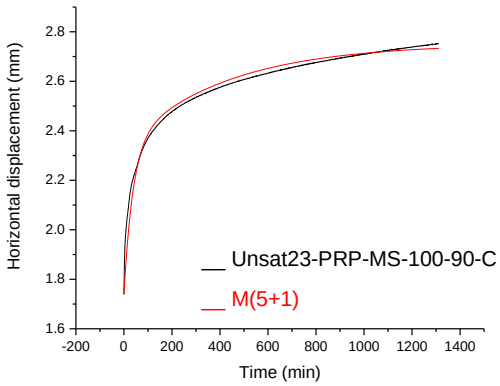

Figure 6.11 Simulation of creep for unsaturated pre-peak at 100kPa vertical stress and w=23%

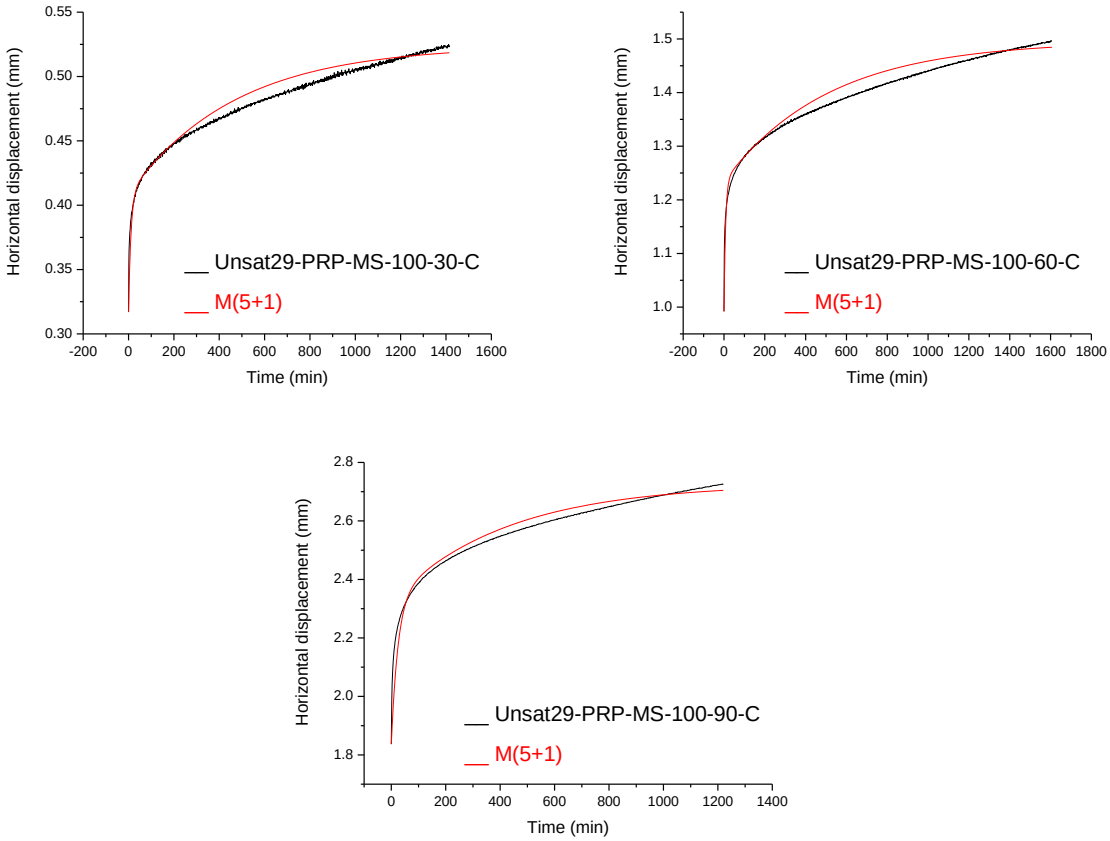

Figure 6.12 Simulation of creep for unsaturated pre-peak at 100kPa vertical stress and w=29%

6.3 PARAMETERS INTERPRETATION

Model parameters were plotted against controlling variables to see how the parameters evolve under certain conditions. In our case, the variables considered were the initial shear stress, the initial (creep) displacement, and the ratio between tangential stress and normal stress. The parameters were plotted in a semi-log graph, with a logarithmic scale on the y-axis, and a linear scale on the x-axis.

6.3.1 Viscous parameters for saturated specimens in the pre-peak range

Table 6.2 shows the parameters from the (5+1) elements visco-elastic model gained over modelling simulation for creep response at saturated conditions. Evolutions of these parameters in saturated state and in pre-peak condition were first assessed with the initial (creep) displacement γ_0 and the initial shear stress τ_0 to chase for any coherent relationship between them.

The model used to simulate the creep response is shown again in Figure 6.13 for the sake of clarity:

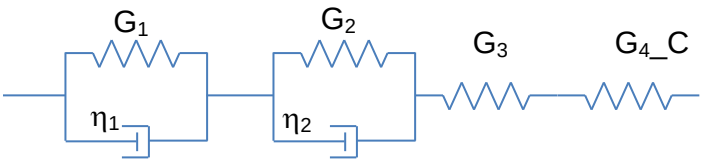

Figure 6.13. M(5+1)-model parameters

The two Kelvin models in series are characterised by the elastic parameters G_1 and G_2 respectively and the viscous parameters η_1 and η_2 respectively. The spring G3 represents the instantaneous elastic response of the soil whereas the parameter G_4_C represents the compliance of the system and its value was determined as described in Section 3.5.2. Of course, this parameter will not be assessed against γ_0 and τ_0.

Table 6.2 Modelling parameters for saturated condition at various conditions

	τ_0 kPa	γ_0 mm	τ_0/σ -	G_1 kPa/mm	G_2 kPa/mm	G_3 kPa/mm	G_4_C kPa/mm	η_1 kPa·min/mm	η_2 kPa·min/mm	G_3/G_1 -	G_3/G_2 -
Sat-PRP-MS-100-50	27.2	0.1	0.3	27.3	56.7	40.0	376.4	1.0E+03	7.5E+04	1.5	0.7
Sat-PRP-MS-100-75	40.5	0.6	0.4	37.3	149.3	20.0	376.4	5.0E+02	7.0E+04	0.5	0.1
Sat-PRP-MS-100-90	49.2	1.0	0.5	17.2	68.3	10.8	376.4	3.0E+02	3.5E+04	0.6	0.2
Sat-PRP-S-100-75	40.5	0.1	0.4	22.6	39.8	30.0	376.4	9.5E+02	4.0E+04	1.3	0.8
Sat-PRP-S-100-90	48.6	0.4	0.5	25.5	46.2	13.3	376.4	3.2E+02	2.0E+04	0.5	0.3
Sat-PRP-MS-200-25	21.4	0.1	0.1	971.6	826.4	340.0	376.4	2.0E+04	2.0E+05	0.3	0.4
Sat-PRP-MS-200-50	40.6	0.1	0.2	150.8	176.5	136.4	376.4	1.3E+04	2.4E+05	0.9	0.8
Sat-PRP-MS-200-75	63.9	0.3	0.3	71.3	140.6	36.7	376.4	2.3E+03	7.0E+04	0.5	0.3
Sat-PRP-MS-200-90	76.7	0.7	0.4	32.7	111.1	19.2	376.4	5.0E+02	5.0E+04	0.4	0.1
Sat-POP-S-100-68	30.0	0.4	0.3	885.8	3198.3	590.9	376.4	6.0E+04	9.5E+06	0.7	0.2
Sat-POP-S-200-98	67.5	0.3	0.3	208.1	729.1	128.6	376.4	7.0E+04	9.5E+05	0.6	0.2

Figure 6.14 shows the evolution of model parameters for saturated specimens under pre-peak conditions versus the initial shear stress, τ_0. The 'elastic' parameter G_3 consistently decreases with the initial shear stress τ_0 (the parameter G_3 was taken from the tangent to the shear stress versus horizontal displacement curve at the initial shear stress τ_0). It is worth noticing that there is no significant difference between single stage and multistage tests at 100 kPa normal stresses confirming that multi-stage-stage procedure did not affect results. It can also be observed that G_3 increases at 200 kPa normal stress as one would expect (stiffness tends to increase with normal stress in soils).

Similar trend is also observed for G_1, G_2 (with the exception of one data point in multistage at 200 kPa normal stress), η_2, and η_1. Model parameters from single stage and multistage procedures do not appear to be much different and parameter values increase from 100 to 200 kPa normal stress.

In an attempt to unify data from tests at 100 kPa and 200 kPa normal stresses, the correlation in terms of stiffness ratios G_3/G_1 and G_2/G_1 was explored but not clear trend was observed.

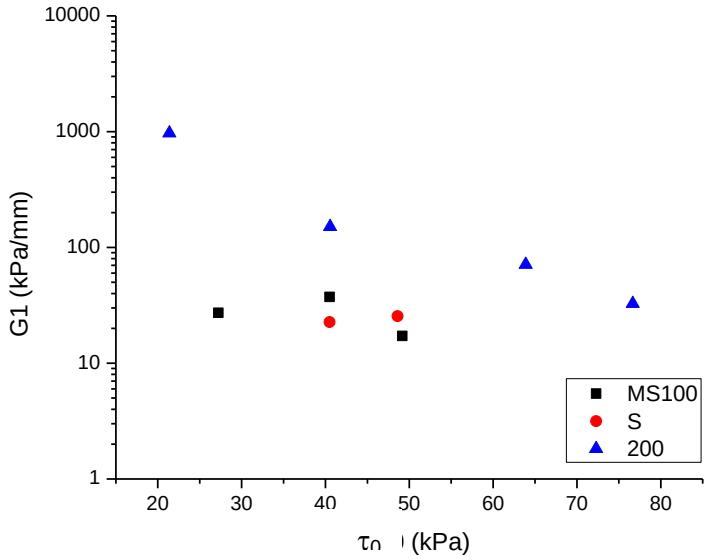

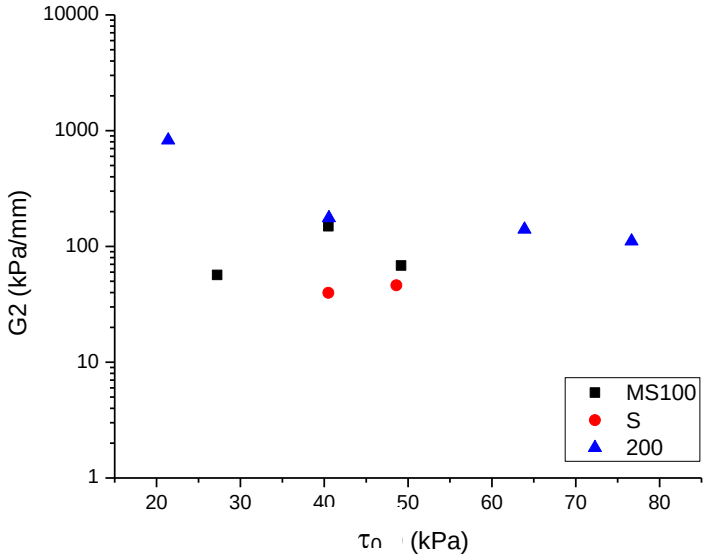

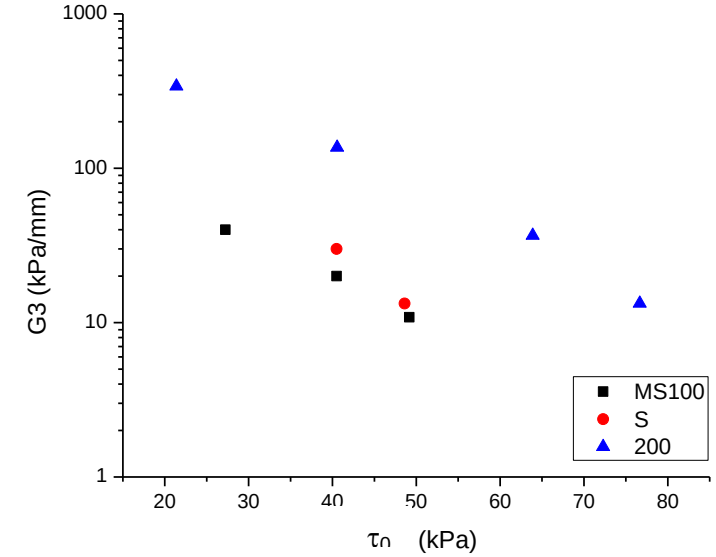
1000
100
10
1
G3 (kPa/mm)
20
30
40
50
60
70
80
τ0 (kPa)
MS100
S
200

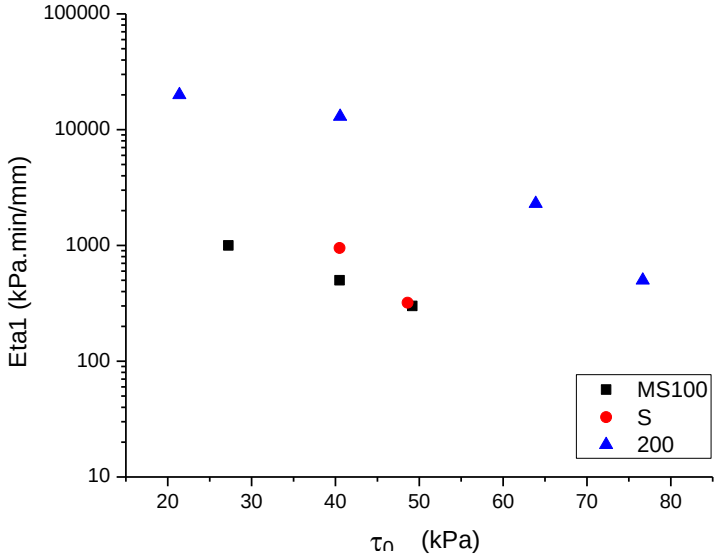
100000
10000
1000
100
10
Eta1 (kPa.min/mm)
20
30
40
50
60
70
80
τ0 (kPa)
MS100
S
200

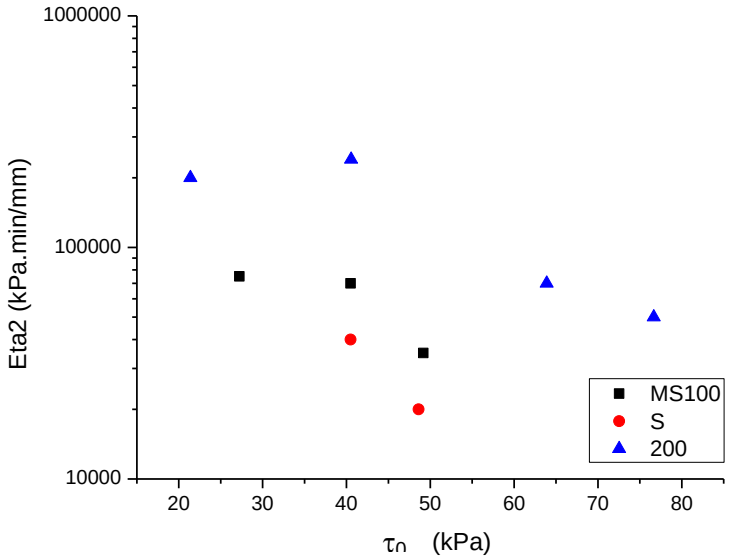
1000000
100000
10000
Eta2 (kPa.min/mm)
20
30
40
50
60
70
80
τn (kPa)
MS100
S
200

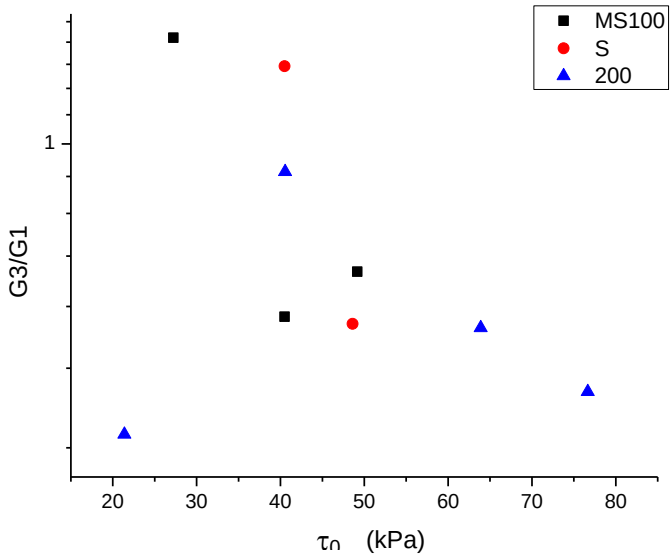
1
G3/G1
20
30
40
50
60
70
80
τn (kPa)
MS100
S
200

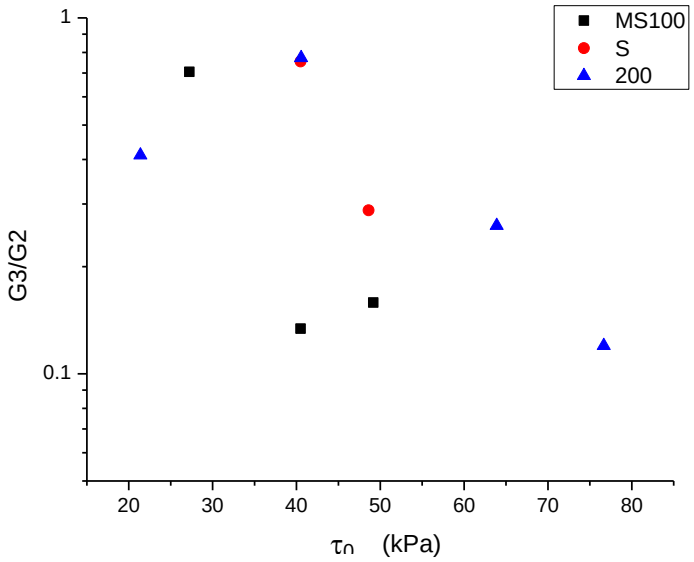

Figure 6.14 Evolution of modelling parameters at saturated in pre-peak condition with initial shear stress, τ_0

In the same attempt to unify data from tests at 100 kPa and 200 kPa normal stress, the model parameters were plotted against the initial displacement γ_0. Model parameters remain scattered with the exception of G_3/G_1 and G_2/G_1 (Figure 6.15).

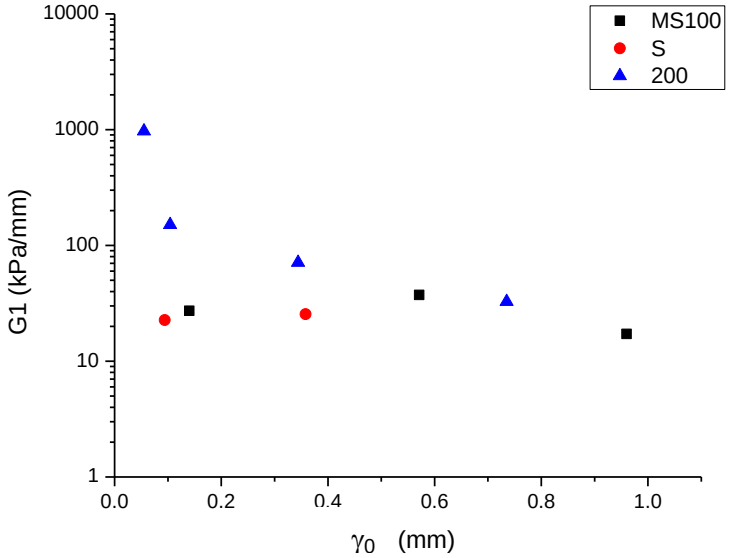

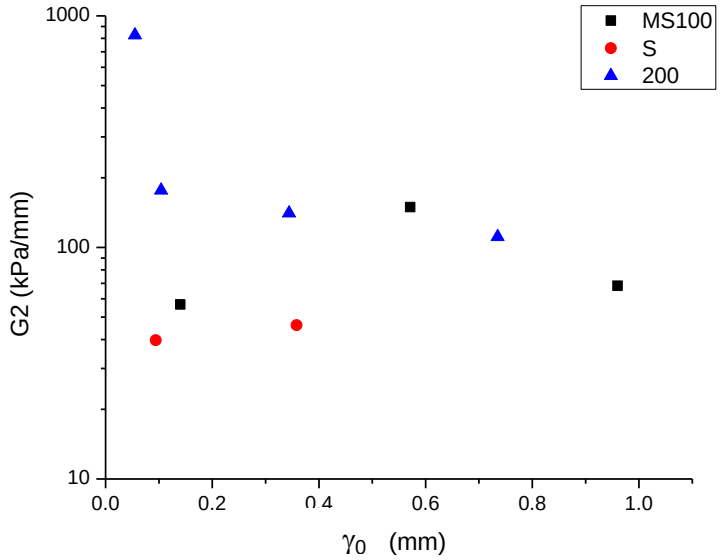
MS100
S
200
G2 (kPa/mm)
1000
100
10
0.0
0.2
0.4
0.6
0.8
1.0
γ0 (mm)

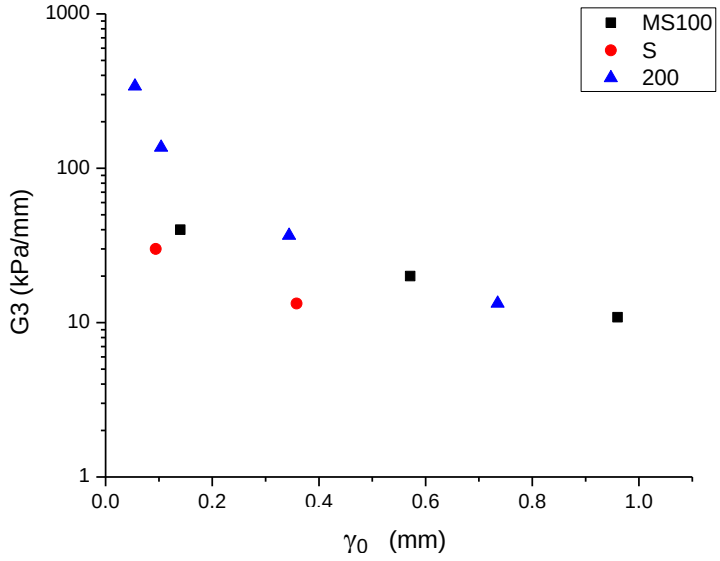
MS100
S
200
G3 (kPa/mm)
1000
100
10
1
0.0
0.2
0.4
0.6
0.8
1.0
γ0 (mm)

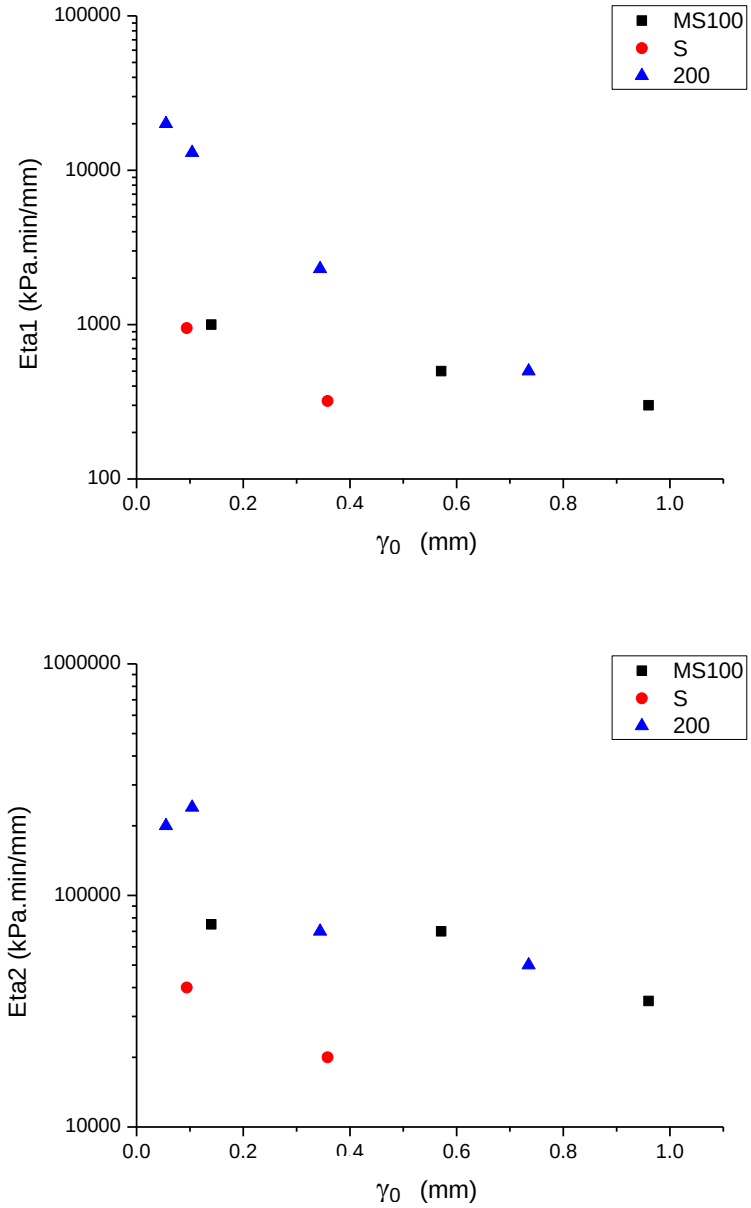

Figure 6.15 Evolution of modelling parameters at saturated in pre-peak condition with initial (creep) displacement, γ_0

Figure 6.16 shows the evolution of model parameters for saturated states versus the ratio between the initial shear stress and normal stress, τ_0/σ. This time round, parameters from both pre-peak and residual conditions are plotted together.

For the case of pre-peak parameters, all parameters tend to decrease with the ratio τ_0/σ and, overall, it appears that model parameters show the same trend regardless of the

normal stress. The ratio τ_0/σ appears as the 'scaling' factor capable of unifying viscous parameters at various normal stresses.

Parameters for residual conditions were significantly different from those associated with the pre-peak condition. Since each vertical stress represented by only a single point, and each single point was representing a different shear stress level (low shear stress at 100kPa vertical stress and high shear stress at 200kPa vertical stress), both were grouped as one to determine the evolution with the ratio τ_0/σ. From observation, parameters G_3, G_2, G_1, and η_2 showed decreasing trend with the increased of τ/σ, similar to the condition at pre-peak. Parameter η_1 seems to remain constant with increasing of τ_0/σ. The highest values for the parameters η_1 and η_2 indicate that the creep displacements in the residual state evolve much more slowly than the case of pre-peak state.

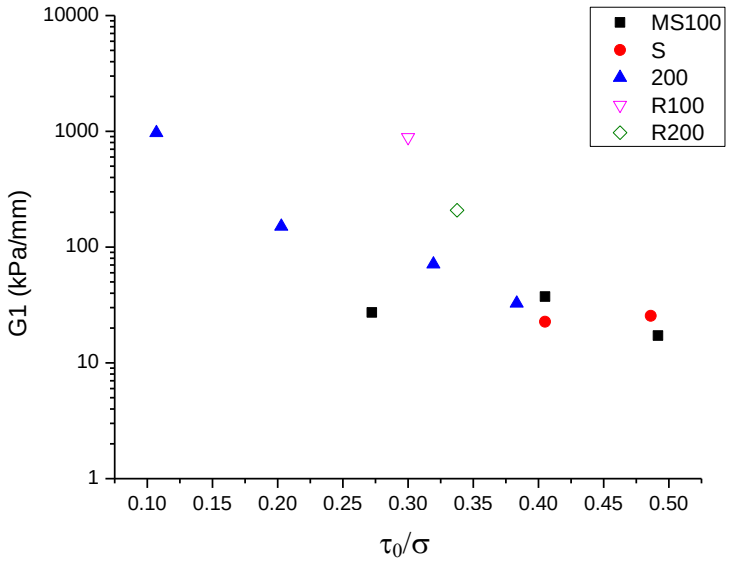

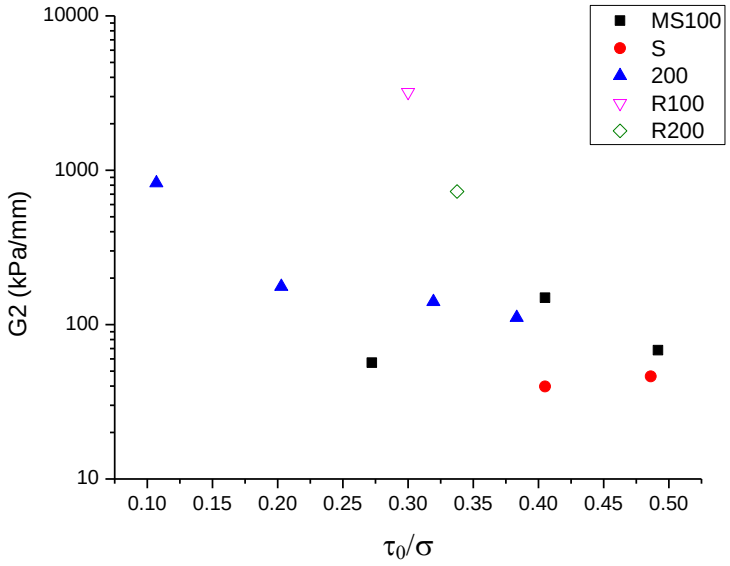
MS100
S
200
R100
R200
G2 (kPa/mm)
10000
1000
100
10
0.10
0.15
0.20
0.25
0.30
0.35
0.40
0.45
0.50
τ0/σ

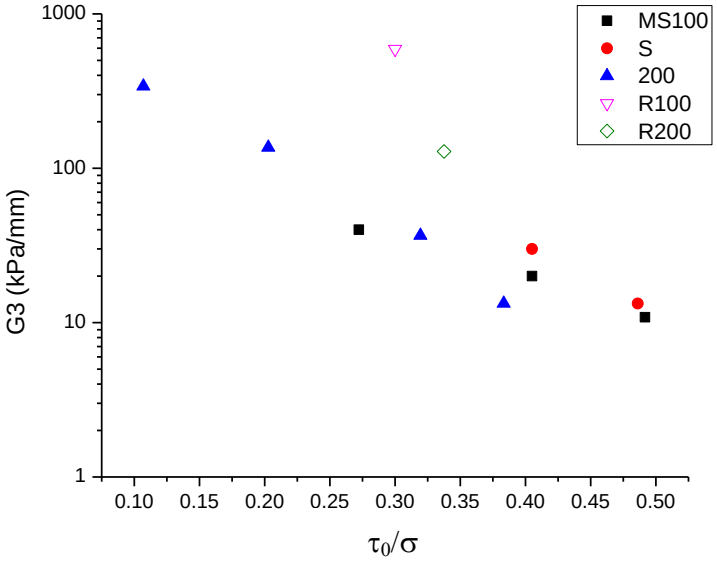
MS100
S
200
R100
R200
G3 (kPa/mm)
1000
100
10
1
0.10
0.15
0.20
0.25
0.30
0.35
0.40
0.45
0.50
τ0/σ

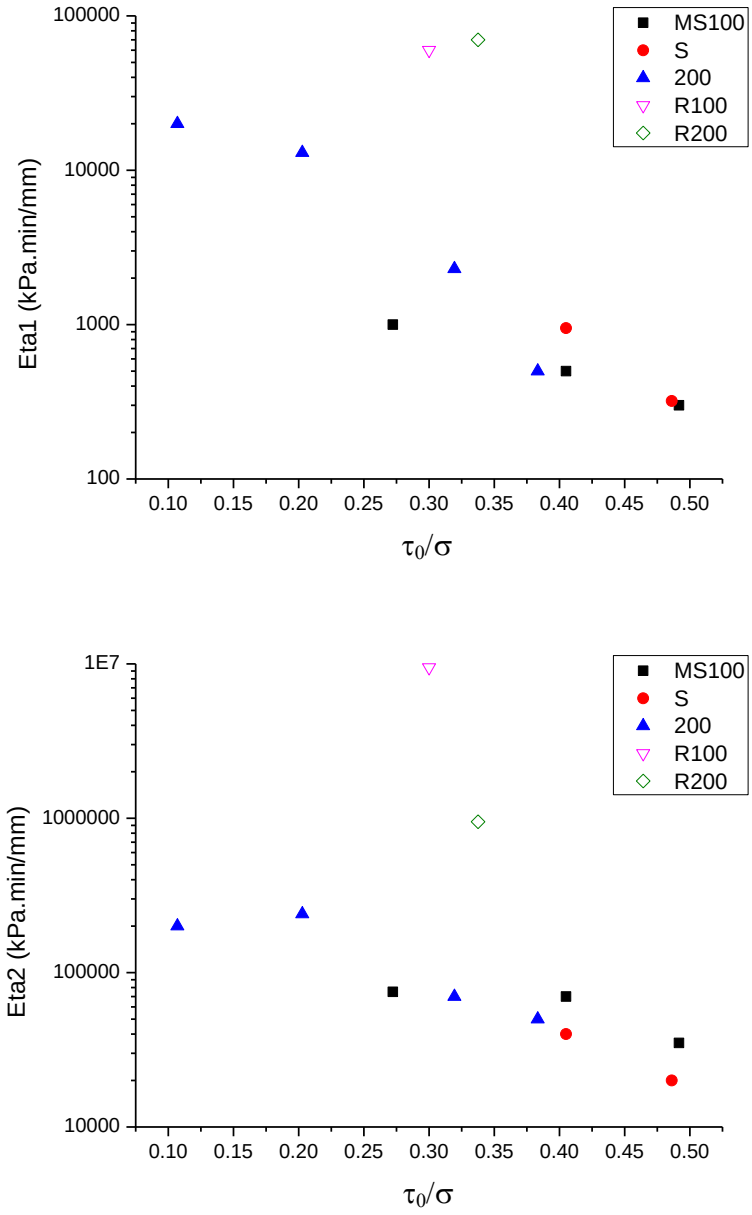

Figure 6.16 Parameters evolution in saturated modelling at pre-peak condition against τ/σ

6.3.2 Unsaturated parameters

Table 6.3 shows the model parameters for unsaturated conditions at w=23% and w=29%, respectively. Figure 6.17 shows the evolution of 'unsaturated' parameters against the ratio τ_0/σ, where σ is to be intended here as vertical stress.

The elastic parameters G_3, G_2, and G_1 tend to remain either constant or slightly decrease. The same applies to the viscous parameters η_1 and η_2. With respect to the case of saturated specimens, the variability of model parameters with τ_0/σ is less pronounced.

Table 6.3 Modelling parameters for unsaturated conditions at w=23% and w=29%

	τ_0	γ_0	τ_0/σ	G_1	G_2	G_3	G_{4_C}	η_1	η_2	G_3/G_1	G_3/G_2
	kPa	mm	-	$\frac{kPa}{mm}$	$\frac{kPa}{mm}$	$\frac{kPa}{mm}$	$\frac{kPa}{mm}$	$\frac{kPa \cdot min}{mm}$	$\frac{kPa \cdot min}{mm}$	-	-
Unsat23-PRP-MS-100-30	78.1	0.3	0.8	374.9	252.2	126.3	376.4	1.2E+04	1.3E+05	0.3	0.5
Unsat23-PRP-MS-100-60	156.1	0.9	1.6	161.9	116.2	53.8	376.4	6.0E+03	2.5E+05	0.3	0.5
Unsat23-PRP-MS-100-90	234.2	1.7	2.3	119.6	176.4	46.7	376.4	4.5E+03	7.5E+04	0.4	0.3
Unsat29-PRP-MS-100-30	75.8	0.3	0.8	367.0	289.8	147.1	376.4	4.0E+03	1.4E+05	0.4	0.5
Unsat29-PRP-MS-100-60	151.9	1.0	1.5	252.9	234.1	73.9	376.4	2.0E+03	1.2E+05	0.3	0.3
Unsat29-PRP-MS-100-90	227.8	1.8	2.3	61.4	75.5	17.2	376.4	1.5E+03	3.2E+04	0.3	0.2

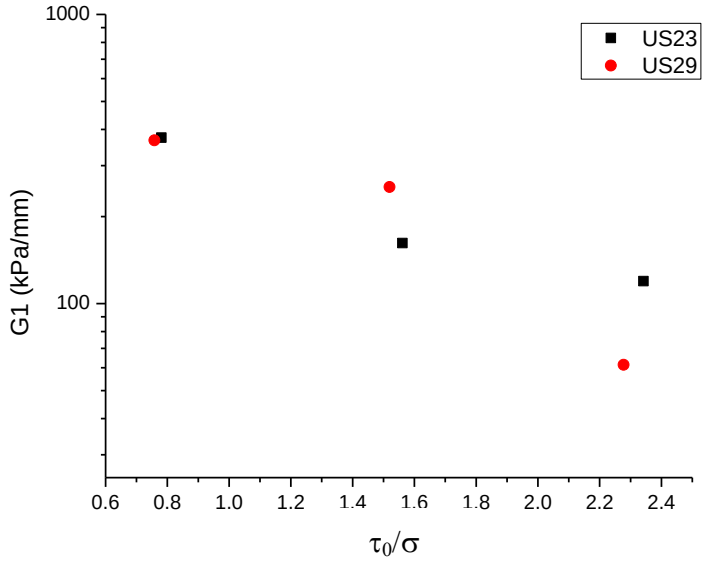

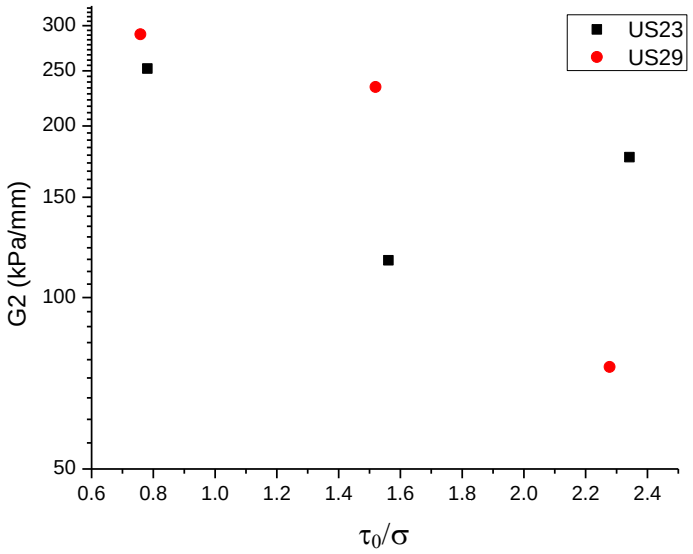
US23
US29
G2 (kPa/mm)
300
250
200
150
100
50
0.6
0.8
1.0
1.2
1.4
1.6
1.8
2.0
2.2
2.4
τ0/σ

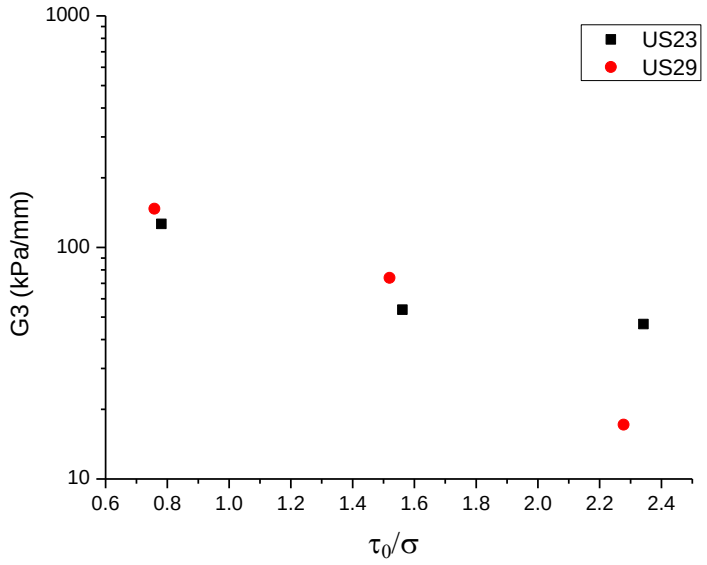
US23
US29
G3 (kPa/mm)
1000
100
10
0.6
0.8
1.0
1.2
1.4
1.6
1.8
2.0
2.2
2.4
τ0/σ

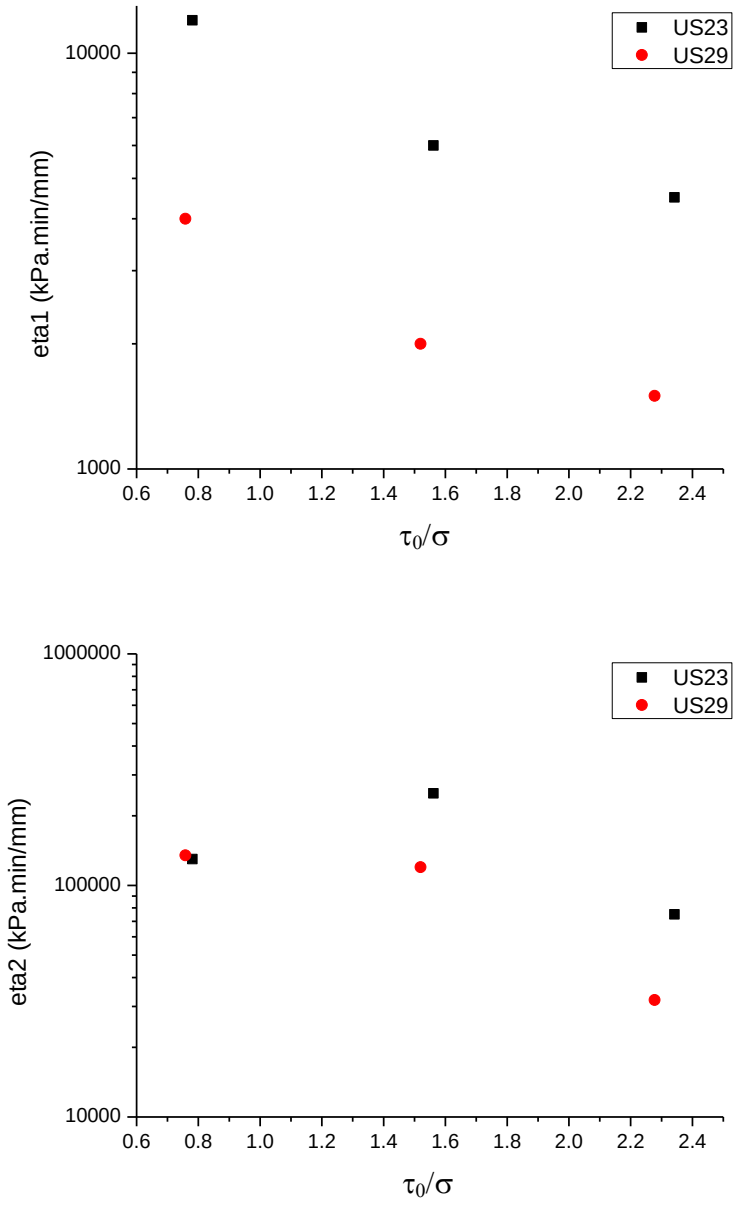

Figure 6.17 Parameters evolution in unsaturated modelling plotted against τ/σ

Figure 6.18 shows the comparison of model parameters for saturated and unsaturated conditions. For both saturated and unsaturated states, parameters appear to decrease with increasing τ_0/σ despite some scattering. When moving from saturated to unsaturated conditions, there appears to be a gap separating the two states. This is associated with the role of matric suction and degree of saturation which is not accounted for in the total stress σ. A different interpretation was therefore sought for the unsaturated data to include the effect of suction and degree of saturation.

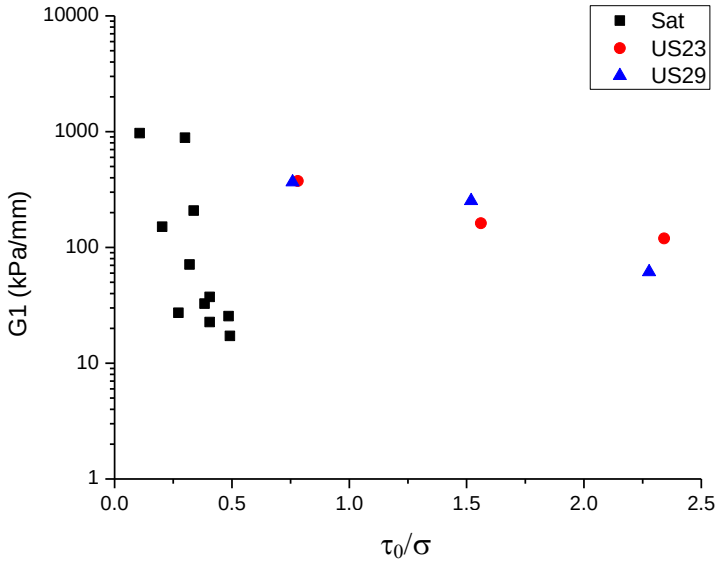
Sat
US23
US29
G1 (kPa/mm)
10000
1000
100
10
1
0.0
0.5
1.0
1.5
2.0
2.5
τ0/σ

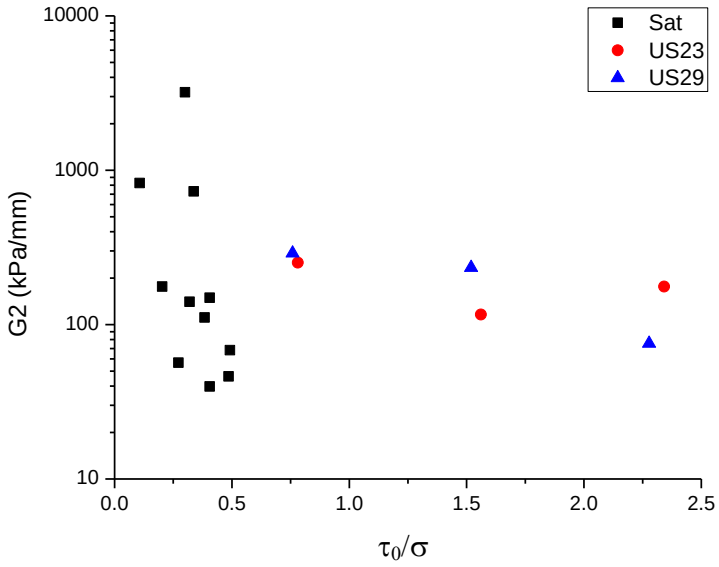
Sat
US23
US29
G2 (kPa/mm)
10000
1000
100
10
0.0
0.5
1.0
1.5
2.0
2.5
τ0/σ

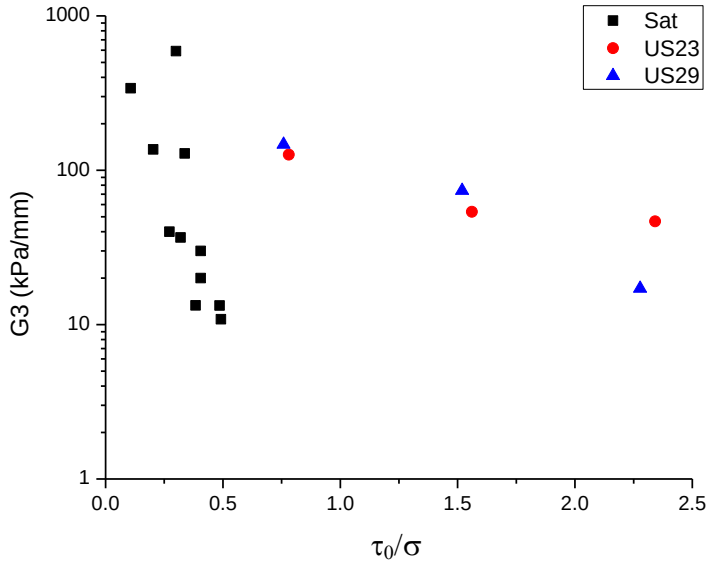
Sat
US23
US29
G3 (kPa/mm)
1000
100
10
1
0.0
0.5
1.0
1.5
2.0
2.5
τ0/σ

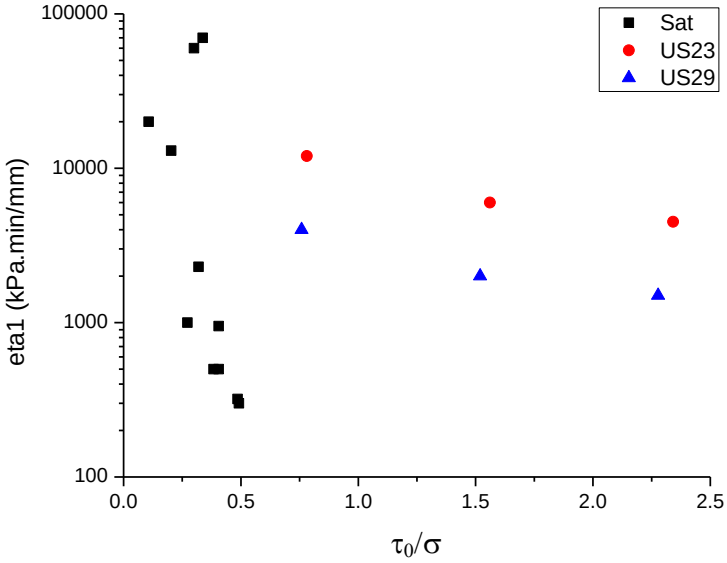
Sat
US23
US29
eta1 (kPa.min/mm)
100000
10000
1000
100
0.0
0.5
1.0
1.5
2.0
2.5
τ0/σ

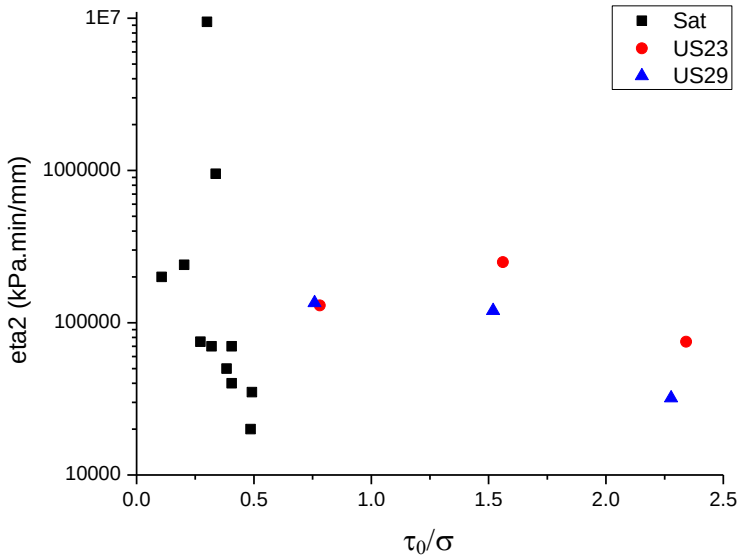
Sat
US23
US29
1E7
1000000
100000
10000
eta2 (kPa.min/mm)
0.0
0.5
1.0
1.5
2.0
2.5
τ0/σ

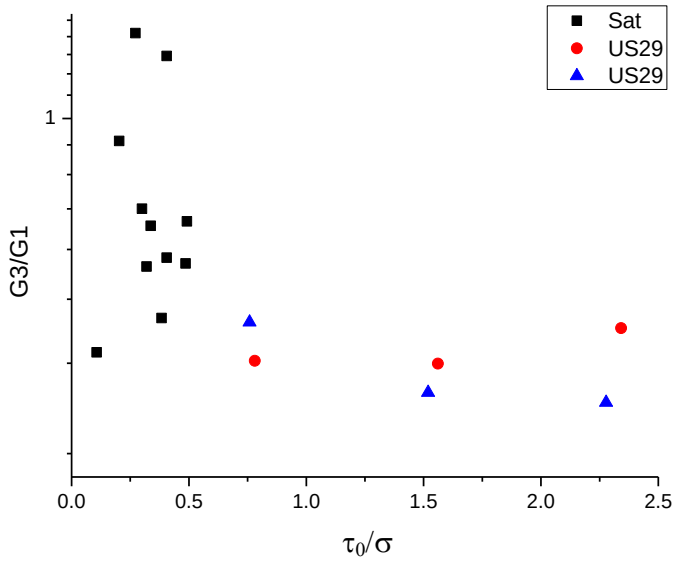
Sat
US29
US29
1
G3/G1
0.0
0.5
1.0
1.5
2.0
2.5
τ0/σ

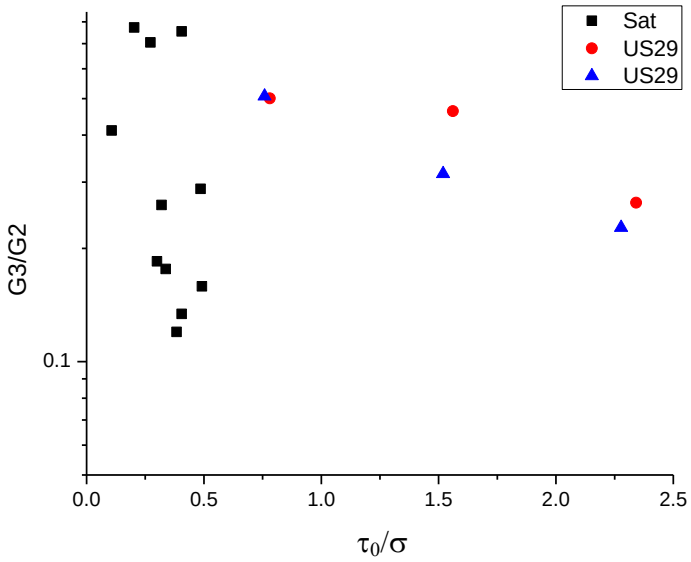

Figure 6.18 Evolution of model parameters for saturated and unsaturated conditions in terms of shear stress versus total stress ratio, τ_0/σ.

6.3.3 Unsaturated parameters with τ/σ"

It was tentatively assumed that unsaturated data should be interpreted in terms of 'effective stress' σ" for unsaturated shear strength, according to the shear strength criterion presented by Tarantino & Tombolato (2005)

$$\tau = tan\phi' \cdot \sigma" \qquad [3]$$

with

$$\sigma" = \left(\sigma + s\frac{e_w - e_{wm}}{e - e_{wm}}\right) \qquad [4]$$

where ϕ' is the friction angle, σ is the total stress, *s* is the matric suction, *e* is the void ration, e_w is the water ratio, and e_{wm} is the 'microstructural' water ratio, which separates the region of inter-aggregate porosity from the region of intra-aggregate porosity (Romero & Vaunat, 2000).

In this criterion, the matric suction *s* and the 'microstructural' water ratio e_{wm} have to be estimated to quantify σ". To assess the matric suction of the two unsaturated specimens tested, the total suction measured needs to be corrected for the osmotic component of suction. The osmotic component of suction was assessed by measuring the matric suction at two water contents (red data points in the Figure 6.19) It can be seen that the matric suction is lower than the total suction, the difference being the osmotic component of suction.

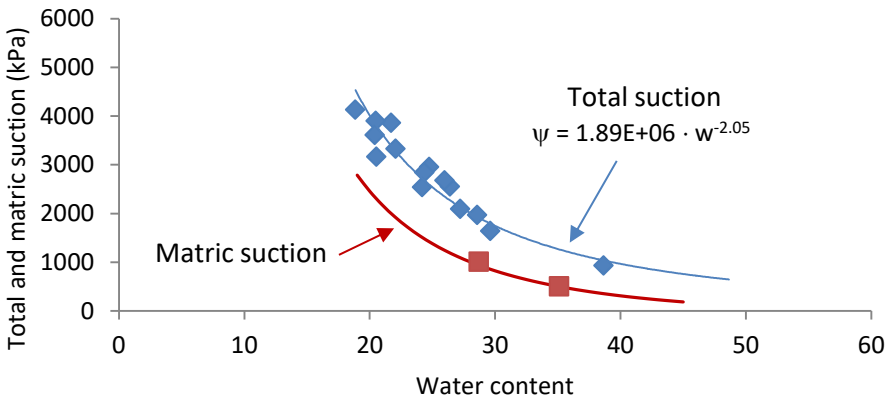

Figure 6.19 Matric suction and total suction

The matric suction, *s* was modelled as a function of water content *w* by modelling separately the total suction and the osmotic suction. The total suction ψ was fitted using a power function of the water content as shown in the Figure 6.18:

$$\psi = 1.89^{6} kPa \cdot w\%^{-2.05} \quad [5]$$

The osmotic suction was also assumed to depend on the water content. The lower the water content, the higher is the salt concentration and the higher is the osmotic suction. The model proposed by Peroni and Tarantino (2003) was used to model the osmotic suction π as a function of the water content:

$$\pi = \frac{A}{w - w_{bonded}} \quad [6]$$

where *w* is the water content, w_{bonded} is the water content associated with the bonded water, and A is a soil parameter. By combining equations 5 and 6, the matric suction is given by:

$$s = \psi - \pi = [1.89^{6} kPa \cdot w\%^{-2.05}] - \left[\frac{A}{w - w_{bonded}}\right] \quad [7]$$

The w_{bonded} was assumed to be equal to the hygroscopic water content at 92% RH (w_{bonded} =5.7%). The parameter A was finally determined by best fitting the two matric data point (A=23 MPa). The matric suction given by equation 7 is shown in figure 6.19. Using equation 7, the matric suction of the two unsaturated specimens tested in shear could be estimated. The 'microstructural' water ratio e_{wm} was estimated according to the empirical

equation suggested by Romero & Vaunat (2000) and verified by Tarantino & Tombolato (2005)

$$e_{wm} = 0.16 + 0.057 \cdot \ln(S_a) \quad [8]$$

where S_a is the specific surface in m^2/g.

To derive the specific surface, the approach discussed by Tarantino (2010) was pursued. The specific surface can be derived from the hygroscopic water content w_h as follow:

$$S_a = \frac{w_h}{\delta \, \varrho_w} \quad [9]$$

where δ is the thickness of the adsorbed water film surrounding the clay particle and ρ_w is the density of water. In turn, the thickness δ can be related to the total suction (chemical potential) of adsorbed water through the following relationship according to Iwamatsu & Horii (1996):

$$\delta = \sqrt[3]{\frac{A_{svl}}{6\pi\psi}} \quad [10]$$

where ψ is the total suction and A_{svl} is the Hamaker constant, which can be assumed to be equal to 6×10^{-20} J according to Tuller & Or (2005).

Total suction ψ can be inferred from the measurement of relative humidity of the air in equilibrium with the adsorbed film through the 'psychrometric law':

$$\psi = -\frac{RT}{v_w} \ln \frac{p_v}{p_{v0}(T)} = -\frac{RT}{v_w} \ln RH \quad [11]$$

where T is the absolute temperature, R is the universal gas constant, v_w is the molar volume of liquid water, p_v is the pressure of the vapour in equilibrium with the liquid, p_{v0} is the saturated vapour pressure at the same temperature, and RH is the relative humidity.

By combining Eqs (9), (10) and (11) and considering that the hygroscopic water content for the ball clay was w_h=1.4% at RH=45% and T=293K, S_a=45 m^2/g was derived. According to Eq. 8, this leads to a microstructural water ratio e_{wm} = 0.37, which is consistent with the value of e_{wm} = 0.34 derived by Tarantino & Tombolato (2005) for a kaolinitic clay, which has lower plasticity index than the Ball clay. Figure 6.20 shows the evolution of parameters when moving from saturated to unsaturated condition by plotting them for the unsaturated specimens against τ/σ". It appears that the parameters are now more consistent with the ones derived from saturated specimens when the effect from matric suction is considered. The distribution of parameters is showing a continuous decreasing trend with the increase of τ/σ''.

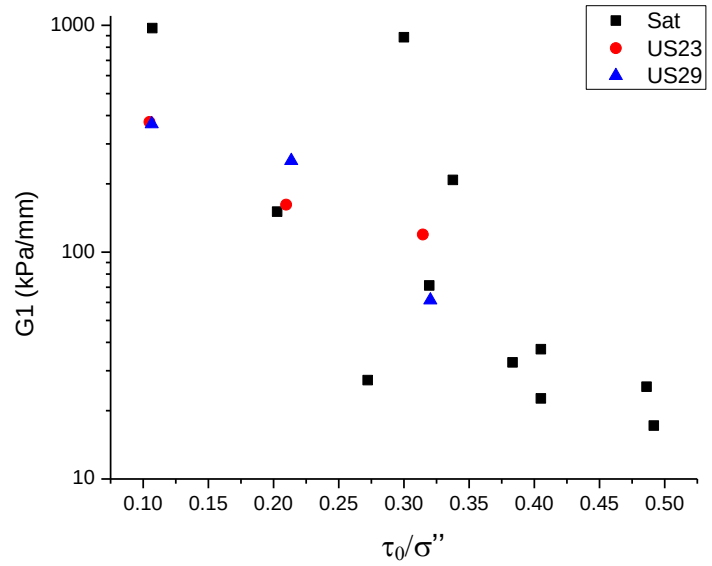
Sat
US23
US29
1000
100
10
G1 (kPa/mm)
0.10
0.15
0.20
0.25
0.30
0.35
0.40
0.45
0.50
τ0/σ''

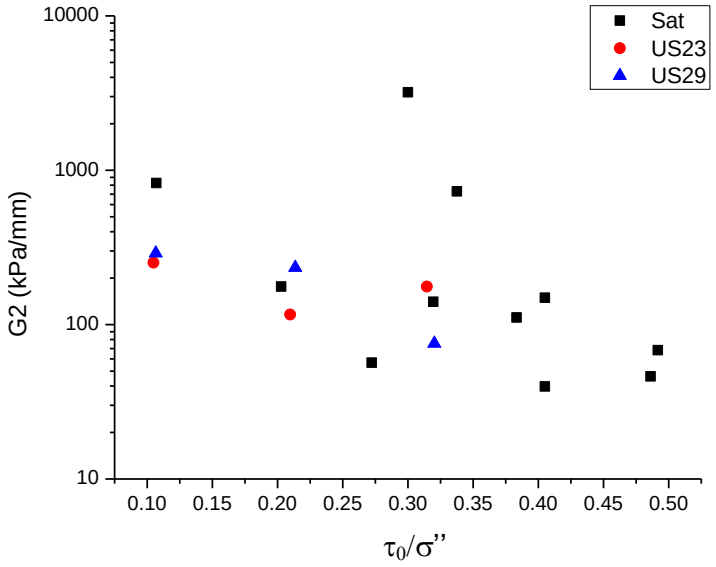
Sat
US23
US29
10000
1000
100
10
G2 (kPa/mm)
0.10
0.15
0.20
0.25
0.30
0.35
0.40
0.45
0.50
τ0/σ''

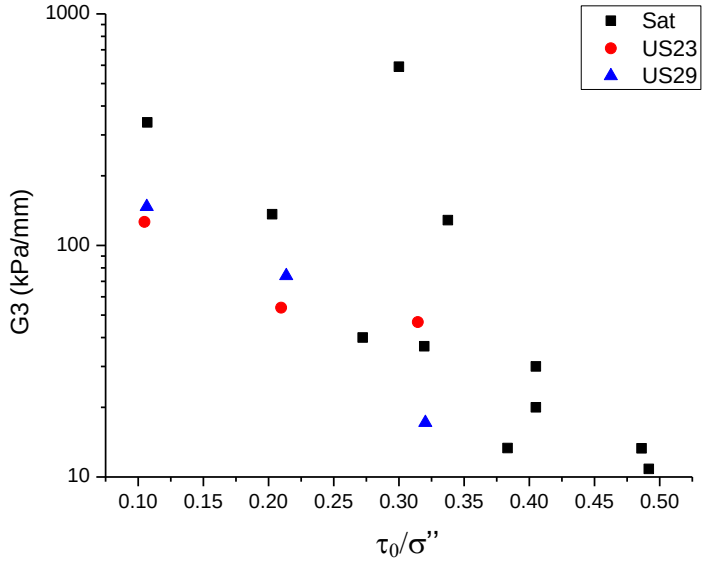
Sat
US23
US29
G3 (kPa/mm)
1000
100
10
0.10
0.15
0.20
0.25
0.30
0.35
0.40
0.45
0.50
τ0/σ''

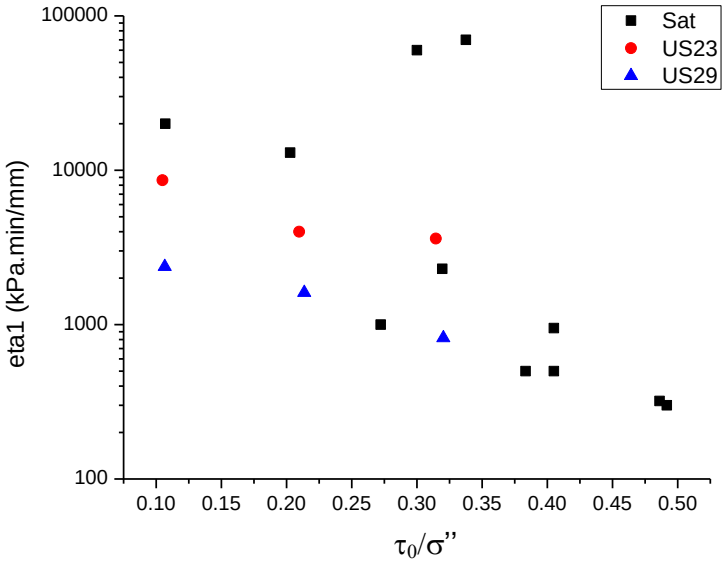
Sat
US23
US29
eta1 (kPa.min/mm)
100000
10000
1000
100
0.10
0.15
0.20
0.25
0.30
0.35
0.40
0.45
0.50
τ0/σ''

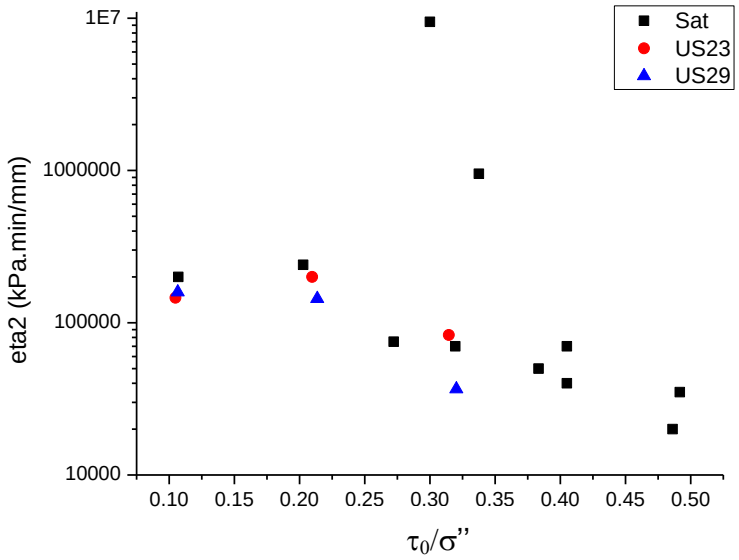

Figure 6.20. Evolution of parameters considering τ_0/σ'' for unsaturated condition

6.4 DISCUSSION

Understanding viscous response under unsaturated conditions was one of the aims of this thesis. Initially, experimental tests and modelling simulations were performed on the specimens under saturated conditions. Only when firm experimental procedures and satisfying modelling for saturated conditions were achieved, then similar procedures were taken to the unsaturated specimens.

Experimental testing was meant to investigate the viscous response in shear from a qualitative and a quantitative point of view. The viscous response in terms of creep displacement was measured in a matter of mm, although very small, their existence is not negligible when considered for long term periods (Di Maio et al., 2013). Modelling via mechanical analogues based on combinations of springs and dashpots helped to understand the viscous response in shear of clayey geo-materials from a quantitative standpoint. Evidence from experimental data and modelling therefore highlighted that the viscous response under unsaturated conditions may be as significant as under saturated conditions.

Lai et al (2014) reported that for the case of creep in shear, the creep strain and creep strain rate were found to be stress and suction dependent. The axial creep strain and creep strain rate were found to increase with increasing deviator stress level and decreasing matric suction.

This is consistent with the data shown in Figure 6.20. An increase in the deviator stress may be associated with an increase in τ/σ in the direct shear test. If τ/σ increases, the elastic parameters G_1 and G_2 decrease and, hence, the creep shear displacement increases. A decrease in G_2 is also associated with an increase in the tangent at the

inflection point, which can be associated with the shear displacement rate. Similarly, when suction decreases, σ" decreases and τ/σ" increases. Again, the data in Figure 6.20 would predict an increase in creep shear displacement.

The fact that model parameters in the unsaturated range can be captured by the effective stress for unsaturated shear strength σ" has a very powerful implication in the prediction of unsaturated viscous response. Extension of saturated models to the unsaturated states can be achieved without the need of assessing additional parameters, in contrast with the approach pursued by Lai et al (2014) for example where an empirical relationship had to be established between suction and some of the model parameters.

CHAPTER 7
CONCLUSIONS

7.0 CONCLUSIONS

Viscous response of Ball Clay in shear has been was investigated under different normal stresses, stress history (pre-peak and residual state) and degree of saturation. A first research question addressed in this thesis is whether relaxation and creep can be captured by a single set of 'constitutive' parameters. It was shown that this can be achieved provided the experimental data are corrected to account for the compliance of the loading system. In the relaxation tests, once the step motor connected to the loading arm is stopped, the shear stress decays causing a deformation of the loading and holding arm. In other words, relaxation does not occur under ideal 'zero' shear displacement conditions because of the deformation if the loading system. However, if the deformability of the loading system is accounted for in the modelling, this effect can be 'corrected'. A different procedure was considered to quantify the stiffness of the loading system depending on whether tests were carried out in displacement-control (both loading and holding arm were considered) or stress control (only the holding arm was considered).

Using a Kelvin model in series with a spring (plus the additional spring to account for the compliance of the system), it was shown the stress decay ratio and the shear displacement increase ratio can be reasonably captured by a single set of parameters using this model. This paves the way for an approach to modelling viscos behaviour using conceptual models rather than empirical ones. The advantage of a unified model for creep and relaxation is the viscous response of landslides, for example, is never 'pure' creep. The effective stress varies due to rainwater infiltration and groundwater fluctuation and, hence, creep response always occurs in combination with a relaxation process. The approach proposed allows modelling the two combined effects (relaxation and creep) simultaneously. The second advantage of the approach proposed is that the creep behaviour can be investigated experimentally using the conventional displacement-controlled shear box, which is available in the majority of research and commercial laboratories, and there is no need to modify the shear box to operate in the stress-controlled mode.

The limitation of the model named M(3+1), consisting of a Kelvin model in series with a spring, i.e. only one dashpot included in the mechanical model, is that the transient (viscous response) was not captured adequately. A closer inspection of the creep response showed that creep behaviour is characterised by two distinct branches, hence the need to include a second dashpot with the addition of a second Kelvin model. This model, referred to as M(5+1) in the thesis, was only implemented for the creep tests.

For saturated conditions in the pre-peak range, the model parameters and, hence, the viscous response, appeared to be controlled by the ratio between the initial tangential stress (at the onset of the creep/relaxation process) and the normal stress. The elastic and viscous parameters decrease with increasing initial shear stress to normal stress ratio, τ_0/σ'. In other

words, the creep displacement increases and the rate of deformation increases with increasing τ_0/σ'. If the curves fitting the model parameters are extrapolated to values $\tau_0/\sigma'>\tan \phi'$, the tertiary creep can be potentially captured.

Parameters for residual conditions were significantly different from those associated with the pre-peak condition. The highest value for the viscosity parameters η_1 and η_2 indicates that the creep displacements in the residual state evolve much more slowly than the case of pre-peak state. Similarly, the higher values of the stiffness parameters indicate that creep displacement in the residual range are lower than the pre-peak range.

Viscous response under both saturated and unsaturated states were found to be similar despite the presence of matric suction in unsaturated conditions.

For viscous response in the unsaturated range, the model parameters could be captured by the effective stress for unsaturated shear strength σ". Extension of saturated models to the unsaturated states could be achieved without the need of assessing additional parameters, in contrast to the approach pursued by Lai et al (2014) for example where an empirical relationship had to be established between suction and some of the model parameters. Overall, viscous response under unsaturated conditions were found to be as significant as the viscous response under saturated conditions and parameters G1, G2, G3, η1 and η2 from both conditions were found to decrease with the increase of τ/σ''.

7.1 RECOMMENDATIONS FOR FUTURE WORK

Based on the results obtained and the knowledge acquired through the development of this research, the following recommendations for future work can be made:

- Experimental tests concerning saturated specimens in pre-peak range should consider more test points near to peak shear strength to assess the evolution of secondary and tertiary creep
- Time taken to conduct the viscous test should be longer than one day to allow the creep displacement and shear stress reaches an asymptotic value as predicted by the model.
- Experimental tests concerning saturated specimens in post-peak range should be done at various shear stress levels for detailed investigation of the viscous response in residual conditions
- Experimental tests concerning unsaturated specimens should be extended to various level of water content for different matric suction range coverage
- Changes in matric suction during shear are interesting aspects to look at and this could not be achieved in this research because of cavitation of the tensiometer when the water content of a specimen was too low causing it to come into contact with the atmosphere. Installation of tensiometer with facility to monitor matric suction into the shear box as proposed by Caruso & Tarantino (2004) should be designated in a way that it allows the creep or stress relaxation response to be captured accordingly without cavitation

- Incorporation of the results obtained with a model to simulate landslide displacements was not addressed properly in the thesis. Justification should be made by either qualitative or quantitative stand point.
- Models presented in this thesis are only capable for primary viscous response simulation and no proves yet that they could simulate secondary or tertiary viscous response. At this point, some modifications to the existing model would have been necessary to capture such responses with different velocity (maybe to replaced G3 spring with dashpot?).

REFERENCES

Adachi, T., & F. Oka. 1982. Constitutive equation for normally consolidated clays based on elastoviscoplasticity. Soils and Foundations 22:57-70

Augustesen, A., Liingaard, M. and Lade, P.V., 2004. Evaluation of time-dependent behavior of soils. *International Journal of Geomechanics*, *4*(3), pp.137-156.

Barden, L. 1969, 'Time dependent deformation of normally consolidated clays and peats', *Journal of the Soil Mechanics and Foundations Division*, vol. 95, pp. 1- 31.

Bernardie, S., Desramaut, N., Malet, J.P., Gourlay, M. and Grandjean, G., 2015. Prediction of changes in landslide rates induced by rainfall.*Landslides*, *12*(3), pp.481-494.

Berry, P.L. & Poskitt, T.J. 1972, 'The consolidation of peat', *Geotechnique*, vol. 22, no.1, pp. 27-52.

Bhat, D.R., Bhandari, N.P., Yatabe, R. and Tiwari, R.C., 2011. Residual-state creep test in modified torsional ring shear machine: methods and implications. *Int J Geomate*, *1*(1), pp.39-43.

Bhat, D.R., Bhandary, N.P. and Yatabe, R., 2013. Residual-state creep behavior of typical clayey soils. *Natural hazards*, *69*(3), pp.2161-2178.

Bhat, D.R., Bhandary, N.P. and Yatabe, R., 2014. Residual-state Creep Behavior of Clayey Soils and its Implication in Landslide Displacement Prediction.

Bjerrum, L., 1967. Engineering geology of Norwegian normally-consolidated marine clays as related to settlements of buildings.

Borja, R. I., & Kavazanjian, E. Jr. 1985. A constitutive Model for the Stress-Strain-Time Behaviour of 'Wet' Clay. Geotechnique, Vol. 35, No. 3

Borja, R.I., 1992. Generalized creep and stress relaxation model for clays.*Journal of geotechnical engineering*, *118*(11), pp.1765-1786.

Capparelli, G. and Versace, P., 2014. Analysis of landslide triggering conditions in the Sarno area using a physically based model. *Hydrology and Earth System Sciences*, *18*(8), pp.3225-3237.

Christensen, R.W. & Wu, T.H. 1964, 'Analysis of clay deformation as a rate process', *Journal of the Soil Mechanics and Foundation*, no. 90, pp. 125-157.

Christie, I.F. & Tonks, D.M. 1985, 'Developments in the time-line theory of consolidation' *The 11th International Conference on Soil Mechanics and Foundation Engineering*, San Francisco, pp. 423-426.

Conte, E., Donato, A. and Troncone, A., 2013. A finite element approach for the analysis of active slow-moving landslides. *Landslides*, *11*(4), pp.723-731.

Corominas, J., Moya, J., Ledesma, A., Lloret, A. and Gili, J.A., 2005. Prediction of ground displacements and velocities from groundwater level changes at the Vallcebre landslide (Eastern Pyrenees, Spain). Landslides,2(2), pp.83-96.

Corominas, J. 2007. Experience on landslide risk management in the Eastern Pyrenees (Spain and Andorra): achievements and challenges. In: Ho, K., Li, V. (Eds.), The 2007 International Forum on Landslide Disaster Management. The Hong Kong Institution of Engineers, Hong Kong, vol. 1, 49–70

Crooks, J.H.A., Becker, D.E., Jefferies, M.G. and McKenzie, K., 1984. Yield behaviour and consolidation. I: Pore pressure response. In *Sedimentation Consolidation Models—Predictions and Validation* (pp. 356-381). ASCE.

de Jong, G.J. and Verruijt, A., 1965. *Primary and secondary consolidation of a spherical clay sample*.

Decagon Devices, Inc, 2015, accessed 10 August 2016, https://www.decagon.com/en/soils/benchtop-instruments/wp4c-water-potential-meter/

Desai, C.S. and Zhang, D., 1987. Viscoplastic model for geologic materials with generalized flow rule. *International Journal for Numerical and Analytical Methods in Geomechanics*, *11*(6), pp.603-620.

Desai, C.S., Samtani, N.C. and Vulliet, L., 1995. Constitutive modeling and analysis of creeping slopes. *Journal of geotechnical engineering*, *121*(1), pp.43-56.

DiBiagio, E. and Kjekstad, O., 2007. Early warning, instrumentation and monitoring landslides. *2nd Regional Training Course, RECLAIM II, 29th January–3rd February*.

Di Maio, C., Vassallo, R. and Vallario, M., 2013. Plastic and viscous shear displacements of a deep and very slow landslide in stiff clay formation.*Engineering Geology*, *162*, pp.53-66.

Fatahi, B., Le, T.M., Le, M.Q. and Khabbaz, H., 2013. Soil creep effects on ground lateral deformation and pore water pressure under embankments.*Geomechanics and Geoengineering*, *8*(2), pp.107-124.

Fang H-Y. 1990. Foundation engineering handbook. Springer, Berlin

Furuya, G., Sassa, K., Hiura, H. and Fukuoka, H., 1999. Mechanism of creep movement caused by landslide activity and underground erosion in crystalline schist, Shikoku Island, southwestern Japan. *Engineering geology*,*53*(3), pp.311-325.

Garlanger, J.E. 1972, 'The consolidation of soils exhibiting creep under constant effective stress', *Geotechnique*, vol. 22, no. 1, pp. 71-78.

Gibson, R.E. and Lo, K.Y., 1961. A theory of consolidation of soils exhibiting secondary consolidation. *Oslo. Norwegian Geotechnical Institute*, (41).

Graham, J. & Yin, J.H. 2001, 'On the time-dependent behaviour of soft soils', *Proceedings of the 3rd International Conference on Soft Soil Engineering*, Lisse, Exton: A.A. Balkema Publishers Hong Kong, pp. 13-24.

Grim, R.E. 1962, *Applied clay mineralogy*, McGraw-Hill New York.

Gupta, B. 1964, 'Creep of saturated soil at different temperatures', University of British Columbia, Canada.

Guzzetti, F., Peruccacci, S., Rossi, M. and Stark, C.P., 2007. Rainfall thresholds for the initiation of landslides in central and southern Europe.*Meteorology and atmospheric physics*, *98*(3-4), pp.239-267.

Guzzetti, F., Peruccacci, S., Rossi, M. and Stark, C.P., 2008. The rainfall intensity–duration control of shallow landslides and debris flows: an update.*Landslides*, *5*(1), pp.3-17.

He, Y., *Study on the creep mechanism and stability drop prediction of slope*(Doctoral dissertation, MS thesis. Chongqing: Chongqing University, China, 2005 [in Chinese]).

Huang, W., Liu, D. Y., Zhao, B. Y., Feng, Y. B., Xia, Y. C. Study on the Rheological Properties and Constitutive Model of Shenzhen Mucky Soft Soil. J . Eng. Sci. Technol. Rev, 7(3), 55-61. (2014)

Intrieri, E., Gigli, G., Mugnai, F., Fanti, R. and Casagli, N., 2012. Design and implementation of a landslide early warning system. *Engineering Geology*,*147*, pp.124-136.

Intrieri, E., Gigli, G., Casagli, N. and Nadim, F., 2013. Brief communication" Landslide Early Warning System: toolbox and general concepts". *Natural hazards and earth system sciences*, *13*(1), pp.85-90.

Iveronova, M.I., 1964. Stationary studies of the recent denudation processes on the slopes of the R. *Tchou-Kizilsi Basin, Tersky Alatan ridge, Tien-Shan. Zeit f. Geomorph. Supplementband*, *5*.

Iwamatsu, M. and Horii, K., 1996. Capillary condensation and adhesion of two wetter surfaces. *Journal of colloid and interface science*, *182*(2), pp.400-406.

Kaliakin, V. N., & Dafalias, Y. F. 1990. Theoretical aspects of the elastoplastic-viscoplastic bounding surface model for isotropic cohesive soils. Soils Found., 30(3), 11-24

Komamura, F., & Huang, R. J. 1974. A new rheological model for soil behavior. J. Geotech. Engng. Div., A.S.C.E., 100: 807–824

Krahn, J. and Fredlund, D.G., 1972. On total, matric and osmotic suction.*The Emergence of Unsaturated Soil Mechanics*, p.35.

Kuhn, M.R. & Mitchell, J.K. 1993, 'New perspectives on soil creep', *Journal of Geotechnical Engineering*, vol. 119, no. 3, pp. 507-524.

Kutter, B. L., & Sathialingam, N. 1992. Elastic viscoplastic modelling of the rate-dependent behaviour of clays. Geotechnique 42(3), 427- 441

Kwok, C.-Y. & Bolton, M. 2010, 'DEM simulations of thermally activated creep in soils', *Geotechnique*, vol. 60, no. 6, pp. 425-433.

Lacerda, W.A. & Houston, W.N. 1973, 'Stress relaxation in soils', *Proceedings of the 8th International conference on soil mechanics and foundation engineering*, vol. 1, Moscow, Russian, pp. 221-227

Lai, X.L., Wang, S.M., Ye, W.M. and Cui, Y.J., 2014. Experimental investigation on the creep behavior of an unsaturated clay. *Canadian Geotechnical Journal*, *51*(6), pp.621-628.

Larsen, M.C. and Simon, A., 1993. A rainfall intensity-duration threshold for landslides in a humid-tropical environment, Puerto Rico. *Geografiska Annaler. Series A. Physical Geography*, pp.13-23.

Le, T.M., 2015. *Analysing Consolidation Data to Optimise Elastic Visco–plastic Model Parameters for Soft Clay* (Doctoral dissertation, University of Technology, Sydney).

Lebouteiller, C., 2008. Climatic and anthropogenic effects on soil transport rates and hillslope evolution. *Sediment Dynamics in Changing Environments*, (325), p.417.

Leroueil, S. 2004. Geotechnics os slopes before failure. Lacerda et al. (eds), Landslides: Evaluation and Stabilization, 1:863-884

Liingaard, M., Augustesen, A. and Lade, P.V., 2004. Characterization of models for time-dependent behavior of soils. *International Journal of Geomechanics*, *4*(3), pp.157-177.

Lim, T.T., Rahardjo, H., Chang, M.F. and Fredlund, D.G., 1996. Effect of rainfall on matric suctions in a residual soil slope. *Canadian Geotechnical Journal*, *33*(4), pp.618-628.

Lopes, B.D.C.F.L., 2016. *Microstructural-based approach to the interpretation of clays and transitional soils behaviour.* PhD thesis. University of Brasilia. Available

Main, I. G. 2000. A damage mechanics model for power-law creep and earthquake aftershock and foreshock sequences. Geophys J Int 142(1):151–161

Maugeri, M., Motta, E. and Raciti, E., 2006. Mathematical modelling of the landslide occurred at Gagliano Castelferrato (Italy). *Natural Hazards and Earth System Science*, *6*(1), pp.133-143.

Melinda, F., Rahardjo, H., Han, K., & Leong, E. 2004. Shear Strength of Compacted Soil under Infiltration Condition. J. Geotech. Geoenviron. Eng., 130(8), 807–817

Mesri, G. 1973, 'Coefficient of Secondary Compression', *Journal of the Soil Mechanics and Foundations Division*, vol. 99, no. 1, pp. 123-137.

Mesri, G. & Godlewski, P.M. 1977, 'Time and stress-compressibility interrelationship', Journal of the Geotechnical Engineering Division, vol. 103, no. 5, pp. 417-430.

Mesri, G. 2003, 'Primary compression and secondary compression', *Geotechnical Special Publication*, pp. 122-166.

Mitchell, J.K., 1964. Shearing resistance of soils as a rate process. Journal of Soil Mechanics & Foundations Div, 90(Proc. Paper 3773).

Mitchell, J.K. & Soga, K. 2005, Fundamentals of soil behavior, 3rd edn, John Wiley & Sons.

Murayama, S. and Shibata, T., 1966. Flow and stress relaxation of clays. In*Rheology and Soil Mechanics/Rhéologie et Mécanique des Sols* (pp. 99-129). Springer Berlin Heidelberg.

Navarro, V. & Alonso, E. 2001, 'Secondary compression of clays as a local dehydration process', *Geotechnique*, vol. 51, no. 10, pp. 859-869.

Okamoto, T., Larsen, J. O., Matsuura, S., Asano, S., Takeuchi, Y., & Grande, L. 2004. Displacement properties of landslide masses at the initiation of failure in quick clay deposits and the effects of meteorological and hydrological factors. Eng Geol 72(3–4):233–251

Peroni, N. and Tarantino, A., 2005. Measurement of osmotic suction using the squeezing technique. In *Unsaturated Soils: Experimental Studies* (pp. 159-168). Springer Berlin Heidelberg.

Perzyna, P. 1963. The Constitutive Equations for Rate Sensitive Materials. Quarter of Applied Mathematics, Vol. 20, pp. 321-332

Perzyna, P. 1966. Fundamental problems in viscoplasticity. Rec. Adv. Appl. Mech. 9, 243–377. Academic Press, New York

Petley, D. N., & Allison, R. J. 1997. The mechanics of deep-seated landslides. Earth Surf Proc Landforms 22:747-758

Petley, D. N., Hearn, G. J., & Hart, A. 2005a. Towards the development of a landslide risk assessment for rural roads in Nepal. In: Glade T, Anderson M, Crozier MJ (eds) Landslide hazard and risk. Wiley, New York, pp 597–619

Petley, D. N., Higuchi, T., Dunning, S., Rosser, N. J., Petley, D. J., Bulmer, M. H., Carey, J. 2005b. A new model for the development of movement in progressive landslides. In: Hungr O, Fell R, Couture R, Eberhardt E (eds) International conference on landslide risk management. Taylor & Francis Ltd., Vancouver, pp 350–358

Petley, D. N., Petley, D. J., & Allison, R. J. 2008. Temporal prediction in landslides—Understanding the Saito effect. In: Chen Z, Zhang J-M, Ho K, Wu F-Q, Li Z-K (eds) Landslides and engineered slopes: from the past to the future. Taylor & Francis, Xi'an, pp. 794–800

Picarelli, L., Urciuoli, S., & Russo, C. 2000. Mechanics of slope deformation and failure in stiff clays and clay shales as a consequence of pore pressure fluctuation. Proceedings 8th International Symposium on Landslides, Cardiff, vol. 4,34 pp

Picarelli, L., Urciuoli, G. and Russo, C., 2004a. Effect of groundwater regime on the behaviour of clayey slopes. *Canadian Geotechnical Journal*, *41*(3), pp.467-484.

Picarelli, L., & Russo, C. 2004b. Remarks on the mechanics of slow active landslides and the interaction with man-made works. In: Lacerda W, Ehrlich M, Fontoura SAB, Sayao AS (eds) Landslides: evaluation and stabilization. Ninth international symposium on landslides. A.A. Balkema Publishers, Leiden, pp 1141–1176

Puzrin, A.M. and Schmid, A., 2011, September. Progressive failure of a constrained creeping landslide. In *Proceedings of the Royal Society of London A: Mathematical, Physical and Engineering Sciences* (Vol. 467, No. 2133, pp. 2444-2461). The Royal Society.

Puzrin, A. M. & Schmid, A. (2012). Ge´otechnique 62, No. 6, 491–501

Ranalli, M., Medina-Cetina, Z., Gottardi, G. and Nadim, F., 2013. Probabilistic Calibration of a Dynamic Model for Predicting Rainfall-Controlled Landslides. *Journal of Geotechnical and Geoenvironmental Engineering*,*140*(4), p.04013039.

Reches, Z., & Lockner, D. A. 1994. Nucleation and growth of faults in brittle rocks. J Geophys Res 99(B9):18159–18173. Accessed 6 Oct 2010

Riemer, W. 1992. Landslide and reservoir (keynote paper). In: Proceedings of the 6th International Symposium on Landslides. p. 1373–2004

Romero, E. and Vaunat, J., 2000. Retention curves of deformable clays.*Experimental evidence and theoretical approaches in unsaturated soils*, pp.91-106.

Schulz, W.H., McKenna, J.P., Kibler, J.D. and Biavati, G., 2009. Relations between hydrology and velocity of a continuously moving landslide—evidence of pore-pressure feedback regulating landslide motion?. *Landslides*,*6*(3), pp.181-190.

Sheng, D., 2011. Review of fundamental principles in modelling unsaturated soil behaviour. *Computers and Geotechnics*, *38*(6), pp.757-776.

Tarantino, A. and Mongiovi, L., 2003. CALIBRATOIN OF TENSIOMETER FOR DIRECT MEASUREMENT OF MATRIC SUCTION. *Géotechnique*,*53*(1).

Tarantino, A. and Tombolato, S., 2005. Coupling of hydraulic and mechanical behaviour in unsaturated compacted clay. *Géotechnique*, *55*(4), pp.307-317.

Tarantino, A., 2010, September. Unsaturated soils: compacted versus reconstituted states. In *5th International Conference on Unsaturated Soil* (pp. 113-136).

Taylor, D.W. and Merchant, W., 1940. A theory of clay consolidation accounting for secondary compression. *Journal of Mathematics and Physics*, *19*(1), pp.167-185.

Ter-Stepanian, G., 1975. Creep of a clay during shear and its rheological model. *Geotechnique*, *25*(2), pp.299-320.

Terzaghi, K., 1941. *Undisturbed clay samples and undisturbed clays*. Harvard University.

Tuller, M. and Or, D., 2005. Water films and scaling of soil characteristic curves at low water contents. *Water Resources Research*, *41*(9).

Uchida, T., Kosugi, K., & Mizuyama, T. 2001. Effects of pipeflow on hydrological process and its relation to landslide: a review of pipeflow studies in forested headwater catchments, Hydrol. Process. 15, 2151-2174

Van Asch, T.W., Van Beek, L.P.H. and Bogaard, T.A., 2007. Problems in predicting the mobility of slow-moving landslides. *Engineering geology*, *91*(1), pp.46-55.

Vassallo, R., Grimaldi, G.M. and Di Maio, C., 2015. Pore water pressures induced by historical rain series in a clayey landslide: 3D modeling.*Landslides*, *12*(4), pp.731-744.

Vermeer, P. A., & Neher, H. P. 1999. A soft soil model that accounts for creep, In Bringreve, R.B.J. (Ed.), Proceedings of the Int. Symposium “Beyond 2000 in Computational Geotechnics”: 249-261, Amsterdam, A.A. Balkema

Veveakis, E., Vardoulakis, I. & Di Toro, G. 2007. Thermoporomechanics of creeping landslides: The 1963 Vaiont slide, northern Italy. Journal of Geophysical Research 112

Wang, F., Zhang, Y., Huo, Z., Peng, X., Araiba, K., & Wang, G. 2008. Movement of the Shuping landslide in the first four years after the initial impoundment of the Three Gorges Dam Reservoir, China. Landslides. 5(3):321–9

Wang, Y. H. & Xu, D. 2007, 'Dual Porosity and Secondary Consolidation', *Journal of Geotechnical and Geoenvironmental Engineering*, vol. 133, no. 7, pp. 793-801.

Yang, D., & Lu, G. 1993. Natural disasters. Beijing: Surveying and Mapping Publishing House

Yin, J.-H., & Graham, J. 1989. Viscous-elastic-plastic modelling of one-dimensional time-dependent behaviour of clays. Canadian Geotechnical Journal, 26: 199-209

Yin, J.-H., & Graham, J. 1994. Equivalent time and one-dimensional elastic viscoplastic modelling of time dependent stress-strain behaviour of clays. Canadian Geotechnical Journal, 31: 42-52

Yin, J.-H., & Tong, F. 2011. Constitutive Modelling of the Time-dependant Stress-strain Behaviour of Saturated Soils Exhibiting both Creep and Swelling. Canadian Geotechnical Journal 48(12), 1870-1885

Yin, J.H. & Cheng, C.M. 2006, 'Comparison of Strain-rate Dependent Stress-Strain Behavior from K o -consolidated Compression and Extension Tests on Natural Hong Kong Marine Deposits', *Marine Georesources & Geotechnology*, vol. 24, no. 2, pp. 119-147.

Young, A. 1972. Slopes. Oliver and Boyd, Edinburgh, pp 288

Zeevart, L. 1986, 'Consolidation in the intergranular viscosity of highly compressible soils', *Consolidation of soil: Testing and evaluation, ASTM STP*, vol. 892, pp. 257-281.

Zienkiewcz, O. C., & Cormeau, I. C. 1974. Int. J. Num. Meth. Eng. 8

ANNEX A

SENSITIVITY TEST FOR PARAMETERS FROM (5+1)a-ELEMENT MODEL

Figure A.1 presents the sensitivity study carried out for the parameters in the (5+1)a-element visco-elastic model using dataset from saturated specimens, at 100kPa normal stress, 50% of peak shear strength. Table A.1 shows the interpretations of the results obtained by the analyses of the graphs as shown in Figure A.1. The sensitivity analysis was carried out for viscous parameters acquired from best-fitting procedures, the $\eta 1$ and $\eta 2$. The elastic parameters, G1, G2, G3 and G4 of which acquired from either experimentally or computed through equations derived from the constitutive model, were kept constant. Figure A.1a shows the simulation response when the parameter $\eta 1$, which controls the instantaneous creep response varies between (100,1000 and 10 000). Figure A.1b shows the simulation response when the parameter n2, which controls the creep response at second branch varies between (10 000, 75 000 and 200 000).

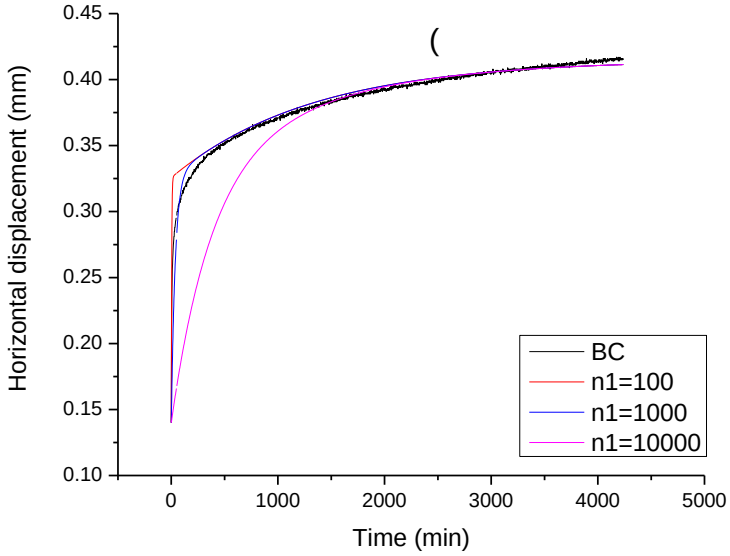

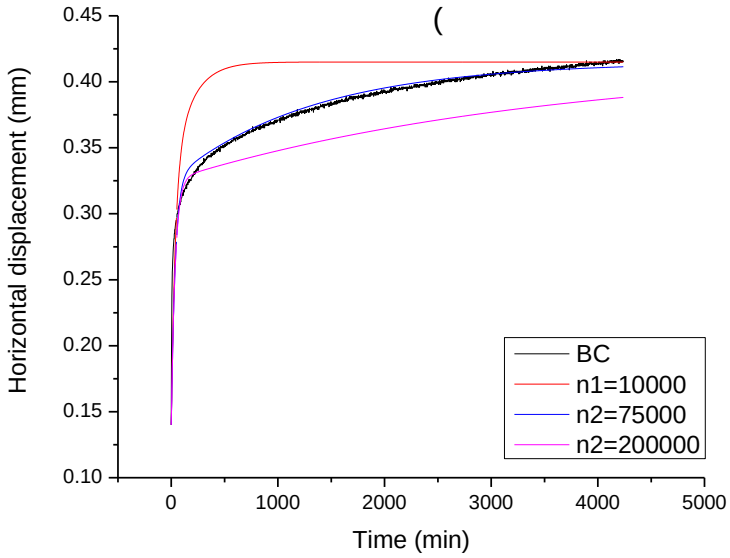

Figure A. 1 Sensitivity tests for Model 5+1a a) responses for $\eta 1$ b) response for $\eta 2$

Table A.1 Results interpretation of the sensitivity tests analysis for $\eta 1$ and $\eta 2$ parameters

	Transient creep response
$\eta 1$	
Increase	Underestimated
Decrease	Oversestimated
$\eta 2$	
Increase	Underestimated
Decrease	Oversestimated

ANNEX B

TANGENT FROM DISPLACEMENT-CONTROLLED TEST FOR G3 DETERMINATION

Figures B.1, B.2, B.3, B.4, B.5 and B.6 shows the tangent obtained from displacement-controlled test for each dataset.

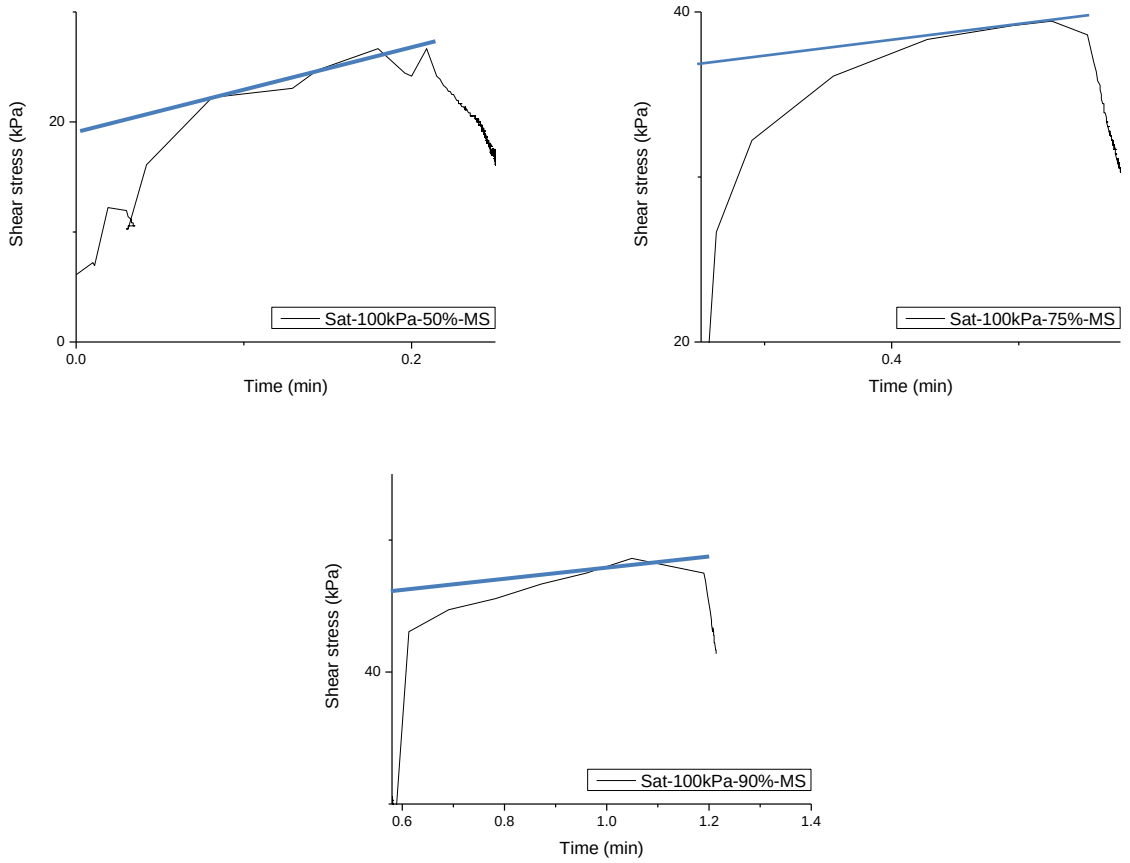

Figure B.1 Tangent for G3 parameters for specimens at saturated, 100kPa normal stress from multistage test

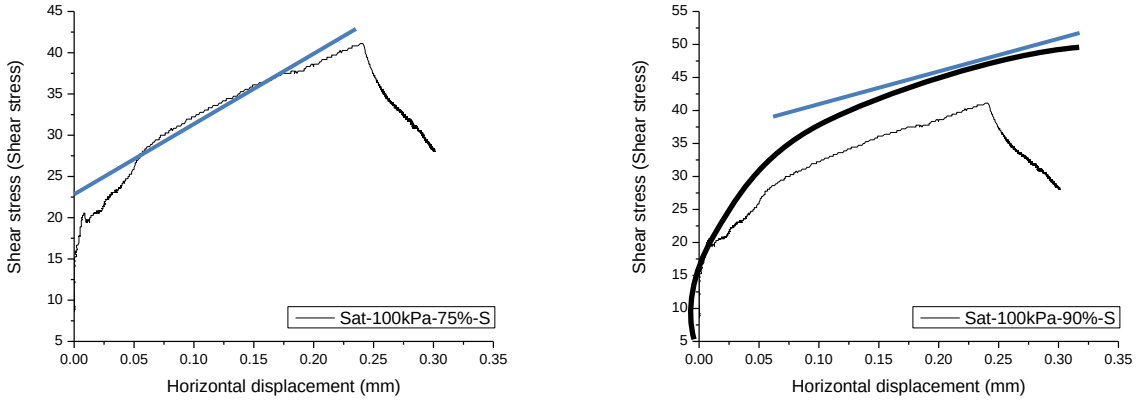

Figure B.2 Tangent for G3 parameters for specimens at saturated, 100kPa normal stress from single stage tests

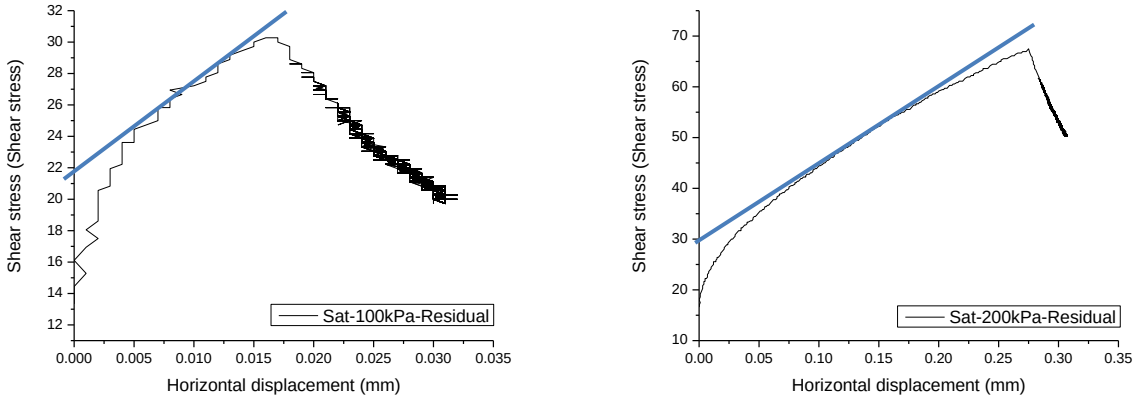

Figure B.3 Tangent for G3 parameters for specimens at saturated range in post-peak condition

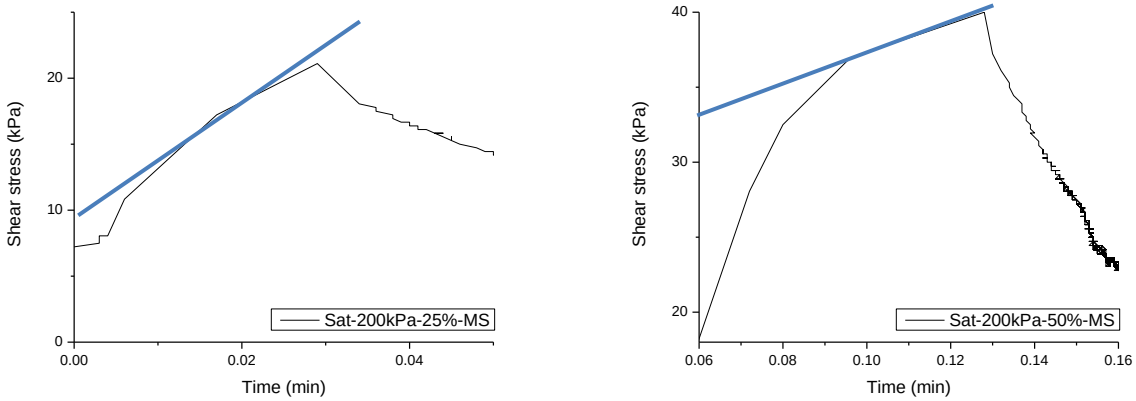

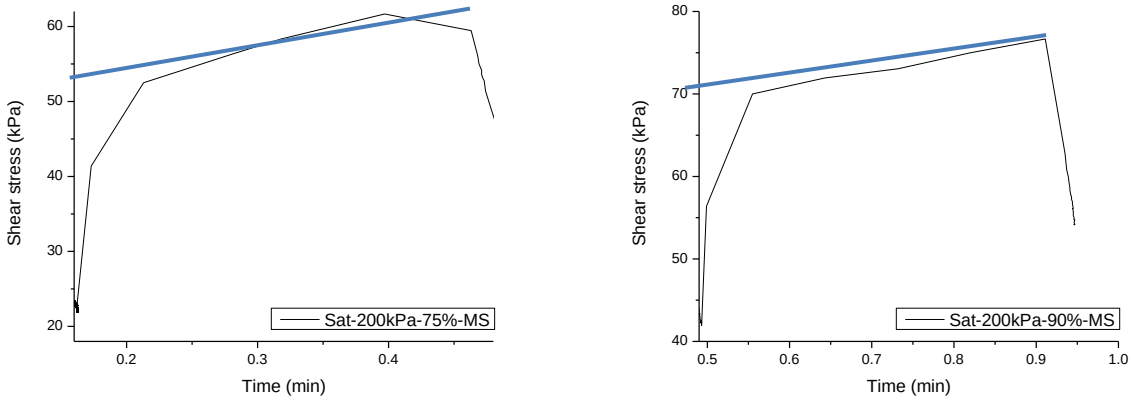

Figure B.4 Tangent for G3 parameters for specimens at saturated, 200kPa normal stress from multistage test

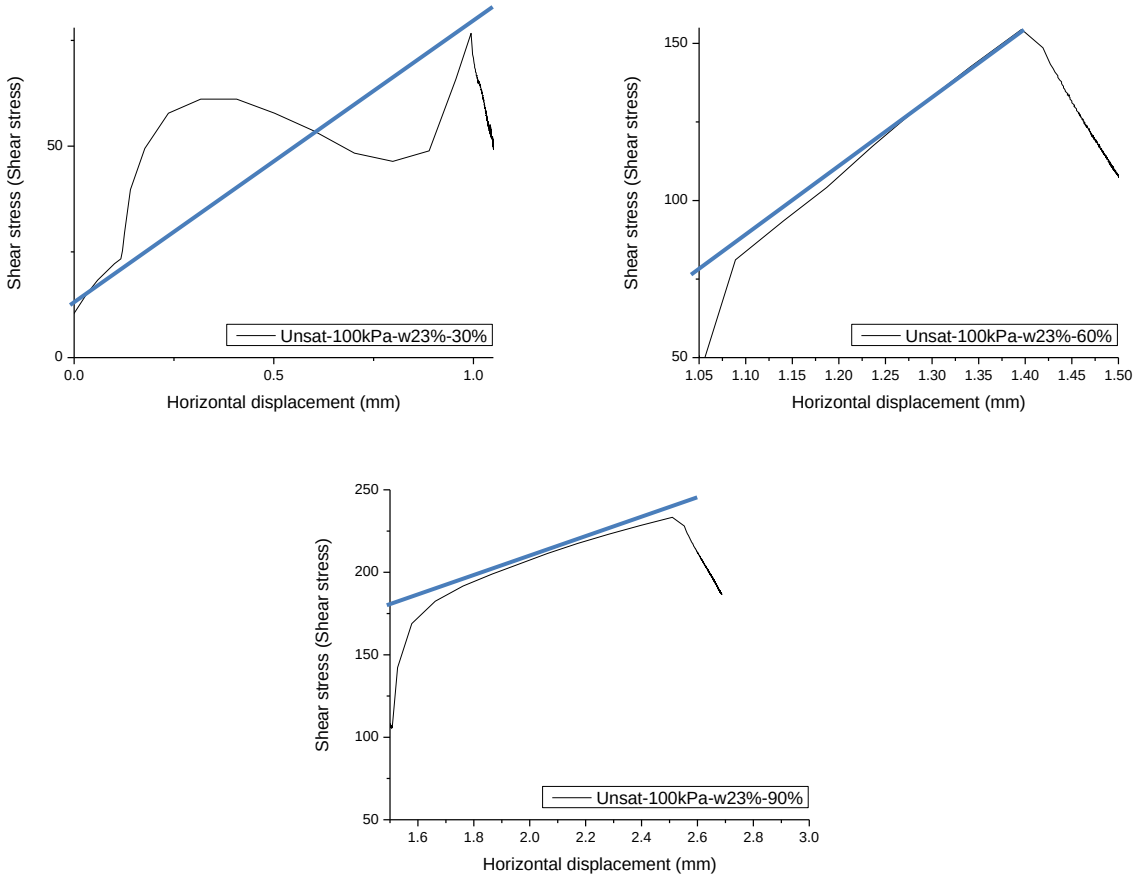

Figure B.5 Tangent for G3 parameters for specimens at unsaturated, with water content 23% and 100kPa normal stress

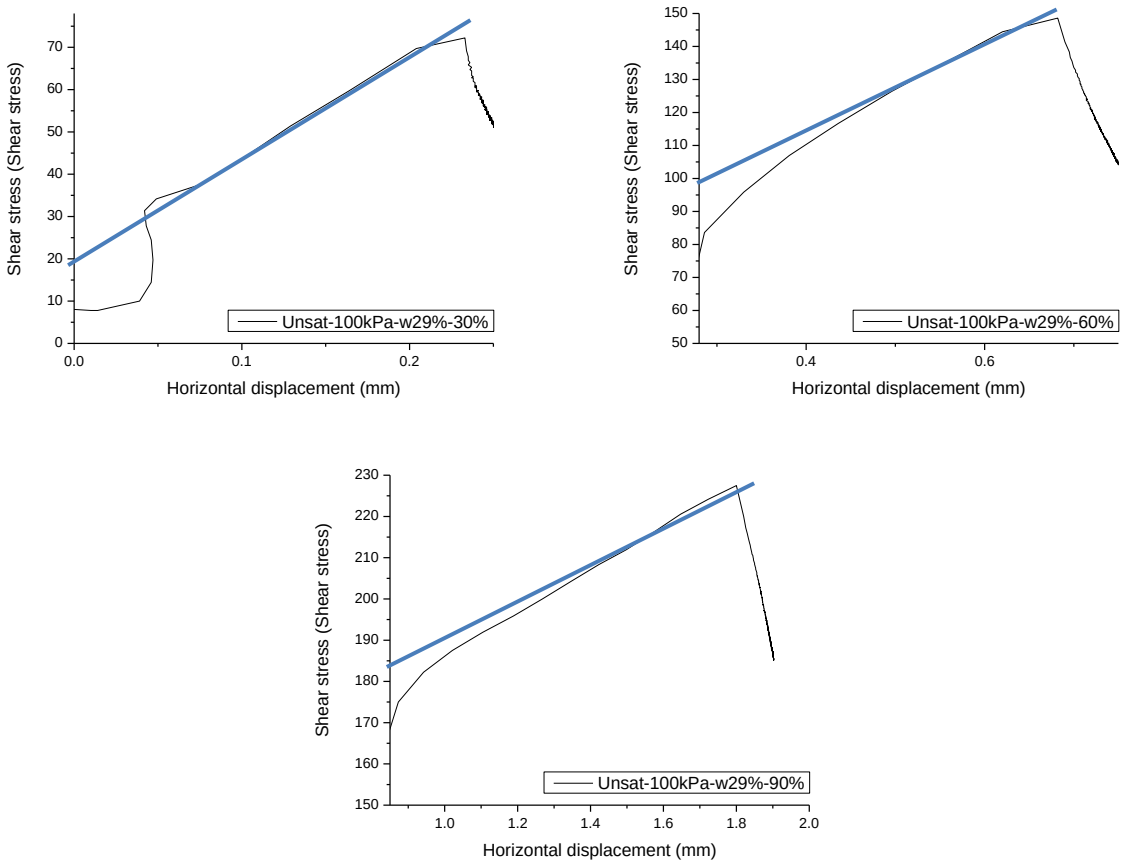

Figure B.6 Tangent for G3 parameters for specimens at unsaturated, with water content 29% and 100kPa normal stress

ANNEX C

TANGENT FROM 2ND BRACH OF SEMI-LOG GRAPH-HORIZONTAL DISPLACEMENT VS TIME FOR PARAMETER G1 DETERMINATION

Figures C.1, C.2, C.3, C.4, C.5 and C.6 show the tangent obtained from the 2nd branch of creep response in experimental datasets. To obtain the parameter G1, tangent acquired from the slope was calculated with the equations given as follows:
For t>> τ_1 (second branch)

$$\gamma = \left\{\frac{1}{G_2}\left[1 - exp\left(-\frac{t}{\tau_2}\right)\right] + \frac{1}{G_1} + \frac{1}{G_3} + \frac{1}{G_4}\right\}\frac{G_3 G_4}{G_3 + G_4}\gamma_0$$

$$\frac{d\gamma}{dln(t)} = \frac{G_3 G_4}{G_3 + G_4}\gamma_0 t\frac{d}{dt}\left\{\frac{1}{G_2} - \frac{1}{G_2}exp\left(-\frac{t}{\tau_2}\right) + \frac{1}{G_1} + \frac{1}{G_3} + \frac{1}{G_4}\right\} = \frac{G_3 G_4}{G_3 + G_4}\gamma_0 t\frac{d}{dt}\left\{-\frac{1}{G_2}exp\left(-\frac{t}{\tau_2}\right)\right\}$$
$$= \frac{G_3 G_4}{G_3 + G_4}\gamma_0\frac{1}{G_2}\frac{1}{\tau_2}t \cdot exp\left(-\frac{t}{\tau_2}\right)$$

$$\left[\frac{d\gamma}{dln(t)}\right]_{IP2} = \frac{G_3 G_4}{G_3 + G_4}\gamma_0\frac{1}{G_2}\frac{1}{\tau_2}\tau_2 \cdot exp\left(-\frac{\tau_2}{\tau_2}\right) = \frac{G_3 G_4}{G_3 + G_4}\gamma_0\frac{1}{G_2} \cdot exp(-1)$$

$$G_2 = \frac{G_3 G_4}{G_3 + G_4}\frac{1}{\left[\frac{d\gamma}{dln(t)}\right]_{IP2}}\gamma_0 \cdot exp(-1)$$

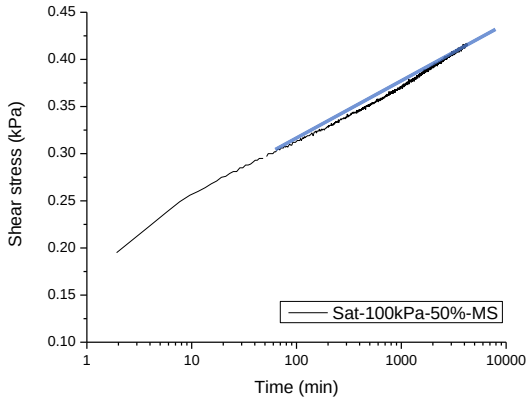

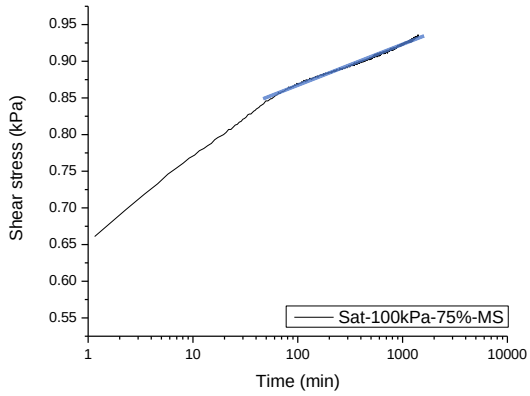

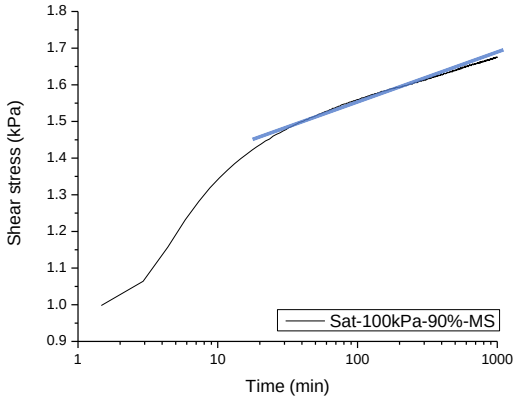

Figure C.1 Tangent from 2nd branch of saturated specimens at pre-peak condition, under 100kPa vertical and multi stage

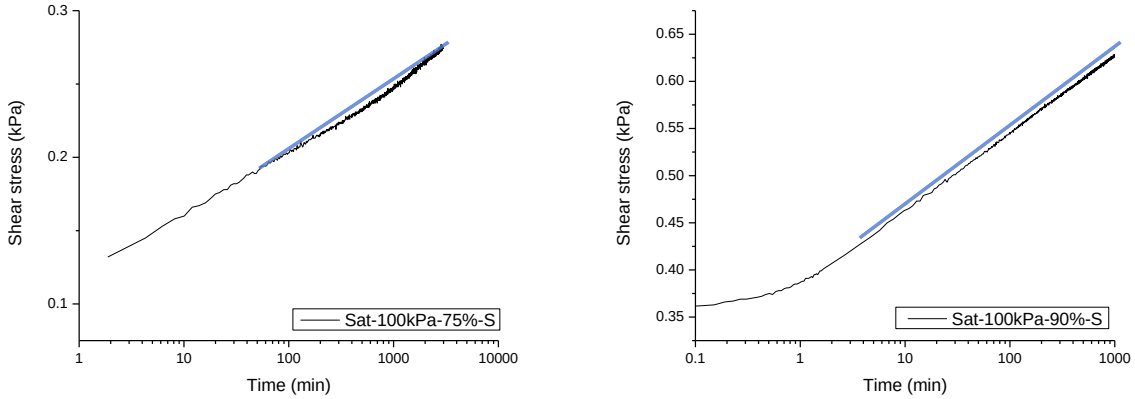

Figure C.2 Tangent from 2nd branch of saturated specimens at pre-peak condition, under 100kPa vertical and single stage

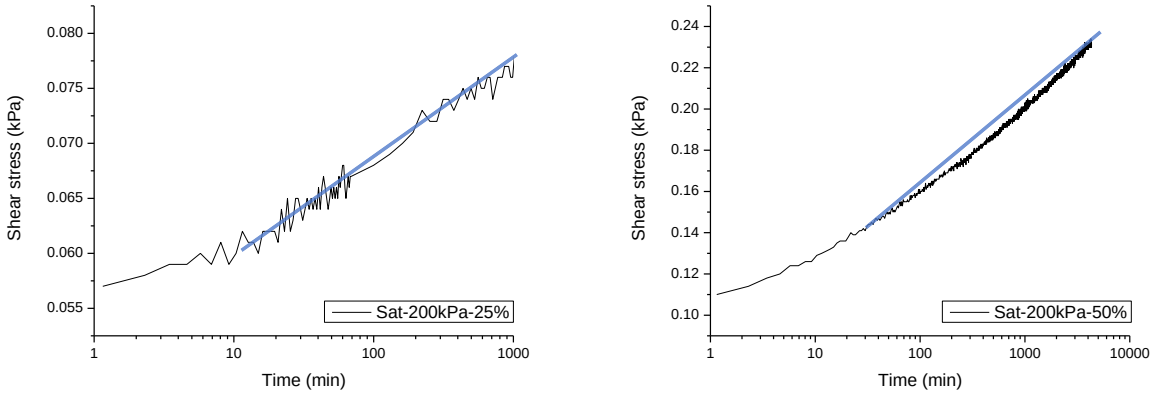

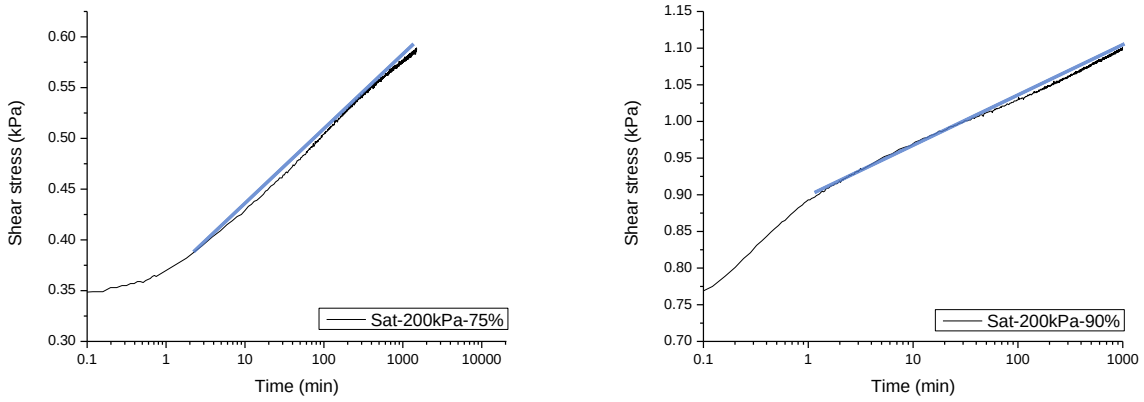

Figure C.3 Tangent from 2nd branch of saturated specimens at pre-peak condition, under 200kPa vertical and multi stage

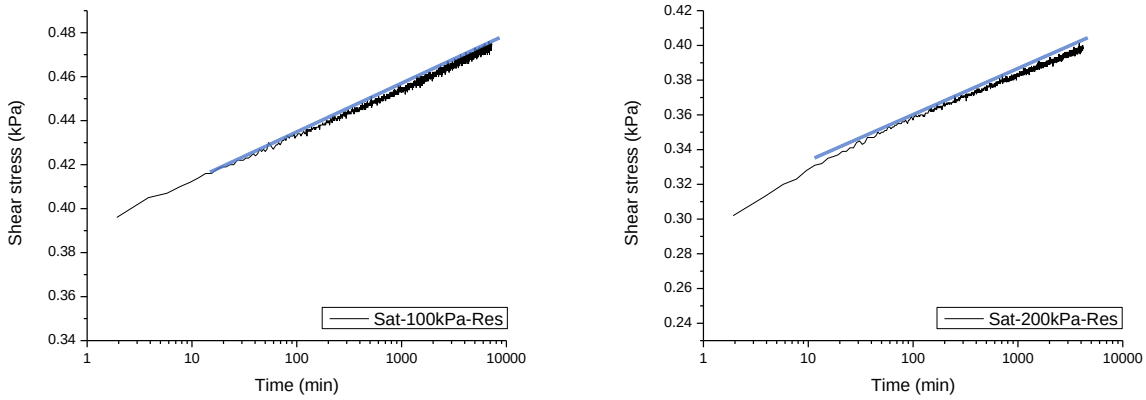

Figure C.4 Tangent from 2nd branch of saturated specimens at post-peak condition from single stage

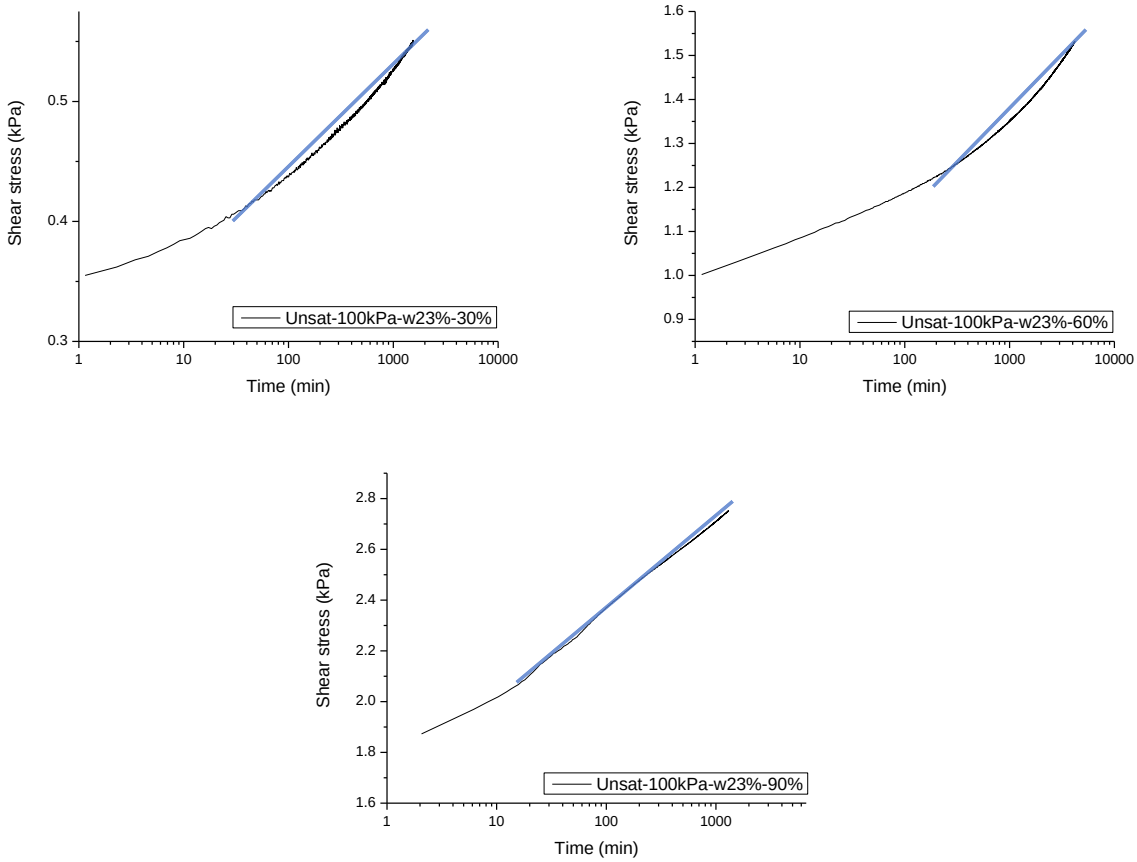

Figure C.5 Tangent from 2nd branch of unsaturated specimens at pre-peak condition, at water content w=23%, under 100kPa vertical and multi stage

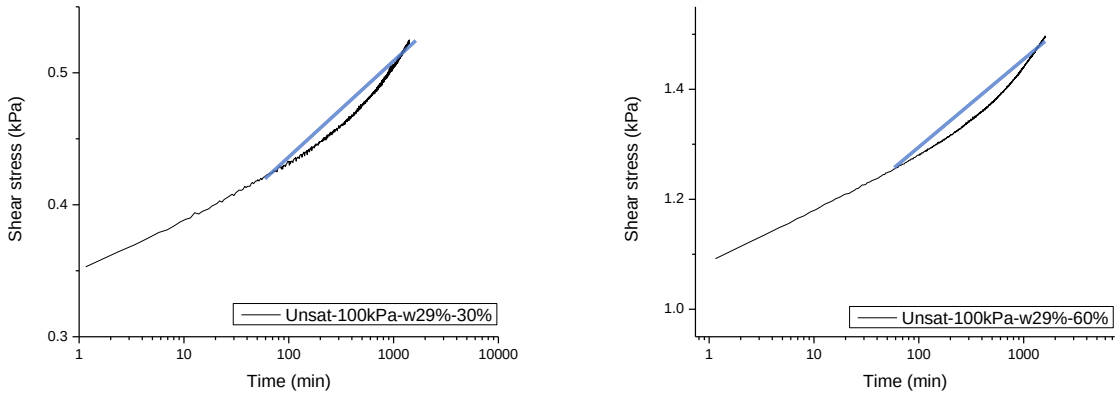

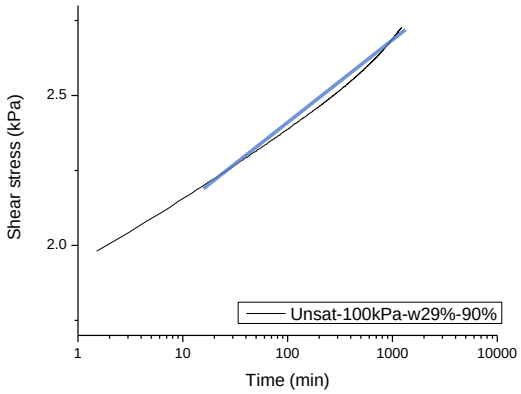

Figure C.6 Tangent from 2nd branch of unsaturated specimens at pre-peak condition, at water content w=29%, under 100kPa vertical and multi stage

ANNEX D

CONSTITUTIVE EQUATIONS DEVELOPMENT FOR 3-ELEMENT MODEL (WITHOUT ADDITIONAL SPRING FOR COMPLIANCE SYSTEM)

Model 3a

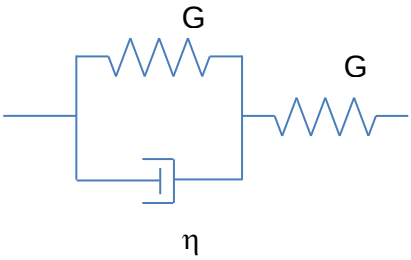

Stress-strain relationships in elements 1 and 2

$\sigma_1 = G_1\gamma_1$

$\sigma_2 = G_2\gamma_2 + \eta_2\dot{\gamma}_2$

Because elements 1 and 2 are in series, then

$\sigma_2 = \sigma_1 = \sigma$

$\gamma = \gamma_1 + \gamma_2$

We can manipulate equations as follows:

$\sigma_1 = \sigma = G_1\gamma_1 \Rightarrow \gamma_1 = \frac{\sigma}{G_1}$

$\sigma_1 = \sigma = G_1\gamma_1 \Rightarrow \dot{\sigma} = G_1\dot{\gamma}_1 \quad \Rightarrow \boxed{\dot{\gamma}_1 = \frac{\dot{\sigma}}{G_1}}$

$\sigma_2 = \sigma = G_2\gamma_2 + \eta_2\dot{\gamma}_2 \Rightarrow \boxed{\dot{\gamma}_2 = \frac{\sigma - G_2\gamma_2}{\eta_2} = \frac{\sigma - G_2(\gamma - \gamma_1)}{\eta_2} = \frac{\sigma}{\eta_2} - \frac{G_2}{\eta_2}\gamma + \frac{G_2}{\eta_2}\gamma_1 = \frac{\sigma}{\eta_2} - \frac{G_2}{\eta_2}\gamma + \frac{G_2}{\eta_2}\frac{\sigma}{G_1}}$

$\gamma = \gamma_1 + \gamma_2 \Rightarrow \dot{\gamma} = \dot{\gamma}_1 + \dot{\gamma}_2$

We can then write

$\dot{\gamma} = \dot{\gamma}_1 + \dot{\gamma}_2;$

$\dot{\gamma} = \left(\frac{\dot{\sigma}}{G_1}\right) + \left(\frac{\sigma}{\eta_2} - \frac{G_2}{\eta_2}\gamma + \frac{G_2}{\eta_2}\frac{\sigma}{G_1}\right);$

$\dot{\gamma} + \frac{G_2}{\eta_2}\gamma = \frac{\dot{\sigma}}{G_1} + \left(\frac{1}{\eta_2} + \frac{G_2}{\eta_2}\frac{1}{G_1}\right)\sigma;$

Multiplying by $G_1\eta_2$ we can finally write

$$G_1\eta_2\dot{\gamma} + G_1\eta_2\frac{G_2}{\eta_2}\gamma = G_1\eta_2\frac{\dot{\sigma}}{G_1} + \left(G_1\eta_2\frac{1}{\eta_2} + G_1\eta_2\frac{G_2}{\eta_2}\frac{1}{G_1}\right)\sigma;$$

$$\boxed{G_1\eta_2\dot{\gamma} + G_1G_2\gamma = \eta_2\dot{\sigma} + (G_1 + G_2)\sigma;}$$

CREEP

Solving partial differential equation for $\dot{\sigma} = 0$ and the boundary condition given by:

$\gamma(0) = \frac{\sigma}{G_1}$

we can write

$$\gamma = \underbrace{\left\{\left[1 - exp\left(-\frac{t}{\tau_2}\right)\right]\frac{1}{G_2} + \frac{1}{G_1}\right\}}_{J(t)}\sigma \qquad \tau_2 = \frac{\eta_2}{G_2}$$

$$\gamma = \underbrace{\left\{\left[1 - exp\left(-\frac{t}{\tau_2}\right)\right]\frac{1}{G_2} + \frac{1}{G_1}\right\}}_{J(t)}\gamma(0)G_1 \qquad \tau_2 = \frac{\eta_2}{G_2}$$

$$\gamma = \underbrace{\left\{\left[1 - exp\left(-\frac{t}{\tau_2}\right)\right]\frac{G_1}{G_2} + \frac{G_1 1}{G_1}\right\}}_{J(t)}\gamma(0) \qquad \tau_2 = \frac{\eta_2}{G_2}$$

$$\gamma = \underbrace{\left\{\left[1 - exp\left(-\frac{t}{\tau_2}\right)\right]\frac{G_1}{G_2} + 1\right\}}_{J(t)}\gamma(0) \qquad \tau_2 = \frac{\eta_2}{G_2}$$

RELAXATION

Solving partial differential equation for $\dot{\gamma} = 0$ and the boundary condition given by:

$\sigma(0) = G_1\gamma$

We have

$$\sigma = \underbrace{\frac{G_1}{G_1+G_2}\left\{G_2 + G_1 \cdot exp\left(-\frac{t}{\tau'}\right)\right\}}_{G(t)}\gamma \qquad \tau' = \frac{\eta_2}{G_1+G_2}$$

Since

$\sigma_0 = G_1\gamma$

then

$$\sigma = \frac{G_1}{G_1 + G_2}\left\{G_2 + G_1 \cdot exp\left(-\frac{t}{\tau'}\right)\right\}\frac{\sigma_0}{G_1};$$

$$\boxed{\sigma = \frac{1}{G_1 + G_2}\left\{G_2 + G_1 \cdot exp\left(-\frac{t}{\tau'}\right)\right\}\sigma_0;}$$

In addition

$$\sigma_\infty = \frac{G_2}{G_1 + G_2}\sigma_0;$$

$$\sigma_\infty = \frac{1}{\frac{G_1}{G_2} + \frac{G_2}{G_2}}\sigma_0;$$

$$\frac{G_1}{G_2} = \frac{\sigma_0}{\sigma_\infty} - 1$$

Model 3a – Full analytical developments

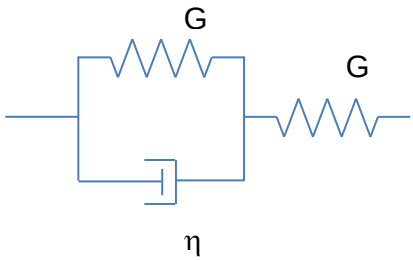

Stress-strain relationships in elements 1 and 2

$\sigma_1 = G_1\gamma_1$

$\sigma_2 = G_2\gamma_2 + \eta_2\dot{\gamma}_2$

Because elements 1 and 2 are in series, then

$\sigma_2 = \sigma_1 = \sigma$

$\gamma = \gamma_1 + \gamma_2$

We can manipulate equations as follows:

$\sigma_1 = \sigma = G_1\gamma_1 \Rightarrow \gamma_1 = \frac{\sigma}{G_1}$

$\sigma_1 = \sigma = G_1\gamma_1 \Rightarrow \dot{\sigma} = G_1\dot{\gamma}_1 \quad \Rightarrow \boxed{\dot{\gamma}_1 = \frac{\dot{\sigma}}{G_1}}$

$\sigma_2 = \sigma = G_2\gamma_2 + \eta_2\dot{\gamma}_2 \Rightarrow \boxed{\dot{\gamma}_2 = \frac{\sigma - G_2\gamma_2}{\eta_2} = \frac{\sigma - G_2(\gamma - \gamma_1)}{\eta_2} = \frac{\sigma}{\eta_2} - \frac{G_2}{\eta_2}\gamma + \frac{G_2}{\eta_2}\gamma_1 = \frac{\sigma}{\eta_2} - \frac{G_2}{\eta_2}\gamma + \frac{G_2}{\eta_2}\frac{\sigma}{G_1}}$

$\gamma = \gamma_1 + \gamma_2 \Rightarrow \dot{\gamma} = \dot{\gamma}_1 + \dot{\gamma}_2$

We can then write

$\dot{\gamma} = \dot{\gamma}_1 + \dot{\gamma}_2;$

$\dot{\gamma} = \left(\frac{\dot{\sigma}}{G_1}\right) + \left(\frac{\sigma}{\eta_2} - \frac{G_2}{\eta_2}\gamma + \frac{G_2}{\eta_2}\frac{\sigma}{G_1}\right);$

$\dot{\gamma} + \frac{G_2}{\eta_2}\gamma = \frac{\dot{\sigma}}{G_1} + \left(\frac{1}{\eta_2} + \frac{G_2}{\eta_2}\frac{1}{G_1}\right)\sigma;$

Multiplying by $G_1\eta_2$ we can finally write

$$G_1\eta_2\dot{\gamma} + G_1\eta_2\frac{G_2}{\eta_2}\gamma = G_1\eta_2\frac{\dot{\sigma}}{G_1} + \left(G_1\eta_2\frac{1}{\eta_2} + G_1\eta_2\frac{G_2}{\eta_2}\frac{1}{G_1}\right)\sigma;$$

$$\boxed{G_1\eta_2\dot{\gamma} + G_1G_2\gamma = \eta_2\dot{\sigma} + (G_1 + G_2)\sigma;}$$

CREEP

Solving partial differential equation for $\dot{\sigma} = 0$

$$G_1\eta_2\dot{\gamma} + G_1G_2\gamma = (G_1 + G_2)\sigma;$$

$$G_1\eta_2\frac{d\gamma}{dt}+G_1G_2\gamma=(G_1+G_2)\sigma;$$

$$G_1\eta_2\frac{d\gamma}{dt}=(G_1+G_2)\sigma-G_1G_2\gamma;$$

$$\frac{d\gamma}{(G_1+G_2)\sigma-G_1G_2\gamma}=\frac{1}{G_1\eta_2}dt;$$

$$\int\frac{d\gamma}{(G_1+G_2)\sigma-G_1G_2\gamma}=\int\frac{1}{G_1\eta_2}dt\,;$$

$$-\frac{ln[(G_1+G_2)\sigma-G_1G_2\gamma]}{G_1G_2}=\frac{1}{G_1\eta_2}t+C\,;\qquad\qquad(C=constant)$$

$$ln[(G_1+G_2)\sigma-G_1G_2\gamma]=-\frac{G_1G_2}{G_1\eta_2}t+G_1G_2C$$

$$exp\{ln[(G_1+G_2)\sigma-G_1G_2\gamma]\}=exp\left\{-\frac{G_2}{\eta_2}t+G_1G_2C\right\}$$

$$(G_1+G_2)\sigma-G_1G_2\gamma=exp\left\{-\frac{G_2}{\eta_2}t\right\}exp\{G_1G_2C\}$$

$$(G_1+G_2)\sigma-G_1G_2\gamma=C^*exp\left\{-\frac{G_2}{\eta_2}t\right\}\qquad\qquad(C^*=exp\{G_1G_2C\})$$

$$G_1G_2\gamma=(G_1+G_2)\sigma-C^*exp\left\{-\frac{G_2}{\eta_2}t\right\}$$

$$\gamma=\frac{G_1+G_2}{G_1G_2}\sigma-C^*exp\left\{-\frac{G_2}{\eta_2}t\right\}$$

The boundary condition is given by:

$$\gamma(0)=\frac{\sigma}{G_1}$$

and the constant C* can be determined as follows:

$$\frac{\sigma}{G_1}=\frac{G_1+G_2}{G_1G_2}\sigma-C^*exp\left\{-\frac{G_2}{\eta_2}\cdot0\right\}$$

$$C^*=\frac{G_1+G_2}{G_1G_2}\sigma-\frac{\sigma}{G_1}=\quad\left(\frac{G_1+G_2}{G_1G_2}-\frac{1}{G_1}\right)\sigma=\left(\frac{G_1+G_2}{G_2}-1\right)\frac{\sigma}{G_1}=\left(\frac{G_1+G_2-G_2}{G_2}\right)\frac{\sigma}{G_1}=\frac{\sigma}{G_2}$$

We can finally write

$$\gamma=\frac{G_1+G_2}{G_1G_2}\sigma-C^*exp\left\{-\frac{G_2}{\eta_2}t\right\}=\frac{G_1+G_2}{G_1G_2}\sigma-\frac{\sigma}{G_2}exp\left\{-\frac{G_2}{\eta_2}t\right\}=$$

$$=\frac{G_1}{G_1G_2}\sigma+\frac{G_2}{G_1G_2}\sigma-\frac{\sigma}{G_2}exp\left\{-\frac{G_2}{\eta_2}t\right\}=\frac{1}{G_2}\sigma+\frac{1}{G_1}\sigma-\frac{\sigma}{G_2}exp\left\{-\frac{G_2}{\eta_2}t\right\}=$$

$$= \frac{\sigma}{G_2} + \frac{\sigma}{G_1} - \frac{\sigma}{G_2} exp\left\{-\frac{G_2}{\eta_2} t\right\} = \left\{\left[1 - exp\left(-\frac{t}{\eta_2/G_2}\right)\right]\frac{1}{G_2} + \frac{1}{G_1}\right\}\sigma$$

Finally

$$\gamma = \underbrace{\left\{\left[1 - exp\left(-\frac{t}{\tau_2}\right)\right]\frac{1}{G_2} + \frac{1}{G_1}\right\}}_{J(t)}\sigma \qquad \tau_2 = \frac{\eta_2}{G_2}$$

RELAXATION

Solving partial differential equation for $\dot{\gamma} = 0$

$$G_1 G_2 \gamma = \eta_2 \dot{\sigma} + (G_1 + G_2)\sigma;$$

$$G_1 G_2 \gamma = \eta_2 \frac{d\sigma}{dt} + (G_1 + G_2)\sigma;$$

$$G_1 G_2 \gamma - (G_1 + G_2)\sigma = \eta_2 \frac{d\sigma}{dt};$$

$$\frac{1}{\eta_2} dt = \frac{d\sigma}{G_1 G_2 \gamma - (G_1 + G_2)\sigma};$$

$$\int \frac{1}{\eta_2} dt = \int \frac{d\sigma}{G_1 G_2 \gamma - (G_1 + G_2)\sigma};$$

$$\frac{1}{\eta_2} t = -\frac{ln[G_1 G_2 \gamma - (G_1 + G_2)\sigma]}{G_1 + G_2} + C;$$

$$\frac{ln[G_1 G_2 \gamma - (G_1 + G_2)\sigma]}{G_1 + G_2} = C - \frac{1}{\eta_2} t;$$

$$ln[G_1 G_2 \gamma - (G_1 + G_2)\sigma] = (G_1 + G_2)C - \frac{G_1 + G_2}{\eta_2} t;$$

$$exp\{ln[G_1 G_2 \gamma - (G_1 + G_2)\sigma]\} = exp\left\{(G_1 + G_2)C - \frac{G_1 + G_2}{\eta_2} t\right\};$$

$$G_1 G_2 \gamma - (G_1 + G_2)\sigma = exp\{(G_1 + G_2)C\} exp\left\{-\frac{G_1 + G_2}{\eta_2} t\right\};$$

$$G_1 G_2 \gamma - (G_1 + G_2)\sigma = exp\{(G_1 + G_2)C\} exp\left\{-\frac{G_1 + G_2}{\eta_2} t\right\};$$

$$(G_1 + G_2)\sigma = G_1 G_2 \gamma - exp\{(G_1 + G_2)C\} exp\left\{-\frac{G_1 + G_2}{\eta_2} t\right\};$$

$$\sigma = \frac{G_1 G_2}{G_1 + G_2}\gamma - \frac{exp\{(G_1 + G_2)C\}}{G_1 + G_2} exp\left\{-\frac{G_1 + G_2}{\eta_2} t\right\};$$

$$\sigma = \frac{G_1 G_2}{G_1 + G_2}\gamma - C^* exp\left\{-\frac{G_1 + G_2}{\eta_2}t\right\};$$

The boundary condition is given by:

$\sigma(0) = G_1\gamma$

and the constant C* can be determined as follows:

$$G_1\gamma = \frac{G_1 G_2}{G_1 + G_2}\gamma - C^* exp\left\{-\frac{G_1 + G_2}{\eta_2}0\right\};$$

$$C^* = \frac{G_1 G_2}{G_1 + G_2}\gamma - G_1\gamma = \left(\frac{G_1 G_2}{G_1 + G_2} - G_1\right)\gamma = \left(\frac{G_1 G_2 - G_1^2 - G_1 G_2}{G_1 + G_2}\right)\gamma = \left(-\frac{G_1^2}{G_1 + G_2}\right)\gamma$$

We can finally write

$$\sigma = \frac{G_1 G_2}{G_1 + G_2}\gamma - \left(-\frac{G_1^2}{G_1 + G_2}\right)\gamma \cdot exp\left\{-\frac{G_1 + G_2}{\eta_2}t\right\};$$

$$\sigma = \frac{G_1}{G_1 + G_2}\left\{G_2\gamma + G_1\gamma \cdot exp\left\{-\frac{G_1 + G_2}{\eta_2}t\right\}\right\};$$

$$\sigma = \frac{G_1}{G_1 + G_2}\left\{G_2 + G_1 \cdot exp\left(-\frac{G_1 + G_2}{\eta_2}t\right)\right\}\gamma;$$

$$\sigma = \frac{G_1}{G_1 + G_2}\left\{G_2 + G_1 \cdot exp\left(-\frac{G_1 + G_2}{\eta_2}t\right)\right\}\gamma;$$

By posing

$$\tau' = \frac{\eta_2}{G_1 + G_2}$$

Then

$$\sigma = \underbrace{\frac{G_1}{G_1 + G_2}\left\{G_2 + G_1 \cdot exp\left(-\frac{t}{\tau'}\right)\right\}}_{\boldsymbol{G(t)}}\gamma$$

Since

$\sigma_0 = G_1\gamma$

then

$$\sigma = \frac{G_1}{G_1 + G_2}\left\{G_2 + G_1 \cdot exp\left(-\frac{t}{\tau'}\right)\right\}\frac{\sigma_0}{G_1};$$

$$\boxed{\sigma = \frac{1}{G_1 + G_2}\left\{G_2 + G_1 \cdot exp\left(-\frac{t}{\tau'}\right)\right\}\sigma_0;}$$

In addition

$$\sigma_\infty = \frac{G_2}{G_1 + G_2}\sigma_0;$$

$$\sigma_\infty = \frac{1}{\frac{G_1}{G_2} + \frac{G_2}{G_2}}\sigma_0;$$

$$\frac{G_1}{G_2} = \frac{\sigma_0}{\sigma_\infty} - 1$$

Model 3b

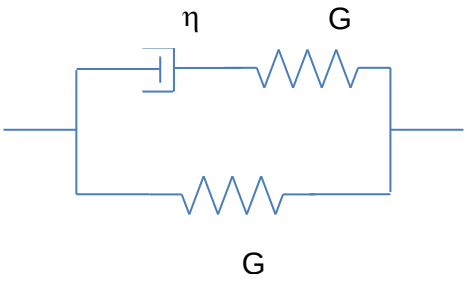

Stress-strain relationships in elements 1 and 2

$$\dot{\gamma}_2 = \frac{\dot{\sigma}_2}{G_2} + \frac{\sigma_2}{\eta_2}$$

$$\dot{\gamma}_1 = \frac{\dot{\sigma}_1}{G_1}$$

Because elements 1 and 2 are in parallel, then

$$\sigma = \sigma_1 + \sigma_2$$

$$\dot{\gamma} = \dot{\gamma}_1 = \dot{\gamma}_2$$

Since

$$\dot{\sigma} = G_1\dot{\gamma} + G_2\left(\dot{\gamma} - \frac{\sigma_2}{\eta_2}\right);$$

$$\dot{\sigma} = G_1\dot{\gamma} + G_2\dot{\gamma} - G_2\frac{\sigma_2}{\eta_2};$$

$$\dot{\sigma} = (G_1 + G_2)\dot{\gamma} - G_2\frac{\sigma - \sigma_1}{\eta_2};$$

$$\dot{\sigma} = (G_1 + G_2)\dot{\gamma} - \frac{G_2}{\eta_2}\sigma + \frac{G_2}{\eta_2}\sigma_1;$$

$$\dot{\sigma} = (G_1 + G_2)\dot{\gamma} - \frac{G_2}{\eta_2}\sigma + \frac{G_2}{\eta_2}G_1\gamma;$$

$$\dot{\sigma} + \frac{G_2}{\eta_2}\sigma = (G_1 + G_2)\dot{\gamma} + \frac{G_2}{\eta_2}G_1\gamma;$$

$$\boxed{\dot{\sigma} + \frac{\sigma}{\tau_2} = (G_1 + G_2)\dot{\gamma} + \frac{G_1}{\tau_2}\gamma; \qquad \left(\tau_2 = \frac{\eta_2}{G_2}\right)}$$

CREEP

Solving partial differential equation for $\dot{\sigma} = 0$ and the boundary condition given by:

$$\gamma(0) = \frac{\sigma}{G_1 + G_2}$$

we can write

$$\gamma = \underbrace{\left\{\frac{1}{G_1} - \frac{G_2}{G_1(G_1 + G_2)} exp\left(-\frac{t}{\tau'}\right)\right\}}_{J(t)}\sigma \qquad \tau' = \frac{G_1 + G_2}{G_1}\frac{\eta_2}{G_2}$$

$$\gamma = \underbrace{\left\{\frac{1}{G_1} - \frac{G_2}{G_1(G_1 + G_2)} exp\left(-\frac{t}{\tau'}\right)\right\}}_{J(t)}\gamma(0)(G_1 + G_2) \qquad \tau' = \frac{G_1 + G_2}{G_1}\frac{\eta_2}{G_2}$$

$$\gamma = \underbrace{\left\{\frac{(G_1 + G_2)}{G_1} - \frac{G_2(G_1 + G_2)}{G_1(G_1 + G_2)} exp\left(-\frac{t}{\tau'}\right)\right\}}_{J(t)}\gamma(0) \qquad \tau' = \frac{G_1 + G_2}{G_1}\frac{\eta_2}{G_2}$$

$$\gamma = \underbrace{\left\{1 + \frac{G_2}{G_1} - \frac{G_2}{G_1} exp\left(-\frac{t}{\tau'}\right)\right\}}_{J(t)}\gamma(0) \qquad \tau' = \frac{G_1 + G_2}{G_1}\frac{\eta_2}{G_2}$$

RELAXATION

Solving partial differential equation for $\dot{\gamma} = 0$ and the boundary condition given by:
$\sigma(0) = (G_1 + G_2)\gamma$

We have

$$\sigma = \underbrace{\left\{G_1 + G_2 \exp\left(-\frac{t}{\tau_2}\right)\right\}}_{G(t)}\gamma \qquad \tau_2 = \frac{\eta_2}{G_2}$$

Since

$\sigma_0 = (G_1 + G_2)\gamma$

then

$$\sigma = \left[G_1 + G_2 \exp\left(-\frac{t}{\tau_2}\right)\right]\frac{\sigma_0}{G_1 + G_2}$$

In addition

$\sigma_\infty = \frac{G_1}{G_1 + G_2}\sigma_0;$

$\frac{G_1 + G_2}{G_1} = \frac{\sigma_0}{\sigma_\infty};$

$$\frac{G_2}{G_1} = \frac{\sigma_0}{\sigma_\infty} - 1;$$

ANNEX E

CONSTITUTIVE EQUATIONS DEVELOPMENT FOR 3-ELEMENT MODEL (WITH ADDITIONAL SPRING FOR COMPLIANCE SYSTEM)

Model (3+1)a

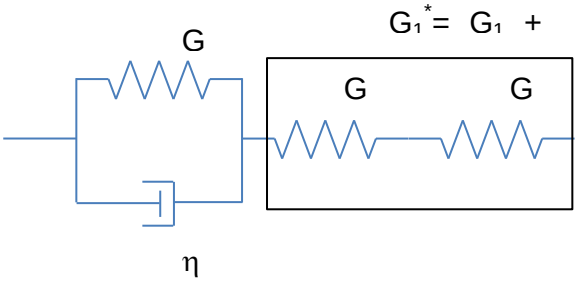

Stress-strain relationships in elements 1 and 2

$\sigma_1 = G_1^* \gamma_1$

$\sigma_2 = G_2 \gamma_2 + \eta_2 \dot{\gamma}_2$

Because elements 1 and 2 are in series, then

$\sigma_2 = \sigma_1 = \sigma$

$\gamma = \gamma_1^* + \gamma_2$

With similar developments as for Model (3+1)a

$$\boxed{G_1^* \eta_2 \dot{\gamma} + G_1^* G_2 \gamma = \eta_2 \dot{\sigma} + (G_1^* + G_2)\sigma;}$$

CREEP

Solving partial differential equation for $\dot{\sigma} = 0$ and the boundary condition given by:

$$\gamma(0) = \frac{\sigma}{G_1^*}$$

we can write (according to the equation derived for Model(3+1)a)

$$\gamma = \underbrace{\left\{\left[1 - exp\left(-\frac{t}{\tau_2}\right)\right]\frac{G_1^*}{G_2} + 1\right\}}_{J(t)}\gamma(0) \qquad \tau_2 = \frac{\eta_2}{G_2}$$

$$\gamma = \underbrace{\left\{\left[1 - exp\left(-\frac{t}{\tau_2}\right)\right]\frac{G_1^*}{G_2} + 1\right\}}_{J(t)}\gamma(0) \qquad \tau_2 = \frac{\eta_2}{G_2}$$

$$\boxed{\gamma = \left\{\left[1 - exp\left(-\frac{t}{\tau_2}\right)\right]\frac{(G_1 + G_3)}{G_2} + 1\right\}\gamma(0) \qquad \tau_2 = \frac{\eta_2}{G_2}}$$

RELAXATION

Solving partial differential equation for $\dot{\gamma} = 0$ and the boundary condition given by:
$\sigma(0) = G_1^* \gamma$

we can write (according to the equation derived for Model (3+1)a)

$$\sigma = \frac{1}{G_1^* + G_2}\left\{G_2 + G_1^* \cdot exp\left(-\frac{t}{\tau'}\right)\right\}\sigma_0; \qquad \tau' = \frac{\eta_2}{G_1^* + G_2}$$

$$\boxed{\sigma = \frac{1}{G_1 + G_3 + G_2}\left\{G_2 + (G_1 + G_3) \cdot exp\left(-\frac{t}{\tau'}\right)\right\}\sigma_0; \qquad \tau' = \frac{\eta_2}{G_1 + G_3 + G_2}}$$

In addition

$$\frac{G_1^*}{G_2} = \frac{\sigma_0}{\sigma_\infty} - 1$$

$$\frac{G_1 + G_3}{G_2} = \frac{\sigma_0}{\sigma_\infty} - 1$$

Model (3+1)b

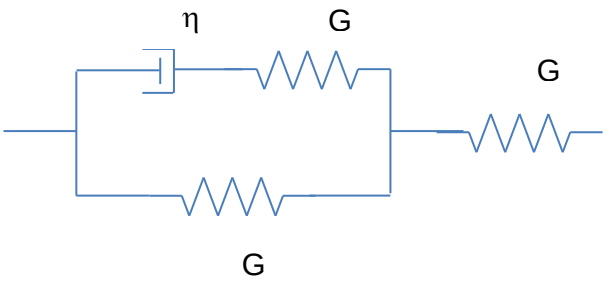

Stress-strain relationships in elements 1, 2 and 3 are

$$\dot{\gamma}_2 = \frac{\dot{\sigma}_2}{G_2} + \frac{\sigma_2}{\eta_2}$$

$$\dot{\gamma}_1 = \frac{\dot{\sigma}_1}{G_1}$$

$$\dot{\gamma}_3 = \frac{\dot{\sigma}_3}{G_3}$$

Because elements 1 and 2 are in parallel, in turn in series with element 3 then

$$\sigma = \sigma_1 + \sigma_2 = \sigma_3$$

$$\dot{\gamma}_1 = \dot{\gamma}_2$$

$$\dot{\gamma} = \dot{\gamma}_1 + \dot{\gamma}_3$$

Since

$$\dot{\sigma} = G_1\dot{\gamma}_1 + G_2\left(\dot{\gamma}_1 - \frac{\sigma_2}{\eta_2}\right);$$

$$\dot{\sigma} = G_1\dot{\gamma}_1 + G_2\dot{\gamma}_1 - \frac{G_2}{\eta_2}\sigma_2;$$

$$\dot{\sigma} = (G_1 + G_2)\dot{\gamma}_1 - \frac{G_2}{\eta_2}\sigma_2;$$

$$\dot{\sigma} = (G_1 + G_2)(\dot{\gamma} - \dot{\gamma}_3) - \frac{G_2}{\eta_2}(\sigma - \sigma_1);$$

$$\dot{\sigma} = (G_1 + G_2)\left(\dot{\gamma} - \frac{\dot{\sigma}_3}{G_3}\right) - \frac{G_2}{\eta_2}(\sigma - G_1\gamma_1);$$

$$\dot{\sigma} = (G_1 + G_2)\left(\dot{\gamma} - \frac{\dot{\sigma}}{G_3}\right) - \frac{G_2}{\eta_2}(\sigma - G_1\gamma_1);$$

$$\dot{\sigma} = (G_1 + G_2)\dot{\gamma} - \frac{G_1 + G_2}{G_3}\dot{\sigma} - \frac{G_2}{\eta_2}\sigma + \frac{G_2}{\eta_2}G_1\gamma_1;$$

$$\dot{\sigma} = (G_1 + G_2)\dot{\gamma} - \frac{G_1 + G_2}{G_3}\dot{\sigma} - \frac{G_2}{\eta_2}\sigma + \frac{G_2}{\eta_2}G_1(\gamma - \gamma_3);$$

$$\dot{\sigma} = (G_1 + G_2)\dot{\gamma} - \frac{G_1 + G_2}{G_3}\dot{\sigma} - \frac{G_2}{\eta_2}\sigma + \frac{G_2}{\eta_2}G_1\left(\gamma - \frac{\sigma}{G_3}\right);$$

$$\dot{\sigma} = (G_1 + G_2)\dot{\gamma} - \frac{G_1 + G_2}{G_3}\dot{\sigma} - \frac{G_2}{\eta_2}\sigma + \frac{G_1 G_2}{\eta_2}\gamma - \frac{G_1 G_2}{\eta_2 G_3}\sigma;$$

$$\dot{\sigma} + \frac{G_1 + G_2}{G_3}\dot{\sigma} + \frac{G_2}{\eta_2}\sigma + \frac{G_1 G_2}{\eta_2 G_3}\sigma = (G_1 + G_2)\dot{\gamma} + \frac{G_1 G_2}{\eta_2}\gamma;$$

$$\left(1 + \frac{G_1 + G_2}{G_3}\right)\dot{\sigma} + \left(\frac{G_2}{\eta_2} + \frac{G_1 G_2}{\eta_2 G_3}\right)\sigma = (G_1 + G_2)\dot{\gamma} + \frac{G_1 G_2}{\eta_2}\gamma;$$

$$\left(1 + \frac{G_1 + G_2}{G_3}\right)\dot{\sigma} + \left(1 + \frac{G_1}{G_3}\right)\frac{G_2}{\eta_2}\sigma = (G_1 + G_2)\dot{\gamma} + G_1\frac{G_2}{\eta_2}\gamma;$$

$$\boxed{\left(1 + \frac{G_1 + G_2}{G_3}\right)\dot{\sigma} + \left(1 + \frac{G_1}{G_3}\right)\frac{\sigma}{\tau_2} = (G_1 + G_2)\dot{\gamma} + \frac{G_1}{\tau_2}\gamma; \qquad \left(\tau_2 = \frac{\eta_2}{G_2}\right)}$$

$$\boxed{\dot{\sigma} + \frac{\sigma}{\tau_2} = (G_1 + G_2)\dot{\gamma} + \frac{G_1}{\tau_2}\gamma; \qquad \left(\tau_2 = \frac{\eta_2}{G_2}\right) \qquad \text{Model } (3+1)\text{b}}$$

CREEP

Initial condition:

$$\sigma = \gamma_1(0)\, G_1 + \gamma_2(0)\, G_2 = \gamma_1(0)(G_1 + G_2)$$

$$\gamma_0 = \gamma_1(0) + \gamma_3(0) = \left(\frac{1}{G_1 + G_2} + \frac{1}{G_3}\right)\sigma$$

Partial differential equation is solved for $\dot{\sigma} = 0$:

$$\left(1 + \frac{G_1}{G_3}\right)\frac{\sigma}{\tau_2} = (G_1 + G_2)\dot{\gamma} + \frac{G_1}{\tau_2}\gamma;$$

$$\left(1 + \frac{G_1}{G_3}\right)\frac{\sigma}{\tau_2} = (G_1 + G_2)\frac{d\gamma}{dt} + \frac{G_1}{\tau_2}\gamma;$$

$$\left(1 + \frac{G_1}{G_3}\right)\frac{\sigma}{\tau_2} - \frac{G_1}{\tau_2}\gamma = (G_1 + G_2)\frac{d\gamma}{dt};$$

$$\frac{1}{G_1 + G_2}dt = \frac{d\gamma}{\left(1 + \frac{G_1}{G_3}\right)\frac{\sigma}{\tau_2} - \frac{G_1}{\tau_2}\gamma};$$

$$\int \frac{1}{G_1 + G_2}dt = \int \frac{d\gamma}{\left(1 + \frac{G_1}{G_3}\right)\frac{\sigma}{\tau_2} - \frac{G_1}{\tau_2}\gamma};$$

$$\frac{1}{G_1 + G_2}t + C = -\frac{ln\left[\left(1 + \frac{G_1}{G_3}\right)\frac{\sigma}{\tau_2} - \frac{G_1}{\tau_2}\gamma\right]}{\frac{G_1}{\tau_2}}$$

$$-\frac{G_1}{\tau_2}\frac{1}{G_1 + G_2}t - \frac{G_1}{\tau_2}C = ln\left[\left(1 + \frac{G_1}{G_3}\right)\frac{\sigma}{\tau_2} - \frac{G_1}{\tau_2}\gamma\right]$$

$$exp\left(-\frac{G_1}{\tau_2}\frac{1}{G_1+\ G_2}t-\frac{G_1}{\tau_2}C\right)=\left(1+\frac{G_1}{G_3}\right)\frac{\sigma}{\tau_2}-\frac{G_1}{\tau_2}\gamma$$

$$\frac{G_1}{\tau_2}\gamma=\left(1+\frac{G_1}{G_3}\right)\frac{\sigma}{\tau_2}-exp\left(-\frac{G_1}{\tau_2}\frac{1}{G_1+\ G_2}t-\frac{G_1}{\tau_2}C\right)$$

$$\gamma=\left(1+\frac{G_1}{G_3}\right)\frac{\sigma}{G_1}-\frac{\tau_2}{G_1}exp\left(-\frac{G_1}{\tau_2}\frac{1}{G_1+\ G_2}t-\frac{G_1}{\tau_2}C\right)$$

$$\gamma=\left(1+\frac{G_1}{G_3}\right)\frac{\sigma}{G_1}-\frac{\tau_2}{G_1}\left[exp\left(-\frac{G_1}{\tau_2}\frac{1}{G_1+\ G_2}t\right)\cdot exp\left(-\frac{G_1}{\tau_2}C\right)\right]$$

$$\gamma=\left(1+\frac{G_1}{G_3}\right)\frac{\sigma}{G_1}-\left[exp\left(-\frac{G_1}{\tau_2}\frac{1}{G_1+\ G_2}t\right)\cdot\frac{\tau_2}{G_1}exp\left(-\frac{G_1}{\tau_2}C\right)\right]$$

$$\gamma=\left(1+\frac{G_1}{G_3}\right)\frac{\sigma}{G_1}-\left[exp\left(-\frac{G_1}{\tau_2}\frac{1}{G_1+\ G_2}t\right)\cdot C^*\right]\qquad\left[C^*=\frac{\tau_2}{G_1}exp\left(-\frac{G_1}{\tau_2}C\right)\right]$$

Imposing the initial condition (t=0)

$$\gamma(0)=\left(\frac{1}{G_1+\ G_2}+\frac{1}{G_3}\right)\sigma=\left(1+\frac{G_1}{G_3}\right)\frac{\sigma}{G_1}-C^*$$

$$C^*=\left(1+\frac{G_1}{G_3}\right)\frac{\sigma}{G_1}-\left(\frac{1}{G_1+\ G_2}+\frac{1}{G_3}\right)\sigma$$

$$C^*=\left(\frac{1}{G_1}+\frac{1}{G_3}\right)\sigma-\left(\frac{1}{G_1+\ G_2}+\frac{1}{G_3}\right)\sigma$$

$$C^*=\left[\left(\frac{1}{G_1}+\frac{1}{G_3}\right)-\left(\frac{1}{G_1+\ G_2}+\frac{1}{G_3}\right)\right]\sigma$$

$$C^*=\left[\frac{1}{G_1}+\frac{1}{G_3}-\frac{1}{G_1+\ G_2}-\frac{1}{G_3}\right]\sigma$$

$$C^*=\left[\frac{1}{G_1}-\frac{1}{G_1+\ G_2}\right]\sigma$$

we finally have

$$\gamma=\left(1+\frac{G_1}{G_3}\right)\frac{\sigma}{G_1}-\left[\left(\frac{1}{G_1}-\frac{1}{G_1+\ G_2}\right)exp\left(-\frac{G_1}{\tau_2}\frac{1}{G_1+\ G_2}t\right)\cdot\sigma\right]$$

$$\gamma=\left[\left(1+\frac{G_1}{G_3}\right)\frac{1}{G_1}-\left(\frac{1}{G_1}-\frac{1}{G_1+\ G_2}\right)exp\left(-\frac{G_1}{\tau_2}\frac{1}{G_1+\ G_2}t\right)\right]\sigma$$

$$\gamma=\left[\left(\frac{1}{G_1}+\frac{1}{G_3}\right)-\frac{G_2}{G_1(\ G_1+\ G_2)}exp\left(-\frac{t}{\tau'}\right)\right]\sigma\qquad\tau'=\frac{G_1+G_2}{G_1}\frac{\eta_2}{G_2}$$

$$\gamma=\left[\left(\frac{1}{G_1}+\frac{1}{G_3}\right)-\frac{G_2}{G_1(\ G_1+\ G_2)}exp\left(-\frac{t}{\tau'}\right)\right]\sigma\qquad\tau'=\frac{G_1+G_2}{G_1}\frac{\eta_2}{G_2}$$

Since

$$\gamma_0 = \left(\frac{1}{G_1 + G_2} + \frac{1}{G_3}\right)\sigma$$

$$\frac{\gamma(0)}{\frac{1}{G_1 + G_2} + \frac{1}{G_3}} = \sigma$$

$$\frac{\gamma(0)}{\frac{G_1 + G_2 + G_3}{(G_1 + G_2)G_3}} = \sigma$$

$$\frac{(G_1 + G_2)G_3}{G_1 + G_2 + G_3}\gamma(0) = \sigma$$

then

$$\gamma = \left[\left(\frac{1}{G_1} + \frac{1}{G_3}\right) - \frac{G_2}{G_1(G_1 + G_2)}exp\left(-\frac{t}{\tau'}\right)\right]\frac{(G_1 + G_2)G_3}{G_1 + G_2 + G_3}\gamma(0) \qquad \tau' = \frac{G_1 + G_2}{G_1}\frac{\eta_2}{G_2}$$

$$\gamma = \left[\left(\frac{1}{G_1} + \frac{1}{G_3}\right)\frac{(G_1 + G_2)G_3}{G_1 + G_2 + G_3} - \frac{G_2}{G_1(G_1 + G_2)}\frac{(G_1 + G_2)G_3}{G_1 + G_2 + G_3}exp\left(-\frac{t}{\tau'}\right)\right]\gamma(0)$$

$$\gamma = \left[\left(\frac{G_1 + G_3}{G_1G_3}\right)\frac{(G_1 + G_2)G_3}{G_1 + G_2 + G_3} - \frac{G_2}{G_1}\frac{G_3}{G_1 + G_2 + G_3}exp\left(-\frac{t}{\tau'}\right)\right]\gamma(0) \qquad \tau' = \frac{G_1 + G_2}{G_1}\frac{\eta_2}{G_2}$$

$$\gamma = \left[\left(\frac{G_1 + G_3}{G_1}\right)\frac{(G_1 + G_2)}{G_1 + G_2 + G_3} - \frac{G_2}{G_1}\frac{G_3}{G_1 + G_2 + G_3}exp\left(-\frac{t}{\tau'}\right)\right]\gamma(0) \qquad \tau' = \frac{G_1 + G_2}{G_1}\frac{\eta_2}{G_2}$$

$$\boxed{\gamma = \left[\frac{\left(1 + \frac{G_2}{G_1}\right)}{1 + \frac{G_2}{G_1 + G_3}} - \frac{G_2}{G_1}\frac{1}{1 + \frac{G_1}{G_3} + \frac{G_2}{G_3}}exp\left(-\frac{t}{\tau'}\right)\right]\gamma_0 \qquad \tau' = \frac{G_1 + G_2}{G_1}\frac{\eta_2}{G_2}}$$

$$\gamma = \underbrace{\left\{1 + \frac{G_2}{G_1} - \frac{G_2}{G_1}exp\left(-\frac{t}{\tau'}\right)\right\}}_{\hat{J}(t)}\gamma(0) \qquad \tau' = \frac{G_1 + G_2}{G_1}\frac{\eta_2}{G_2} \qquad \text{Model } (3+1)\text{b}$$

RELAXATION

Initial condition:

$$\gamma = \left(\frac{1}{G_1 + G_2} + \frac{1}{G_3}\right)\sigma_0$$

$$\gamma = \left[\frac{G_1 + G_2 + G_3}{(G_1 + G_2)G_3}\right]\sigma_0$$

$$\sigma_0 = \frac{(G_1 + G_2)G_3}{G_1 + G_2 + G_3}\gamma$$

Solving partial differential equation for $\dot{\gamma} = 0$:

$$\left(1 + \frac{G_1 + G_2}{G_3}\right)\dot{\sigma} + \left(1 + \frac{G_1}{G_3}\right)\frac{\sigma}{\tau_2} = \frac{G_1}{\tau_2}\gamma; \qquad \left(\tau_2 = \frac{\eta_2}{G_2}\right)$$

$$\left(1 + \frac{G_1 + G_2}{G_3}\right)\frac{d\sigma}{dt} + \left(1 + \frac{G_1}{G_3}\right)\frac{\sigma}{\tau_2} = \frac{G_1}{\tau_2}\gamma;$$

$$\left(1 + \frac{G_1 + G_2}{G_3}\right)\frac{d\sigma}{dt} = \frac{G_1}{\tau_2}\gamma - \left(1 + \frac{G_1}{G_3}\right)\frac{\sigma}{\tau_2};$$

$$\frac{\tau_2\left(1 + \frac{G_1 + G_2}{G_3}\right)}{G_1\gamma - \left(1 + \frac{G_1}{G_3}\right)\sigma}d\sigma = dt;$$

$$\tau_2\left(1 + \frac{G_1 + G_2}{G_3}\right)\int \frac{1}{G_1\gamma - \left(1 + \frac{G_1}{G_3}\right)\sigma}d\sigma = \int dt\,;$$

$$-\tau_2\left(1 + \frac{G_1 + G_2}{G_3}\right)\frac{ln\left[G_1\gamma - \left(1 + \frac{G_1}{G_3}\right)\sigma\right]}{\left(1 + \frac{G_1}{G_3}\right)} = t + C;$$

$$ln\left[G_1\gamma - \left(1 + \frac{G_1}{G_3}\right)\sigma\right] = -\frac{\left(1 + \frac{G_1}{G_3}\right)}{1 + \frac{G_1 + G_2}{G_3}}\frac{t}{\tau_2} - \frac{\left(1 + \frac{G_1}{G_3}\right)}{1 + \frac{G_1 + G_2}{G_3}}\frac{1}{\tau_2}C;$$

$$ln\left[G_1\gamma - \left(1 + \frac{G_1}{G_3}\right)\sigma\right] = -\frac{\left(\frac{G_1 + G_3}{G_3}\right)}{\frac{G_1 + G_2 + G_3}{G_3}}\frac{t}{\tau_2} - C'; \qquad C' = \frac{\left(1 + \frac{G_1}{G_3}\right)}{1 + \frac{G_1 + G_2}{G_3}}\frac{1}{\tau_2}C$$

$$ln\left[G_1\gamma - \left(1 + \frac{G_1}{G_3}\right)\sigma\right] = -\frac{G_1 + G_3}{G_1 + G_2 + G_3}\frac{t}{\tau_2} - C'\,;$$

$$G_1\gamma - \left(1 + \frac{G_1}{G_3}\right)\sigma = exp\left(-\frac{G_1 + G_3}{G_1 + G_2 + G_3}\frac{t}{\tau_2}\right)exp(-C')\,;$$

$$G_1\gamma - \left(1 + \frac{G_1}{G_3}\right)\sigma = C^*exp\left(-\frac{G_1 + G_3}{G_1 + G_2 + G_3}\frac{t}{\tau_2}\right); \qquad C^* = exp(-C')$$

$$\left(1 + \frac{G_1}{G_3}\right)\sigma = G_1\gamma - C^*exp\left(-\frac{G_1 + G_3}{G_1 + G_2 + G_3}\frac{t}{\tau_2}\right);$$

$$\sigma = \frac{G_1}{1 + \frac{G_1}{G_3}}\gamma - \frac{C^*}{1 + \frac{G_1}{G_3}}exp\left(-\frac{G_1 + G_3}{G_1 + G_2 + G_3}\frac{t}{\tau_2}\right); \qquad C^* = exp(-C')$$

Imposing the initial condition

$$\sigma_0 = \frac{1}{\frac{1}{G_1 + G_2} + \frac{1}{G_3}}\gamma = \frac{G_1}{1 + \frac{G_1}{G_3}}\gamma - \frac{C^*}{1 + \frac{G_1}{G_3}}$$

$$\left(\frac{1}{\frac{1}{G_1+\ G_2}+\frac{1}{G_3}}-\frac{G_1}{1+\frac{G_1}{G_3}}\right)\gamma=-\frac{C^*}{1+\frac{G_1}{G_3}}$$

$$\left(\frac{1}{\frac{1}{G_1+\ G_2}+\frac{1}{G_3}}\left(1+\frac{G_1}{G_3}\right)-\frac{G_1}{1+\frac{G_1}{G_3}}\left(1+\frac{G_1}{G_3}\right)\right)\gamma=-C^*$$

$$\left(\frac{1+\frac{G_1}{G_3}}{\frac{1}{G_1+\ G_2}+\frac{1}{G_3}}-G_1\right)\gamma=-C^*$$

$$\left(\frac{1+\frac{G_1}{G_3}-G_1\left(\frac{1}{G_1+\ G_2}+\frac{1}{G_3}\right)}{\frac{1}{G_1+\ G_2}+\frac{1}{G_3}}\right)\gamma=-C^*$$

$$\left(\frac{1+\frac{G_1}{G_3}-\frac{G_1}{G_1+\ G_2}-\frac{G_1}{G_3}}{\frac{1}{G_1+\ G_2}+\frac{1}{G_3}}\right)\gamma=-C^*$$

$$\left(\frac{1-\frac{G_1}{G_1+\ G_2}}{\frac{1}{G_1+\ G_2}+\frac{1}{G_3}}\right)\gamma=-C^*$$

$$\left(\frac{\frac{G_2}{G_1+\ G_2}}{\frac{1}{G_1+\ G_2}+\frac{1}{G_3}}\right)\gamma=-C^*$$

$$\left(\frac{G_2}{1+\frac{G_1+\ G_2}{G_3}}\right)\gamma=-C^*$$

$$C^*=-\left(\frac{G_2}{1+\frac{G_1+\ G_2}{G_3}}\right)\gamma$$

By substituting C^*

$$\sigma=\frac{G_1}{1+\frac{G_1}{G_3}}\gamma-\frac{-\left(\frac{G_2}{1+\frac{G_1+\ G_2}{G_3}}\right)\gamma}{1+\frac{G_1}{G_3}}exp\left(-\frac{G_1+G_3}{G_1+\ G_2+\ G_3}\frac{t}{\tau_2}\right);$$

$$\sigma = \frac{G_1}{1+\frac{G_1}{G_3}}\gamma + \frac{\left(\frac{G_2}{1+\frac{G_1+G_2}{G_3}}\right)\gamma}{1+\frac{G_1}{G_3}} exp\left(-\frac{G_1+G_3}{G_1+G_2+G_3}\frac{t}{\tau_2}\right);$$

$$\boxed{\sigma = \frac{1}{1+\frac{G_1}{G_3}}\left[G_1 + \left(\frac{G_2}{1+\frac{G_1+G_2}{G_3}}\right) exp\left(-\frac{G_1+G_3}{G_1+G_2+G_3}\frac{t}{\tau_2}\right)\right]\gamma;}$$

$$\sigma = \underbrace{\left\{G_1 + G_2 \exp\left(-\frac{t}{\tau_2}\right)\right\}}_{G(t)}\gamma \qquad \tau_2 = \frac{\eta_2}{G_2} \qquad \text{Model } (3+1)\text{b}$$

By substituting the initial stress σ(0):

$$\sigma = \frac{1}{1+\frac{G_1}{G_3}}\left[G_1 + \left(\frac{G_2}{1+\frac{G_1+G_2}{G_3}}\right) exp\left(-\frac{G_1+G_3}{G_1+G_2+G_3}\frac{t}{\tau_2}\right)\right]\frac{G_1+G_2+G_3}{(G_1+G_2)G_3}\sigma_0;$$

$$\sigma = \frac{1}{1+\frac{G_1}{G_3}}\left[\frac{1}{G_3}G_1(G_1+G_2+G_3) + \left(\frac{1}{G_3}\frac{G_2(G_1+G_2+G_3)}{\frac{G_1+G_2+G_3}{G_3}}\right) exp\left(-\frac{G_1+G_3}{G_1+G_2+G_3}\frac{t}{\tau_2}\right)\right]\frac{1}{(G_1+G_2)}\sigma_0;$$

$$\sigma = \frac{1}{1+\frac{G_1}{G_3}}\left[\frac{1}{G_3}G_1(G_1+G_2+G_3) + G_2 exp\left(-\frac{G_1+G_3}{G_1+G_2+G_3}\frac{t}{\tau_2}\right)\right]\frac{1}{(G_1+G_2)}\sigma_0;$$

$$\boxed{\sigma = \frac{1}{1+\frac{G_1}{G_3}}\left[G_1\left(\frac{G_1}{G_3}+\frac{G_2}{G_3}+1\right) + G_2 exp\left(-\frac{\frac{G_1}{G_3}+1}{\frac{G_1}{G_3}+\frac{G_2}{G_3}+1}\frac{t}{\tau_2}\right)\right]\frac{1}{(G_1+G_2)}\sigma_0; \qquad \left[\tau_2 = \frac{\eta_2}{G_2}\right]}$$

$$\sigma = \left[G_1 + G_2 \exp\left(-\frac{t}{\tau_2}\right)\right]\frac{\sigma_0}{G_1+G_2} \qquad \text{Model } (3+1)\text{b}$$

In addition:

$$\sigma_\infty = \frac{1}{1+\frac{G_1}{G_3}}\left[G_1\left(\frac{G_1}{G_3}+\frac{G_2}{G_3}+1\right)\right]\frac{1}{(G_1+G_2)}\sigma_0$$

$$\sigma_\infty = \frac{1}{\frac{G_1+G_3}{G_3}}\left[G_1\left(\frac{G_1}{G_3}+\frac{G_2}{G_3}+1\right)\right]\frac{1}{(G_1+G_2)}\sigma_0$$

$$\sigma_\infty = \frac{1}{G_1+G_3}\left[G_1\left(\frac{G_1}{G_3}G_3+\frac{G_2}{G_3}G_3+G_3\right)\right]\frac{1}{(G_1+G_2)}\sigma_0$$

$$\sigma_\infty = \frac{1}{G_1+G_3}[G_1(G_1+G_2+G_3)]\frac{1}{(G_1+G_2)}\sigma_0$$

$$\sigma_\infty = \frac{\frac{G_1}{G_3}+\frac{G_2}{G_3}+1}{\frac{G_1}{G_3}+1}\frac{1}{1+\frac{G_2}{G_1}}\sigma_0$$

$$\frac{\sigma_\infty}{\sigma_0} = \frac{\frac{G_1}{G_3}+\frac{G_2}{G_3}+1}{\frac{G_1}{G_3}+1}\frac{1}{1+\frac{G_2}{G_1}}$$

$$\boxed{\frac{\sigma_0}{\sigma_\infty} = \frac{\frac{G_1}{G_3}+1}{\frac{G_1}{G_3}+\frac{G_2}{G_3}+1}\left(1+\frac{G_2}{G_1}\right)}$$

ANNEX F

CONSTITUTIVE EQUATIONS DEVELOPMENT FOR 5-ELEMENT MODEL (WITH ADDITIONAL SPRING FOR COMPLIANCE SYSTEM)

Basic Kelvin Model

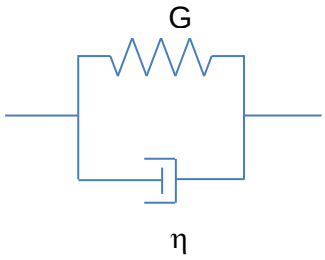

Constitutive equation:

$\sigma = G_1\gamma_1 + \eta_1\dot{\gamma}_1$

CREEP

Solving partial differential equation for $\dot{\sigma} = 0$ $(\sigma = constant)$, we can write

$\sigma = G_1\gamma_1 + \eta_1 \frac{d\gamma_1}{dt};$

$\sigma - G_1\gamma_1 = \eta_1 \frac{d\gamma_1}{dt};$

$dt = \eta_1 \frac{d\gamma_1}{\sigma - G_1\gamma_1};$

$\int dt = \eta_1 \int \frac{d\gamma_1}{\sigma - G_1\gamma_1};$

$t = -\frac{\eta_1}{G_1} ln(\sigma - G_1\gamma_1) + C;$

$ln(\sigma - G_1\gamma_1) = -\frac{t}{\frac{\eta_1}{G_1}} + C;$

$ln(\sigma - G_1\gamma_1) = -\frac{t}{\frac{\eta_1}{G_1}} + C; \qquad \tau_1 = \frac{\eta_1}{G_1}$

$\sigma - G_1\gamma_1 = C^* exp\left(-\frac{t}{\tau_1}\right); \qquad \tau_1 = \frac{\eta_1}{G_1}$

$\gamma_1 = \frac{\sigma}{G_1} - \frac{C^*}{G_1} exp\left(-\frac{t}{\tau_1}\right); \qquad \tau_1 = \frac{\eta_1}{G_1}$

Considering the boundary condition given by:

$\gamma(0) = 0$

we have

$$0 = \frac{\sigma}{G_1} - \frac{C^*}{G_1}; \qquad \tau_1 = \frac{\eta_1}{G_1}$$

and then

$$\gamma_1 = \frac{\sigma}{G_1}\left[1 - exp\left(-\frac{t}{\tau_1}\right)\right]; \qquad \tau_1 = \frac{\eta_1}{G_1} \tag{1}$$

Model (5+1)a

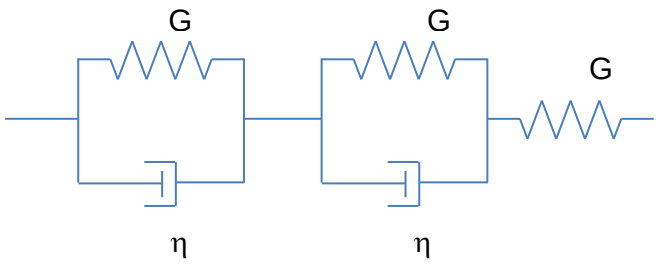

Stress-strain relationships in elements 1, 2, and 3

$$\sigma_1 = G_1\gamma_1 + \eta_1\dot{\gamma}_1$$
$$\sigma_2 = G_2\gamma_2 + \eta_2\dot{\gamma}_2 \tag{2}$$
$$\sigma_3 = G_3\gamma_3$$

Because elements 1, 2, and 3 are in series, then

$$\sigma_3 = \sigma_2 = \sigma_1 = \sigma$$
$$\gamma = \gamma_1 + \gamma_2 + \gamma_3 \tag{3}$$

CREEP (σ=constant, by using solution Analog No. 4)

By using Eqs (3) and using the solution from Eq. (1), we can write

$$\gamma = \gamma_1 + \gamma_2 + \gamma_3$$
$$\gamma = \frac{\sigma}{G_1}\left[1 - exp\left(-\frac{t}{\tau_1}\right)\right] + \frac{\sigma}{G_2}\left[1 - exp\left(-\frac{t}{\tau_2}\right)\right] + \frac{\sigma}{G_3} \tag{4}$$

where

$$\tau_1 = \frac{\eta_1}{G_1}\,; \tau_2 = \frac{\eta_2}{G_2}\,;$$

CREEP (σ=constant, by solving ODE)

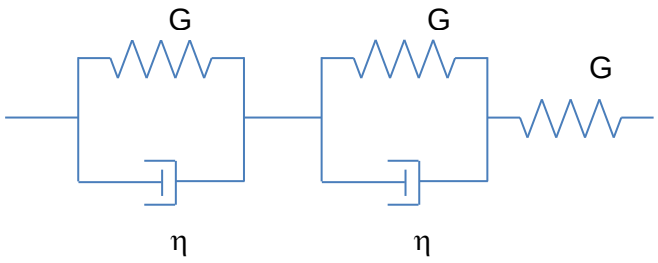

Stress-strain relationships in elements 1, 2, and 3

$$\sigma_1 = G_1\gamma_1 + \eta_1\dot{\gamma}_1$$
$$\sigma_2 = G_2\gamma_2 + \eta_2\dot{\gamma}_2 \quad (5)$$
$$\sigma_3 = G_3\gamma_3$$

Because elements 1, 2, and 3 are in series, then

$$\sigma_3 = \sigma_2 = \sigma_1 = \sigma$$
$$\gamma = \gamma_1 + \gamma_2 + \gamma_3 \quad (6)$$

Since

$$\dot{\sigma} = 0 \quad (7)$$

then

$$\dot{\gamma}_3 = 0 \quad (8)$$

From Eqs (5) and taking into account Eqs (6)

$$\dot{\gamma}_1 = \frac{\sigma}{\eta_1} - \frac{G_1}{\eta_1}\gamma_1$$
$$\dot{\gamma}_2 = \frac{\sigma}{\eta_2} - \frac{G_2}{\eta_2}\gamma_2$$

We can therefore write

$$\dot{\gamma} = \dot{\gamma}_1 + \dot{\gamma}_2 + \dot{\gamma}_3$$
$$\dot{\gamma} = \left(\frac{\sigma}{\eta_1} - \frac{G_1}{\eta_1}\gamma_1\right) + \left(\frac{\sigma}{\eta_2} - \frac{G_2}{\eta_2}\gamma_2\right) + 0$$
$$\dot{\gamma} = \frac{\sigma}{\eta_1} - \frac{G_1}{\eta_1}\gamma_1 + \frac{\sigma}{\eta_2} - \frac{G_2}{\eta_2}(\gamma - \gamma_1 - \gamma_3)$$
$$\dot{\gamma} = \frac{\sigma}{\eta_1} - \frac{G_1}{\eta_1}\gamma_1 + \frac{\sigma}{\eta_2} - \frac{G_2}{\eta_2}\gamma + \frac{G_2}{\eta_2}\gamma_1 + \frac{G_2}{\eta_2}\gamma_3$$
$$\dot{\gamma} = \frac{\sigma}{\eta_1} + \frac{\sigma}{\eta_2} - \left(\frac{G_1}{\eta_1} - \frac{G_2}{\eta_2}\right)\gamma_1 - \frac{G_2}{\eta_2}\gamma + \frac{G_2}{\eta_2}\gamma_3$$

$$\left(\frac{G_1}{\eta_1}-\frac{\dot{G}_2}{\eta_2}\right)\gamma_1=-\dot{\gamma}+\frac{\sigma}{\eta_1}+\frac{\sigma}{\eta_2}-\frac{G_2}{\eta_2}\gamma+\frac{G_2}{\eta_2}\frac{\sigma}{G_3} \tag{5}$$

$$\gamma_1=\frac{\left(\frac{1}{\eta_1}+\frac{1}{\eta_2}+\frac{1}{\eta_2}\frac{G_2}{G_3}\right)\sigma-\frac{G_2}{\eta_2}\gamma-\dot{\gamma}}{\frac{G_1}{\eta_1}-\frac{G_2}{\eta_2}} \tag{9}$$

By deriving Eq. (5)

$$\dot{\gamma}_1=\frac{\left(\frac{1}{\eta_1}+\frac{1}{\eta_2}+\frac{1}{\eta_2}\frac{G_2}{G_3}\right)\dot{\sigma}-\frac{G_2}{\eta_2}\dot{\gamma}-\ddot{\gamma}}{\frac{G_1}{\eta_1}-\frac{G_2}{\eta_2}}$$

$$\dot{\gamma}_1=\frac{-\frac{G_2}{\eta_2}\dot{\gamma}-\ddot{\gamma}}{\frac{G_1}{\eta_1}-\frac{G_2}{\eta_2}} \tag{10}$$

By combining Eqs. (5), (9), and (10), we have

$$\sigma=G_1\gamma_1+\eta_1\dot{\gamma}_1$$

$$\sigma=G_1\frac{\left(\frac{1}{\eta_1}+\frac{1}{\eta_2}+\frac{1}{\eta_2}\frac{G_2}{G_3}\right)\sigma-\frac{G_2}{\eta_2}\gamma-\dot{\gamma}}{\frac{G_1}{\eta_1}-\frac{G_2}{\eta_2}}+\eta_1\frac{-\frac{G_2}{\eta_2}\dot{\gamma}-\ddot{\gamma}}{\frac{G_1}{\eta_1}-\frac{G_2}{\eta_2}}$$

$$\sigma\left(\frac{G_1}{\eta_1}-\frac{G_2}{\eta_2}\right)=\left(\frac{G_1}{\eta_1}+\frac{G_1}{\eta_2}+\frac{G_1}{\eta_2}\frac{G_2}{G_3}\right)\sigma-\frac{G_1G_2}{\eta_2}\gamma-G_1\dot{\gamma}+-\eta_1\frac{G_2}{\eta_2}\dot{\gamma}-\eta_1\ddot{\gamma}$$

$$0=\left(-\frac{G_1}{\eta_1}+\frac{G_2}{\eta_2}+\frac{G_1}{\eta_1}+\frac{G_1}{\eta_2}+\frac{G_1}{\eta_2}\frac{G_2}{G_3}\right)\sigma-\frac{G_1G_2}{\eta_2}\gamma-G_1\dot{\gamma}+-\eta_1\frac{G_2}{\eta_2}\dot{\gamma}-\eta_1\ddot{\gamma}$$

$$0=\frac{1}{\eta_2}\left(G_1+G_2+\frac{G_1G_2}{G_3}\right)\sigma-\frac{G_1G_2}{\eta_2}\gamma-\left(G_1+\eta_1\frac{G_2}{\eta_2}\right)\dot{\gamma}-\eta_1\ddot{\gamma}$$

$$0=-\frac{1}{\eta_2}\left(G_1+G_2+\frac{G_1G_2}{G_3}\right)\sigma+\frac{G_1G_2}{\eta_2}\gamma+\left(G_1+\eta_1\frac{G_2}{\eta_2}\right)\dot{\gamma}+\eta_1\ddot{\gamma}$$

$$\eta_1\ddot{\gamma}+\left(G_1+\eta_1\frac{G_2}{\eta_2}\right)\dot{\gamma}+\frac{G_1G_2}{\eta_2}\gamma-\frac{1}{\eta_2}\left(G_1+G_2+\frac{G_1G_2}{G_3}\right)\sigma=0$$

$$\ddot{\gamma}+\left(\frac{G_1}{\eta_1}+\frac{G_2}{\eta_2}\right)\dot{\gamma}+\frac{G_1G_2}{\eta_1\eta_2}\gamma-\frac{1}{\eta_1\eta_2}\left(G_1+G_2+\frac{G_1G_2}{G_3}\right)\sigma=0 \tag{11}$$

The characteristic equation of the associated homogenous is:

$$x^2+\left(\frac{G_1}{\eta_1}+\frac{G_2}{\eta_2}\right)x+\frac{G_1G_2}{\eta_1\eta_2}=0;$$

The determinant of the equation $\Delta=(b^2-4ac)$ is

$$\left(\frac{G_1}{\eta_1}+\frac{G_2}{\eta_2}\right)^2-4\frac{G_1G_2}{\eta_1\eta_2}=\frac{G_1^2}{\eta_1^2}+\frac{G_2^2}{\eta_2^2}+2\frac{G_1}{\eta_1}\frac{G_2}{\eta_2}-4\frac{G_1G_2}{\eta_1\eta_2}=\frac{G_1^2}{\eta_1^2}+\frac{G_2^2}{\eta_2^2}-2\frac{G_1G_2}{\eta_1\eta_2}=\left(\frac{G_1}{\eta_1}-\frac{G_2}{\eta_2}\right)^2>0$$

The roots of the characteristic equations are:

$$x_1=\frac{-b-\sqrt{b^2-4ac}}{2a}=\frac{-\left(\frac{G_1}{\eta_1}+\frac{G_2}{\eta_2}\right)-\left(\frac{G_1}{\eta_1}-\frac{G_2}{\eta_2}\right)}{2}=\frac{-\frac{G_1}{\eta_1}-\frac{G_2}{\eta_2}-\frac{G_1}{\eta_1}+\frac{G_2}{\eta_2}}{2}=-\frac{G_1}{\eta_1}$$

$$x_2=\frac{-b+\sqrt{b^2-4ac}}{2a}=\frac{-\left(\frac{G_1}{\eta_1}+\frac{G_2}{\eta_2}\right)+\left(\frac{G_1}{\eta_1}-\frac{G_2}{\eta_2}\right)}{2}=\frac{-\frac{G_1}{\eta_1}-\frac{G_2}{\eta_2}+\frac{G_1}{\eta_1}-\frac{G_2}{\eta_2}}{2}=-\frac{G_2}{\eta_2};$$

The solution of the homogenous associated is therefore:

$$\gamma=c_1\exp(x_1t)+c_2\exp(x_2t)=c_1\exp\left(-\frac{G_1}{\eta_1}t\right)+c_2\exp\left(-\frac{G_2}{\eta_2}t\right)$$

A particular solution of Eq. (11) is given by

$$\frac{G_1G_2}{\eta_1\eta_2}\gamma-\frac{1}{\eta_1\eta_2}\left(G_1+G_2+\frac{G_1G_2}{G_3}\right)\sigma=0$$

$$\frac{G_1G_2}{\eta_1\eta_2}\gamma=\frac{1}{\eta_1\eta_2}\left(G_1+G_2+\frac{G_1G_2}{G_3}\right)\sigma$$

$$\gamma=\left(\frac{G_1}{G_1G_2}+\frac{G_2}{G_1G_2}+\frac{G_1G_2}{G_1G_2G_3}\right)\sigma$$

$$\gamma=\left(\frac{1}{G_1}+\frac{1}{G_2}+\frac{1}{G_3}\right)\sigma$$

The general solution of Eq. (11) is then given by:

$$\gamma=c_1\exp\left(-\frac{G_1}{\eta_1}t\right)+c_2\exp\left(-\frac{G_2}{\eta_2}t\right)+\left(\frac{1}{G_1}+\frac{1}{G_2}+\frac{1}{G_3}\right)\sigma \qquad (12)$$

Since,

$$\gamma(0)=\frac{\sigma}{G_3}$$

we can write:

$$\gamma=c_1+c_2+\left(\frac{1}{G_1}+\frac{1}{G_2}+\frac{1}{G_3}\right)\sigma=\frac{\sigma}{G_3}$$

$$c_1+c_2+\frac{\sigma}{G_1}+\frac{\sigma}{G_2}=0 \qquad (13)$$

For η_1=0 and G_1=∞, Eq. (13) becomes:

$$c_2 + \frac{\sigma}{G_2} = 0$$

$$c_2 = -\frac{\sigma}{G_2} \tag{14}$$

For η_2=0 and G_2=∞, Eq. (13) becomes:

$$c_1 + \frac{\sigma}{G_1} = 0$$

$$c_1 = -\frac{\sigma}{G_1} 0 \tag{15}$$

By replacing Eqs. (14) and (15) in Eq. (12), we can write:

$$\gamma = c_1 \exp\left(-\frac{G_1}{\eta_1} t\right) + c_2 \exp\left(-\frac{G_2}{\eta_2} t\right) + \left(\frac{1}{G_1} + \frac{1}{G_2} + \frac{1}{G_3}\right)\sigma\,;$$

$$\gamma = -\frac{\sigma}{G_1} \exp\left(-\frac{G_1}{\eta_1} t\right) - \frac{\sigma}{G_2} \exp\left(-\frac{G_2}{\eta_2} t\right) + \left(\frac{1}{G_1} + \frac{1}{G_2} + \frac{1}{G_3}\right)\sigma\,;$$

$$\gamma = \frac{\sigma}{G_1}\left[1 - \exp\left(-\frac{G_1}{\eta_1} t\right)\right] + \frac{\sigma}{G_2}\left[1 - \exp\left(-\frac{G_2}{\eta_2} t\right)\right] + \frac{\sigma}{G_3}; \tag{16}$$

which coincides with Eq. (4).